8-25-2014 12:00 AM

On the Interfacial Fracture Mechanics of Long-fibre Reinforced Polymer Composites

Ian N. Swentek
The University of Western Ontario

Supervisor
Dr. Jeffrey T. Wood
The University of Western Ontario

Graduate Program in Mechanical and Materials Engineering
A thesis submitted in partial fulfillment of the requirements for the degree in Doctor of Philosophy

Recommended Citation

Swentek, Ian N., "On the Interfacial Fracture Mechanics of Long-fibre Reinforced Polymer Composites" (2014). *Electronic Thesis and Dissertation Repository*. 2378.
https://ir.lib.uwo.ca/etd/2378

ON THE INTERFACIAL FRACTURE MECHANICS OF LONG-FIBRE REINFORCED POLYMER COMPOSITES

Thesis format: Monograph

by

Ian N. Swentek

Graduate Program in Engineering
Faculty of Mechanical and Materials Engineering

A thesis submitted in partial fulfillment
of the requirements for the degree of
Doctor of Philosophy

The School of Graduate and Postdoctoral Studies
The University of Western Ontario
London, Ontario, Canada

Abstract

Fibre-reinforced polymer composites are being widely adopted as the de facto material for automotive lightweight design, but lack the material models capable of accurately predicting fracture. To address this research gap, three large-scale experimental studies are undertaken to characterize thermoset polymers during cure, understand the fibre-matrix interfacial bond strength, and predict the fracture of random long-fibre composites via the energy of fracture. In conjunction with the Fraunhofer Project Center in London, Ontario, sample sheet moulded composites were used to verify the key findings with several industrial composite samples. With refined interfacial strength measurement methods, and accurate predictions of the composite residual strength, the fracture toughness of composites has been more accurately determined than previous research. These improvements directly translate to improved material and fracture models for fibre reinforced polymer composites. It is thus determined that utilizing the interfacial strength of a composite, failure can be predicted with increased confidence.

Keywords

Polymer Matrix Composites (PMCs)

Sheet Moulding Compound (SMC)

Random, long-fibre composite

Residual/internal Stress

Interface/interphase

Failure Criteria

Mechanical Testing

Computational Modeling

Composite Toughness

Dedication

To God: the ultimate source of all knowledge and comprehension.

To Frances: my wife, comforter, provider and friend.

Acknowledgments

Evgueni Bordatchev kindly donated time to perform laser and optical scanning of composite surface finishes.

Paul Charpentier graciously provided access to laboratory facilities vital to the analysis and characterization of the polymers studied in this thesis.

Clayton Cook from the University Machine Services does not get enough praise for his excellent customer service, prompt assistance, and willingness to help at personal expense.

Brian Dennis was a constant source for inspiration and specialized chemistry facilities needed to perform the fabrication of unique test specimens.

Ryan Guterman aided in performing the differential scanning calorimetric and thermal gravimetric analysis.

Dave Lunn loaned out videography systems and technical advice needed for multiple aspects of the experimental studies.

Zeinab Mousavi aided in arranging and performing the thermal tensile testing at McMaster University.

Tobias Potyra of the Fraunhofer Institute for Chemical Technology provided assistance and support in composite materials engineering.

Paul Sheller of Engineering Stores made substantial effort to provide service and response that translated to “improved” experimental testing.

Jeff Wood: mentor and supervisor extraordinaire.

Vanja Ugresic of the Fraunhofer Project Center provided the SMC samples and polyester resin along with insights into the SMC process.

Table of Contents

List of Tables

List of Figures

List of Appendices

Nomenclature

a	Thermal diffusivity
a_T	Temperature dependent shift factor for polymer modulus
A_1, A_2	Cure reaction rate constants
A_o	Initial area
C	Lap-shear force constant
C_α	Magnitude of diffusion during cure
C_1, C_2	Williams-Landel-Ferry constants for temperature shift of modulus
C_P	Heat capacity at constant pressure
d	Fibre diameter
d_e	Effective fibre diameter
D	Lap-shear disk diameter
dU	Change in elastic energy
da	Change in crack area
E	Young’s modulus
E_a	Activation energy for cure reaction
E_c	Composite Young’s modulus
E_f	Young’s modulus of the fibre
E_m	Young’s modulus of the matrix
E_L, E_U	Lower and upper Hashin-Shtrikman Young’s moduli
F	Normal force
g	Gravitational acceleration
G	Shear modulus
G_c	Critical strain energy release rate

G_f	Shear modulus of the fibre
G_m	Shear modulus of the matrix
G_I, G_{II}	Mode I, II strain energy release rate
G_{Ic}, G_{IIc}	Mode I, II critical strain energy release rate
$G_{Ic,f}$	Mode I critical strain energy release rate of the fibre
$G_{Ic,i}, G_{IIc,i}$	Mode I, II critical strain energy release rate of the interface
$G_{Ic,m}, G_{IIc,m}$	Mode I, II critical strain energy release rate of the matrix
$G_{pullout}$	Critical strain energy release rate due to pullout
G_r	Instantaneous rubbery component of shear modulus
G_r^{∞}	Fully developed rubbery component of shear modulus
H	Heat of reaction
ΔH_r	Total heat of reaction
I	Identity matrix
k	Thermal conductivity
k	Matrix strain hardening coefficient
K	Chemical reaction rate
K_c	Critical stress intensity factor
K_I, K_{II}	Mode I, II fracture toughness
K_{Ic}, K_{IIc}	Mode I, II critical fracture toughness
l	Fibre length
l_c	Critical fibre length for stress transfer
l_d	Fibre debond length
l_m	Mean fibre fragment length
l_p	Fibre pullout length

L	Convection cell length
m	Autocatalytic reaction order
n	Non-autocatalytic reaction order
n	Matrix power law toughness exponent
n_f	Number of fibres
P	Residual stress composite stress acting on fibre
r	Lap-shear disk radius
r_p	Matrix plastic radius
R	Fibre separation
R	Ideal gas constant
R_a	Arithmetic average surface roughness
Ra_L	Rayleigh number
R_{hx}	Fibre separation in a hexagonal array
R_{sq}	Fibre separation in a square array
s	Fibre aspect ratio (length/diameter)
t	Time
t_o	Lap-shear disk thickness
T	Temperature
T_o	Reference temperature; generally room temperature of 22°C
T_g	Glass transition temperature
v_f	Volume fraction fibres
v_ϕ	Volume fraction fillers
α	Degree of cure
α_c	Cure onset of diffusion

α_{gel}	Gel point
β_l	Linear coefficient of thermal expansion
γ	Shear strain
γ_l	Linear coefficient of cure shrinkage
δ	Incremental displacement
ε	Normal strain
η_f	Area fraction of fibres to unit cell
$\eta_{i,n}$	Area fraction of normal interface to unit cell
$\eta_{i,s}$	Area fraction of shear interface to unit cell
η_m	Area fraction of matrix to unit cell
η_o	Area fraction of pullout to unit cell
η_p	Area fraction of reduced matrix plastic radius
η_ϕ	Correction due to fillers
θ	Global composite loading angle
κ_r	Radius of curvature
λ_i	Dashpot relaxation of i^{th} branch of the Maxwell model
μ	Dynamic coefficient of friction
μ_o	Static component of modulus
μ_i	Transient component of modulus of i^{th} branch of the Maxwell model
ν	Poisson’s ratio
ν_o	Reference Poisson’s ratio at gel point
ρ	Density
ρ_o	Reference density of liquid polymer or mixed monomers
σ	Normal stress

σ_f	Normal fibre stress
σ_f^*	Fibre fracture stress
σ_i	Interfacial normal strength
$\sigma_{i,f}$	Interfacial normal failure stress
$\sigma_{y,m}$	Matrix yield strength
τ	Shear stress
τ_i	Interfacial shear strength
$\tau_{i,f}$	Interfacial shear failure strength
$\tau_{ts,m}$	Matrix shear tensile strength
$\tau_{y,m}$	Matrix shear yield strength
υ	Kinematic viscosity
φ	Local fibre alignment angle
Φ	Polymer reaction efficiency

Image Editing

All images contained in this thesis have all been edited for clarity and printing purposes.

Photographs were captured with digital cameras using native settings, unless otherwise indicated (e.g. polarized filter).

Using *IrfanView*©, available freely at www.irfanview.com, large raw camera images were first resampled to reduce the image size but maintain a high dot per inch (dpi) ratio; this was done using at a constant width-to-height ratio – small images were not adjusted. Further, the images were colour corrected, cropped, and converted to grayscale. Brightness, contrast, and gamma correction were avoided, though some images were sharpened with a standard Gaussian filter. Images were edited as a whole, with no local or fine-editing taking place.

Image compilation was done using *Microsoft Powerpoint*®, without any further image tonal editing.

All raw images are available upon request.

1 Introduction

The German engineer Dr. -Ing. Holger Hanselka recently said that “2/3 of all innovations are based on material innovations” [1]. This is the motivation to investigate new materials – to build the foundation through which further innovation and invention are possible. Among other considerations, a perfect material must meet or exceed all the design specifications at a minimum cost. Supposing such a perfect material was discovered / developed today, it would need to be fully characterized before reaching a commercial application – a lengthy and expensive process. Thus the main goal of this work is to reduce the effort involved in this material development process, specifically for composite materials. A desirable composite material is a combination of components such that the best attributes of each constituent result in a sum greater than its parts. This research is focused on polymer reinforced fibre composites because of the high-volume productions needed for any major industrial application, availability of the base materials, and the maturity in processing technology. What is currently lacking is a numerical way to assess material combinations for a given application. In short, the overarching hypothesis is this: a better composite failure model will lead to better material selection and component design.

The primary objectives in selecting a structural material are to minimize the mass while realizing a maximum stiffness. In the transportation industries this directly translates to fuel and energy savings. Consider a typical wheeled automobile, the four driving resistances are: rolling, air, inertial, and gravitational. With the exception of air resistance, they are all a function of the vehicle mass; thus reducing mass reduces driving resistance. The aerospace industry has seen tremendous success in reducing the vehicle volumetric mass utilizing the benefits of composite materials. The automotive industry would like to replicate these improvements, if certain barriers were overcome. Unlike a plane, a consumer vehicle sees far reduced utilization so component costs become a key design factor. Crash requirements for automotive passenger safety incur additional material requirements. Finally, cars currently roll off an assembly line about every 20 seconds requiring production processes which can supply at this economy of scale.

Therefore, a holistic approach is needed to material selection: considering not only the technical requirements, but also the cost, lifecycle, efficiency, production – even consumer emotional response.

The current government commitments to environmentally sustainable technology and energy conservation are pushing the automotive industry to seek these alternate structural materials which help reach ever restrictive fuel consumption and emission requirements [2, 3]. To address this legislative requirement, a lightweight development strategy is adopted to realize defined system functionality with given boundary conditions by a solution of minimized mass in an economic way [4]. Though composite materials have the potential to address this requirement, being both stiffer and less dense than traditional engineering materials [5], they pose two additional design constraints: anisotropy and non-linear thermal response [6]. To be able to use a composite material for consumer design, it must be fully simulated to ensure user safety. Such simulations demand an understanding of both elastic and inelastic mechanical response, which are in turn dependent on the materials, the processing, and the final microstructure. It is these process-property relationships which underpin all material models that are used to model and predict material behaviour.

A brute force method, to build and test every material combination, could be used to ascertain the desired material properties and determine post-production performance. This, however, is impractical in a number of ways: the vast number of possible combinations, the time required to perform and analyze all the data, and the astronomical cost. An improved method would be to determine the phenomenological material performance based on constituent materials and microstructural arrangement. While the prediction and modeling of elastic behaviour is relatively straightforward, a priori prediction of the inelastic response of these materials is considerably more difficult. Unlike traditional materials which have consistent fracture mechanism(s), composite materials combine the fracture mechanisms of each of the constituents, while also adding mechanisms for the constituent geometry and interface. It is this interface, commonly (and mistakenly) assumed as perfectly bonded, which is the central focus of this thesis, though newer work has examined the challenging problem of imperfect interfaces [7].

Having an understanding of the interfacial strength and the factors affecting this strength will lead to a better fracture model. The fracture model, in turn, bolsters an improved ability to simulate and predict composite behaviour, which then leads to better up-front material selection and improved processing parameters.

1.1 Understanding Fracture

The efforts of Hinton and Kaddour in their world-wide failure exercises (WWFE) over the last few decades illustrate two things regarding the state-of-the-art in composite failure: there remains an outstanding philosophical question of what constitutes failure in a composite and that there is no agreed upon method to approach and predict composite failure [8, 9]. Single materials exhibit common failure mechanisms within their material family. In metals, yielding and failure is focused on the presence, motion, creation, and interaction of microstructural crystal defects. Brittle ceramic failure is concerned about the size and distribution of impurities and cracks. Polymer deformation, which is temperature sensitive, is dependent on the molecular configuration, constitution, and conformation. Though a composite may be a linear combination of materials, it is not a linear combination of the failure mechanisms.

It is proposed that a composite can be mechanically described by a combination of the mechanical properties of the constituent materials, the spatial arrangement of the reinforcing phase, and a measure of the strength of the connecting bond(s). While bulk testing of composites can determine the formulation-specific properties, it lacks the predictive capability needed for material selection and optimization. Since there already exist comprehensive property databases for single materials, and spatial arrangement is a direct function of the processing, all that remains is to determine the interfacial strength. The fibre matrix interface is focus of this research, whereby several questions arise regarding this interface:

- Is there a good way to measure the interfacial strength?
- What are the major factors influencing the interfacial strength?

- How does the interfacial strength contribute to the composite failure?
- Does there exist an ideal interfacial strength to maximize fracture toughness?

If these questions can be answered in a satisfying way, then it should be possible to provide a new and more complete picture of the failure of composites. This type of material model is readily needed in the first regard to screen candidate material combinations for a given design application, second to perform failure simulations, and finally to tune the processing parameters to achieve the desired composite behaviour.

To address material failure, an energy approach is selected. Not only has this approach been backed by some of the best available fracture models: Pinho [10], Carrere [11], Puck [12, 13], but this approach allows a direct link between a fracture mechanism and the energy required by that mechanism. This mechanistic approach results in a firm connection to the reality of composite failure and is a simulation friendly method to describe non-linear material behaviour. These models also offer the detail required to integrate interfacial considerations into their failure energy calculations to better predict the material response at failure and the subsequent damage accumulation. In short, it is expected that with a better interface model, composite failure can be immediately improved using the existing failure theories.

1.2 Application to SMC

Also unlike traditional engineering materials, composites have very different production methods. A solid fibrous material is combined with a liquid matrix which either solidifies upon cooling or cures on heating, depending on whether the polymer is a thermoplastic or thermoset, respectively. Arranging and maintaining the distribution of the load-bearing fibres is a subject unto itself, though there are limited options when selecting a high-stiffness, low-cost fibre. These fibres are almost always coated to promote compatible adhesion to a particular polymer. Processing therefore focuses on selecting and controlling one of the myriad of available polymers, though typically an economical one. It is this processing which is of interest and its relationship to the observed material performance.

Sheet moulding compound (SMC) is one of the largest (by material volume) processes which exist to manufacture composite parts for the automotive industry [14]. Because SMC parts are compression moulded, there exists substantial flexibility in terms of final part size, geometry, and finish. The current parts are non- or semi-structural in nature, in part due to the limited understanding of failure. Examples can be seen commonly as seat frames, body panels, and bumpers, to name a few. It seems logical to apply the fracture mechanics approach to this process, as the research will have greatest impact. This process typically combines chopped e-glass fibres within a polyester matrix. Here, industry adds complexity: fibre coatings, particulate fillers, and polymer additives. These changes are meant to address the processing challenges like material handling, mould-filling, component tolerances, and finish. While some of these challenges are out of the scope of this research (e.g. mould flow behaviour), items affecting the polymer morphology, the interfacial strength, or the composite failure will be addressed.

Therefore, with the ultimate goal of furthering composite material models, a comprehensive study is undertaken to examine the role of the interface. First, the literature is consulted to ascertain the specific weaknesses and current understanding of composite failure. Then, two thermosetting polymers are characterized to determine their cure behaviour, mechanical response, and fracture properties. With well understood polymers in hand, attention is shifted to several interfacial studies. Composite interfacial strength is determined using several experimental techniques, two of which were developed as part of this research. Fibre coatings, processing parameters, fillers, and environment are among the conditions tested to examine their impact on interfacial strength. The polymer and interfacial knowledge is then applied to predict and simulate several test composites. Processing parameters and residual stresses are assessed numerically to determine how the interfacial strength is affected in a bulk composite. The resulting material model incorporates the interfacial criteria to better predict composite failure. The validation of this model is conducted by comparing the fracture behaviour of a lab-made composite and an industrially-made composite to the predicted response. Along the way, several connected applications are summarily investigated to provide ties to addressing other issues with composite materials, identifying areas for further research, and suggesting alternate applications for the present research.

The result in studying this interfacial bonding phenomena of fibre reinforced polymer composites is a holistic approach to improving and commercializing all composite materials. To conclude the research, several visions are presented to indicate where future research efforts are expected to yield substantial research gains.

2 Literature Review

Three main academic topics are addressed in pursuit of an improved composite failure model: polymer modeling, measuring interfacial strength, and composite failure. The polymer modeling is aimed at examining the chemical, mechanical, and processing influences on the composite interfacial strength. How the interfacial strength has previously been measured and determining the best method to measure the interfacial strength is of primary interest. Further it is necessary to determine if the polymer model and/or the measured interfacial strength are best suited to improve a current theory or create a new bulk composite failure criterion. For each topic, a review of the current literature is conducted to present the current state-of-the-art. The underlying theory is presented as a foundation from which the current work can be constructed. Each section will identify the strengths and weaknesses of the current techniques and methodologies, with a spotlight on the current gaps in research. In essence, these gap analyses will form the targets for novelty and the development of new insights for both the academic and commercial communities.

2.1 Polymer Cure Behaviour

There are two groups of engineering polymers, the thermoplastics and the thermosets. The thermoplastics are large molecular weight polymers held together by weak van der Waals bonds between the hydrocarbon chains. These polymers are typically semi-crystalline, exhibiting a strong viscoelastic response to stress. While they do not suffer from cure shrinkage during processing, they do exhibit thermal shrinkage. Thermosets, on the other hand, contain many covalent bonds between the polymer chains which provides both higher modulus and yield strength than their thermoplastic counterparts, at the expense of ductility and recyclability. Thermosets also exhibit a viscoelastic mechanical response to stress, albeit greatly reduced, but now have to deal with both thermal and cure shrinkage during processing. In both cases, the resulting composite properties are dependent on the processing methods to homogenize the constituent materials. Though there are a number of fascinating topics related to polymer melt flow behaviour, modeling mould-filling, and polymer/fibre interaction, this research, however, is focused on the final properties of a composite, and only the processing variables which influence those final properties.

To describe the post-processing mechanical behaviour of a polymer, it is necessary to capture the individual physical phenomena directly related to those properties. Here the assumption is made that thermosets can be considered as complicated versions of thermoplastics. Mathematically, if a thermoset is fully described by a series of terms, say for the residual stress, a thermoplastic could be described by the same equation by dropping the irrelevant terms. The desire then is to understand the more complicated polymer, which defines the behaviour of the less complicated polymer along the way. Unlike a crystalline material, where the micromechanics of the unit-cell model scale well to the bulk mechanics, the amorphous or semi-crystalline nature of polymers requires a different approach. Thus a physically-based phenomenological approach is taken to describe polymer behaviour in terms of the relevant physical systems.

Most composites are produced with the matrix in a liquidous form to conform to the fibre arrangement. Thus, the solid properties of a composite develop from nothing as a liquid to their final value as a room-temperature solid. Cure kinetics is employed to describe the progress of the cure reactions as related to the energy required/released by the reaction. Thermodynamics captures heat transfer and thermal behaviour of our polymer system, for which polymers are known to be strongly dependent. Solid mechanics describes the mechanical properties as they develop, considering both the elastic and entropic components. Fluid dynamics is briefly examined to determine if this group of physics is applicable to the subsequent experimentation and simulation.

2.1.1 Fluid Dynamics

Since the simulations and experiments will be conducted with the composite in a stationary reference frame, i.e. mould-filling is not examined in the present work, the remaining utility of fluid dynamics is in the development of internal convection cells during polymer solidification. Using Rayleigh-Bernard convection (Equation 2.1) and conservative values for the fluidic properties, from Table 2.1, the size of the convection cell is found to be on the order of 1 mm^3.

$$Ra_L = \frac{g\beta_l}{\upsilon a}(T - T_o)L^3 \tag{2.1}$$

In a bulk composite, this would correspond to, at most, a fibre volume fraction << 1%. With the possible exception of nano-reinforced composites, where the scale effects would matter, this suggests that fluid dynamics can be ignored without impact.

Table 2.1 – Rayleigh-Bernard fluid dynamic parameters for internal convection.

Parameter	Description	Assumed Value	Units
Ra_L	Rayleigh number	650	
g	Gravitational acceleration	9.81	$m \cdot s^{-2}$
β_l	Thermal expansion coefficient	5×10^{-5}	K^{-1}
υ	Kinematic viscosity	4×10^{-7}	$m^2 \cdot s^{-1}$
a	Thermal diffusivity	3×10^{-7}	$m^2 \cdot s^{-1}$
T_o	Upper surface temperature	293	K
T	Bottom surface temperature	393	K

2.1.2 Cure Kinetics

To describe the developed mechanical properties of a thermosetting polymer, it is necessary to describe the liquid-to-solid transformation behaviour. This is captured by selecting a reaction rate equation which describes the particular polymer chemistry during cross-linking. The starting point follows from the work of Ozawa [15], who assumed first order behaviour:

$$\frac{d\alpha}{dt} = K(T)(1 - \alpha) \tag{2.2}$$

where:

$$K(T) = Ae^{\left(\frac{-E_a}{RT}\right)} \tag{2.3}$$

The degree of cure, α, at a given time in the reaction, t, is based on Arrhenius type temperature dependence, and assumes atmospheric pressure. Borchardt and Daniels [16] had previously approached this work, but instead used nth order reaction model as:

$$\frac{d\alpha}{dt} = K(T)(1 - \alpha)^n \tag{2.4}$$

This model broadly captures the cure kinetics for most polymer systems, though Sourour and Kamal [17] demonstrated a refined model for epoxy systems which included an autocatalytic reaction of order m, with an associated autocatalytic rate term:

$$\frac{d\alpha}{dt} = (K_1 + K_2\alpha^m)(1 - \alpha)^n \tag{2.5}$$

All these kinetic models assume the degree of cure always reaches 100%. As the reaction progresses past the gel point, when the polymer can begin to be described as a solid, diffusion effects become important to describe the change in reaction rate. DiBenedetto expressed this onset of diffusion as a change of the glass transition temperature with respect to cure [18]. Though this does capture the diffusion phenomena, implementing the diffusion controlled rate constant using the Williams-Landel-Ferry (WLF) equation, as is commonly attempted, becomes cumbersome to both experimentally determine and to mathematically model [19]. A semi-empirical model, proposed by Chern and Poehlien [20] has been shown to fit many thermosetting polymer systems, which is considerably less burdensome:

$$K_d = K \cdot \exp[-C(\alpha - \alpha_c)] \tag{2.6}$$

where C and α_c are experimentally determined constants describing the magnitude and onset of diffusion respectively; ‘K’ is the overall chemical kinetics rate constant. The the overall rate effects are separable such that an isolated function could be used to describe a diffusion factor:

$$f(\alpha) = \frac{1}{1 + \exp[C(\alpha - \alpha_c)]} \tag{2.7}$$

Equation 2.7 can then be used in combination with any of the aforementioned rate kinetics to produce a rate equation describing both the chemical kinetics and the diffusion effects for near any thermoset polymer reaction.

2.1.3 Thermodynamics

Heat transfer in the composite is primarily governed by conduction, following Fourier’s law:

$$\rho C_P \frac{\partial T}{\partial t} = \nabla(k \cdot \nabla T) \tag{2.8}$$

A heat generation term is added to account for the exothermic nature of the polymer cure reaction as a product of the total heat of reaction and the instantaneous cure rate:

$$\rho C_P \frac{\partial T}{\partial t} = \nabla(k \cdot \nabla T) + \rho \Phi \Delta H_r \frac{d\alpha}{dt} \tag{2.9}$$

The first term describes the heat storage, the second term the heat conduction, and the last term the heat generation, which requires knowledge of the cure reaction. The variable phi, Φ, describes the reaction efficiency; in the absence of porosity or impurities, this term has the value of unity.

2.1.4 Structural Mechanics

2.1.4.1 Viscoelastic Behaviour

Viscoelastic behaviour can be modeled in a number of ways, the simplest being the spring-dashpot models of Maxwell and separately of Voigt, shown schematically in Figure 2.1. The assumption is made that the material can be modeled as linear viscoelastic so that creep and load can be accounted for separately.

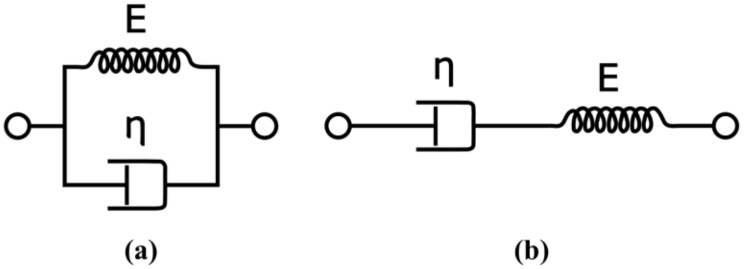

Figure 2.1 – Simple viscoelastic models of a) Kelvin-Voigt and b) Maxwell.

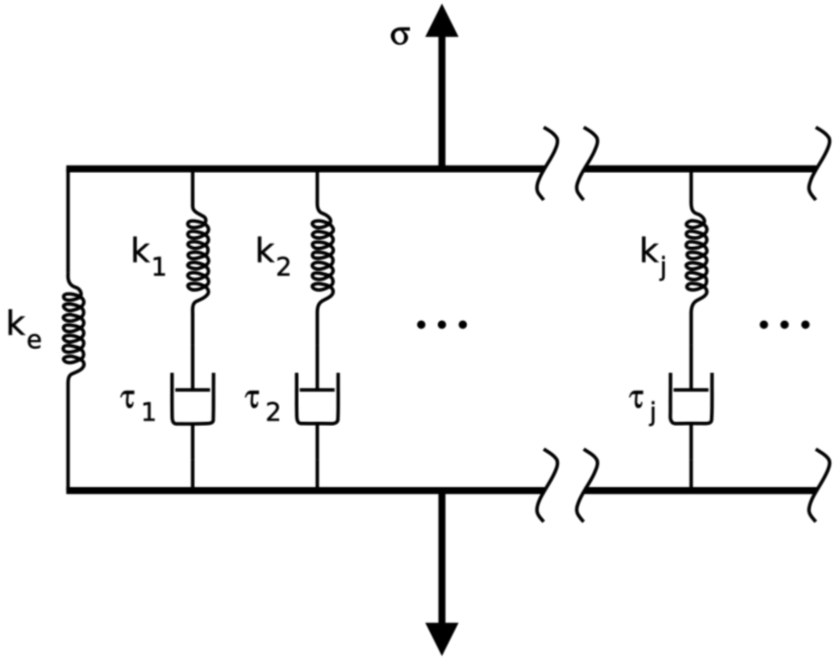

Figure 2.2 – Generalized Maxwell-Weichert viscoelastic model.

This leads to a convenient realization of the generalized Maxwell-Wiechert model (seen in Figure 2.2) using a Prony series:

$$G(t) = G_r\left[\mu_0 + \sum_{i=1}^{N} \mu_i \exp\left(\frac{-t}{\lambda_i}\right)\right] \tag{2.10}$$

It is this approach to curing polymer viscoelasticity that many authors have taken [21-29], as it allows the stress at any time to be separated into function of the static and transient modulus and is efficient both analytically and numerically. To combine the cure and temperature effects, the time-temperature-superposition (TTS) principle is commonly utilized. The central assumption in using a TTS model is that the modulus at a given temperature is equivalent to the modulus measured over a corresponding time scale. This allows for one set of material data, but requires shift factors to account for temperature and cure at the modified time scale. An Arrhenius law can be used to determine the shift factor, but suffers from accuracy [23, 30]. Here a Williams-Landel-Ferry model [19] does prove useful to account for one such shift, despite being empirical:

$$\log a_T = \frac{-C_1(T - T_o)}{C_2 + (T - T_o)} \tag{2.11}$$

The constants C_1 and C_2 are found by fitting relaxation curves at several loading rates. The WLF model is applicable in the range between the glass transition temperature and a hundred degrees above the glass transition temperature, with decreasing accuracy outside this range. This shift factor accounts for the temperature dependence of the modulus. Yang [27] and Zoibery [29] both used a second shift factor to account for the cure dependence as a function of the change in glass transition temperature following Arrhenius behaviour:

$$\log a_\alpha = \frac{-\Delta H_r}{2.303R}\left(\frac{1}{T_{g\alpha}} - \frac{1}{T_g^{ref}}\right) \tag{2.12}$$

An alternate approach was proposed by Adolf [31], who used scaling analysis to incorporate the cure dependence directly into the modulus development:

$$G_r = G_r^\infty \left(\frac{\alpha^2 - \alpha_{gel}^2}{1 - \alpha_{gel}^2}\right)^{8/3} \tag{2.13}$$

2.1.4.2 Cure dependent Properties

Multiple authors have shown that polymer density is linearly related to the cure temperature and degree of cure [25, 27], calculated as:

$$\rho = \rho_o[1 - 3\beta_l(T - T_o) + 3\gamma_l(\alpha)] \tag{2.14}$$

where ρ_o, and T_o are the reference density and temperature respectively; β_l, γ_l are the linear coefficients of thermal expansion and chemical shrinkage respectively.

Nawab performed extensive testing on the thermal conductivity of a thermosetting polymer during cure, showing that the value rarely changed by more than 10% during cure, and could ultimately be taken as a constant value [32].

Poisson's ratio is known to change during cure, but no consensus was seen in the literature to support a single trend. Most authors [22, 28, 33] assume a constant value.

2.2 Determining Interfacial Strength

It is quite a challenge to measure something intrinsically hidden. Consider a typical fibre-matrix interface: suppose the fibre is glass with a diameter of 15μm, and a thermoplastic matrix, say polypropylene, surrounds the fibre. The curvature of the fibre makes examination of a unit area difficult. The brittle fibre is a challenge to handle, be it to make a single-fibre sample, or to apply a load. The size of the fibre requires apparatus and measurements sensitive at this scale. The matrix is opaque, causing challenges to optical measurement techniques. The thermoplastic matrix would also experience a thermal stress related to the processing temperature; a thermoset matrix additionally a cure stress. There is limited ability to place sensors at the interface without disrupting the interface itself. Therefore, the majority of techniques currently employed to determine the interfacial strength are indirect – inferring strength by applying a micromechanics model. There is clear need for a robust, sensitive technique to rapidly assess the interface of an arbitrary fibrous composite. Though there are numerous methods to determine the interfacial strength, each with their strengths and weaknesses, the three most common methods are discussed: the pull-out test, the push-out test, and the fibre fragmentation test.

2.2.1 The Pull-out Test

Though there is no clear first author to describe the pull-out test, the underlying micromechanics are first attributed to Cox [34] who developed the shear-lag model to describe stress transfer from the matrix to an embedded fibre. Both Lawrence [35] and Chua and Piggott [36] adapted this shear lag theory to interpret the load-displacement data obtained from a pull out test. Recently, the stress transfer mechanics have received renewed attention [37]. In principle, a fibre of known dimension is partially embedded in a matrix, loaded, and removed from the matrix, as depicted in Figure 2.3.

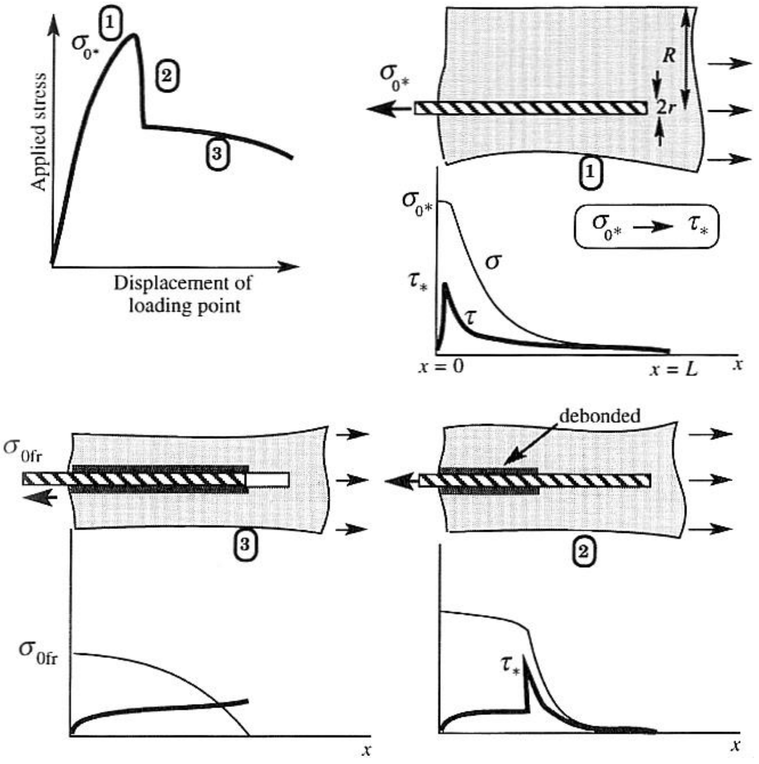

Figure 2.3 – Stress transfer in the single-fibre pull-out test [6].

Because of the nature of the stress transfer from the fibre to the matrix results in a high peak shear stress near the top surface of the matrix, the interfacial shear strength is interpreted as the highest load reached in the test [38]. As the interface debonds, the test continues to measure mode II crack propagation and friction during fibre pull-out.

This test generally represents an idealized single fibre composite, not capturing effects from a true high volume fraction composite, where nearby fibres change the stress transfer characteristics [39]. Challenges to this test method include sample fabrication and dealing with the presence of a meniscus around the fibre [40]. Also troublesome are gripping a brittle fibre and accounting for matrix plasticity and Poisson effects [41].

2.2.2 The Push-out Test

Much like the pull-out test, the push-out (or push-down) test is a single-fibre method to extract the interfacial strength from load-displacement data. This test aims to address several of the shortcomings of the pull-out test by changing the test conditions. No longer is gripping a fibre an issue, nor is controlling the embedded fibre depth, thus these tests are much easier to conduct than their pull-out counterparts. However, reproducibility is still an issue especially due to induced damage during sample preparation [42]. This test has been used to measure interfacial strength on a variety of composites in the past, with greater success using stiff fibres [43]. Typically a thin section, still with fibre aspect ratios around 100, is tested by applying load with a micro indentation device. A simple force balance of the load applied to the fibre with the stress transferred in shear yields the relation:

$$\tau = \frac{\sigma_o}{4s} \tag{2.15}$$

where σ_o is the stress applied to the fibre and s is the fibre aspect ratio. The interfacial strength is assessed as the peak stress reached during the initial linear portion of the push-out test. A troubling challenge with this test is that the common models used to interpret the results, based on the shear-lag theory, can significantly overestimate the interfacial shear stress [6]. Newer approaches to this test aim to understand the mechanics of the stress transfer at the interface using shorter embedded fibre lengths to approach a uniform interface stress distribution, rather than a stress transfer region [44]. Both this and the pull-out test typically suffer from repeatability and reproducibility due to even small sample errors which become magnified by the analysis.

2.2.3 The Fibre Fragmentation Test

The fibre fragmentation test is an indirect method of assessing the interfacial strength by employing the aforementioned shear-lag theory to examine the stress transfer length on single or multiple embedded fibres within a transparent polymer matrix – see Figure 2.4.

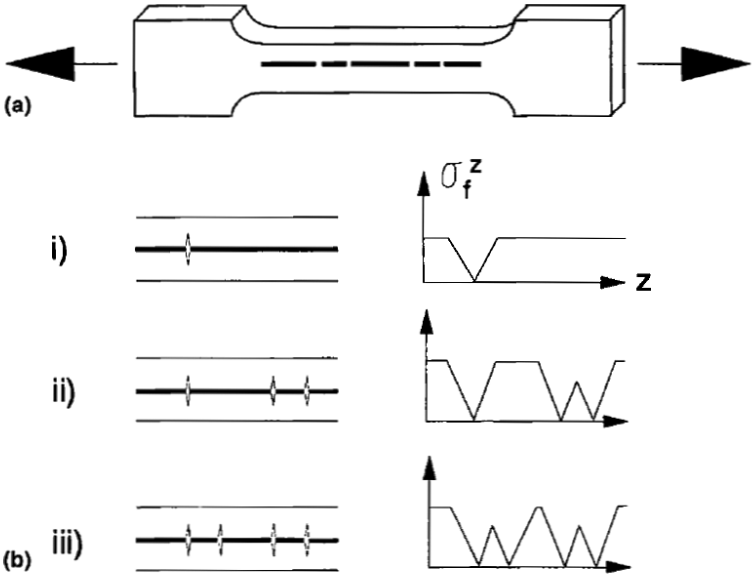

Figure 2.4 – Schematic of a) fragmentation sample and b) progressive fibre fracture and axial fibre stress profile [45].

As the single-fibre composite is loaded, stress is transferred from the matrix to the fibre until the fibre breaks. Since the fibre load at a break is zero, the fibre will continue to fragment into lengths between the critical stress transfer length and half this value such that the fibre length eventually becomes insufficient to reinforce the matrix. Kelly and Tyson expressed this relation as a function of the fibre strength and diameter over the observed critical stress transfer length [46]:

$$\tau_i = \frac{d\sigma_f^*}{2l_c} \tag{2.16}$$

Here, the stress transfer mimics a real composite in that the load is transferred from the matrix to the fibre contrary to the push-out or pull-out tests. Further, the challenges with implementing the shear-lag theory are partially abated since the analysis looks at actual fibre fracture rather than interpreting the stress-strain results. Many authors have used this test to achieve measures for both the fibre-matrix interfacial shear strength [47] and the interfacial strain energy release rate [48]. The relation of Kelly and Tyson has remained consistent since its inception, though recent work has accounted for the statistical distribution of strength [49], the ratio of the moduli [50], and imperfect interfacial bonding [51]. Because of its stability, reproducibility, and simplicity, this test has become one of the best methods to assess the interfacial strength of a composite despite knowing that this test generally under-reports the interfacial strength [6, 52] and will always remain an indirect method. From the three tests presented, there is still a need for a simple test which can be universally applied to any type of composite to measure its interfacial properties directly, and with controllable impact from separate phenomena.

2.3 Composite Failure Criteria

Composites have a unique challenge, compared to other materials, when it comes to failure: their microstructure. Dimensionality, arrangement, and aspect ratio of fibres are strong contributions to the complexity of failure. For this thesis, homogenization methods, representative volumes and determination of elastic mechanical response are all outside the scope of the work; the focus is on failure. However, the elastic composite response is accurately required to determine stresses or strains at which non-linearity begins. Thus, a cursory presentation of the elastic modeling of composites is highlighted to draw the basis for composite failure.

There is no consensus in the literature on what constitutes composite failure. Options include the onset of permanent deformation in any of the constituents, the appearance of cracks, the onset of stable crack growth, the first fibre failure, or the loss of load-carrying capability. This work will focus on the initiation of failure rather than final failure where a collected damage model would be required. To examine the merits of the currently available criteria, it is necessary to loosely group the available theories by their respective approaches depending on whether they are based on the stress state, the energy state, the failure condition or some combination thereof. For each criterion, identification will be made to explicitly state how failure is defined. The two main groups of failure theories are those which are primarily phenomenological in nature, and those which are based on internal energy states. Other theories such as probabilistic models or empirical approaches do exist, but are currently in the minority. Though many criteria are designed for laminated structures with multiple layers of woven fibres, their approach and failure mechanisms can be ported to other composite structures such as the currently studied long fibre composites.

2.3.1 Composite Elastic Properties

By using brittle reinforcing fibres, the fibres themselves can be treated as linear elastic. This immediately reduces the composite complexity by only having one constituent with non-linear mechanical response. To model the non-linear elastic response of a polymer, it is common to use a Ramberg-Osgood formulation to capture the behaviour up to and including the tensile strength. This allows the stress-strain response to be directly considered as [53]:

$$\sigma = \frac{E_o \varepsilon}{\left(1 + \left(\frac{E_o \varepsilon}{\sigma_o}\right)^k\right)^{\frac{1}{k}}} \tag{2.17}$$

The three parameters in this model relate to physical phenomena: the initial elastic modulus, E_o, the asymptotic or tensile stress, σ_o, and the strain-hardening coefficient, k. By adjusting the hardening coefficient, this model can fit a wide array of polymer systems. Further, because this model is positive continuous, the first derivative of Equation 2.17 with respect to strain yields the tangent modulus. This property allows the elastic modeling of any composite to easily capture the non-linear response of the polymer during prediction or simulation.

A short fibre composite is one in which the average fibre length is less than or equal to the critical length required for stress transfer. A long fibre composite is one in which the average fibre length is greater than the critical length, but less than the major length of the composite part. For reference, a continuous fibre composite is one in which the fibre length is effectively unbroken, or extends the whole length of the composite part. There are many models to predict the stiffness of a random-fibre composite, whether short or long fibre. Models take many approaches such as the misfit strain method of Eshelby [54], the concentration method of Mori-Tanaka [55], the bounds method of Hashin-Shtrikman [56], or the computational self-consistent method [57, 58]. There are also a number of simplified averaging methods. Figure 2.5 presents a comparison of stiffness predictions for a random long-fibre composite using properties for a glass / epoxy system.

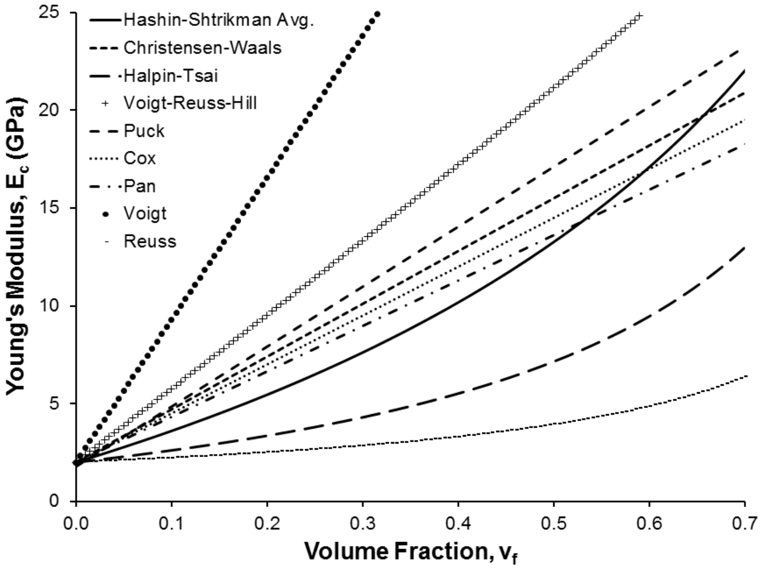

Figure 2.5 – Comparison of several random fibre homogenization schemes to predict the composite Young's modulus as a function of fibre volume fraction.

The equations for each of the Young's moduli in Figure 2.5 are as follows.

Voigt [6]:

$$E_c = v_f E_f + (1 - v_f) E_m \tag{2.18}$$

Reuss [6]:

$$E_c = \frac{E_f E_m}{E_m v_f + E_f\left(1 - v_f\right)} \tag{2.19}$$

The Voigt-Reuss-Hill relation [57] is the average of Equation 2.18 and Equation 2.19.

Modified Cox [34]:

$$E_c = E_m + \frac{E_f v_f}{3} \tag{2.20}$$

Pan [59]:

$$E_c = \frac{v_f}{\pi} E_f + \left(1 - \frac{v_f}{\pi}\right) E_m \tag{2.21}$$

Puck [60]:

$$E_c = v_f\left(\frac{16}{45} E_f + 2E_m\right) + \frac{8}{9} E_m \tag{2.22}$$

Halpin-Tsai [61]:

$$E_c = \frac{E_m\left(1 + 2\eta v_f\right)}{\left(1 - \eta v_f\right)} \tag{2.23}$$

$$\eta = \frac{\left(\frac{E_f}{E_m} - 1\right)}{\left(\frac{E_f}{E_m} + 2\right)} \tag{2.24}$$

Christensen-Waals [62]:

$$E_c = \frac{v_f}{3} E_f + \left(1 + v_f\right) E_m \tag{2.25}$$

Hashin-Shtrikman Average [56]:

$$E_c = \frac{E_L + E_U}{2} \tag{2.26}$$

$$E_L = E_m + \frac{v_f}{\frac{1}{E_f - E_m} + \frac{3\left(1 - v_f\right)}{3E_m + 4G_m}} \tag{2.27}$$

$$E_U = E_f + \frac{1 - v_f}{\frac{1}{E_m - E_f} + \frac{3v_f}{3E_f + 4G_f}} \tag{2.28}$$

2.3.2 Phenomena-Based Failure Criteria

Phenomena based criteria, also termed maximum stress or maximum strain criteria, are those which allow a composite to continue receiving load until either a critical stress or strain is reached. Usually these models incorporate this critical-value problem with a material degradation scheme such that once the composite reaches the initial critical value its mechanical properties are degraded until the composite fails completely at some secondary, ultimate criterion.

A simple model proposed by Bogetti [63] predicts composite failure using a maximum strain model based on the work of Chou [64]. The model relies on the assumption that the reinforcing fibre in a polymer composite is both stiff and brittle compared to the matrix, such that the first point of failure in a composite is typically the fibre. Using what is essentially a table-lookup, the composite behaves following the stress-strain relationship defined by the homogenization scheme until one of six possible scenarios is reached (nine scenarios for triaxial loading). The scenarios are axial tension, axial compression, transverse tension, transverse compression, in-plane shear and interlaminar shear. If values for these strains are sourced only from the constituent materials, then this theory is not very accurate. Using experimental values of the composite or lamina for the failure strains dramatically improves this theory which begins to operate in an elastic-brittle manner. This theory does capture the differences in anisotropic failure, even if only by empiricism, and serves as an upper bound to composite failure theories. The beauty of this theory is its simplicity as it can be easily applied to nearly any composite with few required parameters and little experimental work to determine those parameters.

Stephen Tsai has greatly contributed to composite failure with his quadratic failure criterion [65-67]. Similar to the generalized von Mises equation, the Tsai-Hill or Tsai-Wu criteria are closed-form failure envelopes for composite materials by evaluating the stress (or strain) state. The general criterion is [67]:

$$\frac{\sigma_x^2}{XX'} + \frac{2F_{xy}^*\sigma_x\sigma_y}{\sqrt{XX'YY'}} + \frac{\sigma_y^2}{YY'} + \frac{\sigma_s^2}{S^2} + \left[\frac{1}{X} - \frac{1}{X'}\right]\sigma_x + \left[\frac{1}{Y} - \frac{1}{Y'}\right]\sigma_y = 1 \tag{2.29}$$

where the critical interaction parameter is F_{xy}^*. The individual parameters for Equation 2.29 are fully discussed in Reference [66]. Failure occurs when all the combined stresses acting on the material are sufficient to cause failure as related to the individual maximum stresses in tension, compression and shear. Different from the theory of Bogetti, the Tsai criteria are interactive, meaning that longitudinal, transverse and shear stresses can impact one-another. The latest iteration of the Tsai-Wu criterion includes both initial failure when a critical stress combination is reached, and an iterative degradation scheme until the load-bearing ability of the composite is reduced to zero [65]. Though this theory is relatively simple in application, to be effective it requires all the failure stresses to be initially determined before it can be implemented and again relies upon knowledge of the actual composite strength to predict failure.

A third popular approach to the phenomena criteria is that of Puck [12], who has developed and refined his theory for a multitude of composite structures and failure conditions. Puck implements multiple approaches to composite failure depending on the load direction and type of failure considered. Tensile and compressive failure is separately considered for laminates where the failure mechanisms are different, as is biaxial loading to account for the differences in fibre and inter-fibre failure. One of the unique aspects of Puck's theory is the search for a maximum stress plane from which to determine the inter-fibre failure mode, after Mohr's theory, as seen in Figure 2.6.

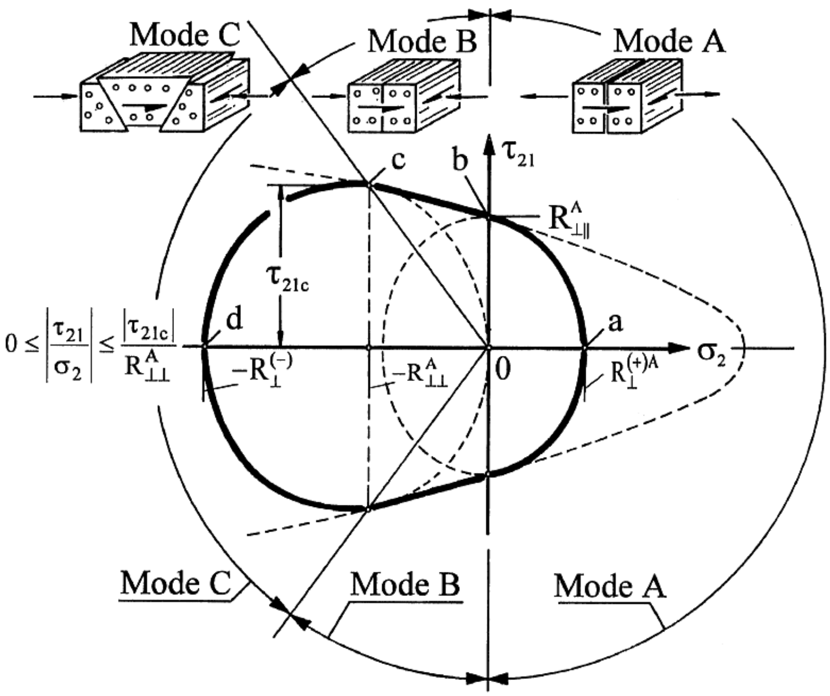

Figure 2.6 – Inter-fibre failure surface as determined for biaxial loading on a composite lamina [12].

Though Puck's theory is primarily geared to composite laminates, the main concept to determine the principle stresses and compare those stresses has long been proven a reliable approach to failure. In this approach, damage can be modeled as a geometrically self-similar reduction to the above failure surface. One down side to such a developed theory is the required calibration with several empirical parameters and computationally intensive search for potential fracture planes.

2.3.3 Energy-Based Failure Criteria

Another approach to composite failure is using an energy-based approach to determine failure based on how much energy is required to initiate and is consumed during failure. This approach is typically favoured over linear elastic fracture mechanics where there exists complex geometry or anisotropy, such as with composite materials. Though models such as that of Puck can approach failure using stresses which model reality quite well, their ability to deal with damage are typically empirical. With an energy approach, there is increased up-front cost to develop the rigor of a theory to account for the same failure mechanisms, but damage becomes an easily handled feature as a result of attaining an energy balance during failure.

One theory which approaches this method with robustness is that of Pinho [8,10]. Again, this theory is based on laminates, but applies to a multitude of composites as the formulation accounts for the energy of fracture in a wide range of scenarios. Figure 2.7 presents the scenario of a laminate experiencing a normal load with the entrapped transverse ply cracking and eventually delaminating.

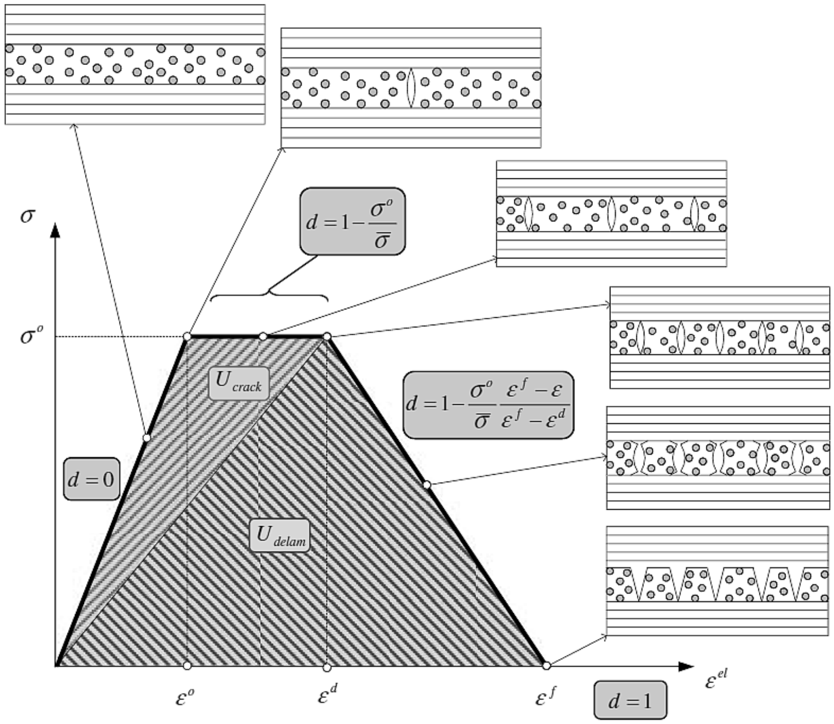

Figure 2.7 – Crack and delamination energies of a laminated composite with damage mechanics from the work of Pinho [10].

Pinho utilized separate strain energy release rates for the onset and propagation of damage for different loading geometries, relating each rate to a corresponding type of failure. The biggest strength of this model is its ability to detail the type, amount, and location of damage during loading at the cost of complexity. Finite element simulations are required to iterate to predict the stress-strain response of a composite and there are a number of calibration factors required beyond material properties to achieve the touted predictive capability.

For random fibre composites, one of the challenges in applying the energy-based failure models is that crack growth does not follow from linear elastic fracture mechanics [68]. The assumption of a traction-free crack is not the case with fibre bridging and a complicated process zone where multiple crack growth opportunities and non-uniform matrix plasticity exist [69]. The mixed failure modes require combined analysis of separate phenomena which can make it difficult to determine clear relationships between different failure modes. Outwater and Murphy [70] previously developed a relationship to determine the stress required for debonding based upon the energy required to debond a fibre as:

$$\sigma_{db} = \sqrt{\frac{8E_f G_{db}}{d}} \tag{2.30}$$

where G_{db} is the debond energy per unit area. This is useful for short fibre composites where pullout and matrix fracture dominate, but further considerations are required for long fibre composites. Also, the determined debond critical strain energy release rates are large values which account for multiple phenomena as the role of the interface and matrix plasticity were ignored. Hibbert and Hannant [71] proposed a semi-empirical model for the toughness of an aligned, long-fibre composite as the summation of fibre fracture and matrix cracking as:

$$U_c = 0.159\omega E_c \varepsilon_{mu}^2 + 0.5\sigma_f \varepsilon_{fu} v_f \tag{2.31}$$

where

$$\omega = \frac{E_m\left(1 - v_f\right)}{E_f v_f} \tag{2.32}$$

This was done primarily as an extension of the Griffith and Irwin toughness models to account for the brittle fibre fracture and matrix plasticity separately during fracture. This model is predictive in the sense that it utilizes constituent properties to predict the composite toughness. The empirical factors do fit for a range of fibre reinforced composites, including ductile fibre composites, but do not retain a basis in reality.

Hull and Clyne [6] analyzed fibre interfacial debonding and pullout from the scenario depicted in Figure 2.8.

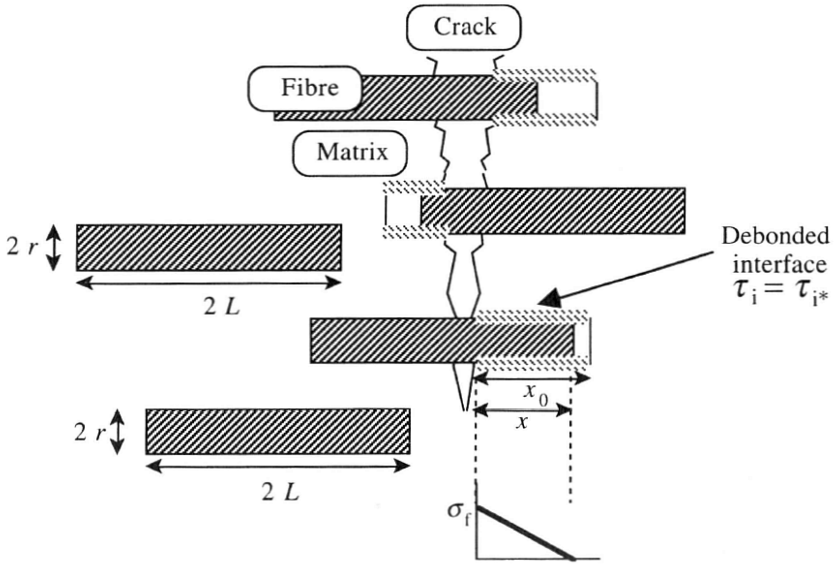

Figure 2.8 – Crack schematic in a long fibre composite with fibre-matrix debonding and fibre pullout.

Their subsequent analysis suggested that interfacial debonding is a relatively small amount of energy (~10 J/m^2), while the energy of pullout is substantial (~80 kJ/m^2). Further, they proposed bounds on the interfacial energy based upon the fibre aspect ratio and fibre fracture energy. These statements may be true for ceramic matrix composites where the interface is relatively weak for the one study quoted [72], but is at odds with recent work which has measured interfacial debond energies of polymer matrix composites in the range of 500-1000 J/m^2 [48]. A recent study commented on this issue stating that it is the breaking of chemical bonds which constitutes debonding, while pullout is reserved for sliding friction [73]. This separation led to more reasonable figures for debond and pullout respectively.

Cook and Gordon have shown that an interface can debond ahead of an advancing crack separately from a pullout event [74]. This, therefore, suggests that analysis to date may be smearing the effects of interface and debond together, when in fact they are separate phenomena. A lot of work has analyzed the effects of fibre aspect ratio on the observed properties and failure behaviour, but typically for small ratios [59, 60, 62]. Still lacking in the literature is a comprehensive failure model for long fibre composites using a mechanistic approach to determining the composite strain energy release rate.

3 Polymer Characterization

“What is the minimum number of mechanical properties that fully defines the mechanical performance of a material?” – Jeff Wood, 2011. For a polymer, there is no easy answer. The standard properties: density, elastic moduli, yield and tensile strengths all apply. However, all polymers exhibit non-linear temperature dependence. Thermoset polymers are also reliant on their crosslink density, and all but the stiffest polymers exhibit viscoelasticity – time dependent deformation. More importantly, how does each of these properties influence the interfacial strength and resulting bulk composite properties? This chapter will examine how these properties are determined and enumerate values for a given thermoset polymer. Trends in material behaviour and confidence for each parameter will be identified where possible. This work will facilitate the isolation of polymer properties from interface properties to examine the individual relationships. Further, by characterizing an industrial polymer, the eventual numerical simulations can be populated with accurate properties to better predict failure, thus performing accurate validation.

3.1 Materials Selection

Two thermosetting polymers are selected to represent different industrial processes, chemical reactions, and material behaviour. Both polymers are translucent and have similar stiffness when cured. A two part epoxy from was sourced from Crosslink Technologies Inc.; resin, CLR 1180, and hardener, CLH 6560. This epoxy, shown chemically in Figure 3.1, reacts in a step-growth reaction over a lengthy cure, resulting in a finely controlled degree of cure. Unsaturated polyester, T320-70 sourced from AOC, is a chain growth reacting polymer, rapidly curing when the activation energy (temperature) is reached. To aid in laboratory processing of the polyester, a peroxide-based polymerization initiator was used, Luperox DDM-9, from Sigma Aldrich. Both polymers were prepared according to the manufacturer guidelines, unless otherwise indicated. The polyester is studied as it matches the desired industrial requirements: rapid cure, cost effective, and able to be highly filled. The epoxy is studied as it matches the desired laboratory specifications: low toxicity, simple fabrication, and a wide range of cure-dependent properties.

The epoxy was used as the polymer of primary study, fully characterized in all the described test methods. This was done to indicate both the important, as well as the less important variables contributing to the resulting composite interfacial strength. The polyester was only tested in a minimum battery of tests as determined from the epoxy characterization. Results will always be shown for the epoxy, but only for the polyester when the testing was necessitated.

Three silanes are used in the interfacial studies in Chapter 4. They are included briefly in this section as their chemistry and bonding characteristics to the polymers are important. These silanes were selected from their representation in literature as the most common for both the epoxy and polyester resin chemistry [75, 76]; all were sourced from Dow Corning:

1. Z6020: [3-(2-Aminoethylamino)propyl]trimethoxysilane
2. Z6030: 3-(Trimethoxysilyl)propyl methacrylate
3. Z6040: (3-Glycidyloxypropyl)trimethoxysilane

Also used briefly is a low density polyethylene to indicate the extension of the interfacial studies with thermoplastic materials. This polyethylene was acquired from Sigma Aldrich in pellet form.

The datasheets for all the materials used can be found in Appendix A.

3.2 Chemical Properties

The chemical properties of the polymers are described first to set up the presentation of the mechanical properties which are dependent on the polymer chemistry. In order to comment on the specifics of the chemical reactions and their influence, a confirmatory study is conducted to verify the chemical composition of the materials. The cure kinetic properties are also recorded, followed by the cure induced chemical shrinkage.

3.2.1 Chemical Analysis

Both mass spectroscopy and nuclear magnetic resonance were conducted on the resin and hardener, as well as the three silanes (coupling agents) eventually used in the interfacial studies. The full chemical analysis can be found in Appendix B which confirms the chemical structures presented in Figure 3.1 for all five species.

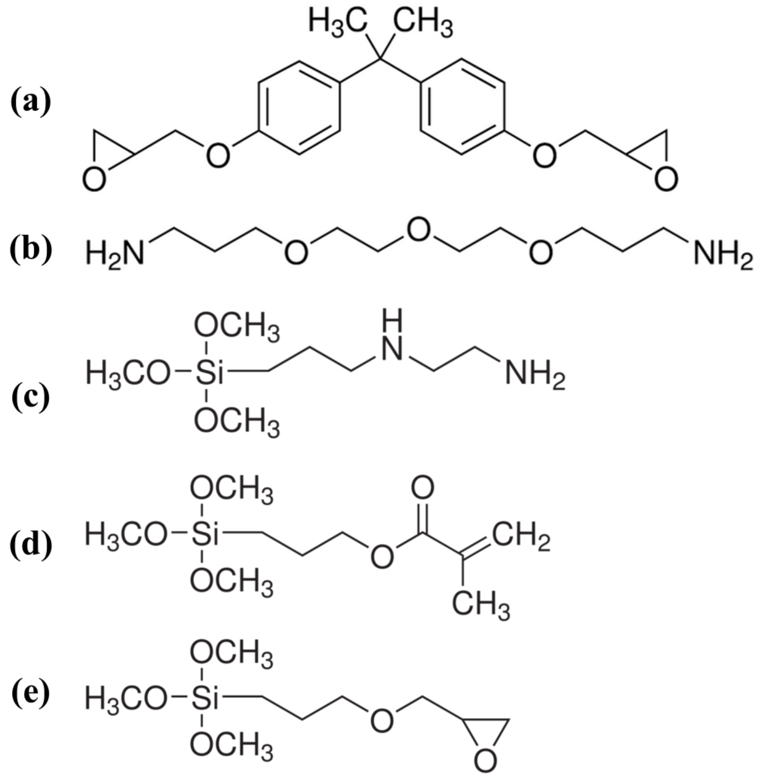

Figure 3.1 – Chemical structures for the a) epoxy resin b) epoxy hardener c) Z6020 silane d) Z6030 silane and e) Z6040 silane

The chemistry of epoxide ring opening and bonding with amines has been well-studied [77, 78]. This reaction proceeds as a step growth reaction, requiring a stoichiometric ratio of resin to hardener to achieve a complete reaction. Conversely, and not pictured in Figure 3.1, the polyester cures rapidly in a chain growth reaction based on the production of free radicals during cure.

Of the silanes from Figure 3.1, it can be seen that Z6020 has the same functional group as the epoxy hardener, and that Z6040 has the same functional group as the epoxy resin. The expectation then is that Z6020 and Z6040 should be fully compatible with this particular epoxy. Since the epoxide functional group is more reactive than the amine group, Z6040 should be the best performing silane with the epoxy, as it is most reactive. A check on the reactivity of the Z6030 functional group indicates that this coupling agent is not very compatible with the epoxy, though it is expected to perform very well with the polyester, where free-radical chain growth reactions will readily react with the double bond.

3.2.2 Degree of Cure

Both polymers studied react exothermically, releasing energy as the cure reaction progresses, though only the epoxy chemistry was studied in detail. This energy, or heat of reaction, is necessary for both the energy balance in simulation and as one method to determine the degree of cure. The heat of reaction was measured by running a high temperature isothermal cure test on a TA Instruments Q20 differential scanning calorimeter (DSC), under nitrogen, at atmospheric pressure. As the DSC is a highly sensitive measurement, it is important that there is no sample mass-loss. So a first test is to check the degradation behaviour of the mixed reactants using thermal gravimetric analysis (TGA) on a TA Instruments SDT Q600. A 20µg sample was extracted from a ~50g batch of mixed epoxy to minimize measurement error. The sample was heated at 20°C/min. from room temperature to 400°C while the mass was recorded. The results of the thermal gravimetric analysis (TGA), presented in Figure 3.2, indicate that there is about 4% water/solvent loss around temperatures of 100 degrees centigrade.

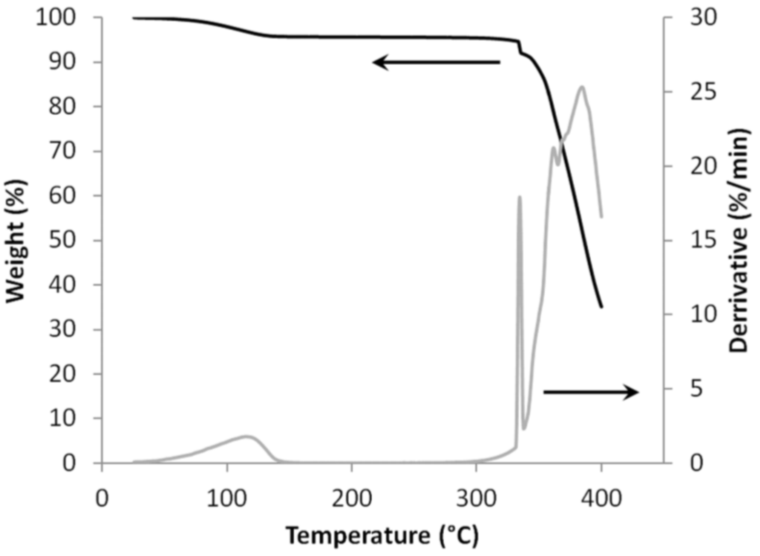

Figure 3.2 – Thermal gravimetric results for epoxy.

Therefore, an isothermal DSC measurement was conducted at several points, from just above room temperature to the highest stable temperature of 90 degrees centigrade. Heat flow per unit mass was recorded as a function of time and can be seen on both a linear and logarithmic scale in Figure 3.3. The heat of reaction was determined by taking the area under the heat flow curve using the initial equilibrium heat flow as the reference point. Only the first 60 minutes of the cure cycle is shown to illustrate the key exothermic peak, though the reactions were recorded for 2, 4, and 12 hours for the 80°C, 60°C and 30°C isothermal cures respectively.. Also, the logarithmic scale is truncated to start at the 6 minute mark to avoid the representation of negative numbers.

Initially, the heat flow curve indicates an endothermic drop following a brief (5 minute) equilibrium at 0°C. This endothermic drop corresponds to the initial intake of energy required before the activation energy is reached and the stable exothermic reaction can proceed; this has been previously observed in other epoxy systems [79].

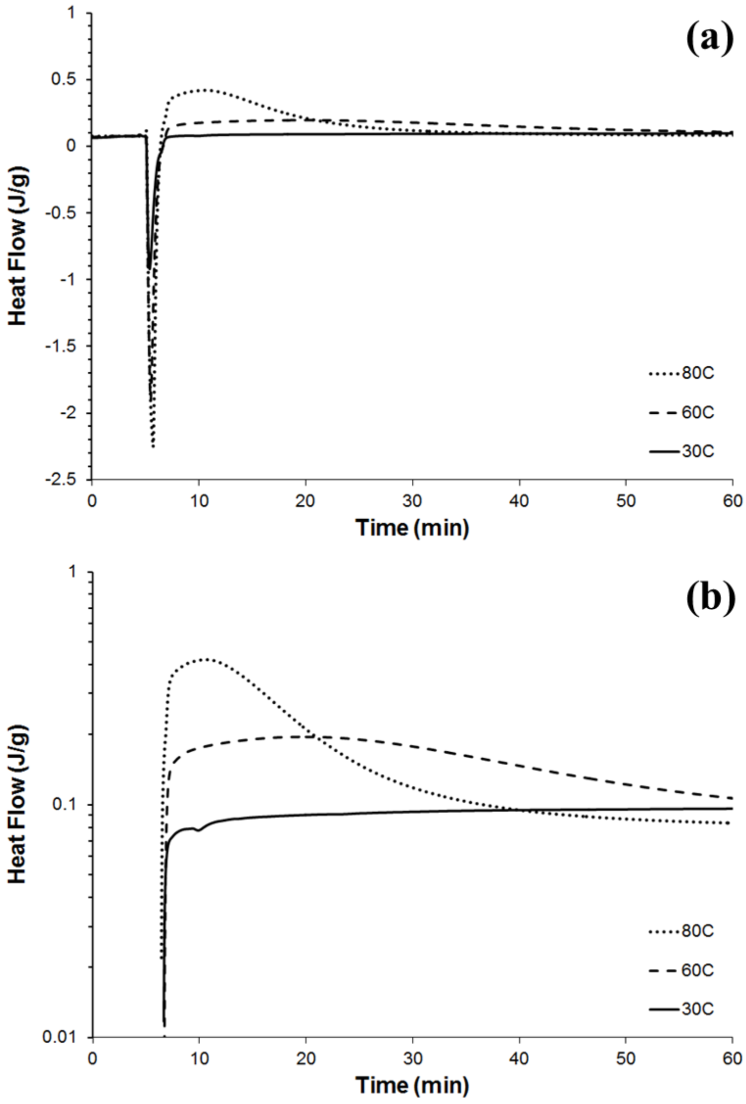

Figure 3.3 – Isothermal DSC curves for the first 60 minutes of cure on a) linear scale b) logarithmic scale

Using a separate 90°C dynamic cure at a heat ramp of 5°C/min, the total heat of reaction is determined as 280.0 $kJ \cdot kg^{-1}$. The instantaneous degree of cure, then, is measured as a ratio of the released heat of reaction to the total heat of reaction as [80]:

$$\alpha = \frac{\int_0^t H}{\Delta H_r} \tag{3.1}$$

where α is the degree of cure, H is the heat of reaction and $\Delta H_r$is the total heat of reaction as independently measured. The experimental DSC data is then re-plotted to determine the degree of cure with respect to the reaction time, as in Figure 3.4.

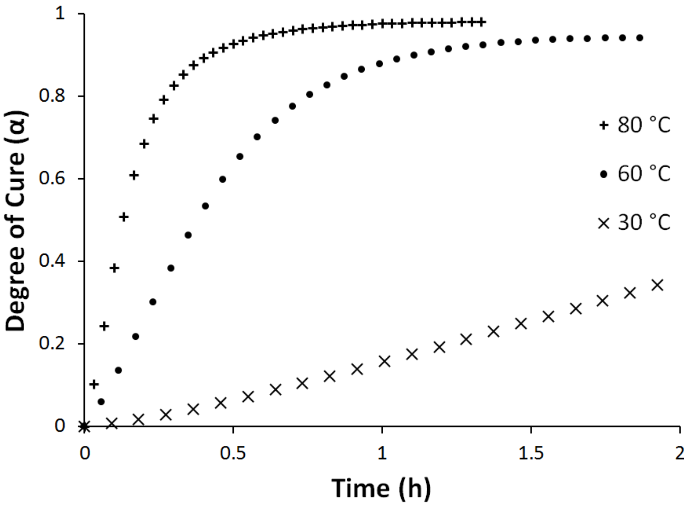

Figure 3.4 – Degree of cure as determined from the DSC isothermal cure experiments

To model this behaviour the works of Sourour and Kamal were combined with those of Chern and Poehlien, from Chapter 2, to yield the overall cure model, in its expanded form (Equation 2.5and Equation 2.7):

$$\frac{d\alpha}{dt} = \frac{\left(A_1 \exp\left(\frac{-E_{a1}}{RT}\right) + A_2 \exp\left(\frac{-E_{a2}}{RT}\right)\alpha^m\right)(1-\alpha)^n}{1+\exp[C_\alpha(\alpha-\alpha_c)]} \tag{3.2}$$

The rate constants, determined following the work of Han [81], and the diffusion constants, determined from least squares fitting, are presented in Table 3.1. From the forthcoming dynamic mechanical analysis of the cured polymer it was determined that the average glass-transition temperature, T_g, for this polymer is only slightly above room temperature. Since T_g is a cure-dependent property, its precise value will depend on the individual degree of cure of a give sample, thus T_g = 27°C is reported for the 60°C isothermal cure following ASTM E 1356 [82], as this cure temperature is the default used for the majority of the mechanical testing. To simplify the analysis, only one set of properties is used to describe this polymer, all of which represent values for a temperature above the glass-transition temperature. Further accuracy would no doubt be obtained by duplicating the experimental work for lower temperatures to capture properties at or below the T_g. Figure 3.5 indicates a good fit between the model and the experimental data.

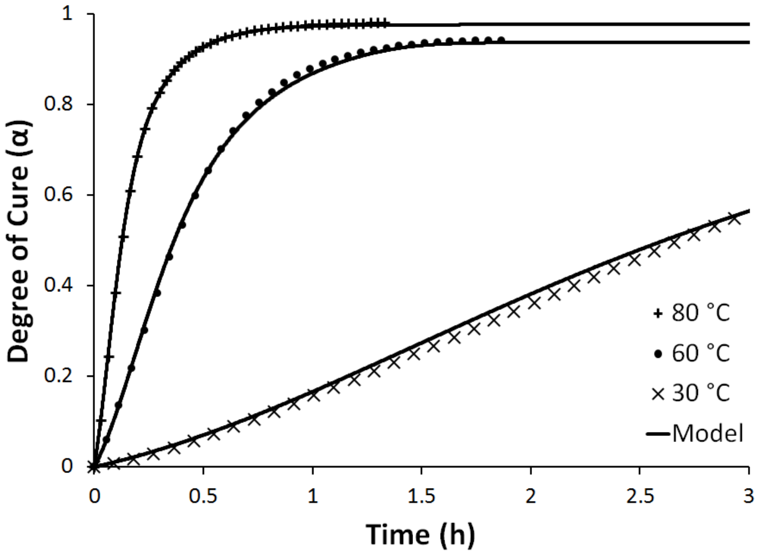

Figure 3.5 – The degree of cure compared between isothermal DSC tests and the cure model

Table 3.1 – Epoxy cure kinetic parameters.

Parameter	Value	Units
E_{a1}	55.03	kJ·mol^{-1}
E_{a2}	48.54	kJ·mol^{-1}
A_1	1.00 x 10^5	s^{-1}
A_2	5.13 x 10^4	s^{-1}
m	0.79	
n	1.53	
C_α	109.4	
α_c	0.0020 T [°C] + 0.817	
α_{gel}	0.0036 T [°C] + 0.609	

Another way to assess the model accuracy is to plot the cure rate with respect to the degree of cure, as shown in Figure 3.6. Here, some of the nuances of the model, and troubles with the experiments are depicted more clearly.

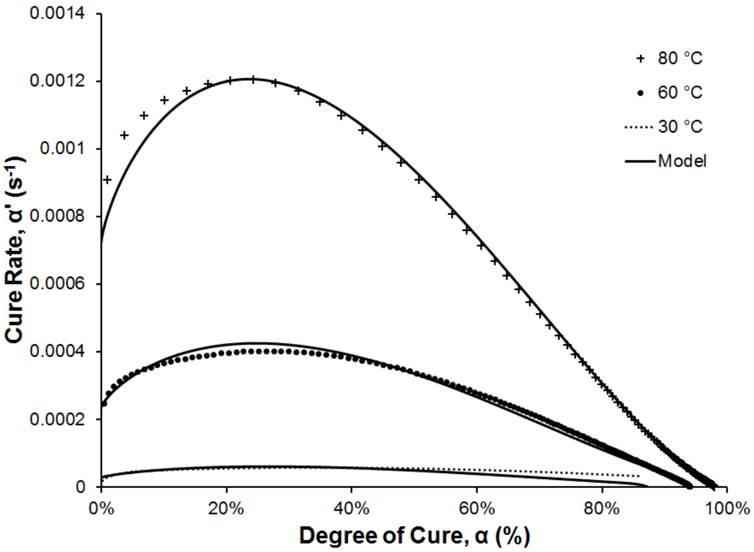

Figure 3.6 – Cure rate versus degree of cure for isothermal DSC experiments plotted against the cure model

Though the model maintains excellent agreement between the different experiments, some trouble is shown in the 30°C experiment. The model predicts that the maximum degree of cure should reach about 87%, while the experimental data suggests that the final degree of cure might be higher (the DSC only recorded the first 12 hours of cure). In consultation with the operator, a possible explanation is with the precision of the DSC: the error due to very small changes in heat flow over long durations can become compounded. Another inconsistency is seen in the initial and peak rates of reaction which is very sensitive to the uniformity and accuracy in mixing the epoxy. Though the epoxy was mixed in a larger 50g batch, there was approximately 0.5% error within the mix ratio of resin to hardener based on the accuracy of the weigh scale used. Moreover, if the resin and hardener were not uniformly mixed, there would not be a uniform reaction rate observed, which would show up in the data as a slight variance in the peak reaction rates as is actually observed. Thus, given the understanding of the curing dynamics, the model is accepted to perform well across the range of temperatures tested, despite some of the experimental irregularities.

In addition to the degree of cure, the cure gel point and onset of diffusion are also cure dependent. The gel point is assessed following ASTM D 4473 [83], while the onset of diffusion is evaluated by fitting the final slope of the cure rate vs. degree of cure curves from Figure 3.6. Note the 90°C dynamic cure DSC data was included here in increase the accuracy of fitting these parameters. Both of these variables are plotted in Figure 3.7, whereby linear relationships are obtained with respect to the cure temperature. In both cases higher gel and diffusion points occur at elevated cure temperatures, where the cure takes place over shorter amounts of time.

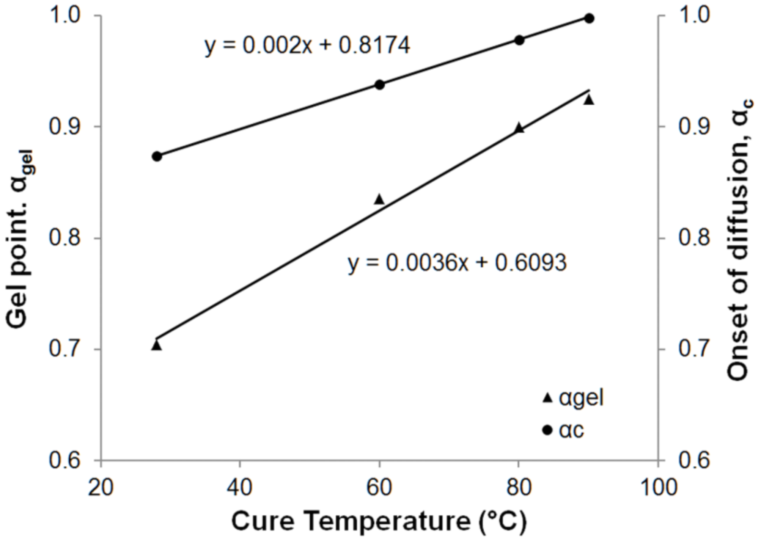

Figure 3.7 – Gel point and diffusion onset point as a function of cure temperature.

These relationships will enable future simulations to be able to account for any cure scheme, whether isothermal or dynamic, as any arbitrary cure point is now modeled based on its base chemistry.

3.2.3 Cure Shrinkage

Chemical shrinkage (also called cure or polymerization shrinkage), the primary source for residual stress during cure, was measured following ASTM D 2566 [84], though there are numerous ways to accomplish this task [85]. Though this standard has been withdrawn, it is the author's opinion that careful experimental procedure using this standard can still yield accurate data. To validate this claim, the cure shrinkage values obtained using ASTM D 2566 are compared to those obtained by monitoring the normal load from the parallel-plate rheometry in Section 3.3.4 and from the slopes obtained in the pycnometry experiments in Section 3.3.3. Figure 3.8 shows the results for all three methods, which were collected using the same isothermal 90°C, 2 hour cure cycle. The high temperature cure was selected to determine the maximum chemical shrinkage in the epoxy.

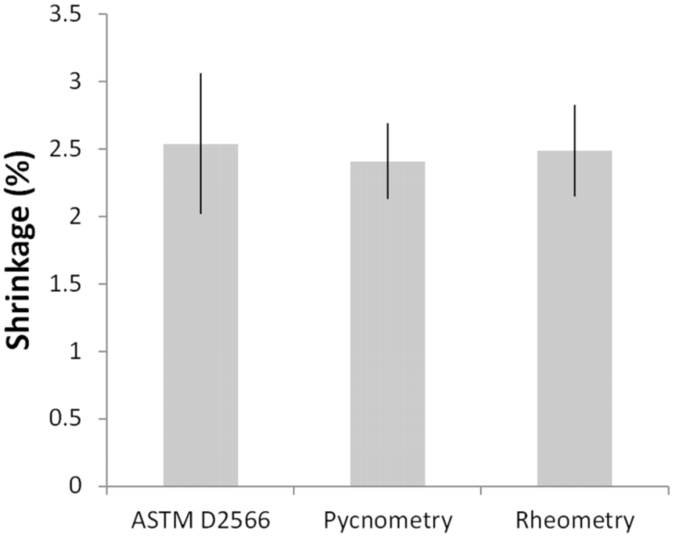

Figure 3.8 – Epoxy cure shrinkage from several experimental methods.

Within statistical deviation, all three methods generate the same cure shrinkage value. Though this was expected, it does give confidence to the use of any of these methods to measure cure shrinkage. This also partially validates the human error inherent to any experiment as the careful attention to detail results in a consistent measurement even when using different testing methods.

Interestingly, the effect of the cure shrinkage can be seen visually in the ASTM D 2566 samples when cured over a variety of temperatures. Figure 3.9 presents three samples cured at room temperature (22°C), 60°C, and 90°C respectively. These samples are in the shape of a long half-cylinder and are viewed facing normal to the flat surface under polarized light. Though not quantitative, the shrinkage can be visualized as the density of the vertical distortion lines, increasing with increasing cure temperature. Also visible is the change in colour of the epoxy from clear to amber, which the manufacturer describes as an indication of reaching a fully cured state. At the 90°C cure, there is evidence the sample was close to boiling, as there is the presence of entrapped gas. Also in Figure 3.9c), the high chemical shrinkage was enough to cause out of plane distortions along the gauge length of the sample. For reference, the width of the pictured samples is 24 mm.

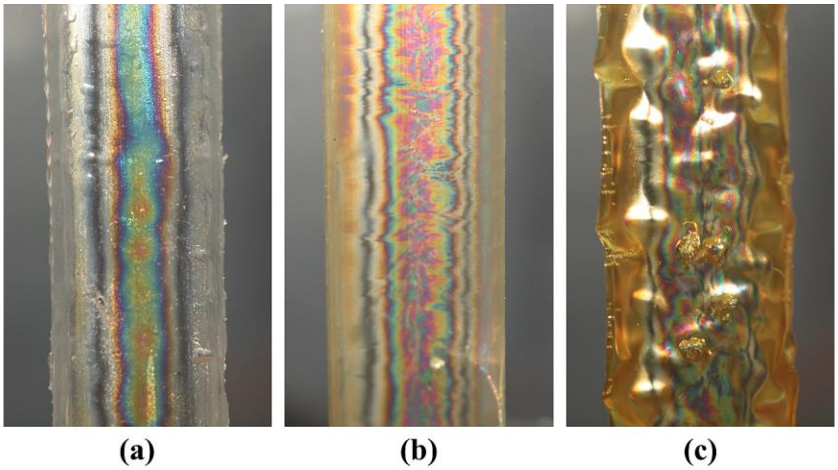

Figure 3.9 – ASTM D 2566 samples, photographed using cross-polarized lenses, cured at a) room temperature (22°C) b) 60°C and c) 90°C

To utilize this cure shrinkage parameter in the mechanical analysis, it is necessary to also relate this value to the degree of cure. Using the normal loads at various points from the 60°C rheology cure at various times, the degree of cure is determined from the relative change with respect to the total cure from the 90°C cure. When plotted in Figure 3.10, the shrinkage is found to be nearly linear to the degree of cure. The error of each point is a set value based on the precision of the load cell.

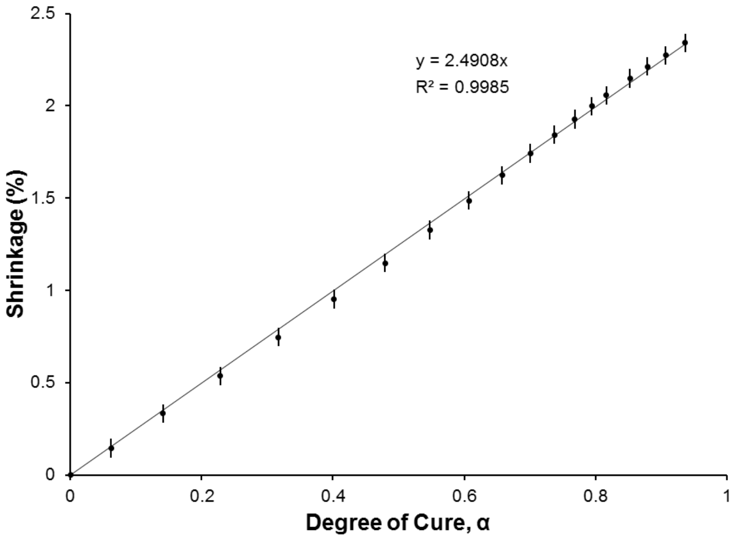

Figure 3.10 – Cure shrinkage with respect to the degree of cure from the rheology experiments.

3.3 Mechanical Properties

The polymers are expected to behave in an isotropic manner, as no effort is made to orient the polymers during cure. To account for experimental error, all properties are determined using sample series consisting of a minimum of 8 samples. The highest and lowest values are discarded, with the remainder averaged to give the presented values to limit the outlier bias [86]. The standard deviation is calculated assuming the samples represent only a portion of the population, rather than the complete population, to give a conservative value for the deviation range. To begin, static properties (modulus, yield, Poisson’s ratio, etc.) are first measured to provide the datum material response. Thermal and viscoelastic responses are determined to better understand the mechanical behaviour during cure. Finally, fracture behaviour is studied to generate inputs into the predictive material model.

3.3.1 Elastic Properties

Quasi-static testing was performed on neat epoxy and polyester in a number of ways. First, the modulus, yield, and tensile properties were obtained by casting neat epoxy and polyester specimens in a split mould (See Figure 3.11) following the ASTM D 638 type V sample geometry [87], but with extended tabs with which to better grip the samples. The pictures show the mould and application of a carnauba wax to aid in the subsequent sample de-moulding. Between uses, the mould was re-polished using an aluminum metal polish and a hand-held rotary polishing tool as well as receiving a thin layer of wax so that the samples would not bond to the mould during cure.

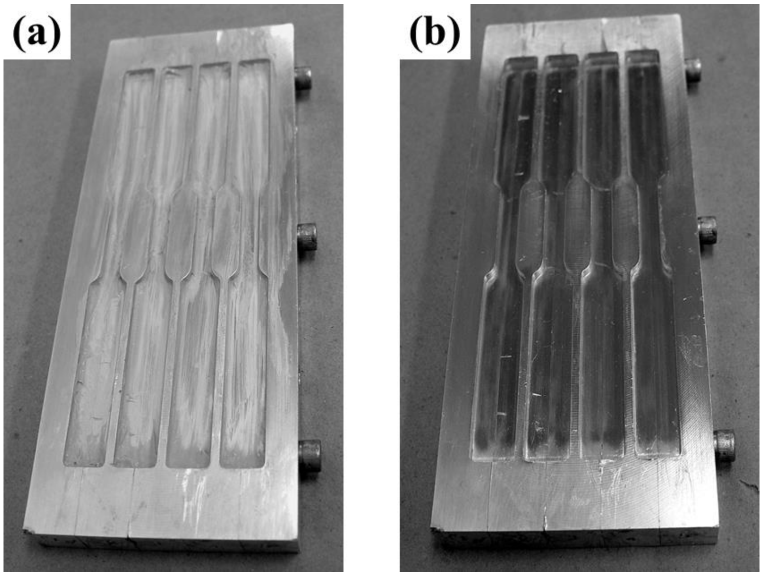

Figure 3.11 – Split aluminum mould used to create polymer tensile samples showing a) application of wax b) polished and buffed mould

These samples were tested on a 5943 Instron equipped with both a 1kN load cell and an independent 25mm gauge extensometer to measure strain. A typical stress-strain result for each polymer is presented in Figure 3.12.

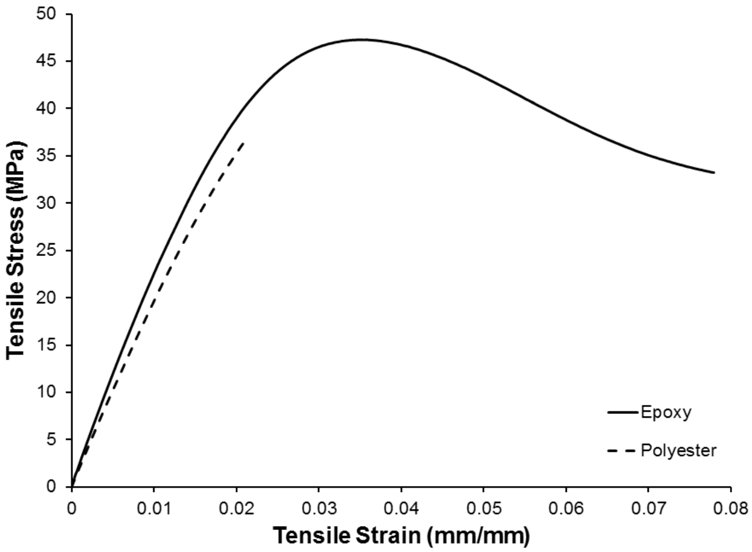

Figure 3.12 – Typical stress-strain response comparison between the selected epoxy and polyester.

The Polyester is seen to behave in a brittle manner, averaging a failure strain of 1.9%. The epoxy shows moderate strengthening behaviour before the tensile strength is reached, with a larger ductility than expected for a typical thermoset. The reported values for the modulus, yield strength, tensile strength, and strain-to-failure are all determined based on the same ASTM D 638 standard and are reported in Table 3.2, below.

Further, epoxy was cast in flat sheets and isothermally cured at temperatures of 22°C, 60°C, 90°C, which corresponds to cures of 87%, 94%, and 100% respectively. Since this testing was chronologically performed prior to the chemical cure analysis, there is no corresponding degree of cure for the shown 120°C case, as this was beyond the safe limits for the DSC characterization. No future testing utilized any cured samples at such an elevated temperature, but the results in this case are important to illustrate a trend in the mechanical properties. Samples were cut and machined according to ASTM D 638 type IV. Poisson’s ratio was measured by means of two independent extensometers and tested using an Instron 8804 load frame with a 5kN load cell. Figure 3.12 displays the trends in modulus, Poisson’s ratio, and work of fracture for the epoxy.

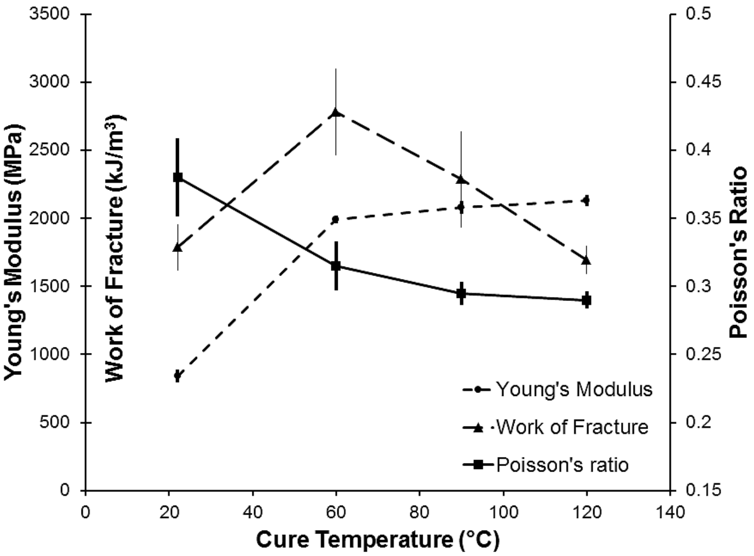

Figure 3.13 – Epoxy mechanical properties as related to cure temperature.

As the cure temperature increases the Young's modulus increases while the Poisson's ratio decreases. Initially the polymer stiffness and ductility increase as the degree of cure increases. However, at some point, the increased degree of cure prevents further ductility, resulting in a lower work of fracture at elevated cure temperatures. Though not explored further, this behaviour represents one avenue to optimize the performance of the bulk composite: to determine the best trade-off between the stiffness and failure strain by controlling the cure temperature (degree of cure). All the measured mechanical properties for both the polyester and the epoxy are collected in Table 3.2 for reference.

Though not clear from Figure 3.13, Poisson's ratio can be modeled as a linear relation to the degree of cure:

$$\nu = \nu_o(D_1 - D_2\alpha) \tag{3.3}$$

where ν_o is the effective liquid Poisson ratio, and D_1 and D_2 are the fitting intercept and slope respectively. This relation gives an R^2 value of 97.9%.

Table 3.2 – Room temperature mechanical properties for Epoxy and Polyester based on their default isothermal cure cycles.

Property	Epoxy	Polyester	Units
Yield Stress	21.7 ±1.0	16.0 ±1.0	MPa
Tensile Stress	48.7 ±1.0	38.5 ±1.0	MPa
Young’s Modulus	2.00 ±0.03	1.60 ±0.07	GPa
Failure strain	7.7 ±1.8	1.9 ±0.2	%
Poisson’s ratio	0.30 ±0.01	0.28 ±0.01	
Density	1.16 ±0.01	1.21 ±0.01	g/cm^3
Cure shrinkage	2.49 ±0.4	2.66 ±0.1	%

3.3.2 Elevated Temperature Yielding

Thermal yield behaviour was determined using samples cast at 60°C and tested using an Instron 3366 load frame and thermal chamber with either a 5kN or 500N load cell, depending on the testing temperature. To gain insight into the changing mechanical response of the epoxy, consider Figure 3.14 where several stress-strain curves at elevated temperatures are graphed. As the temperature increases, the modulus, yield and tensile stress decrease as expected. Unexpected is the transition into viscous flow behaviour which is unusual for a thermoset material. Also interesting is the disappearance of the initial plastic hardening peak synonymous with a polymer tested above its glass transition temperature.

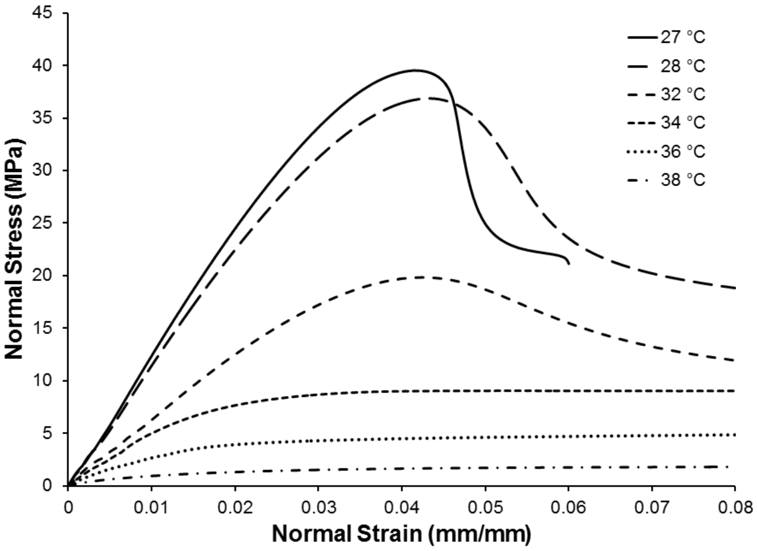

Figure 3.14 – Epoxy stress-strain response for several temperatures shown for the first 8% strain

The combined yield and modulus data over a range of temperature is shown in Figure 3.15. The data for yield is divided to represent the use of the 5kN load cell (dark points) and 500N load cell (light points) for both datasets. The modulus data is also compared with the values for modulus obtained from DMA testing at the lowest frequency of 0.1 Hz. Both the yield and modulus of this epoxy are seen to be highly temperature sensitive, while decreasing in similar magnitude with increasing temperature. The elevated temperature yield data is something not typically reported for thermosetting polymers, but has a great influence on the observed behaviour of this and other polymers during cure. To model this behaviour mathematically, a simple empirical relation was used as a decaying exponential function:

$$\sigma_y = Y_1 \exp(Y_2 T) \tag{3.4}$$

with Y_1 and Y_2 fitting the exponential for temperatures, T, in degrees Celsius and giving a yield stress in megapascals. The yield behaviour below the glass transition temperature is set as a constant.

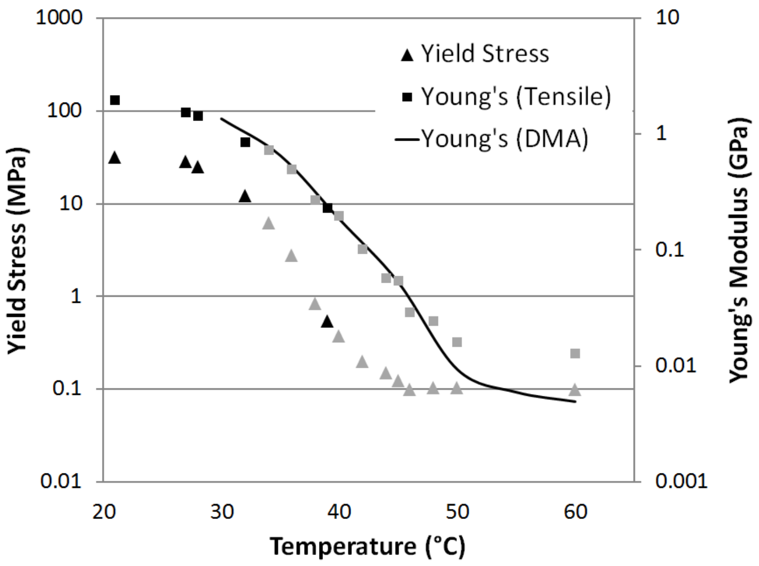

Figure 3.15 – Thermal yield and modulus behaviour for epoxy cured at 60C from tensile and DMA testing.

3.3.3 Density

The epoxy density was measured via pycnometry with the AccuPyc 1340 by Micrometrics for both a room temperature cure and an elevated cure at 60°C. For the room temperature case, measurements were taken every 20 minutes for the first 6 hours of cure, then again at the 16 hour point, and also at 48 hours. At 60°C, the density was measured every 10 minutes for the first hour and a half. This data is collected in Figure 3.16. Room temperature on this particular day averaged a bit high at 24.3°C. Also, the variability in the room temperature data is due to the fluctuating room temperature as the air conditioning was intermittent on a rather warm day.

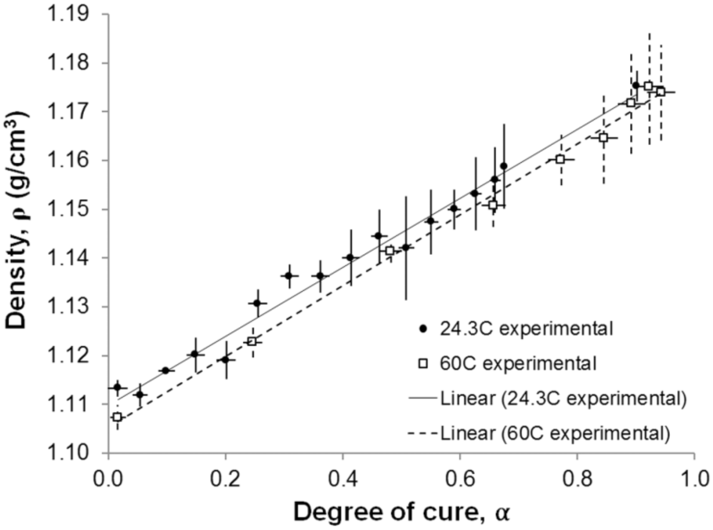

Figure 3.16 – Pycnometric density measurements for room temperature and 60C isothermal cures

Note that no statistical distinction can be made between the two temperature tests. This suggests a small value of thermal expansion, which is indeed the case, as indicated on the manufacturer's datasheet. Though the density does not change substantially over the cure, as even a small change will impact the resulting residual stress, it is important to model this behaviour as carefully as possible.

3.3.4 Viscoelastic Behaviour

The cure, temperature, and time dependent modulus were measured in several ways to ensure accurate data collection. First, the previously presented quasi-static tensile tests were performed on fully cured samples to gather the room-temperature cured behaviour, as in Table 3.2. Second, fully cured samples were tested on a TA Instruments Q800 dynamic mechanical analysis (DMA) machine to determine the temperature influence on the modulus. Using the double cantilever beam setup and multi-frequency mode, the modulus was measured at 20 frequencies (equally spaced on a logarithmic scale) between 1 and 100 Hz at each temperature between 30-70°C in 5°C increments. Finally, using a parallel plate rheometer, the AR 2000ex by TA Instruments, liquid epoxy was cured isothermally at 60°C for 6 hours while the modulus was continually monitored at frequencies of 0.1, 1, and 10Hz, but using a low applied strain of 0.05% as to prevent the experiment from adversely accelerating the cure.

To begin the data presentation, Figure 3.17 shows typical epoxy and polyester thermal response. The epoxy is very sensitive to changes in temperature, with an abrupt drop in modulus past room temperature. The polyester is more thermally stable, with a gradual decrease in performance over a larger temperature range. Both of the presented curves were taken at a frequency of 1Hz using the default isothermal cure cycles as previously described. By composing multiple curves using different loading rates at each temperature, the complete temperature response can be determined for one degree of cure.

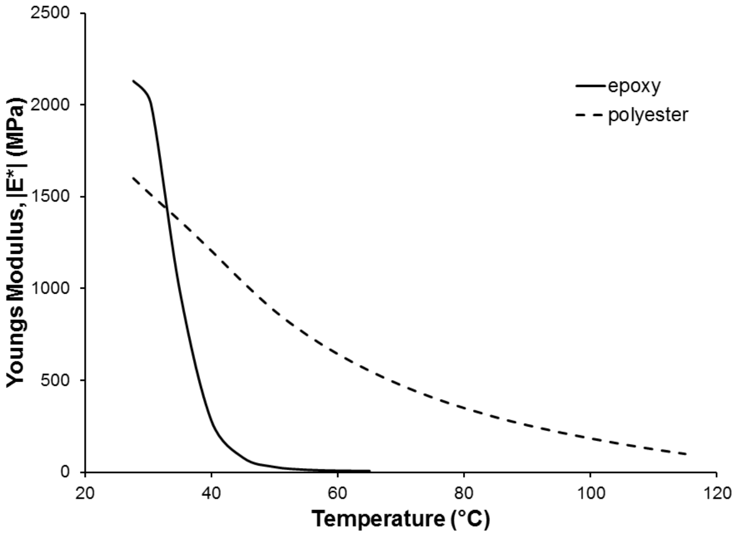

Figure 3.17 – Typical DMA curves for epoxy and polyester measured at 1Hz over a range of temperature.

To model this behaviour, Figure 3.18 shows the rheometric data for the 60°C isothermal cure and the relaxation modulus predicted by Equation 2.13 from Chapter 2. Both the modulus components are also shown which indicate a gel point just after the first hour of cure. This data allows the modulus to be determined at any cure point for one temperature and one loading rate.

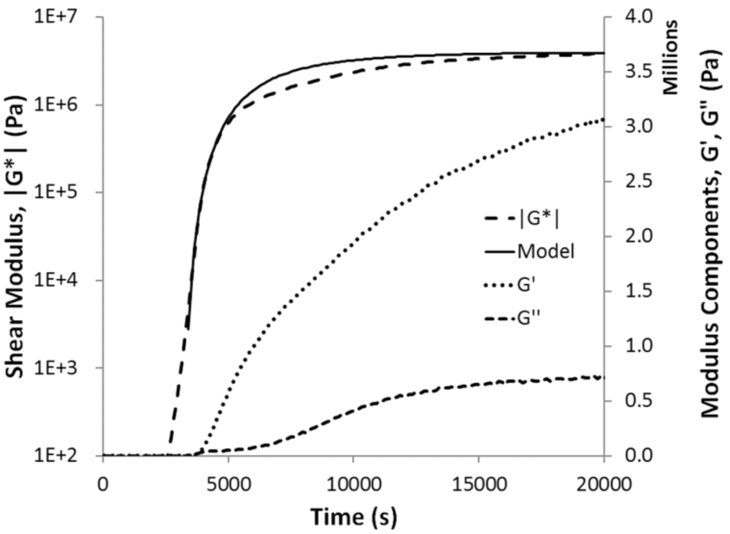

Figure 3.18 – Shear modulus, modulus components, and the selected model for the 60°C isothermal rheometry cure

In order to combine the data from Figures 3.17 and 3.18, to completely model the temperature and cure dependency of the polymer modulus, a link must be made between the modulus at a given temperature and the modulus at a given degree of cure. This is done by conducting an extended rheometric test measuring the modulus as the epoxy cures for several loading rates. The difference between the measured values at different frequencies becomes the shift factors through which to transform the modulus measurements at an arbitrary cure to a modulus at a given time. Figure 3.19 highlights how the modulus viscoelasticity develops past the gel point for several loading rates.

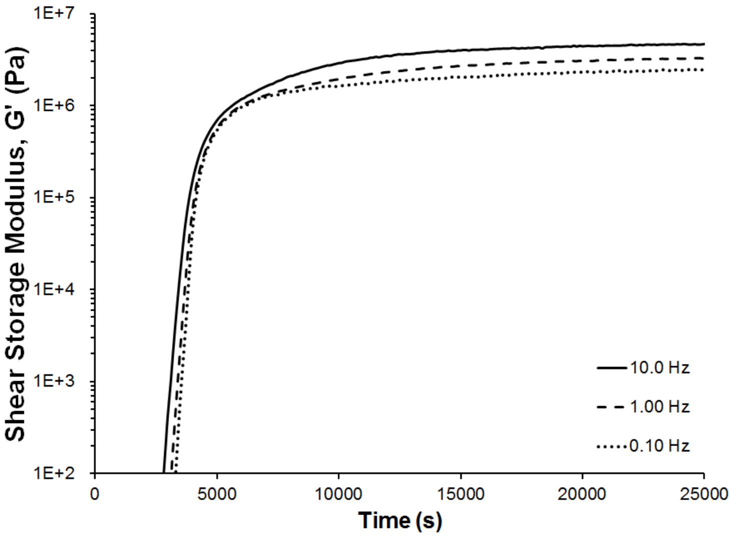

Figure 3.19 – Shear storage modulus of a multi-frequency 60°C isothermal rheometry cure depicting relaxation behaviour during cure

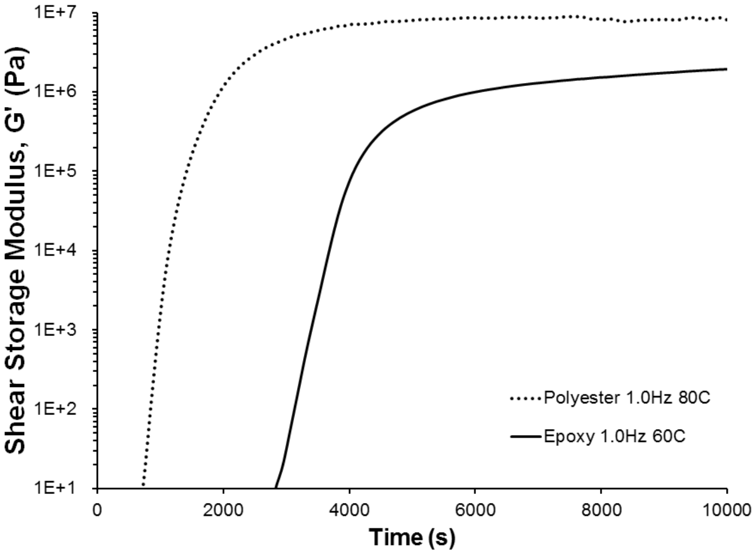

Figure 3.20 – Polyester and epoxy cure comparison using the 1Hz rheometry data.

As a comparison, Figure 3.20 presents the 1Hz curve from the polyester rheometry testing with the 1Hz curve from the epoxy. Though the cure temperatures were different between the epoxy and the polyester, several comparisons can still be made: the polyester cures faster and to a higher degree than the epoxy and the polyester does not exhibit any viscoelastic behaviour. Like the epoxy in Figure 3.20, the polyester was measured at multiple frequencies during cure, but unlike the epoxy, all the rheometry curves overlapped suggesting that there was no viscoelastic response, even during cure.

The final step to describe the complete cure / temperature dependent viscoelastic response is to combine the cure dependent modulus values with the temperature dependent modulus values using the determined shift factors. Figure 3.21 is the result of this composition indicating how the DMA measurements are time shifted to account for the temperature, presented similar to [88]. To interpret how this master curve is utilized, consider how the modulus behaves. A modulus at a given cure is first calculated, then, using this curve to determine the effective relaxation time, the temperature is taken into account. At a low temperature, the modulus is determined over a short time (no relaxation, high modulus), while at a high temperature the modulus is determined over a long time (some relaxation, low modulus).

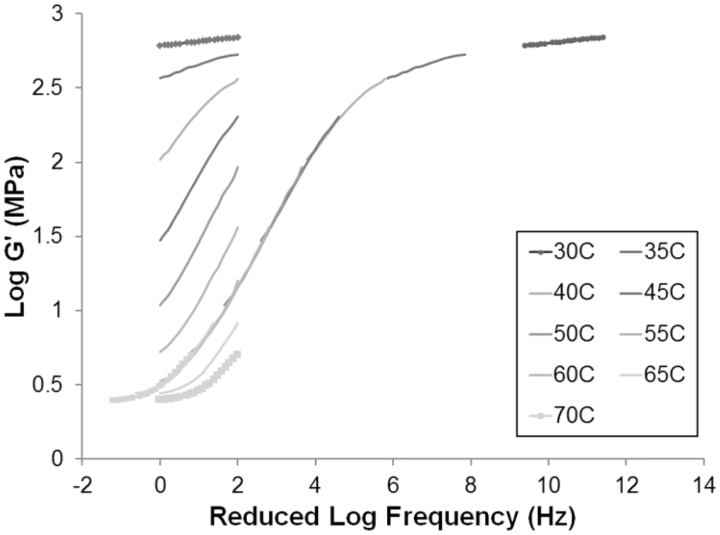

Figure 3.21 – Shear storage modulus from DMA measurements and the time-shifted master curve with reference of 60°C

3.3.5 Fracture Properties

To conclude the presentation of mechanical properties are several tests to determine the fracture behaviour of the epoxy. Though desired, it was not possible to cast the polyester with the large, required sample geometry to conduct the same experimental analysis.

The fracture toughness, or resistance to the propagation of a crack, depends on the mode of loading around the crack. Using ASTM D 5045 [89], the mode I crack opening values were determined with large-cast samples to generate a plain strain condition within the samples. The large plate, shown in Figure 3.22, was cast and allowed to cure at 60°C. By alternating between a hot plate and a freezer, the samples were prevented from curing uncontrollably due to the initial rapid release of energy from the large volume of epoxy. A thermocouple was used throughout the cure, which was continuously monitored for the first 8 hours, to prevent the epoxy from experiencing a temperature change greater than 5 degrees. The lines on the plate indicate where the single end-notch beam (SENB) samples were to be separated and cut; for reference, the plate thickness was 26mm.

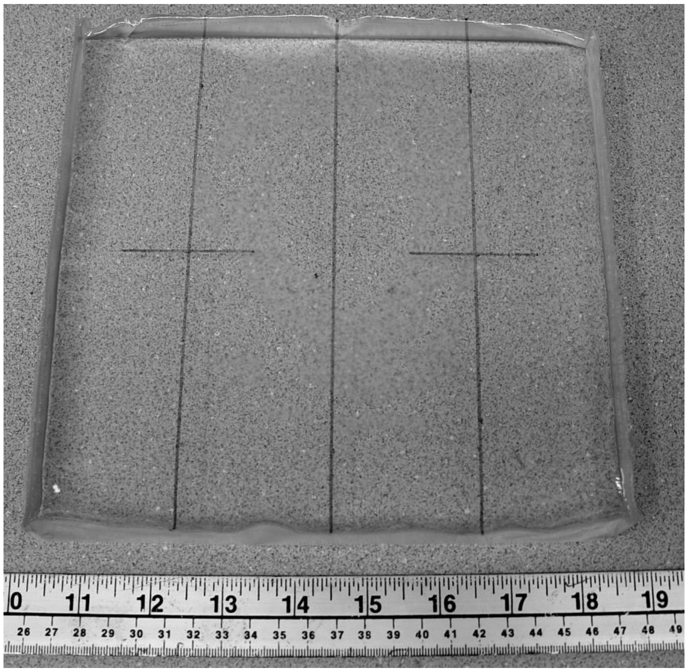

Figure 3.22 – Thick epoxy plate as-cast, prior to the fabrication of the SENB samples.

Two of the created samples were tested as fabricated with the rounded-cut groove. The remaining two samples received an additional pre-crack by tapping a razor blade at the bottom of the larger machined crack. This allowed a comparison of the energies associated with both the crack initiation and crack propagation. However, the low number of samples implies that sample statistics cannot be calculated in this instance. Additionally, as the samples were cast longer than required, the end of one sample was used to perform an indentation test to determine the machine compliance, reducing error from the tested samples. The data is presented in Figure 3.23, showing the indent graph, the two samples without a sharp crack, and the two samples with the sharp crack. Using the analysis of Bakker [90], the K_{1c} and G_{1c} values are given in Table 3.3.

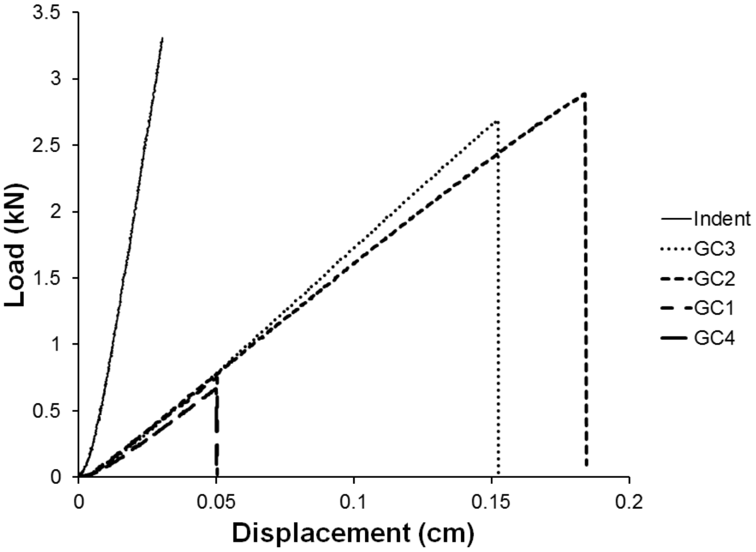

Figure 3.23 – K_{1c} test data with calibration indent, two samples with a sharp pre-crack, and two samples with a rounded pre-crack.

Similar to the ASTM 5045 testing, an asymmetric loading test after Slepetz is used to determine the K_{2c} and G_{2c} values [91]. This test was conducted using the Isopescu test geometry of ASTM D 5379 [92], but using the loading depicted in Figure 3.24.

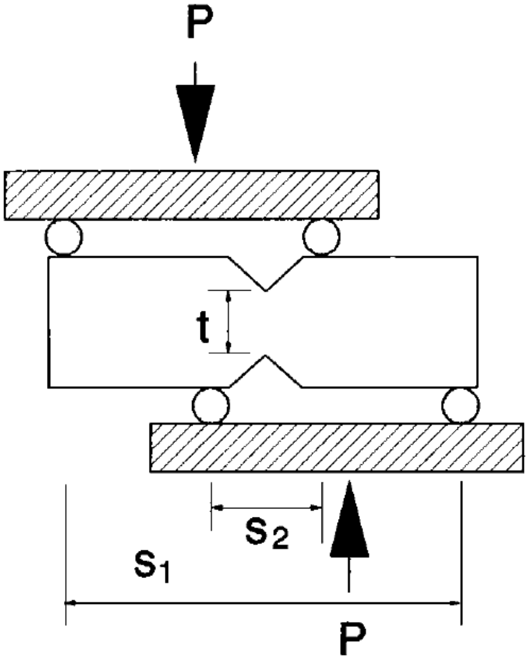

Figure 3.24 – Asymmetric four point load configuration from [45] after [91].

Besides the change in loading mode, the only difference in the analysis is with respect to the determination of the value for the crack magnification factor. As the sample sizes were similar, the crack factor from Yoshihara was used [93]. The values for the K_{2c} and G_{2c} samples are also in Table 3.3. Since these samples are tested under a plain stress condition, the required sample geometry was greatly reduced, and a full sample series was possible to generate the appropriate statistics.

Table 3.3 – Fracture properties of neat epoxy.

Property	Value	Confidence	Units
K_{1c}	1.47	7.8 % error	$MPa\cdot m^{1/2}$
G_{1c}	0.78	9.9 % error	$kJ\cdot m^{-2}$
K_{2c}	2.34	± 0.09 S.D.	$MPa\cdot m^{1/2}$
G_{2c}	1.67	± 0.17 S.D.	$kJ\cdot m^{-2}$

4 Interfacial Strength

Determining composite interfacial strength is the primary aim of this research. Three currently available techniques, the fragmentation test, the push-out test, and the lap shear test are selected for further study. The fragmentation test is presented as a datum test, without modification, to provide a lower bound to all interfacial measurements. The push-out test is modified to generate simplified in-situ results for industrial composites. The lap-shear test is modified to provide quantitative results of the impacts of polymer processing and fibre surface preparation. The lap-shear test is further utilized to distinguish between interfacial normal and interfacial shear strength, something previously missing in the literature. Using these tests, the interfacial strength is assessed under a variety of conditions including fibre surface chemistry, degrees of polymer cure, polymer fillers and temperature.

4.1 The Fragmentation Test

Though known to underestimate the interfacial shear strength (IFSS) [6, 52], the fragmentation test is a relatively simple test to indirectly determine the properties of the fibre-matrix interface, and is considered well-understood [47, 94, 95]. As will be explored later in the simulation section, one reason for this underestimation of strength has to do with the dynamic nature of the fracture events and the resulting stress waves that can cause additional fracture.

Continuing from the work of Bruce [96], a split aluminum mould was used to fabricate the fragmentation samples. Pictures of the sample mould were previously shown in Figure 3.11. The mould follows similar geometry to the ASTM D638 type V sample geometry, but with extended tabs for better sample grip, and importantly, to ensure stress was gradually applied to the fibre for better uniformity in the fibre breaking. For these tests, TG-18-u glass fibres from JB Martin and T700 carbon fibres from Toray were used; both types of fibres were ordered with epoxy-functionalized sizing.

Between the mould segments there is a small recessed groove at either end of the tensile sample through which to slide a fibre. This allows the fibre to be suspended at the midpoint of the sample while the polymer is curing. In order to get good images of the embedded fibre, the mould must be open-air cured, with nothing touching the exposed surface. Also important is to slightly over-fill the mould, with a raised meniscus, such that the cured sample will be as optically flat as possible.

To prepare the fibres, sections of the unidirectional fibre bundles were cut and cleaned. As-delivered, the fibres were coated with an epoxy-compatible sizing which was not disclosed by the manufacturer. Sizing is a proprietary collection of chemicals designed to modify the surface of a fibre, typically containing a coupling agent, a wetting agent, and other additives to protect the fibre during transportation. To understand the impact of different coupling agents, the fibres were baked at high temperature (~600C) to burn away these unknown polymer coatings and rinsed in ethanol. This process was repeated twice before known silanes were applied. The selected silanes were applied by deposition from aqueous alcohol: diluted to 2% in a 95% ethanol/5% water solution as recommended by industry [97]. This solution pH was controlled to the range of 4.5-5.5 with glacial acetic acid. The cleaned fibres were immersed in this solution for 60s before being rinsed in ethanol and baked at 100C for two hours to cure the silanes to the glass surface. Only the glass fibres were prepared in this way; the carbon fibres were left with the original sizing as the burn process would likely have caused excessive damage to the underlying carbon fibre.

Using the prepared mould, fibres, and mixed epoxy, fragmentation samples were cast at 60°C for 4 hours. The samples were tested on an Instron 5943 single column load frame at a constant displacement rate of 1 mm/min until a given strain was reached, at which point the displacement was held for 2 minutes. To track the strain, a 25mm clip gauge extensometer was fitted around each fragmentation sample to measure the strain, but not damage the sample. Fragmentation testing requires that the polymer have a greater strain-to-failure than the fibre in order that the fibre can be properly loaded and fragment without the surrounding matrix failing first. The epoxy was loaded to a strain of 4%, while the polyester could not be tested in this fashion, as its strain to failure of 1.9% was less than that of the glass fibres (2.4%) used in these studies.

Images were taken of each sample gauge length before and after tensile testing. The pre-testing images were used to ensure the fibre was properly located within the sample, to ensure the fibre did not break during fabrication, and to measure the fibre diameter. The post-testing images were used to optically measure the fragmented sections. Figure 4.1 illustrates one such sample, depicting the sample prior to testing, and showing the break patterns following testing. The fragmented section lengths were recorded along the center of each fibre segment.

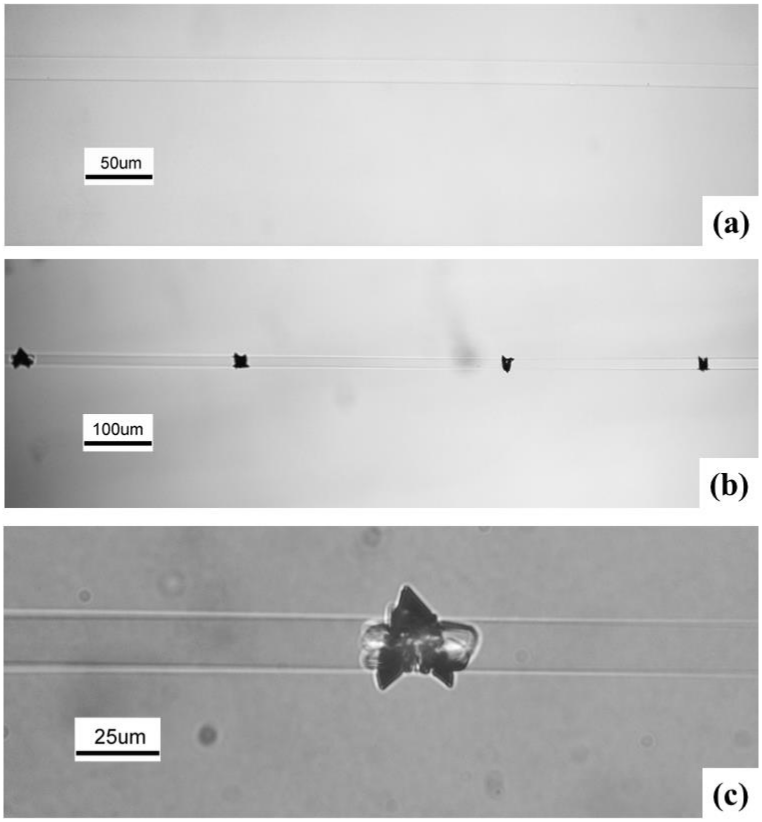

Figure 4.1 – Fragmentation sample a) pre-testing b) post-testing fragments c) high magnification break pattern.

The magnified section of a typical fibre break in Figure 4.1b-c suggests several things. First, the fibre is breaking in a consistent brittle, tensile manner, as evidenced by the regular spacing and vertical fracture. If the fibre were not in line with the tensile sample, it would be expected to experience a bending load, which would manifest as angled fracture segments, and would jeopardize the accuracy of the interfacial strength calculation. The small crack propagation into the matrix confirms the matrix is relatively tough and able to continue stress transfer across a fibre break. Also seen in most images is a lack of debonding along the fibre length, suggesting a strong interface. Figure 4.2 is taken with polarized light to image the matrix deformation around several broken segments. This technique was used to determine the effective loading radius around the fibre for future simulations. It was found that at minimum five fibre diameters into the matrix is required for the load transfer to be effective, as has been observed by other authors [94].

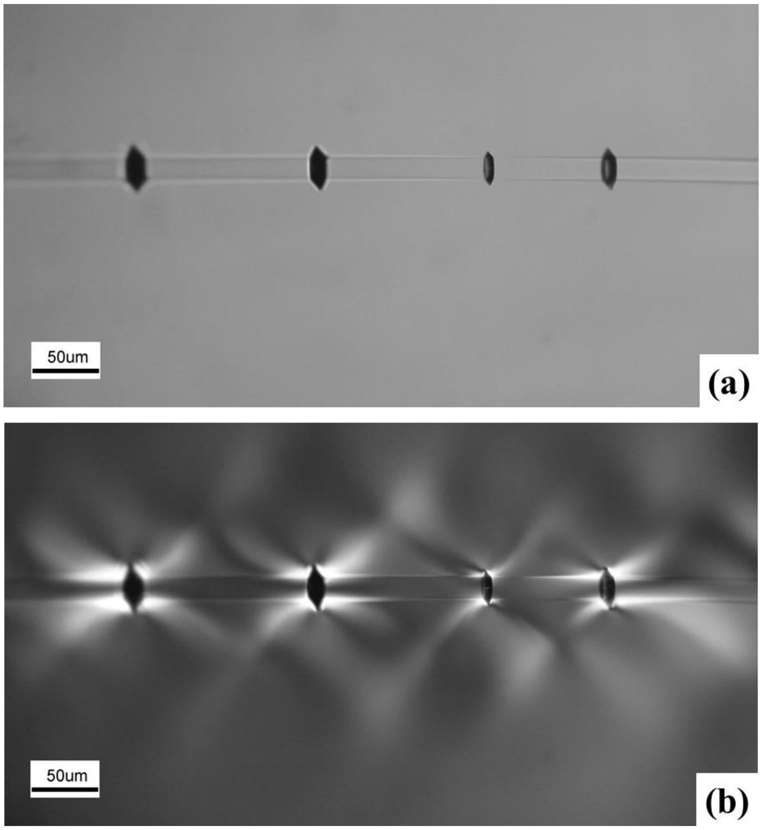

Figure 4.2 – Fragmentation break pattern a) without and b) with cross-polarized lenses to indicate the size and geometry of yielded matrix around fibre.

By recording the length of all broken fibre segments it is possible to determine the statistical average fibre length. A minimum of 100 segments were measured for each type of sample. The results from one of the glass / epoxy fragmentation samples is presented in Figure 4.3 with a superimposed Gaussian curve. While it was expected that a normal distribution of fibre lengths should be observed, the range of values was larger than traditional theory. According to Drzal, the fibre length, l, should vary between the critical transfer length, l_c, and half the critical transfer length [98]:

$$\frac{l_c}{2} \leq l \leq l_c \tag{4.1}$$

However, newer work from Favre and Drzal have determined this is not the case, suggesting a wider range of fragment lengths is possible, as was actually observed [47, 99].

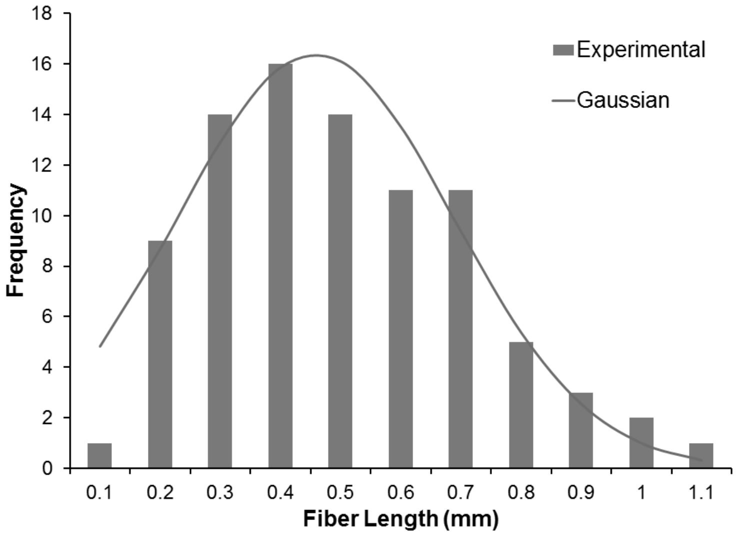

Figure 4.3 – Length distribution from epoxy/clean glass fragmentation samples with superimposed Gaussian distribution

By applying the traditional shear lag theory of Cox [34], Kelly and Tyson [46] determined a simple relation between the interfacial shear stress, τ_i, the fibre diameter, d, the strength of the fibre in tension, σ_f^* , and the critical transfer length:

$$\tau_i = \frac{\sigma_f^* d}{4 l_c} \tag{4.2}$$

From the work of Feih et al., the critical transfer length is equal to 4/3 the mean length of the measured fibre segments [95]. This is one method to account for the distribution of fibre strength, and results in the modified interfacial shear strength as:

$$\tau_i = \frac{3\sigma_f^* d}{16 l_m} \tag{4.3}$$

where l_m is the average fibre length. The fibre strength was provided by the manufacturer as 2600 MPa for the glass fibres and 4900 MPa for the carbon fibres. Using Equation 4.3, the data yields the interfacial strength for the various tests. These results for the glass /epoxy samples are collected in Table 4.1, below, while the carbon samples require additional discussion before the results can be presented. Note these values do not account for the lap-shear disk thickness and are reported for thicknesses of approximately 0.20 mm.

Table 4.1 – Interfacial shear strength of the epoxy / glass fragmentation tests.

System	Interfacial shear strength, τ_i
Epoxy / clean glass	32.4 ±4.2 MPa
Epoxy / Z6020 glass	31.2 ±3.1 MPa
Epoxy / Z6030 glass	24.7 ±2.6 MPa
Epoxy / Z6040 glass	36.3 ±3.7 MPa

The Epoxy / Z6030 coated glass samples were the only ones to indicate a “weak” interface. At the point a fibre fractures, excess strain energy is introduced to the surrounding matrix and interface, which can cause debonding along a weak interface. A weak interface is relative to the yield strength of the matrix. Figure 4.4 presents one segment of a fragmented fibre which was coated in the Z6030 silane.

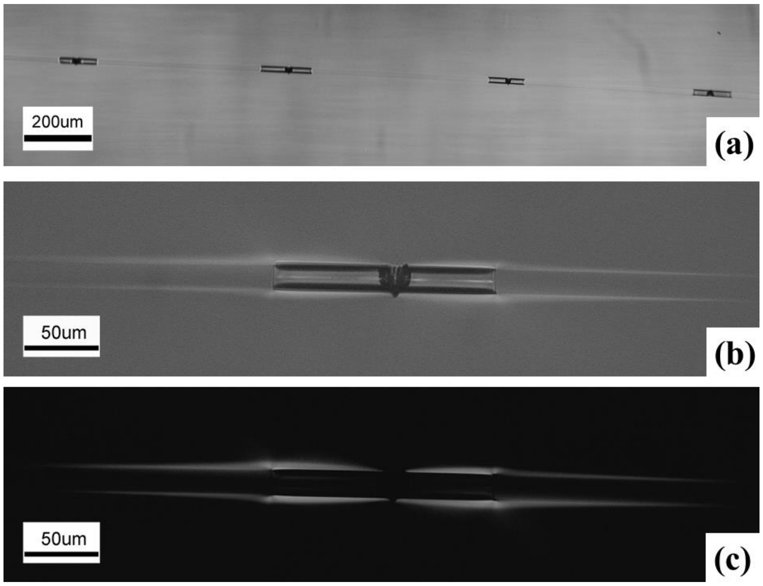

Figure 4.4 – Break pattern for epoxy/Z6030 coated glass of a) break distribution b) single debond section c) matrix yielding under cross-polarized filters

Here several features of the fracture events are notably different from those presented in Figure 4.2. There is a measurable darkened area around both fibre ends at a point of fracture indicating the extent of the interface debonding. There is almost no crack extending into the matrix surrounding a fibre break, as the interface consumed this energy rather than the matrix. Further, the polarized image in Figure 4.4c shows substantially less matrix deformation surrounding a fibre than that seen in Figure 4.2c. Using these images, it is possible to estimate the interfacial debond energy using the equation introduced by Zhou [48]. With an average debond length of 119.4 ±11.8 µm, the interfacial debond energy is calculated as 506.9 ±50.5 J/m^2.

The carbon fibre samples presented additional difficulty to analyze. Figure 4.5 shows an image of the two additional issues: fibre pairs and residual twisting. During industrial fabrication of these PAN-based carbon fibres, they are evidently twisted together, which permanently deforms their shape. Though the twisting is expected to change the fragment transfer length, as the twist was small (about one fibre diameter), no correction was made to the measured fragment length.

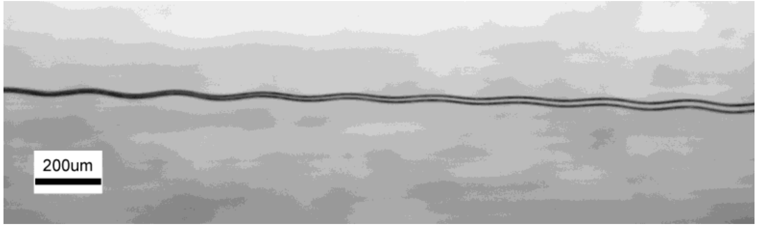

Figure 4.5 – Carbon fibre fragmentation sample.

However, the number of fibres is important consider. Due to their size and the fibre twisting, it was not feasible to isolate a single carbon fibre long enough to be used in the fragmentation samples; thus, pairs of fibres were used. This caused the effective fibre diameter to change. Using the work of Bruce [96], an expression to determine this effective diameter was employed:

$$d_e = d\sqrt{n_f} \tag{4.4}$$

where d_e is the effective diameter, d is the average fibre diameter, and n_f is the number of fibres. Using this diameter in place of a single fibre diameter, the carbon / epoxy interfacial shear strength was determined as 45.0 ±7.0 MPa.

4.2 Modified Push-out Test

A second method to measure the interfacial shear strength is with the push-out test, here modified with improved geometry. In the standard push-out test, a thin sample must be prepared such that the flat surface is normal to the fibre(s) [42, 100]. It can be troublesome both to prevent damage during sample preparation and to properly support the thin sample during indentation testing. Here, a sample is created from a bulk composite by means of focused ion beam (FIB) milling. The novelty is that many samples can be created from an industrial composite without the trouble of creating a thin section. Further, by controlling the geometry, the matrix becomes self-supporting, and eliminates the need for an external fixture or to properly locate the sample within the fixture. Figure 4.6 presents a 3D model of the sample geometry. In Figure 4.6a), the interfacial area is highlighted in white, while Figure 4.6b) indicates the undercut angle.

The undercut was a limitation imposed by the maximum rotation of the FIB beam, but could be eliminated with some sample refinements if desired. This work was initially an exploratory study to test the feasibility of using such a technique to measure the interfacial properties of fibre composites. Thus only three carbon/epoxy samples and three glass/epoxy samples were commissioned, with and additional three glass/epoxy samples that had been fabricated using plasma etching.

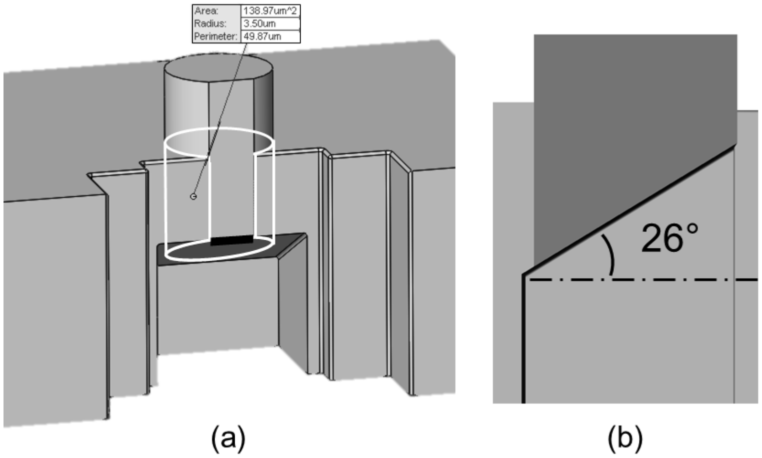

Figure 4.6 – Schematic model of push-out sample: a) 3D rotated view with bond area highlighted b) 2D cutaway side view with indicated 26° undercut angle.

To create these samples, glass fibre and carbon fibre reinforced epoxy sheets were made in a traditional hand-layup method (the same fibres as used in the fragmentation studies). The default 60°C, 4hour cure was used for all the samples. Rectangular samples were cut and mounted perpendicular to the fibre axis using cold-mount epoxy, so as to prevent any change in cure state or damage from thermal cycling using a hot mount process. Once the samples were appropriately polished, fiducial cuts were created using a low-speed diamond saw as seen in Figure 4.7. These cuts became the basis for selecting, locating and milling the micro-pillar samples.

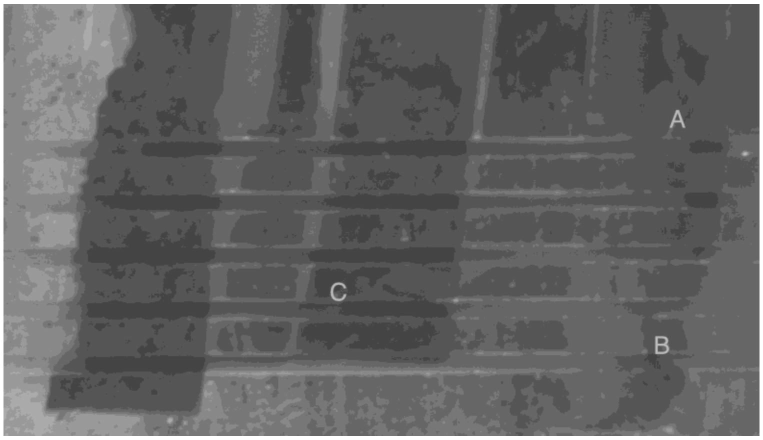

Figure 4.7 – Mounted and polished carbon fibre composite with fiducial cuts, spaced 1mm apart on center; letters indicate locations of the push-out samples.

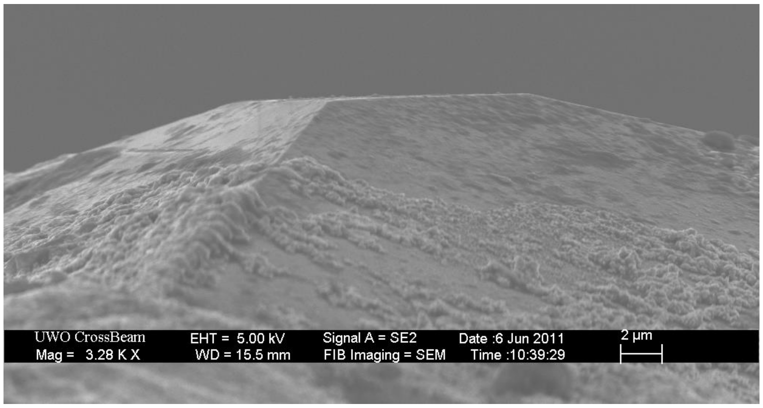

Figure 4.8 – SEM image of flat-top Berkovitch indenter.

The samples were tested using a micro-indentation machine, the NanoTest by Micro Materials Ltd., using a 10µm flat Berkovitch indenter, a picture of which is shown in Figure 4.8. The generated force-displacement data is collected using displacement control at a rate of 0.5 mN/sec until a predetermined displacement of 6 µm was reached, followed by unloading at a rate of 2 mN/sec. The load is measured as the change in capacitance of a parallel plate capacitor, which is temperature corrected individually for each test. The data from the FIB milled glass/epoxy pillars is presented in Figure 4.9.

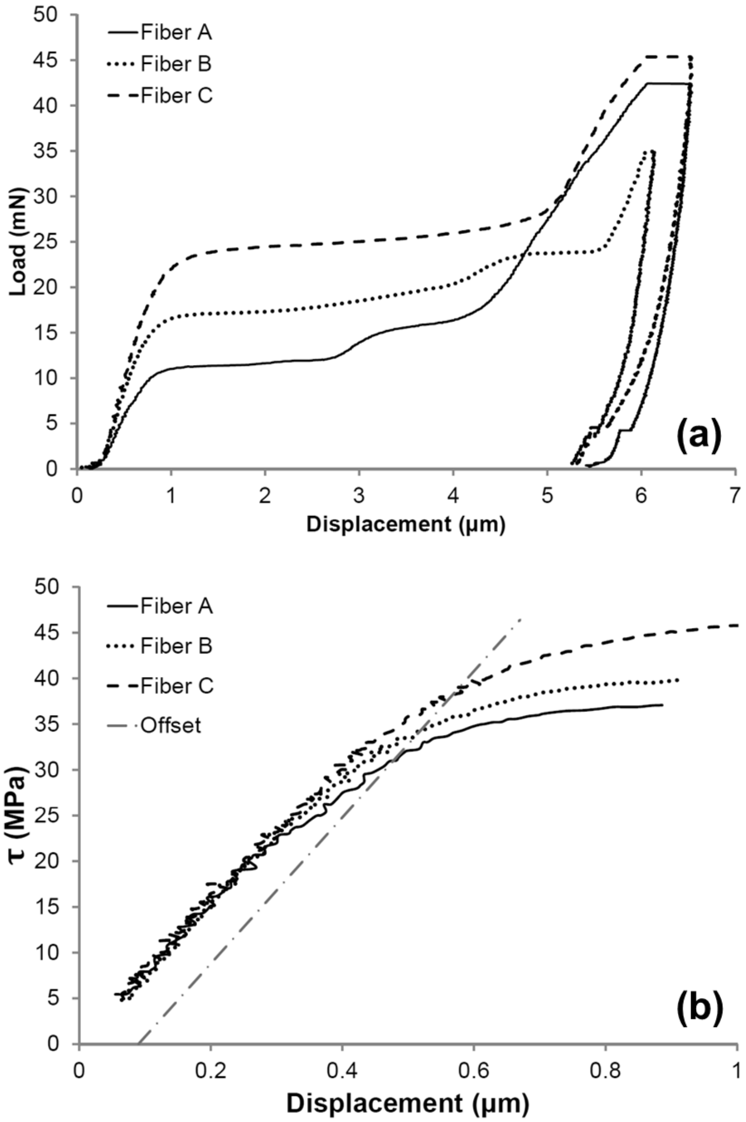

Figure 4.9 – Glass epoxy push-out test results for the three FIB milled samples: a) Load-displacement curves b) corrected stress-displacement curves

The considerable scatter is directly connected to the diameter of the fibres which ranged from 16 – 20μm. To compare the samples, the shear stress was computed as the force acting on the initial bonded fibre area of each sample individually. To determine the contact area of the bonded section, a finite element model was used, as seen previously in Figure 4.6, while the dimensions were taken from SEM micrographs for each fibre. Data below 5MPa was discarded to eliminate toe-in effects, and the three curves were aligned by shifting the displacement data such that each sample's compliance intersected the origin.

Four regions, consistent to all the tests, can be understood as: initial elastic loading, friction and matrix yield, a second rise in slope, and the sample unloading. The second rise in slope is an artefact of the test setup, consistent with the exposed end of the fibre: the punch is bottoming out on the surrounding epoxy. To determine the interfacial shear strength, or the departure from linear behaviour, an offset compliance slope is used. As shear strain is not measured, the offset is made by taking an average compliance of the three samples and shifting by a consistent displacement of 0.1μm. Data for the carbon/epoxy samples is presented in Figure 4.10 with the same slope alignment and offset slope present.

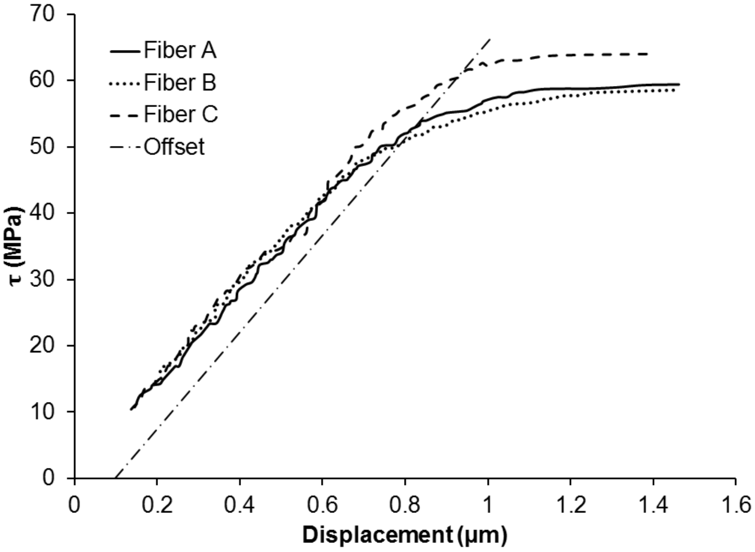

Figure 4.10 – Stress-displacement curves for the carbon / epoxy FIB milled samples.

There already exist rigorous methods to analyze the micromechanics of the stress transfer across the fibre-matrix interface for long embedded fibres (length >> diameter) [101, 102]. Netravali [44] demonstrated that as the sample thickness becomes small (4-10 fibre diameters), the shear stress can be approximated as uniform. In the present study, the embedded length is always less than two fibre diameters, so a similar uniform shear stress is assumed.

The sample undercut angle poses a challenge to the constant shear stress assumption prior to interfacial debond. Therefore, a simple finite element model was constructed to perform a linear elastic analysis. Using symmetry, a half meshed model is shown in Figure 4.11, with the three hidden surfaces having roller boundary conditions. The model uses approximately 330,000 solid elements, large displacements and a compatible surface-to-surface no penetration bonding condition (most accurate). The same dimensions of fibre A in from Figure 4.9b was used to simulate the effect of a fibre with a displacement of 1 μm (applied at the top fibre surface). The resulting shear stress is presented in Figure 4.11c) and indicates a near-uniform interfacial shear stress on par with that measured experimentally.

As a secondary confirmation that the measured stress is in fact the interfacial shear strength, a fractographic analysis can be performed. Figure 4.12 presents a pre- and post-testing image for each type of sample. The post-testing samples maintain their alignment indicating that the fibres did not bend or break during testing. Though there is some epoxy retained on each fibre near the FIB cut-out, all fibres exhibit an otherwise clean surface suggesting that the interface did separate. The observed matrix cracking is expected to occur during the end of the plastic deformation plateau as the frictional force drags the top surface down causing crack on the upper plane. Since the focus is not on the matrix plasticity phenomena, the interfacial shear strength can be determined from the stress-displacement curves obtained at the point of departure from elastic loading. Due to the presence of a consistent interfacial strength and flat frictional sliding behaviour it is possible that steady state crack growth was obtained using this geometry – something notoriously difficult to achieve – but requires further research to prove.

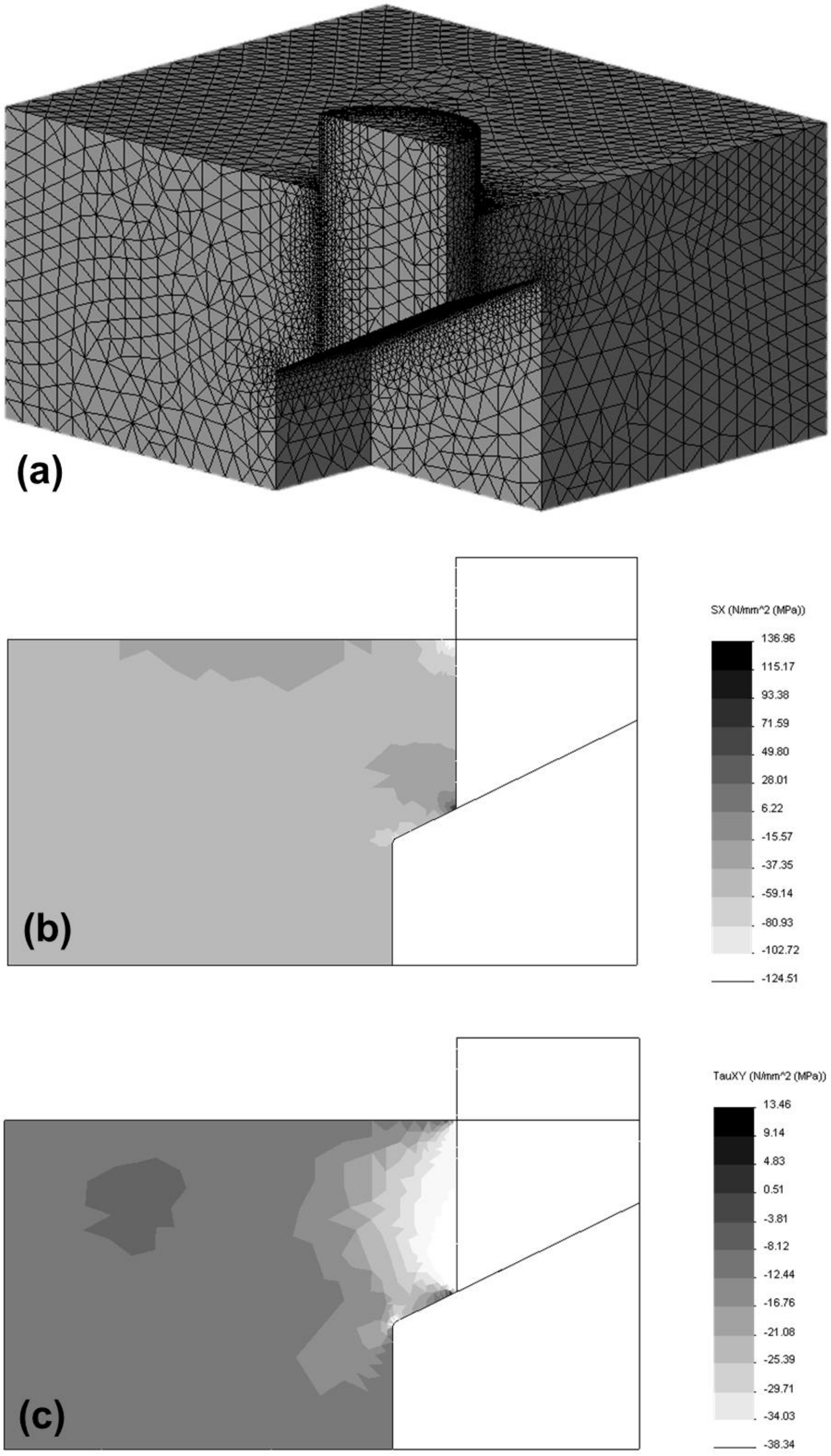

Figure 4.11 – Finite element results for the a) tetrahedral solid element mesh b) normal stresses to the fibre interface c) shear stresses at the fibre interface, using properties for the glass/epoxy samples.

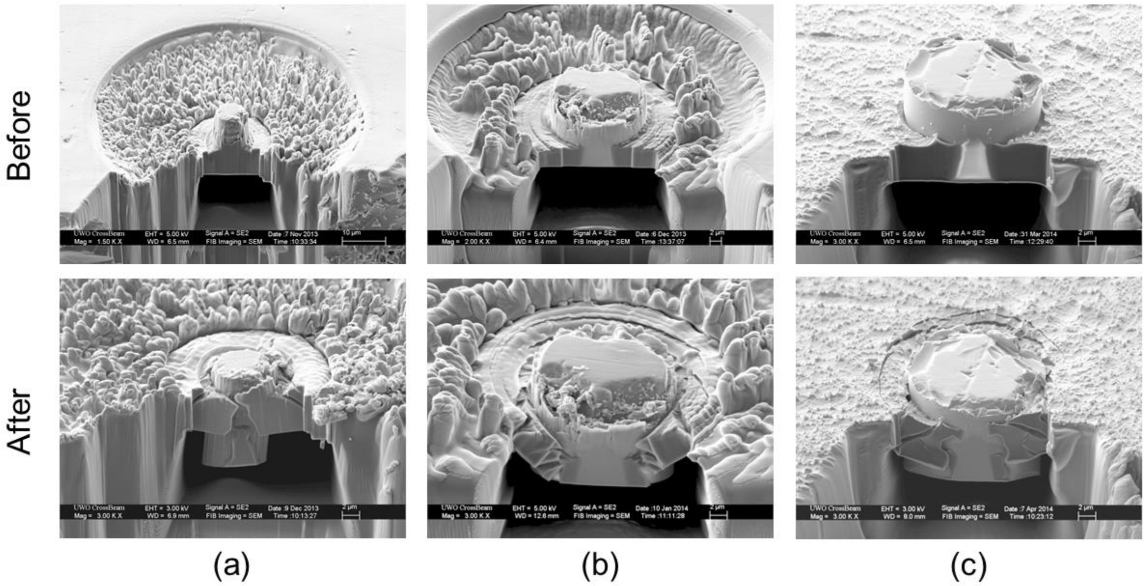

Figure 4.12 – Comparative micrographs pre and post fracture for a single sample of a) carbon fibre FIB b) glass fibre FIB c) glass fibre plasma etch.

All the interfacial shear strength (IFSS) measurements from the push-out tests are collected in Table 4.2 with population standard deviations. Both glass sample production techniques yielded similar strengths and when averaged together, the reported IFSS value is 35.26 ±2.53 MPa. Future testing should utilize the plasma etching process as it is faster and cheaper than the FIB process, and yields cleaner polymer and glass surfaces.

Table 4.2 – Interfacial shear strengths of modified push-out tests.

Material system	Fabrication	Interfacial shear strength, τ_i
Carbon / epoxy	FIB	52.01 ±3.27 MPa
Glass / epoxy	FIB	34.26 ±3.74 MPa
	Plasma etch	36.25 ±1.51 MPa

4.3 Modified Lap-shear Test

A lap-shear test has long been used to test the adhesive strength of joints, but typically only as a qualitative comparison [36, 103-105]. Using a modified version of this test, quantitative results of the interface can be obtained. Newer methods have recently been proposed to arrive at the interfacial shear and interfacial normal strengths [106-109]. This described model system offers a simplified, cost effective sample and rapid testing. The forthcoming presentation forms the bulk of the interfacial studies, comprising some 300+ samples under a wide range of test conditions.

In this model system, glass is used as the substrate in the form of a microscope slide, while a common epoxy is the polymer matrix [109, 110107]. A Teflon mask is employed to control geometry, shown schematically in Figure 4.13. To properly recreate the interface of a true glass fibre / epoxy composite, the glass surface of the model system must match that of the fibre. To achieve this end, microscope slides were first cleaned and baked to dehydrate the surface. Additional testing with silanes required the cleaned glass slides to be coated in silane as per the procedure for the fragmentation samples.

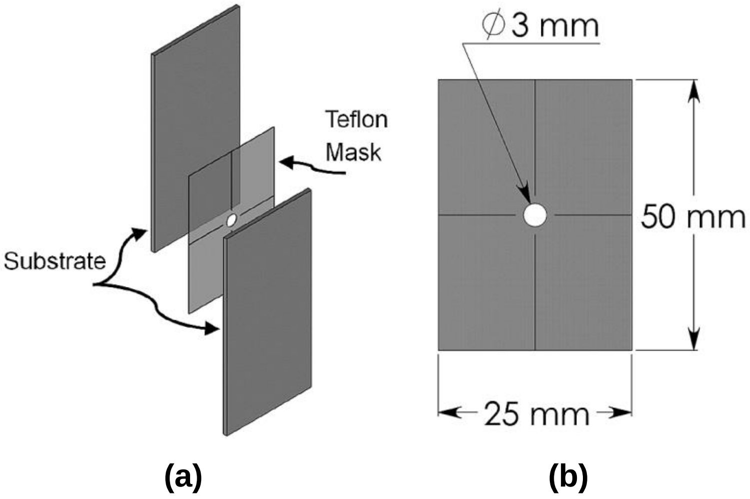

Figure 4.13 – Schematic diagram of a lap-shear specimen assembly with dimensioned Teflon mask.

The Teflon mask was prepared from PTFE 5490 film tape provided by 3M. Sectioned pieces were punched with a 3mm diameter hole and partially cut with 4 near-through slits to ease removal (Figure 4.13b). The Teflon masks were held in place during sample assembly by a piece of electrical tape on one of the glass slides. Using a disposable pipette, mixed epoxy was dropped into the mask of a ready slide. A second slide was immediately placed on top of the first to create the lap shear sample. The samples were placed on a metal baking sheet with appropriately sized spacers to keep the samples level during the cure cycle shown in Figure 4.14. A small piece of metal was used as a straight edge to align the top and bottom slides (not pictured).

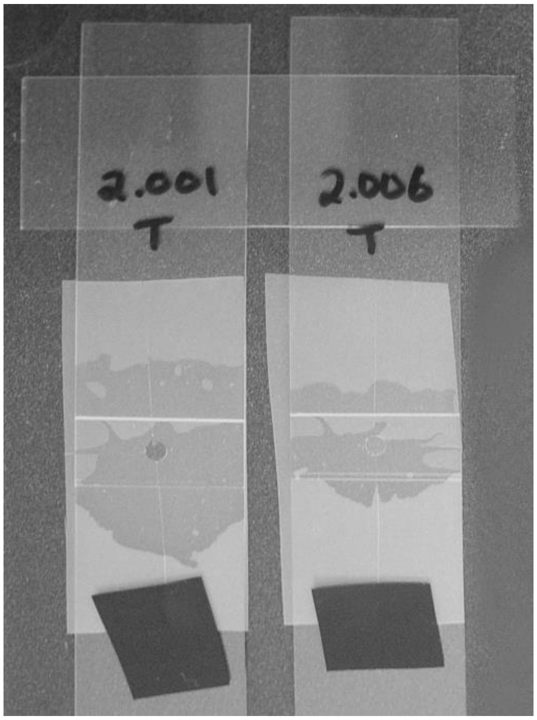

Figure 4.14 – Fabricated lap-shear samples after cure.

Following sample assembly, samples were cured at 60°C for 4 hours, unless otherwise indicated. Prior to testing, each sample was imaged using an optical microscope to measure and account for any entrapped air that may have developed during the cure stage. Excess epoxy from each series was also cast into flat coupons for hardness testing using a Shore D durometer. For the Shore measurements, measurements from a minimum of 6 locations were averaged. Figure 4.15 presents three imaged samples indicating their measured porosity. The measured porosity was used to determine the corrected lap-shear area through which the shear stress was applied.

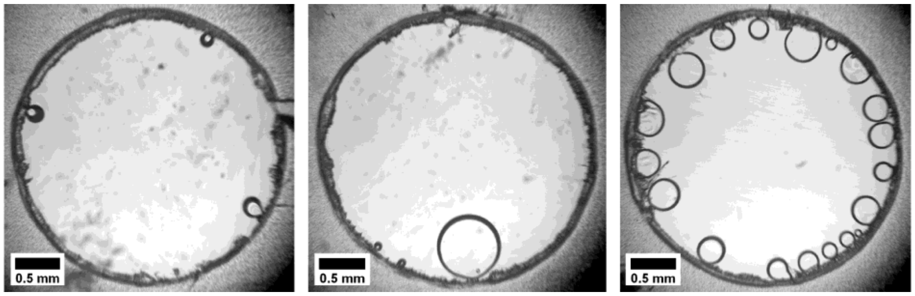

Figure 4.15 – Lap-shear samples of 0.05 mm mask thickness from a reflected light optical microscope showing a) low porosity of 1.1% b) typical porosity of 5.7% c) moderate porosity of 13.5%

Using an Instron 8804 load frame and a 5kN load cell, the samples were tested under a constant displacement rate of 0.5 mm/min. Initially, the glass plates broke when attempting to tighten the apparatus grips. This was prevented using appropriately sized rubber inserts around the glass to increase the gripping compliance, as shown pictorially in Figure 4.16. The first samples were tested in tension; but here the glass fracture toughness was a problem, since solved by testing samples in compression. A 12.5 mm gauge extensometer was attached to each sample prior to testing to capture strain data independently. For the lap-shear samples, electrical tape was attached above and below the lap joint to prevent the knife edges of the extensometer from slipping on the smooth glass surface; spacers were also added to ensure the extensometer correctly measured vertical strain. To reduce the impact of any foreign contaminates or exposure to atmosphere the Teflon mask was removed just prior to testing. Unless otherwise indicated, samples were tested at room temperature within 12 hours of sample fabrication. Humidity was neither measured nor controlled in the testing environment. The tests are presented in logical fashion to build the presentation of the test method, rather than chronologically.

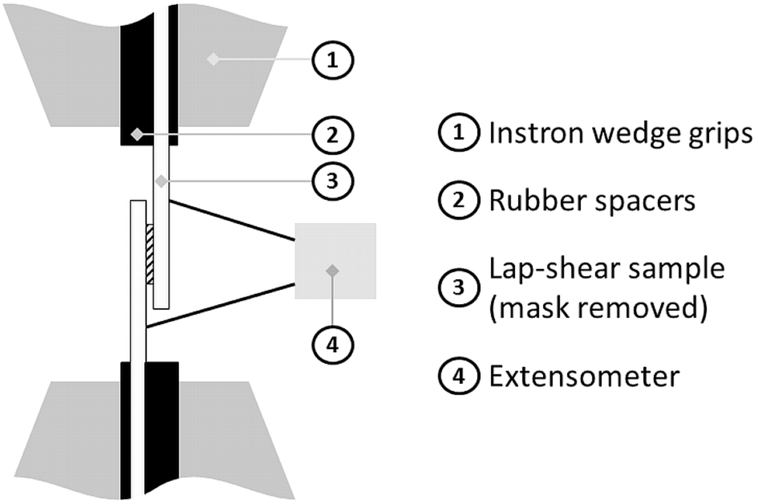

Figure 4.16 – Schematic diagram of the lap-shear compression test setup.

A first test is to perform a sort of convergence study to determine the optimal mask cut-out hole diameter. Figure 4.17 shows three of the four sizes of hole used. The smallest size of 1.5mm, not pictured, resulted in all the samples failing to cure properly. It seemed that any air introduced into the hole cavity of the smallest samples formed a complete pocket of air within the hole, and no resin was left bonding the upper and lower glass surfaces. The hole sizes that produced testable samples was 3mm, 6mm and 9mm, as shown in Figure 4.17. None of the 9mm samples survived testing as the bonded area was too large, causing a high stress which first fractured the glass. Half of the 6mm samples also caused the glass substrate to fracture during the testing, while all of the 3mm samples survived and provided useful interfacial data.

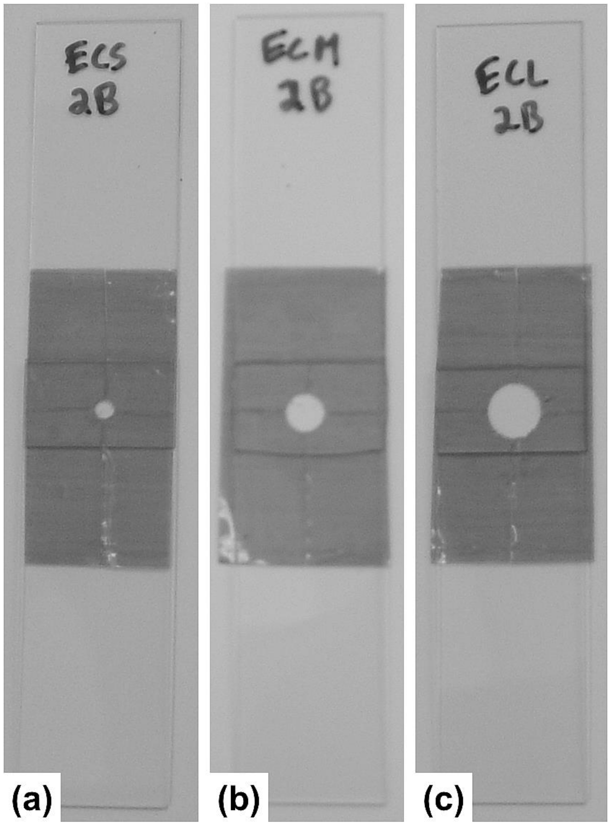

Figure 4.17 – Clean glass / neat epoxy convergence test samples with a) 3mm b) 6mm c) 9mm disk diameters.

From the fracture behaviour alone, the 3mm size mask is determined as the most reliable to measure the interfacial stress consistently. However, one difference is presented in a comparison of a 6mm sample and 3mm sample. Though the loads are dramatically different as would be expected for a larger bonded area, the shear stress and strain are presented in Figure 4.18. As the method to determine the shear stress has not yet been presented, it will be taken as a simple force per unit area relation, with no other corrections to the data. Due to the lower loads recorded, the 3mm data is more susceptible to signal noise. Also, none of the 6mm samples which generated useful data presented with a peak load around the matrix yield strength, instead easing into a flat plateau as seen, suggesting the peak in the 3 mm data is artificial.

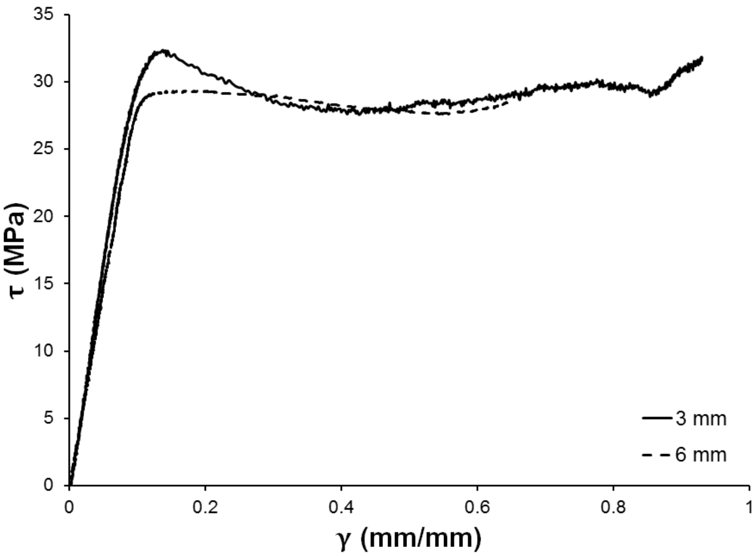

Figure 4.18 – Comparison of shear stress-strain relationship between 3mm and 6mm mask hole diameters for clean glass and neat epoxy samples.

Before presenting all the tested variables the stress analysis is presented to comment on the necessary data corrections. The goal with these lap-shear tests is to qualitatively obtain the interface failure shear stress. Upon inspection of Figure 4.19a), a moment results from the axial loading of a lap-shear sample. The free body diagram in Figure 4.19b) indicates the induced shear stress and normal stress distributions. This initial analysis assumes the epoxy disk is free of defects or porosity, which would otherwise cause stress concentrations.

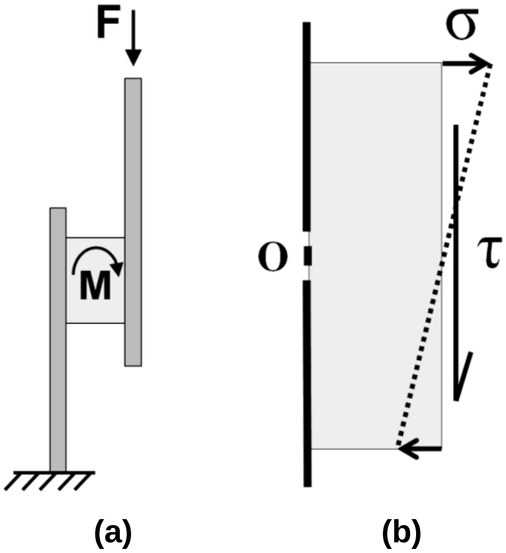

Figure 4.19 – Lap-shear loading and stress distribution in the epoxy disk.

To begin, the average shear stress is given by Equation 4.5, which can be directly determined from the applied load and sample geometry:

$$\bar{\tau} = \frac{F}{A_o} \tag{4.5}$$

where F is the applied force, and A_o is the area of the disk bonded to the substrate. The shear strain is calculated as:

$$\gamma = \arctan\left(\frac{\delta}{t_o}\right) \tag{4.6}$$

where δ is the incremental displacement of the measured by the extensometer, and t_o is the initial thickness of the polymer disk, measured prior to testing by a micrometer. The resultant normal stress arising due to the bending moment form the offset of the glass slides is, however, not immediately obtainable. If it is assumed that the substrate is rigid and does not bend during loading, which is considered valid so long as $E_{substrate} >> E_{polymer}$, then the result is a linear distribution of normal strain across the disk height. The strain, then, is $\varepsilon = Cr$, where C is some constant and r is the radial distance from the center of the disk measured in the direction of loading. The normal force can then be calculated considering the applied force:

$$F_N = CrEA_o \tag{4.7}$$

Where A_o, the area, can be expressed in terms of a radial integration:

$$A_o = 2\int \sqrt{D^2 - r^2}dr \tag{4.8}$$

D is the radius of the disk. Substituting (4.8) into (4.7) and taking the moment about point O in Figure 4.19b), the unknown constant C can be isolated as:

$$C = \frac{Ft_o}{8E_m}\left[\int_0^D r^2\sqrt{D^2 - r^2}dr\right]^{-1} \tag{4.9}$$

The value of the constant is a function of the applied force, the disk geometry, and the material properties. Solving the definite integral yields a normal force distribution across the disk as seen in Figure 4.20. In a perfect disk, this corresponds to a linear distribution of normal stress, as the area the force acts upon changes proportionally. The normal force is at maximum at some radius less than the disk radius – notably important when considering the effect and location of any matrix porosity.

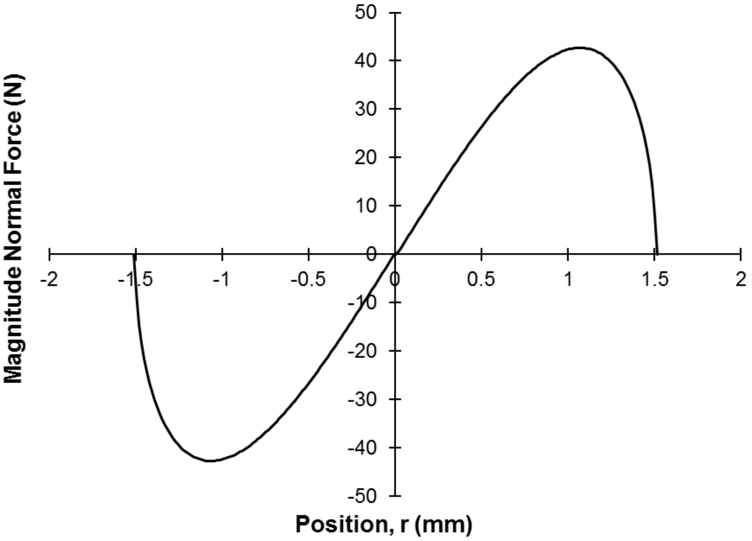

Figure 4.20 – Normal force distribution along centerline of epoxy disk running parallel to the applied load.

Now that the normal and shear stresses are known, the von Mises stress distribution over the disk can be plotted. Setting the force to a typical value (F = 175N), the von Mises stress are shown in Figure 4.21 for several disk thicknesses. As expected, the shear stress is the primary contribution to the von Mises stress, with the normal stress causing only a slight increase near the edge of the disk. Increasing disk thickness causes an increase in the von Mises stress due to the increasing component of normal stress, particularly evident at the edges of the disk.

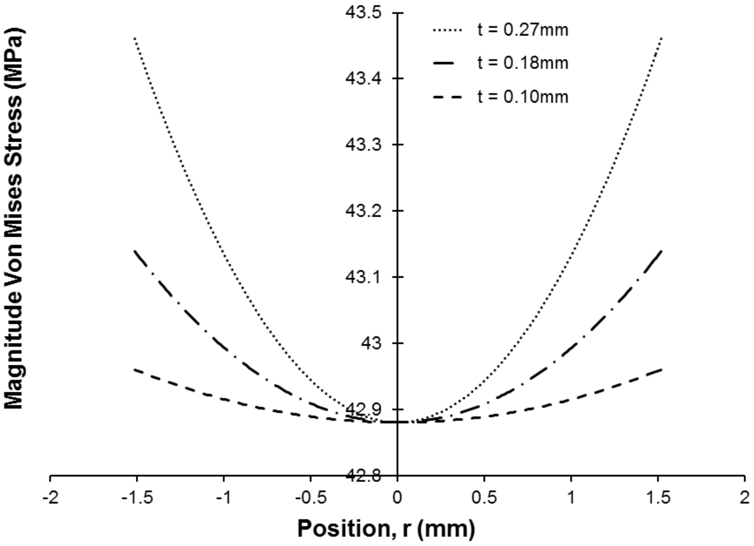

Figure 4.21 – Von Mises stress as a function of position along the centerline of the disk, shown for disk thicknesses of 0.10 mm, 0.18 mm and 0.27 mm.

The Von Mises stress distribution suggests several things about this lap-shear geometry. The peak stresses at the edge of the disk indicate the expected starting location for the failure at the interface. Also, both the location and size of any porosity will matter to the resulting increase in stress, with larger porosity and porosity located near the upper and lower disk edges having the greatest impact. Thus corrections to the raw force-displacement data need to be made before calculating the shear stress and shear strain. First, a minor correction is applied to the raw data to account for the elastic loading of the glass plates within the extensometer gauge. A rectangular area the same width as the glass slides and the same length as the extensometer gauge is calculated, with the maximum correction <2.5% of the strain value of the epoxy disk at peak load. Another, more significant correction is made to account for any porosity within the epoxy disk after it has cured. Using images like those of Figure 4.15, the porosity is measured in each sample assuming cylindrical pores. The bonded area is then reduced by the total pore area, correcting the shear stress. No correction is made for the normal stress as it would require a careful analysis of not just the area of each pore, but also the location relative to the loading direction, which was not feasible for the many experimental studies. This is deemed acceptable as the normal stress contributes little to the von Mises equivalent stress from Figure 4.21. Future work could retroactively examine each image and provide a more accurate correction to the recorded stress. Figure 4.22 highlights a sample of the raw data obtained by compression loading a lap-shear sample created with Z6040 coated glass, neat epoxy, a mask thickness of 0.18mm, and the default cure schedule, while Figure 4.23 presents sample curves for polyester and Z6030 coated glass.

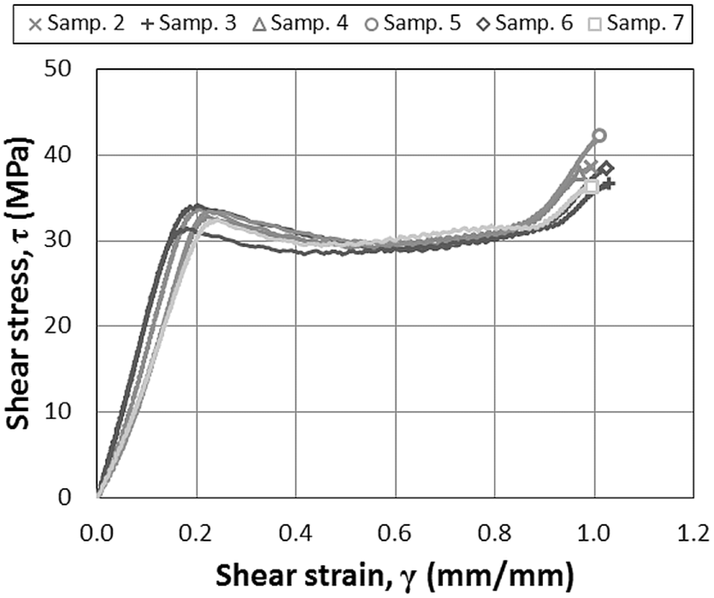

Figure 4.22 – Typical shear stress-strain curves for epoxy / Z6040 coated glass.

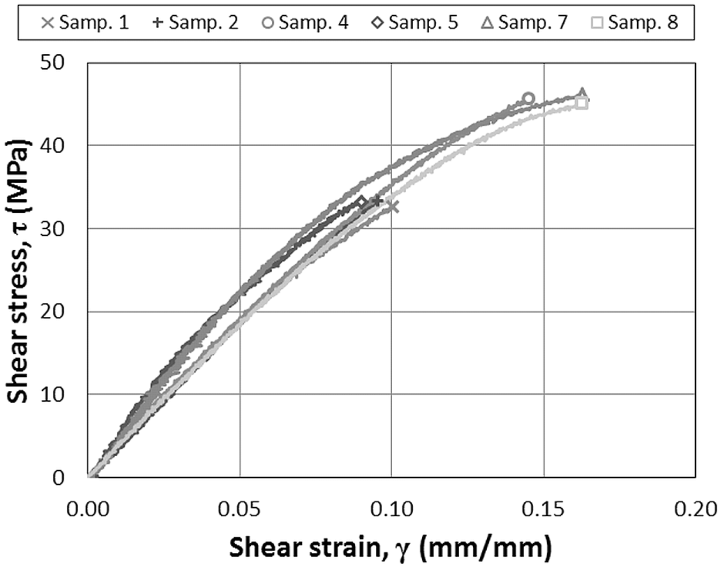

Figure 4.23 – Typical shear stress-strain curves for polyester / Z6030 coated glass.

The differences in the polymer behaviour are again evident with the polyester indicating no significant shear yielding. Also, the brittle polyester is a bit more susceptible to the issues with porosity, so a slightly larger sample size is required to generate an acceptable statistical distribution for the interfacial shear stress. The IFSS value is taken as the highest stress reached before failure.

Here, another question is asked in regard to the effects of the glass surface itself, before the presentation of modified testing parameters, to rule out possible impact with the fabrication of the glass slides. When plate glass is made, it is floated on a bed of molten tin, giving rise to its alternate name: float glass. This has the effect of producing two slightly different surfaces: the upper surface with higher oxides, and the lower surface with higher concentration of embedded tin atoms. Using a short wave ultraviolet light, the tin-side of the glass is identified as the one which gives a soft white glow, as opposed to the shiny purple side. Lap-shear samples were made using a random selection of glass slides, some with only the tin side selected, and some with only the oxide side selected. Figure 4.24 presents the results of the glass surface testing.

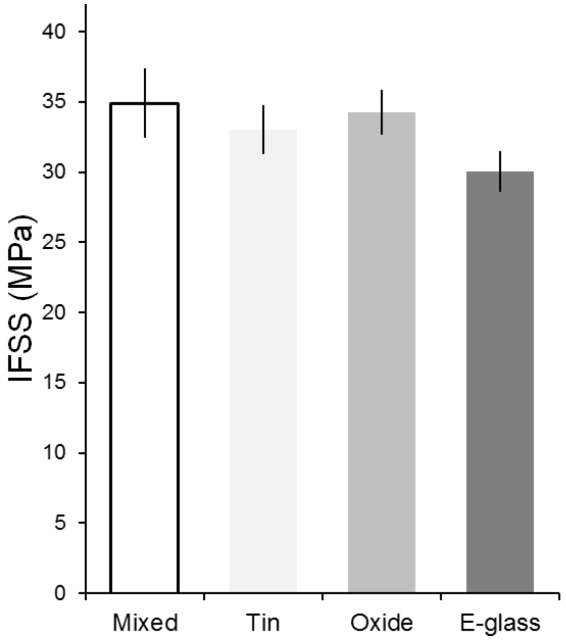

Figure 4.24 – Interfacial shear strength results from random, tin-only, and oxide-only cleaned glass surfaces with epoxy. Also compared are samples made using e-glass rather than the float glass.

Since no statistical distinction can be made between the samples created with different selected glass surfaces, the glass selection will be ignored in the subsequent testing. Along the lines of questioning the glass surface is questioning the glass type. The typical glass in a composite is e-glass, which typically has lower silicon dioxide and higher metal oxide content than its float glass counterpart. While producing e-glass fibres, Johns Mansville was kind enough to extract some liquid e-glass for use in this comparative study. From the molten e-glass, they subsequently cast a rectangular plate and annealed the plate before transportation. In order to use this glass, it was sectioned using a diamond saw and polished to the same degree as the microscope slides. Figure 4.25 presents the as-delivered and stages of glass preparation which was a time-consuming operation. From the fabricated plates in Figure 4.25c) lap shear samples were made in the same fashion as previously described to determine the IFSS value with e-glass.

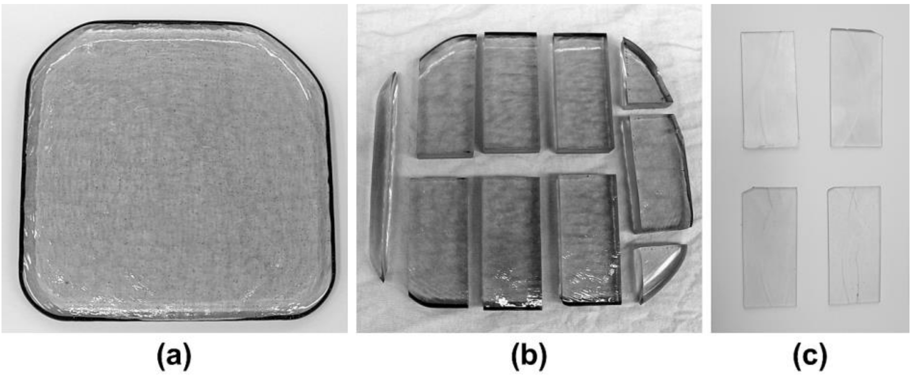
(a) (b) (c)

Figure 4.25 – Fabrication process of e-glass samples showing a) as-delivered plate b) cut blocks c) thin-cut samples prior to polishing.

Referring back to Figure 4.24, the interfacial strength compared between the plate glass and the e-glass samples is different, but only slightly. Thus if it is accepted that all the results from the lap shear testing will be slightly higher with plate glass than their e-glass counterparts, the testing can proceed using the more widely available plate glass microscope slides.

Having addressed the initial setup questions with the modified lap-shear geometry test, it is now possible to proceed in analyzing the variables which influence the interfacial strength. A first test follows from the work done analyzing the effects of cure on the neat polymers. Using the same mask thickness, neat epoxy, and uncoated glass slides, the effects of cure temperature are seen in a recreation of the same test for the neat epoxy. Figure 4.26 presents the effects of the measured interfacial shear strength as a function of cure temperature. The work-of-fracture is also presented which nicely matches that of Figure 3.13. The same logic follows that as the cure degree increases, there are more bonds formed with the glass surface increasing the measured interfacial strength, but at the expense of the matrix ductility.

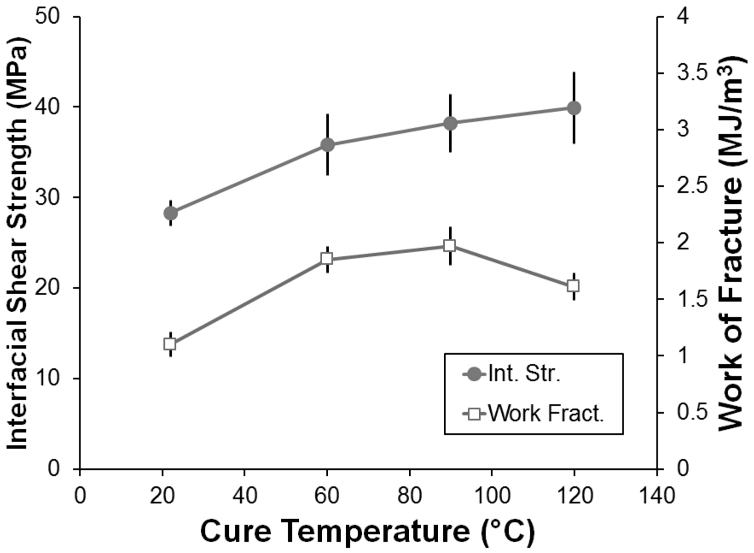

Figure 4.26 – Shear strength and work of fracture for the epoxy / clean glass system as related to cure temperature.

Another test suite examined the effect of the mask thickness on the interfacial strength, which effectively determines the resulting epoxy disk thickness. Since the polymer disk must be some finite thickness, the true interfacial shear strength must be extrapolated by linear regression. Figure 4.27 presents the interfacial strength values vs. disk thickness.

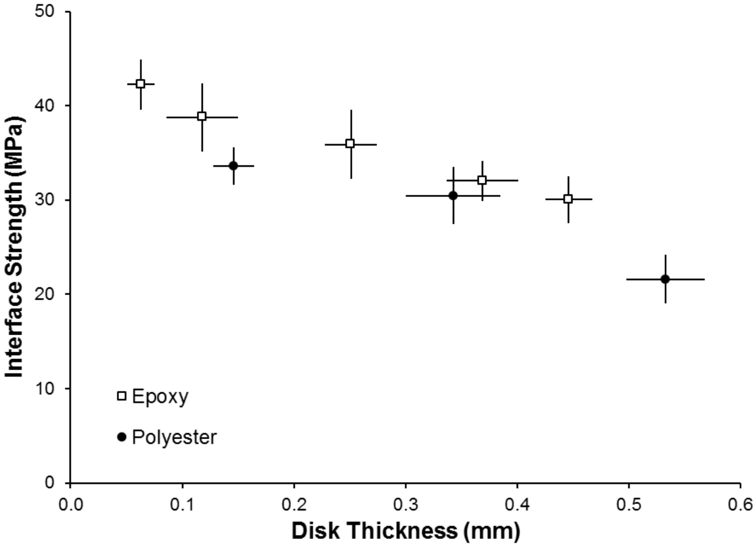

Figure 4.27 – Interfacial shear strength as a function of polymer disk thickness for both epoxy and polyester bonded to clean glass.

Disks with an aspect ratio (thickness / diameter) greater than unity are not recommended as additional failure modes may be incurred and keeping the substrate plates parallel during testing becomes challenging. The regressions from Figure 4.27 give interfacial shear strengths of 42.9 MPa and 37.0 MPa for the epoxy and polyester respectively. Recall, from Figure 4.20a), the imposed moment within a lap-shear sample, which gives rise to a change in loading mode. As the disk thickness approaches 0, the loading mode approaches a pure mode II (in-plane shear) condition. But when the disk thickness is increased, there is an added mode I component meaning the failure is now a function of the mixed-mode loading condition. This is also evidenced by the types of fracture observed within the different disk thickness samples seen in Figure 4.28.

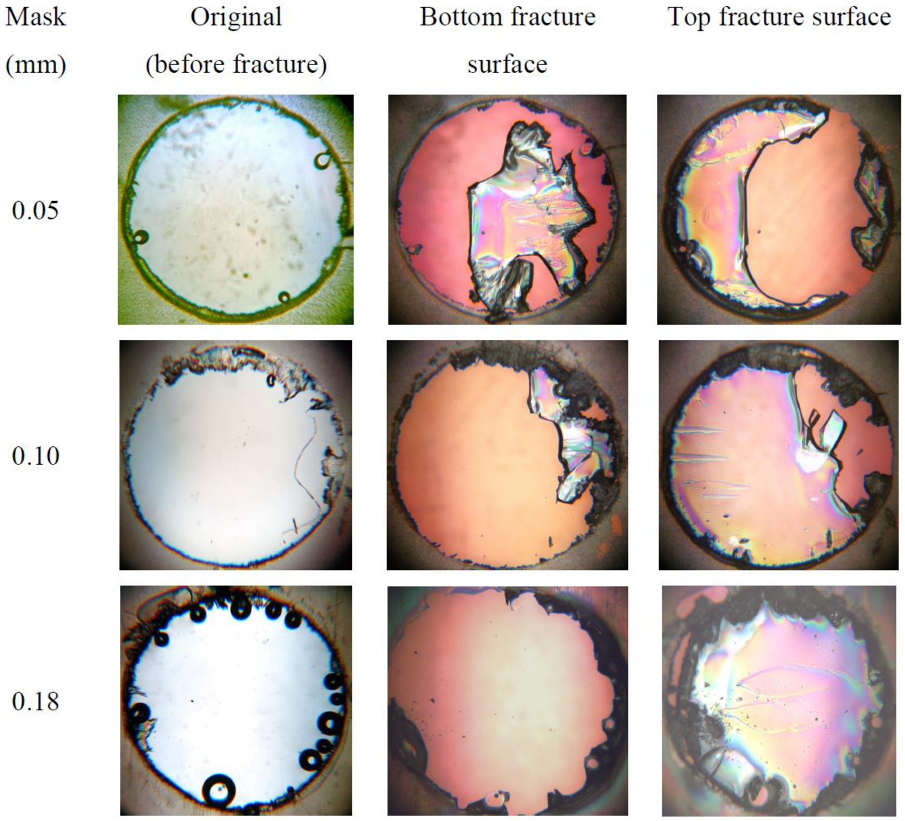

Figure 4.28 – Fracture surfaces from samples of various thicknesses taken under polarized light along with their original (before fracture) image. Loading direction is left-right; the images have been rotated and aligned to ease comparison. The top and bottom fracture surfaces correspond to both the placement of sample in grips and assembly location within oven.

As the mode I component increases with the increase in disk thickness, the disk begins to peel, and there is no longer any evidence of inter-disk fracture occurring. One conclusion that can be made is that the mode I interfacial strength must be less than that of the mode II interfacial failure strength. Thus a separation into the interfacial shear and interfacial normal strengths is required to fully capture the dynamics of the interfacial failure and debond phenomena.

To test the normal interfacial strength, a series of samples were created with unique geometry to be tested in tension. A mask with a larger 6mm hole was used, to compensate for the normal failure stress, which was expected to be less than that of the shear failure stress. First, the samples were created and cured similar to the lap shear samples. Then the samples were mounted between two 6061-T6 aluminum T-brackets with Hysol 9396, provided by the Henkel Corporation, and cured at room temperature. The addition of the aluminum brackets was to facilitate gripping the samples during testing. Critically, the alignment of the upper and lower T-brackets was held in place during cure by a rigid fixture. A 5mm hole was drilled into the side of the aluminum brackets prior to assembly for the attachment of an extensometer. Figure 4.29 shows the final setup just prior to testing, with the Teflon mask removed.

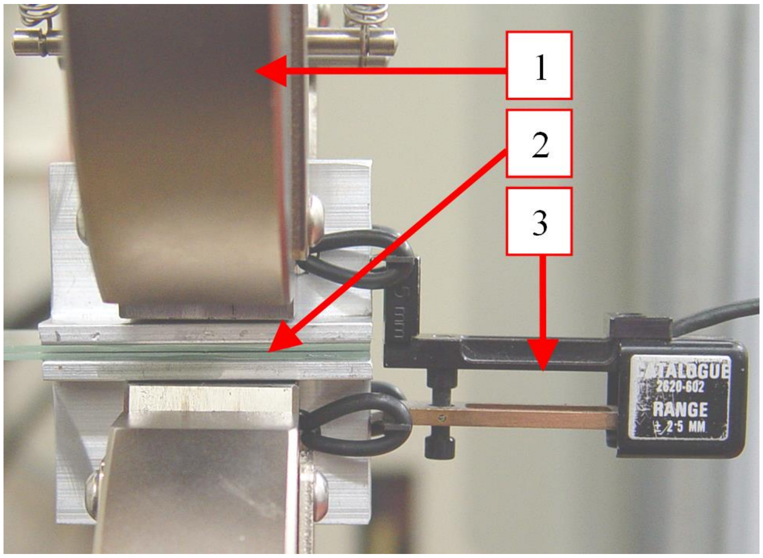

Figure 4.29 – Test setup for interfacial normal strength testing with arrows to the 1) wedge grips, 2) mounted sample, and 3) extensometer.

Since the extensometer is now recording strains which encompass the additional aluminum and Hysol layers, an additional elastic correction is made to the strain data. Figure 4.30 presents some sample data for epoxy bonded to clean glass.

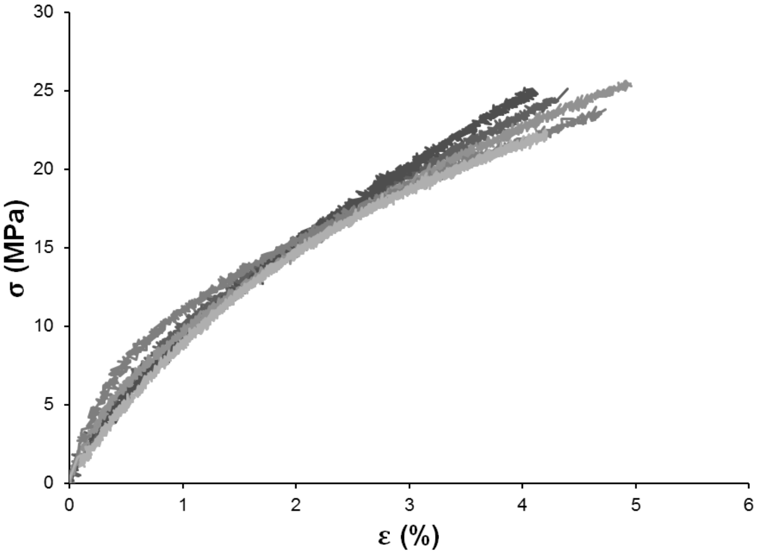

Figure 4.30 – Lap-shear data for the modified samples in mode I testing.

Due to the small, constrained geometry of the epoxy, the strengthening behaviour of the epoxy is suppressed as the interfacial normal strength is first reached. This explains the lack of negative hardening in Figure 4.30 as would have been expected from the epoxy tensile testing from Chapter 3. To combine the mixed mode results together, an acceptable failure criterion at the interface needs to be imposed. The work of Hashin comes to mind when considering the effects of a brittle interface [111]. He proposed that the interface behaves as a combination of the mode I and mode II strengths as:

$$\left(\frac{\tau}{\tau_{i,f}}\right)^2 + \left(\frac{\sigma}{\sigma_{i,f}}\right)^2 \geq 1 \tag{4.10}$$

Together with the normal interfacial failure stress, the samples from Figure 4.27 can be re-plotted with respect to the failure mode, as shown now in Figure 4.31. To provide a reference to the data, the Hashin criterion, Equation 4.10, is also shown for reference. The normal interfacial strengths were determined as 24.5 ±1.1 MPa and 15.7 ±0.9 MPa for the epoxy and polyester respectively.

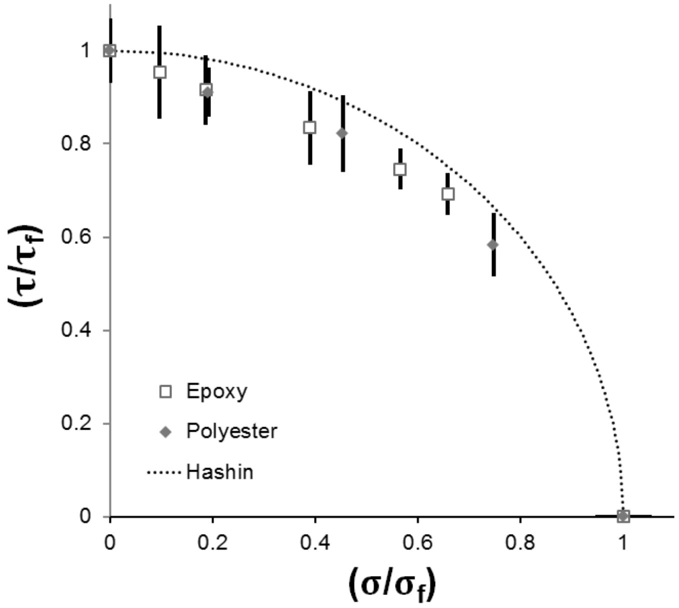

Figure 4.31 – Experimental interfacial failure for epoxy and polyester lap-shear tests plotted with the Hashin failure criterion.

Not only is it evident that the data conforms well to the accepted theory, but it demonstrates that high degrees of mixed-mode loading are possible with the lap-shear test.

To give this data some perspective, the current results are compared against the literature for similarly tested systems as in Figure 4.32. With confidence that the test is useful in a qualitative sense and that it can capture both shear and normal strengths effectively, it is necessary to examine the impact of modified systems on the interfacial bond. It has long been known that a coupling agent improves the chemical bonding between a glass polymer interface [112, 113]. In this work silanes were selected as appropriate coupling agents for their applicability to the material systems being studied.

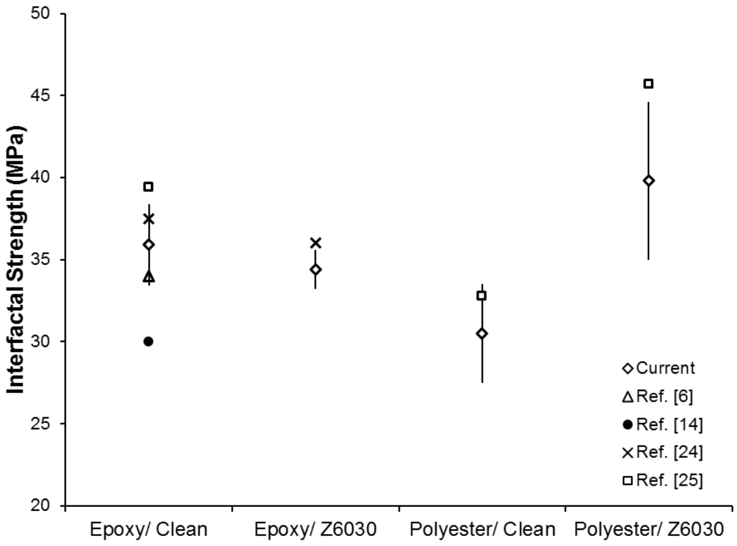

Figure 4.32 – Comparison of interfacial shear strengths against similar composite systems found in the literature [36, 75, 100, 114].

The next series of tests were run to compare the effect of different coupling agents on the glass, as was done with the fragmentation tests. All the coupling agents were applied using the same method as described for their application with the fragmentation samples. It is also now possible to compare the results from all three test methods in Figure 4.33.

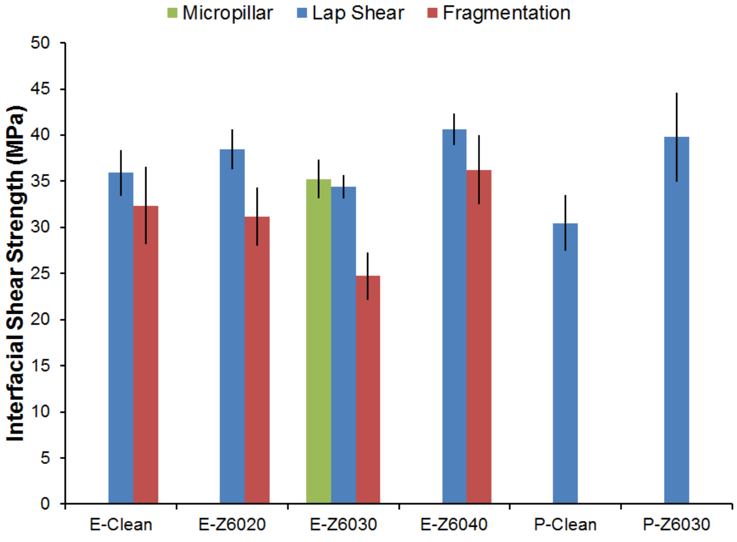

Figure 4.33 – Selected results comparing several interfacial strength measurement methods for both the epoxy and polyester and different coupling agents.

By again returning to the fracture surfaces of the epoxy disks differences resulting from the application of the silanes can be seen. Figure 4.34 presents two similarly thick lap shear samples, one with clean glass, the other with Z6020 coated glass. These samples were selected for comparison as they both had an entrapped air bubble of approximately the same size and location, and both indicated very similar fracture patterns separated only by the interfacial strength. The loading direction was left-right, while the three panels indicate the untested, the lower fracture surface and the upper fracture surface. In Figure 4.34b, the lower fracture surfaces are void of the epoxy; the uncoated glass remains clean while the coated glass has a retained pattern mirroring the upper surface in Figure 4.34c. Both upper surfaces have the presence of chevrons indicating the starting location of fracture was the top lip of the epoxy (to the right in the image) while the coated glass indicates more severe interfacial yielding related to the chevron density. The presence of cracking around the entrapped air bubble indicates that likely starting location for the interface debonding as this coincides with the presence of a stress concentration.

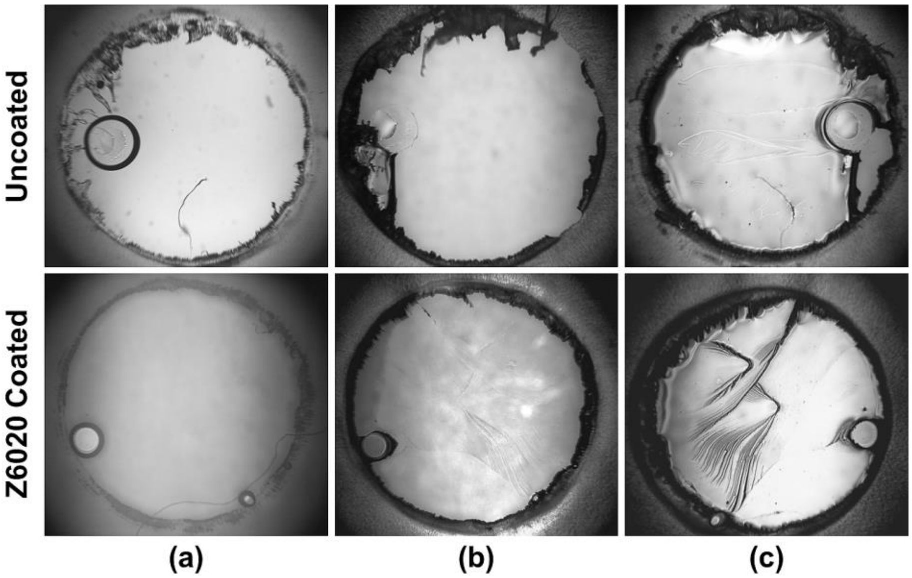

Figure 4.34 – Lap-shear fracture comparison between 0.18 mm thick epoxy disks against uncoated and Z6020 coated glass, showing a) untested sample b) lower glass fracture surface c) upper epoxy fracture surface.

To demonstrate the utility of the lap-shear test with non-standard polymer blends, several tests were performed with fillers added to epoxy against clean glass. These and all the results for epoxy are collected in Table 4.3.

Table 4.3 – Summary of lap-shear experimental results for epoxy.

Series Properties			**Results**		
Glass	Epoxy	Mask, t (mm)	Interfacial Shear Strength, τ_i (MPa)	Shear failure strain, γ_f (%)	Shore D Hardness
Clean	Neat, 60C cure	0.05	40.9 ±4.3	91.8 ±5.6	82.2 ±1.0
		0.10	39.3 ±3.2	89.6 ±2.2	
		0.18	35.8 ±3.4	87.1 ±1.6	
		0.27	32.0 ±1.9	80.2 ±3.3	
		0.36	29.7 ±1.9	73.3 ±3.6	
Clean	Neat, 22C cure	0.18	28.3 ±1.4	84.7 ±3.8	81.7 ±0.5
	Neat, 90C cure		38.2 ±3.2	87.0 ±1.2	84.0 ±0.8
	Neat, 120C cure		39.9 ±4.0	89.1 ±1.6	84.3 ±0.5
Z6020	Neat, 60C cure	0.18	37.2 ±2.9	95.2 ±2.7	82.3 ±0.6
Z6030			34.1 ±1.1	92.0 ±2.1	
Z6040			40.6 ±1.7	96.7 ±1.2	
Clean	2.5% $CaCO_3$, 60C cure	0.18	22.5 ±3.4	82.1 ±2.7	84.0 ±0.7
	5% $CaCO_3$, 60C cure		25.7 ±1.4	76.1 ±3.3	85.0 ±0.7
	10% $CaCO_3$, 60C cure		26.1 ±0.9	63.4 ±9.8	86.7 ±0.7
	10% carbon black, 60C cure		23.2 ±0.7	49.1 ±5.0	85.2 ±0.4
	10% glass beads (150 µm), 60C cure		28.7 ±1.8	19.5 ±9.2	92.4 ±1.0

Regarding the filled epoxy tests, the fillers themselves present interesting additions to the experimental studies. Seen in Figure 4.35, the fillers have varying morphologies from the large, but hollow 150µm glass beads to the crystalline, but clumping calcium carbonate powder or the small, but shard-like carbon black powder. All the fillers were added by % weight to the epoxy. It was not possible to capture an image of the carbon black lap-shear sample as the carbon black made the epoxy completely opaque.

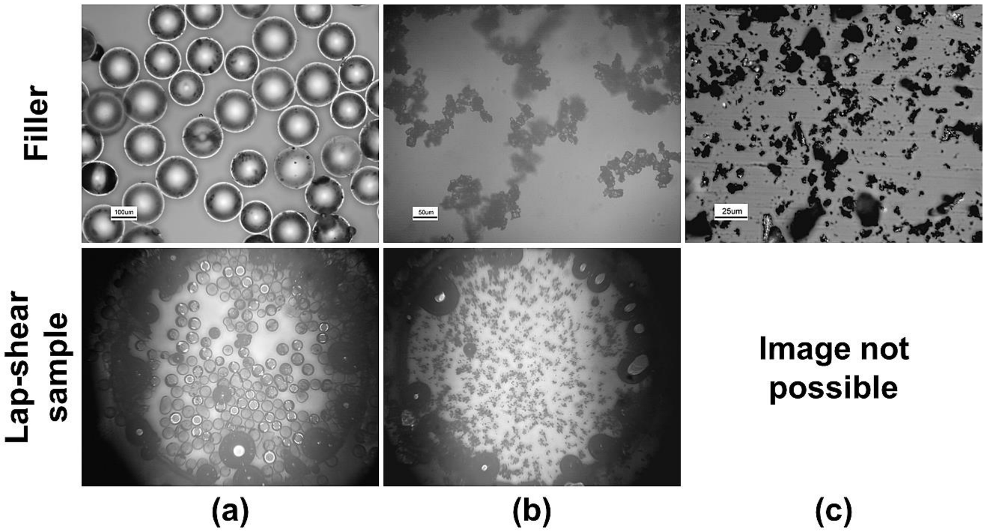

Figure 4.35 – Images of fillers and the resulting lap-shear samples for a) 10% 150µm glass beads b) 2.5% CaCO3 c) 10% 5µm carbon black.

The glass beads were quite large in comparison to the dimensions of the lap-shear samples. Even though there was only 10% added to the epoxy by weight, as they were hollow, their volume was substantial. Though the interfacial strength remained relatively high, the strain-to-failure was greatly reduced. This can be attributed to the fact that even with the reduced epoxy the glass beads were smooth and also bonded with the epoxy in a manner similar to the glass slide.

Neither the calcium carbonate nor carbon black is thought to form covalent bonds with the epoxy, so the addition of either act to reduce the strength of the epoxy and also the interfacial strength. The pointy carbon black pieces likely cause sharp stress concentrations, but at this stage, it is unclear why the small amount of $CaCO_3$ caused such a significant drop in the interfacial shear strength, or why increasing amounts of

$CaCO_3$ caused the interfacial strength to increase. This increase does seem to come with a trade off with the decreasing strain-to-failure, and certainly warrants further investigation.

Another question which arose while running the original lap-shear tests with neat epoxy was whether the data can be used to estimate the interfacial strain energy release rate. To examine how the interface was separating at the peak load, several high speed tests were run using clean and silane coated glass samples. A Redlake MotionScope M3 camera was used with a 35 mm lens to capture the debond process at 4000 frames/second. Figure 4.36 presents the four sequential frames surrounding the debond event which takes place between Figure 4.36b and Figure 4.36c).

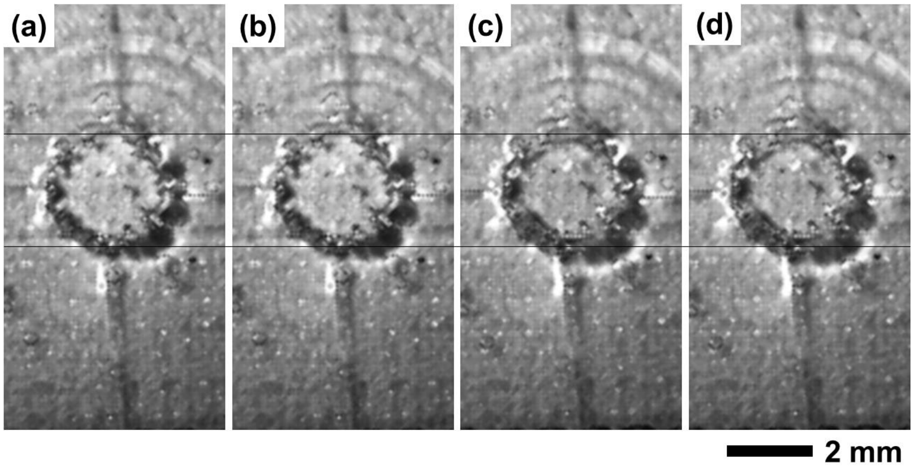

Figure 4.36 – Four sequential high-speed video frames at 4000 frames/sec showing the rapid debond process: (a-b) pre-failure (c-d) post-failure. The horizontal pinstripe lines were added to aid visual comparison.

This rapid fracture process therefore happens in less than 1/4000 seconds. With a near-instantaneous debond the peak load from the shear stress-strain curves is used as a measure of the elastic energy released, as seen in Figure 4.37.

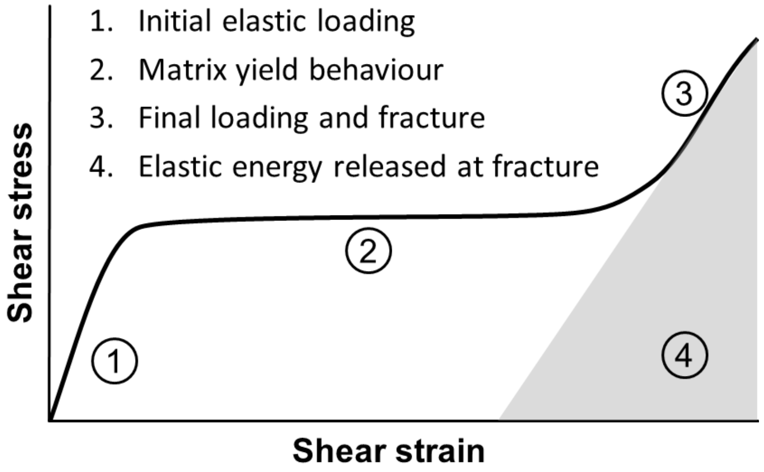

Figure 4.37 – Schematic of lap-shear data indicating the loading behaviour and area used for calculating the debond energy at fracture.

This energy became the basis for the estimate of the interface mode II strain energy release rate, or $G_{IIc,i}$ value, as well as the mode one interfacial strain energy release rate. The strain energy release rate is defined as the change in energy with respect to a change in crack area:

$$G_c = \frac{dU}{da} \tag{4.11}$$

Consider this: if at the point of fracture the entire epoxy disk is debonded from one glass surface at one instant, then the load at that point represents all the strain energy released. Using all the data behind Figure 4.31, the two strain energy release rates can be extrapolated by evaluating the shear and normal components of loading via the Hashin relation. Because the fracture occurs along the flat plane of the glass, and hence the crack must propagate in a self-similar manner, the fracture criterion is:

$$\left(\frac{K_I}{K_{Ic}}\right)^2 + \left(\frac{K_{II}}{K_{IIc}}\right)^2 = 1 \tag{4.12}$$

In terms of the energy of fracture, Equation 4.10 becomes:

$$\frac{G_I}{G_{Ic}} + \frac{G_{II}}{G_{IIc}} = 1 \tag{4.13}$$

By plotting all the individual lap-shear data for differing modes of loading (disk thicknesses), the critical strain energy release rates (CSERR) can be determined by least squares fitting. The normalized plots for both epoxy and polyester are presented in Figure 4.38. Not all the data is used in these plots: samples which exhibited debonding on more than one side of the glass were rejected, as were samples which caused any glass or substantial fracture to the epoxy.

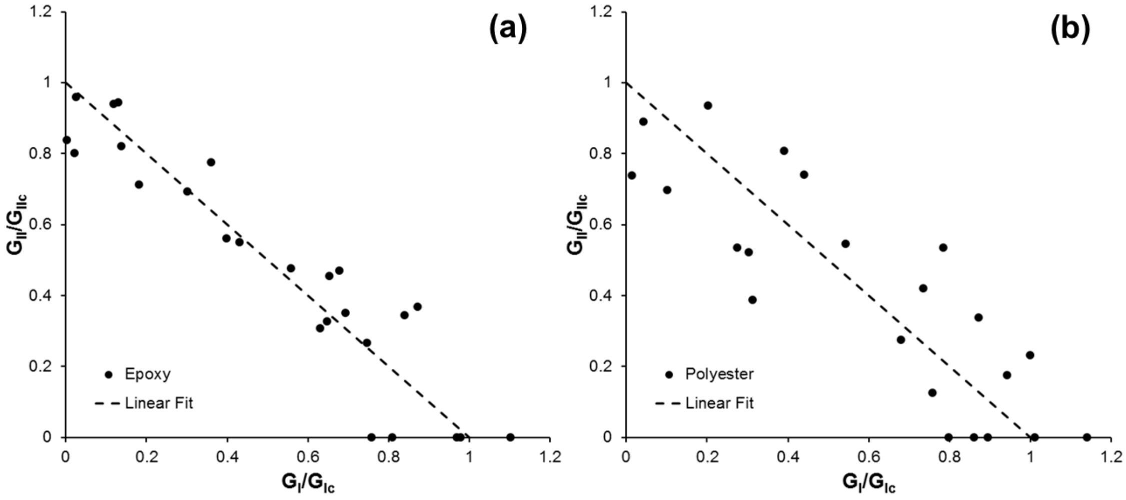

Figure 4.38 – Normalized plots of mode II vs. mode I strain energy release rate for a) the epoxy and b) the polyester.

The primary reason this can even be attempted is due to the ability to accurately measure the bonded area less the effects of porosity. Since the substrate in all of the testing thus far has been glass, it allows the examination of the internal fracture during testing. This would not be as easily accomplished with opaque material systems, as the central assumption that fracture occurs rapidly requires the ability to monitor interior of the specimen.

The Table 4.4 presents the values as determined for the epoxy and polyester systems. The silane coated systems did not have sufficient data to perform the least squares fitting with confidence, thus they were evaluated by taking a flat percentage change from the clean glass cases.

Table 4.4 – Experimental mode I and mode II interfacial strain energy release rates for epoxy and polyester bonded to glass.

System	$G_{Ic,i}$ [J/m^2]	$G_{IIc,i}$ [J/m^2]
Epoxy / clean glass	262.3 ±23.3	498.7 ±44.3
Epoxy / Z6020 glass	281.0 ±20.7	534.2 ±39.4
Epoxy / Z6030 glass	251.2 ±12.1	477.5 ±23.0
Epoxy / Z6040 glass	296.8 ±15.9	281.0 ±20.7
Polyester / clean glass	193.4 ±23.8	401.6 ±49.4
Polyester / Z6030 glass	252.7 ±37.7	524.8 ±78.3

As a sanity check to the reported strain energy release rates, the mode II strain energy release rate is separately determined from the average debond length in the fragmentation testing following the work of Zhou [48]. The determined value is 506.9 ±50.5 J/m^2, which is in agreement with that estimated by the lap-shear testing. This was the only system which exhibited debonding during fragmentation, the Epoxy / Z6030 glass system, and therefore the only system which has been separately verified.

If the above analysis is accepted as true, this provides a substantial boost to the usefulness of the lap-shear test, as no other interfacial test can provide simultaneous measures of both the interfacial shear and normal strength and interfacial shear and normal strain energy release rates.

One interesting offshoot study examined the effect of pressure on the interfacial CSERR. Using the Epoxy / Z6020 coated glass system, samples were fabricated under 400g weights placed on the lap-shear joint during cure. The measured mode II value was 781.0 ±20.0 J/m^2. So while applying the silane resulted in a 7% increase in critical strain energy release rate over the clean glass system, the added pressure during cure resulted in a nearly 57% increase with all other conditions being equal. This increase in interfacial strength is well within reported values for the interfacial CSERR [48, 100, 102, 115], but certainly warrants further study to determine the phenomena behind such a change in toughness.

Before concluding the lap-shear testing, a further investigative test was run to determine if this modified lap-shear test might also apply to thermoplastic matrices, in this case, polypropylene. This particular test proved quite challenging to perform due to the inherently low bonding ability of thermoplastics with glass. Even with a larger 6mm diameter mask cut-out similar to the interfacial normal testing and being very careful to load the sample without applying any initial loading, only 3 samples out of 12 were able to be successfully fabricated and tested, the results presented in Figure 4.39.

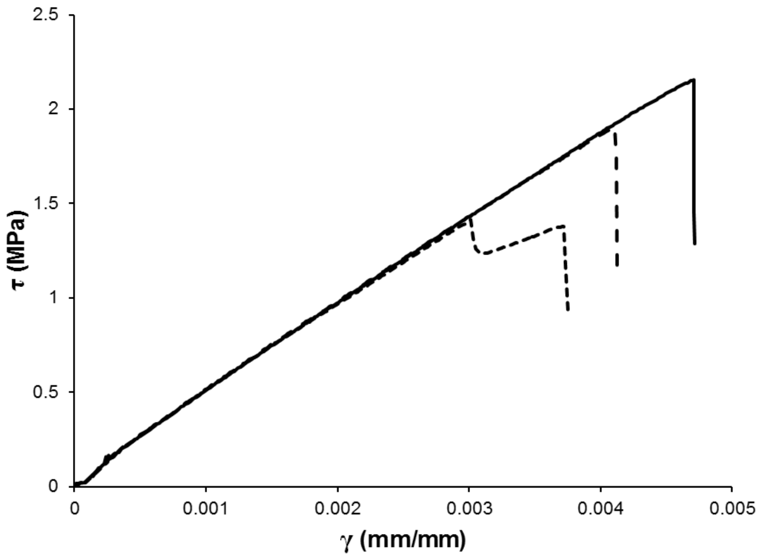

Figure 4.39 – Polypropylene / clean glass lap-shear test results.

Far from conclusive to report an interfacial strength with polypropylene and glass, these tests do indicate that the procedure is possible. If time had allowed, the next size of cut-out would have been used, and the use of coupling agents would have been investigated to generate confident interfacial strength results.

4.4 Correlating Studies

4.4.1 Damage and Constraint

One of the first lap-shear samples ever made had a strange worm-like pattern on it after it was cured, a sample of which is presented in Figure 4.40. Initially, this was thought to be a result of poor glass cleaning or from contaminates. When further samples exhibited this same pattern, however, it was noted that this pattern was not random, but the result of high residual stress causing the interface to debond during cure. It was this realization which first formed the link between polymer cure properties, residual stress, and interfacial stress.

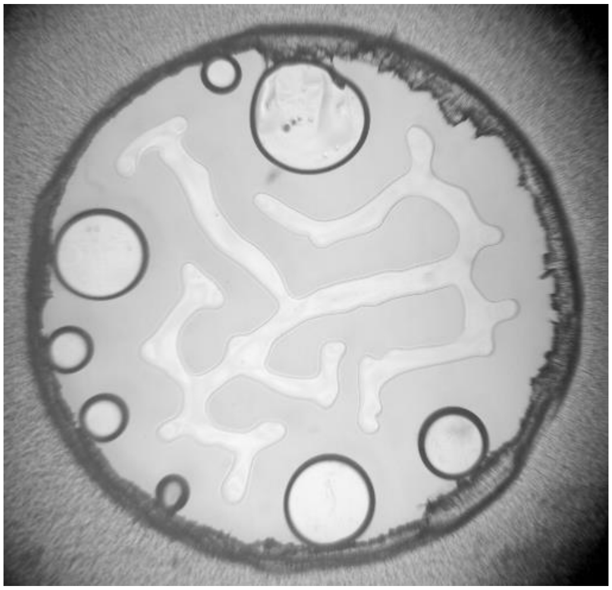

Figure 4.40 – Sample pattern observed following cure; disk diameter is 3mm for reference.

To better understand where the pattern was coming from, and how it was forming, a careful experiment was set up to record the cure process, as seen in Figure 4.41. Two hot plates were setup on either side of an optical microscope with an aluminum bar running between them. The temperature was set such that after reaching equilibrium, the center of the bar was 60°C. The heights of the hot plates were adjusted such that with the sample loaded in the center, the epoxy disk was in focus of the microscope. Images were set to be automatically captured every 30 seconds for the four hour cure duration.

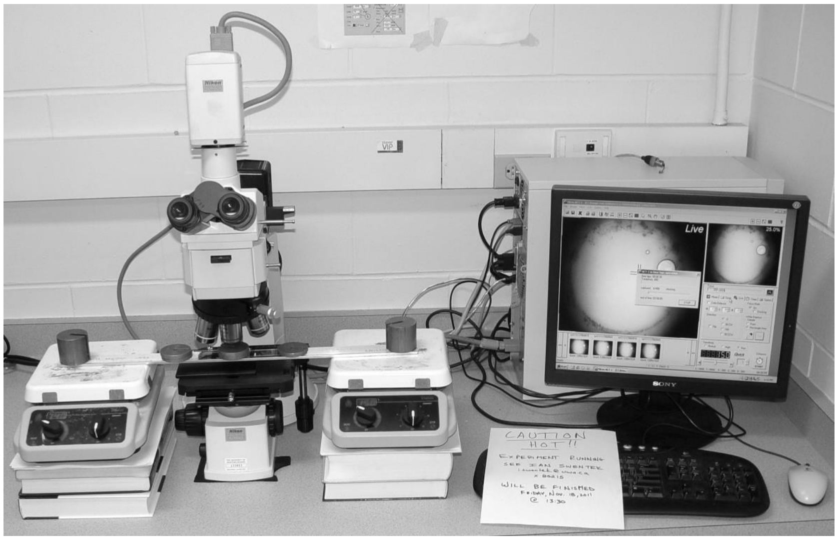

Figure 4.41 – Experimental setup for in-situ cure monitoring.

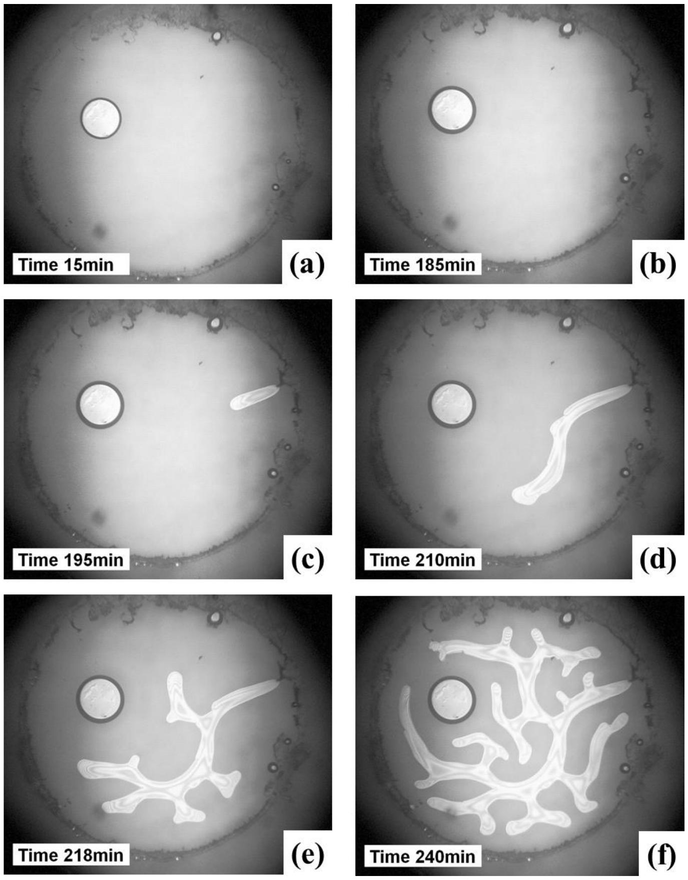

Figure 4.42 – Selected time lapse images during cure depicting the formation of a debond pattern at various times.

Weights were used during the cure process to stabilize the system during cure (both thermal and mechanical stabilization). Selected images from the cure duration are presented in Figure 4.42 indicating the formation of the pattern. A first thing to note is that the pattern doesn't start to appear until near the end of the cure cycle, well after the gel point was reached in the epoxy. Secondly, the pattern is appearing while the sample is at elevated temperature, not during the sample cooling, meaning this is a cure phenomenon, not a cooling phenomenon. Thirdly, the pattern forms in such a way that it never self-intersects, touches any portion of the disk boundary, or contacts any of the porosity bubbles. Finally, and not shown here, is that the pattern only appears in thin samples, where the mask is less than 0.1 mm thick. These last two items suggest this pattern is a function of the system constraint. Figure 4.43 presents this idea of constraint as it relates to the debond pattern observed.

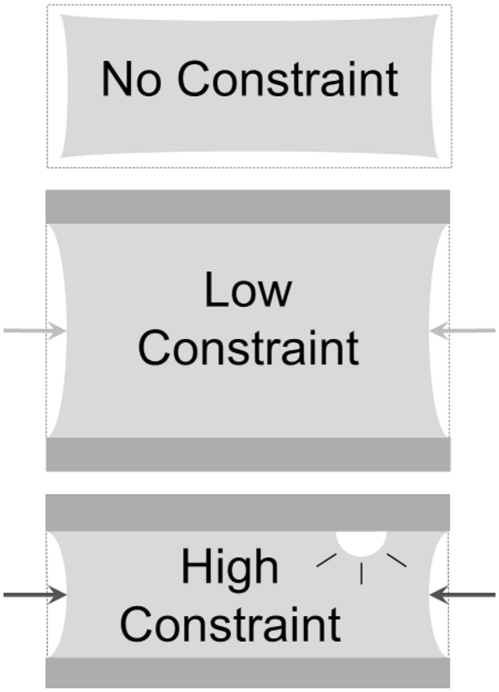

Figure 4.43 – Conceptual description of the effects of constraint on a shrinking polymer matrix.

Without constraint, the epoxy wants to shrink equally in all dimensions due to curing. With low constraint, as the epoxy bonds to the glass surface, a stress is built up as the polymer shrinks. However, with the greater volume of material, this residual stress is gradually dispersed through the epoxy away from the interface. When the constraint becomes high enough, this residual stress is enough to reach the interfacial strength and cause debonding. This suggests that the interfacial strength is at least partially controlled by temperature and that the cure induced stresses are not negligible. From this analysis, it can be concluded that using high volume fractions of fibres within a composite can lead to premature interface failure due to this cure induced debonding. One author examined this exact effect on cure induced debonding within dental composites and noted a similar effect [116].

To further this understanding, another series of tests was carried out with the same sample mask thickness of 0.05 mm, but with differing weights placed on the samples to increase the pressure during cure, seen in Figure 4.44. As the amount of weight increases on the sample, so too is there an increase in the pattern density. Though the branches of the pattern decrease in width with the increased cure pressure, the overall pattern area is increasing with respect to the increase in applied weight. Since the actual pressure on the disk during cure could not be measured, no correlation was possible to relate the pattern with the cure pressure, though a relationship is anticipated.

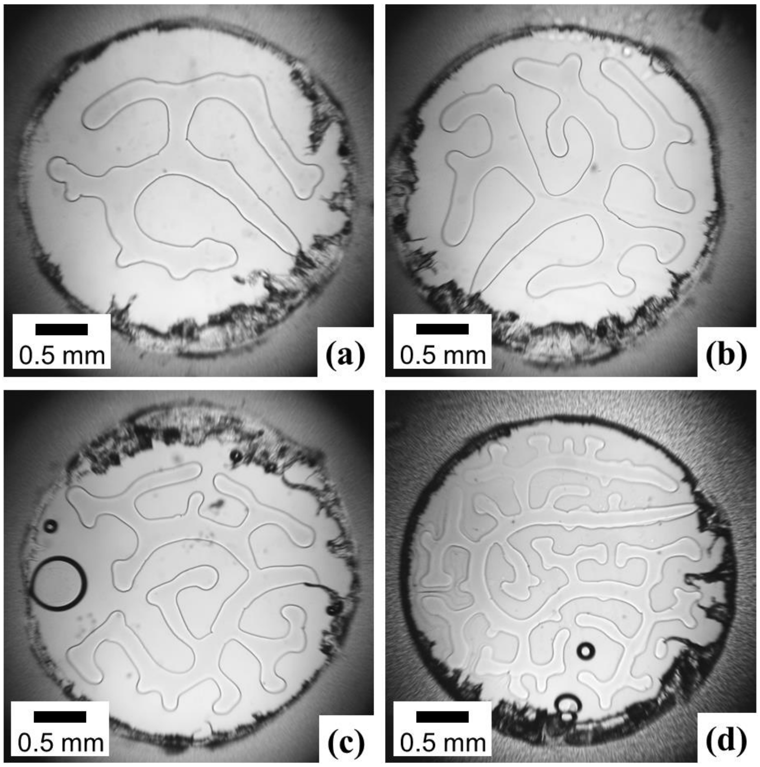

Figure 4.44 – Debond patters generated by applying pressure during cure using a) 100g b) 200g c) 300g d) 400g weights.

This pattern, while interesting, does represent a loss of contact area between the glass and the epoxy, and is perhaps better thought of as initial damage. It should be pointed out that though this effect disappeared with the use of silane coupling agents, the residual stresses are still present even if the interface is not failing during cure. Also, though not utilized in a quantitative manner, the concept of cure induced interface failure is an important one. As industrial composites strive for high levels of reinforcement with faster and higher temperature cures to speed the composite fabrication process, this effect is important to understand to prevent composites from being fabricated with initial amounts of damage.

4.4.2 Time-of-Flight Secondary Ion Mass Spectroscopy

To examine the interfacial behaviour of the lap-shear composite systems, surface analysis was conducted on the uncoated, coated, and post-fracture glass surfaces using time-of-flight secondary ion mass spectrometry (ToF SIMS). The resulting data analysis provides insight into the location and morphology of fracture, while also providing validation to the silane coating procedure previously adopted with the interfacial tests. Baseline spectra were taken of each of the neat surfaces (glass, silane coated glass, epoxy, and polyester) to determine fingerprint regions for subsequent surface comparison. To reduce batch variance, all samples used for the surface analysis were produced at the same time and were tested within 12 hours of fabrication to minimize exposure to contaminants.

An ION-TOF (Gmbh) TOF-SIMS IV equipped with a Bismuth cluster liquid metal ion source was used to measure all the surfaces. A 25 keV Bi3+ cluster primary ion beam pulsed at 10 kHz was used to bombard the sample surface to generate secondary ions. The positive or negative secondary ions, one polarity selected at a time, were extracted from the sample surface. The ions were mass separated and detected via a reflection-type of time-of-flight analyzer, allowing parallel detection of ion fragments having a mass/charge ratio (m/z) up to ~900 within each cycle (100 μs). A pulsed, low energy electron flood was used to neutralize sample charging. Ion mass spectra were collected at 128 × 128 pixels over an area of 500 μm × 500 μm for 60 s. The collected spectra were calibrated using the mass/charge peaks for both hydrogen and carbon.

To be able to distinguish between the different surface chemistry, mass spectra were collected for the four surfaces: clean glass, Z6030 coated glass, epoxy, and polyester, unique mass/charge peaks were manually identified. Here, Z6030 was selected as it was the common silane used with both the epoxy and polyester interfacial testing, and reduces the number of tests required to analyse the post-fracture surfaces. A first step is to identify some of the unique ion mass/charge ratios for each of the surfaces, as listed in Table 4.5. The ion charge was calibrated to unity, so the mass/charge ratio can be directly interpreted as ion mass. To make a distinction between the collection of positive ions and negative ions each sample was effectively scanned twice, but with a chamber cleaning operation between data collection runs.

Table 4.5 – Unique 'fingerprint' ion masses for the four analyzed surfaces.

Surface	Positive ions	Negative ions
Clean glass	28, 63, 91	28
Z6030 glass	73, 147	85
Epoxy	57, 58, 91, 135, 165	35, 93, 133, 211
Polyester	71, 82, 99, 112, 140, 157, 215	27, 57, 71, 115, 155, 173, 271

Smaller ion masses can be easily identified by atomic mass, as there are limited possibilities. For example, the ion mass of 28 can be identified as Silicon. Higher ion masses require a prior knowledge of the molecular structure and additional testing to accurately identify the composition from the many possible atomic mass combinations. The purpose of this study was not to determine composition; thus, unique peaks will be presented solely by their ion mass number, though the subsequent NMR testing presented in Chapter 3 could be used to accurately associate the ion masses with their compositions if so desired.

Fractured surfaces were examined in light of the identified fingerprint mass peaks that each material exhibited. Figure 4.45 presents enlarged sections of the mass spectra for ion masses unique to clean glass and epoxy on each side of a fractured interface. The spectra have been normalized with respect to the total ion count, to accommodate direct comparison.

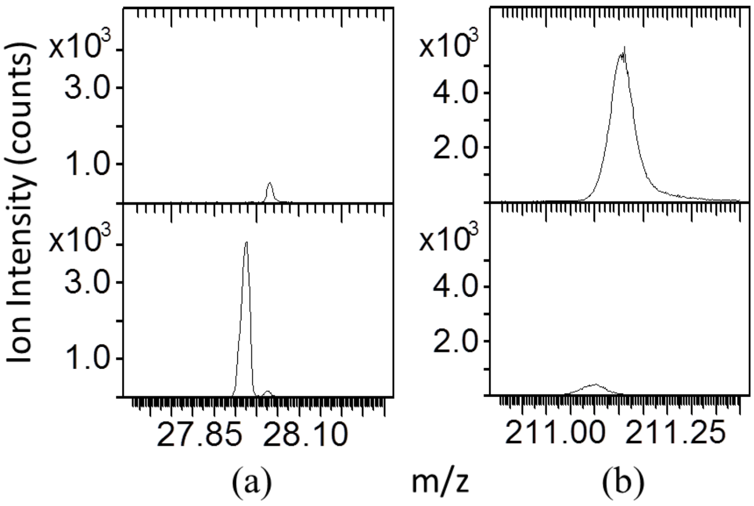

Figure 4.45 – Normalized negative-ion counts at a) glass and b) epoxy fingerprint peaks. Upper and lower frames correspond respectively to one side of a fractured epoxy/glass interface.

On one side of the fractured interface, there exist no measureable ions from the glass, while the epoxy ions are fully present. The other side contains the glass ions and only a small presence of epoxy is detected. A similar result is obtained with the polyester/glass interface, seen in Figure 4.46, though there is more of a polyester presence on the glass-side of the fractured interface. The physical representation of these fracture surfaces can be seen in Figure 4.28, where one side of a fracture is visually void of polymer, while the other side retains the polymer disk. These locations were specifically selected as such to determine what ions were present on each side of the fracture surfaces.

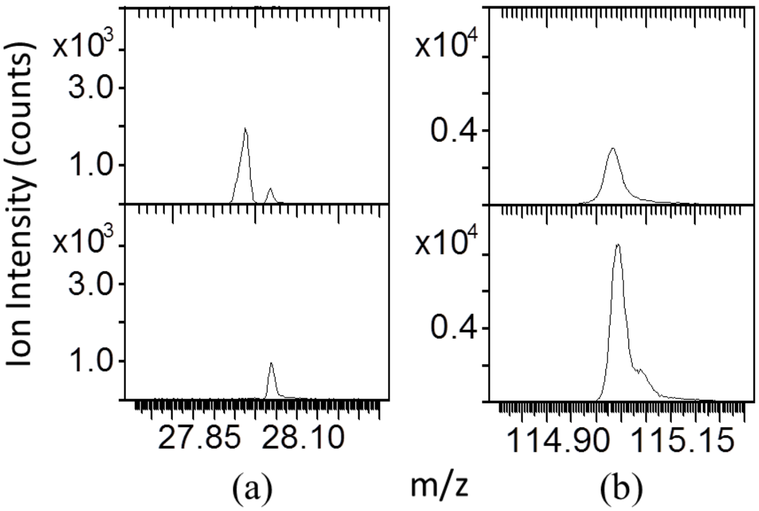

Figure 4.46 – Normalized negative-ion counts at a) glass and b) polyester fingerprint peaks. Upper and lower frames correspond respectively to one side of a fractured polyester/glass interface.

By rastering the ion beam across one of the inspected surfaces, the distribution of ions can be obtained. Recording the ion count at each location gives an understanding of the surface morphology and of the fracture surface using the resulting image intensity. The presented images are not normalized so that intensity can be directly compared. Though the images are taken of fractured surfaces, the locations selected for ToF SIMS analysis do not necessarily align between the image sets of the upper and lower surfaces, as this would have required too much work to mark and locate exact positioning between the fracture locations.

Figure 4.47 provides a visualization of the distribution of ions on the fracture surface of a clean glass/epoxy sample. The epoxy fingerprint ion masses 93 and 211 indicate even distribution of the epoxy on both surfaces, while the relative amounts on each surface are substantially different. The glass indicator, ion mass 28, is nearly absent from Figure 4.47a, which is to be expected on the epoxy-side of the fractured interface.

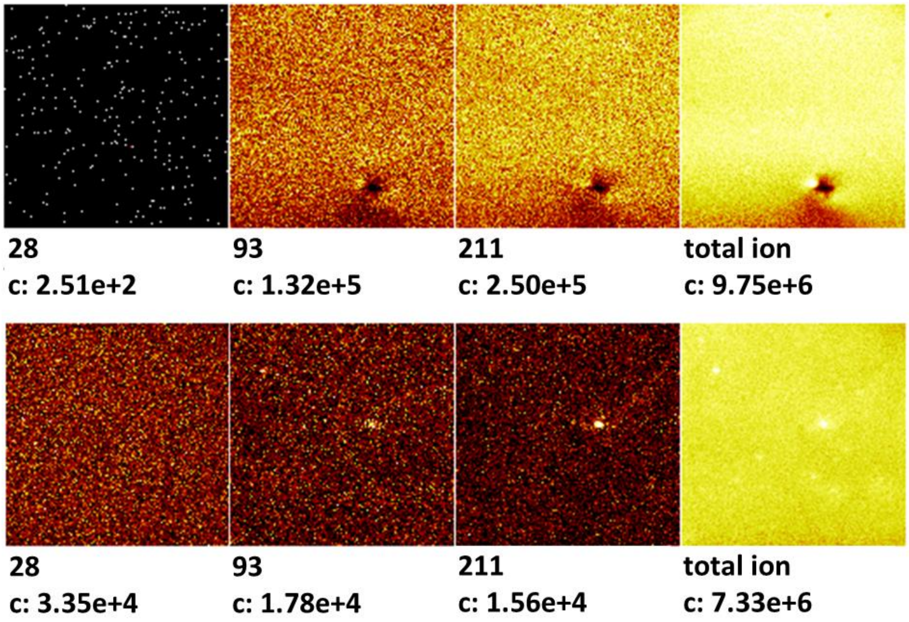

Figure 4.47 – Negative-ion distributions for the two halves of a fractured glass/epoxy interface. The ion mass and ion count are below each image.

The even distribution of epoxy ions in Figure 4.47b indicates a uniform fracture, void of areas of retained polymer. The dark spot in Figure 4.47a is a small bubble just below the epoxy surface causing a warp in the surface, which demonstrates the sensitivity of the measurement to geometric irregularity. The failure of the clean glass and polymer interface is seen to occur right at the interface, as expected. This was observed as true for both epoxy and polyester. This would substantiate the hypotheses that predominate fracture occurs at the chemical interface between the glass and polymer.

The fracture of the Z6030 silane coated glass and polyester interface is presented in Figure 4.48. The silane ion marker, mass 85, is present on both sides of the interface. In Figure 4.48b, the presence of glass is negligible, while the polyester is most noticeable (mass 71), which is again expected for the side of fracture with the retained polymer disk.

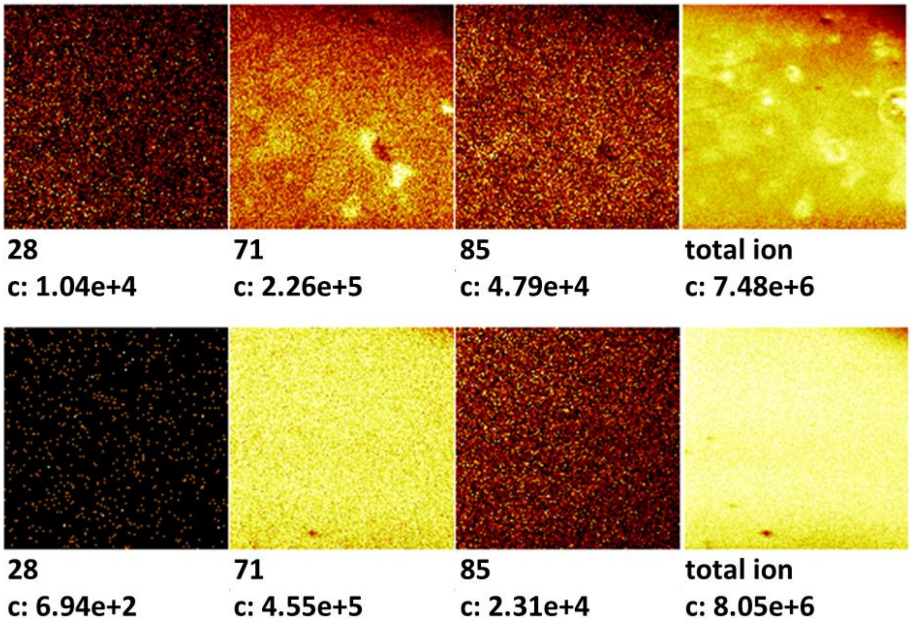

Figure 4.48 – Negative-ion distributions for the two halves of a fractured polyester/coated glass interface. The ion mass and ion count are below each image.

Together, the low presence of glass and distributions of the polyester and the coupling agent suggest that fracture occurs between the coupling agent and the polymer. With the epoxy exhibiting similar results, the following conclusions are drawn:

- The coupling agent is evenly distributed across the glass surface.
- The coupling agent is strongly bonded to the glass
- Interface failure occurs between the glass and polymer in an uncoated system, while it occurs between the coupling agent and the polymer in a strongly bonded coupled system

4.4.3 Alternate Material Systems

It was desired to extend the lap-shear testing to other material systems, namely the use of carbon as a substrate. Now that a glass system has been well understood, applying the same technique to a system where the substrate is opaque is the next step. The challenge here is identical to that of the glass model system: obtaining a representative material which has a similar crystallographic surface as the fibres it represents. Two materials were identified as having the potential to simulate such a surface: isomolded graphite and pyrolytic graphite. Plates of these materials were sourced from GraphiteStore.com.

The pyrolytic graphite is made by the layered growth of grapheme at high temperature in a vacuum furnace. The result is a plate with low porosity, high purity and highly oriented structure. Due to the oriented nature of the plate, the exposed surface mimics that of a PAN-based carbon fibre. The isomolded graphite is a high temperature compression moulded sample of finely ground graphite. This type of graphite has moderate porosity, is isotropic, and has a surface which closely resembles that of a pitch-based carbon fibre.

Both materials were sectioned in similar shape to the previously used microscope slides for the lap shear testing. All the graphite pieces were thoroughly cleaned multiple times with ethanol to remove any particulate matter from the cutting operation. Half of each type of graphite tabs were used in their cleaned state, while the other half were first acid etched in 25% nitric acid to add some functional groups to the exposed surface, acting like a coupling agent, to increase the bonds formed with the polymer. Epoxy was the sole polymer used in all the graphite lap-shear tests. The sample creation and testing procedures followed those presented for the glass-based lap-shear testing. Figure 4.49 presents the collected data amongst all the tests.

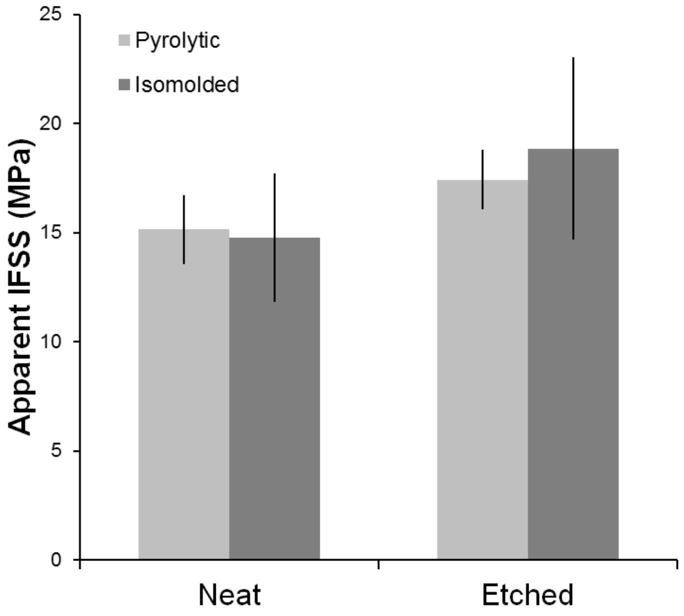

Figure 4.49 – Pyrolytic and Isomolded carbon / epoxy lap-shear test results.

Ultimately, the strength of the substrate material is too low for these materials to be used in this way. None of the samples fractured at the interface; all samples broke some small distance into the carbon substrate such that the recorded strength was actually the shear strength of the carbon tabs, rather than the desired interfacial shear strength. Though a slight increase is seen between the neat tabs and those which were acid etched, the issues with failure location suggest that this is not an interfacial strengthening result. Thus the data in Figure 4.49 does not reflect the interfacial shear strength of the epoxy / carbon systems constructed.

It is expected that the lap-shear test can be utilized with other material systems, but the choice of substrate is seen to be important in order to properly capture the desired interfacial properties. Future testing will need to first ensure that the shear strength of the selected material is greater than the expected interfacial strength in order to be able to measure an acceptable interfacial strength value.

5 Numerical Simulation

The use of numerical simulation is employed to both validate the experimental results and to rapidly test material performance in complex setups. A simulation also acts as a method to combine the developed material models and apply failure criteria using the measured interfacial strengths. The results of which directly support the predictive failure model in the next chapter.

Three validation studies are conducted to examine the failure modes observed in the interface measurement experiments. The fragmentation study examines the stress transfer relationship between the polymer and fibre and includes fibre failure. The push-out study uses a linear-elastic model to determine the stress distributions within the polymer at the point of interface failure. The lap-shear study verifies the experimental failure modes observed against a selected interface failure criterion.

A predictive simulation is also constructed to determine the magnitude and distribution of residual stresses within a polymer composite as a result of the polymer processing. This simulation tests the impact of fibre arrangement on the cure and thermal stresses in the polymer. Multiple material model implementations are used to show the importance of accurate polymer characterization. A predictive study is conducted to estimate the surface finish in a composite part given the fibre arrangement and polymer constitution.

5.1 Fragmentation

A fragmentation study is undertaken to validate the fragment lengths and debond lengths obtained in the experimental studies. This study was done with the use of LS-Dyna and associated material models [117]. Here the goal is to examine how fibre stress transfer operates and to determine if it is possible to replicate the fibre and interface failure against the single fibre fragmentation experiments of Chapter 4.

5.1.1 Boundary and Interface Conditions

To setup the model, symmetry is employed to reduce the computational complexity of the problem by only simulating one eighth of a fragmentation gauge section. Figure 5.1 presents a perspective view of the model geometry with the matrix shown in blue and the fibre coloured in red. The model uses three planes of symmetry to effectively model a 1 mm length of fibre and surrounding matrix. The matrix is modeled such that five fibre diameters worth of material surrounds the fibre, as per the experimental studies. At one end of the model (opposite the symmetry end), a prescribed displacement is given to several of the outer nodes of the matrix in the z-direction to simulate the effect of a tensile load as applied in shear on the matrix.

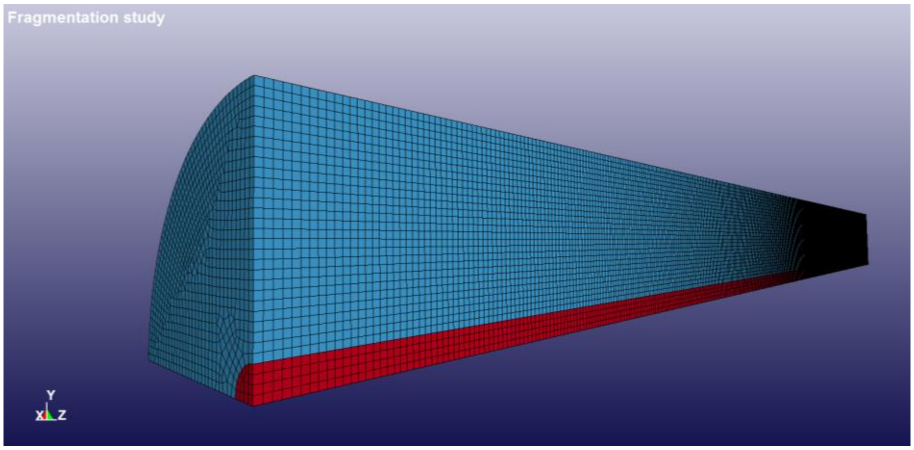

Figure 5.1 – One eighth fragmentation model; the fibre is modeled in red while the matrix is shown in blue the length of which is 1 mm.

The model was composed of about 260,000 solid elements. The matrix was modeled as an elastic solid with kinematic plasticity (LS-Dyna material 012) using the material properties presented in Chapter 3. The fibre is modeled as an elastic brittle solid (LS-Dyna material 013) using the material properties provided by the manufacturer in Appendix A. The same type of fibre was modeled as was used for the fragmentation and push-out tests. A reduced time study was run by rapidly displacing the matrix to just below the load which causes the fibre to fragment, and then slowly displacing for the remainder of the study.

5.1.2 Fracture Studies

After getting the model to successfully converge, the first simulation was run with a perfectly bonded interface condition. Figure 5.2 and Figure 5.3 present the results from this study showing respectively the Von Mises stress and effective strain. In each figure, the model is shown with a) both the fibre and matrix b) just the matrix and c) just the fibre such that the resulting stresses / strains can be examined in detail.

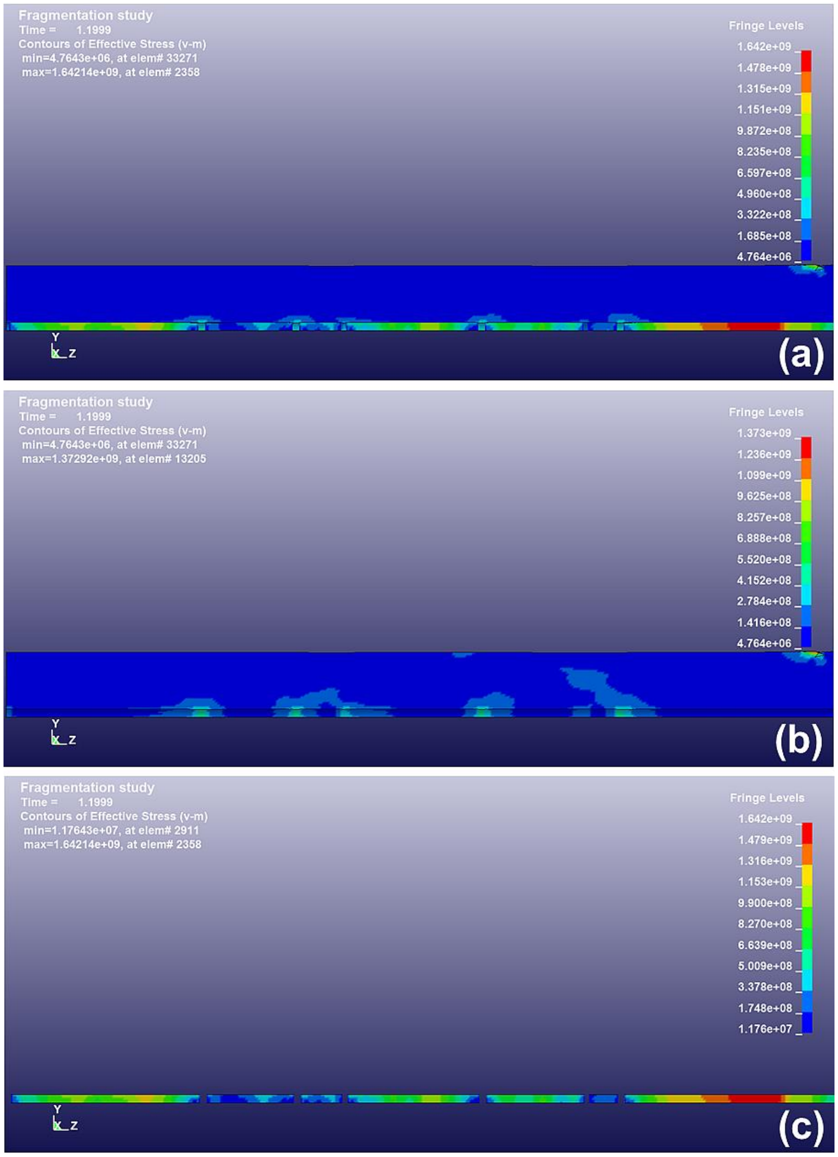

Figure 5.2 – Fragmentation Von Mises stress distribution in a) both fibre and matrix b) just the matrix and c) just the fibre

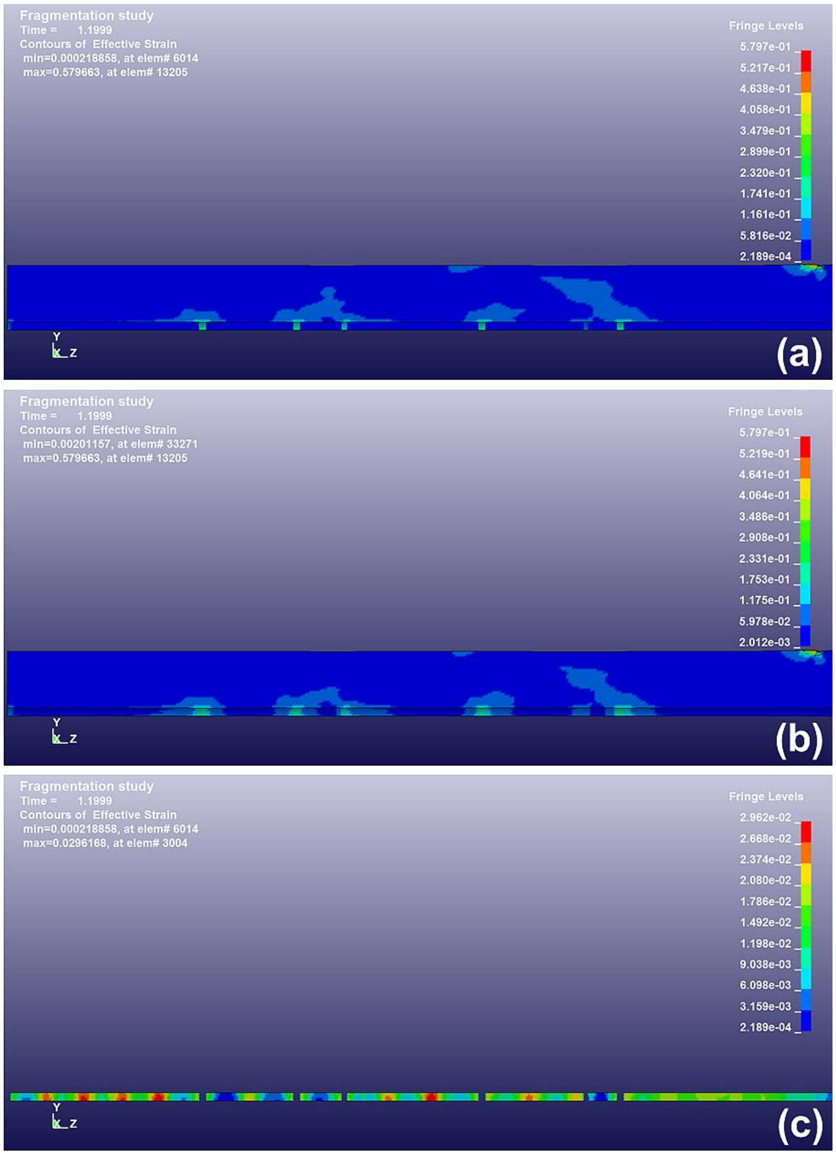

Figure 5.3 – Fragmentation effective strain distribution in a) both fibre and matrix b) just the matrix and c) just the fibre

A first thing to note is that the simulation effectively demonstrated the observed fracture pattern as for a well-bonded fibre. This may seem trivial, but the simulation did show a small distribution of fibre lengths consistent with that of the experimental studies. Secondly, the images of the fibre (Figure 5.2c and 5.3c) still have evidence of the stress waves which formed from the sudden fracture events. Since this first simulation did not include any damping, when these waves superimpose, additional fracture can take place even if the fibre is below the critical transfer length, confirming a previous hypothesis regarding the distribution of fibre lengths.

Confidence checks can be done by comparing the loads or strains against those expected. The fibre is showing peak loads around 2 GPa which is in line with the fracture strength of the fibres. The matrix, however, is indicating peak loads well in excess of its tensile strength. This is due to the stress around the traction load. In a real sample, the tensile grips actually permanently indent into the sample to be able to grip the sample during testing. In the simulation, the matrix is prevented from failing as such, leading to the higher than expected stresses.

A second study was undertaken which added damping to the matrix such that fibre stress waves would be less of an issue causing premature fracture. Despite the implementation of the damping to prevent the stress waves from causing multiple fibre break points simultaneously, here a new challenge was encountered: complete fibre debond. The purpose of this study was to reduce the interfacial strength to that as measured during the experimentation. However, this had the unintended consequence of instigating a sudden interfacial failure during the stress transfer, leading to the complete debond of the fibre without any fragmentation. The explanation for such an event is centered in the material model for the matrix. By preventing the matrix from failing, it was also prevented from absorbing much of the energy associated with fracture. If the matrix were allowed to deform and fail freely either with a removal of elements, or with an energy criterion, then the first place to fail is around the imposed traction displacement, and the simulation ends without the fibre or interface failing. This was thus left as an open problem, since no immediate solution was forthcoming on how to properly set up the material models to allow for the correct stress transfer to occur and observe debond, but also impose the proper limits on the matrix and interface failure.

5.2 Lap-shear

A lap-shear simulation was also conducted through LS-Dyna to examine and validate the Hashin interface failure criterion. Secondarily, this study compared the simulated fracture patters with those obtained experimentally as a measure of confidence in the previous fractographic analysis in Chapter 4.

5.2.1 Model Setup

The basic model is presented in Figure 5.4 using two linear elastic glass blocks bound together with the elastic kinematic plastic epoxy matrix. Here, however, the glass is not provided with fracture properties so that only the epoxy and interface are capable of experiencing damage. Unlike the fragmentation simulation where the epoxy damage was causing unintended issues simulating the interface failure, here the epoxy in not directly loaded so the issues are no longer apparent. The interface is treated as an automatic one-way nodes-to-surface boundary condition with tiebreak [117]. This means that the epoxy cannot penetrate the glass surface, but can be separated from it if a given condition is met. The condition imposed is that of the Hashin failure criteria with the same properties as previously measured.

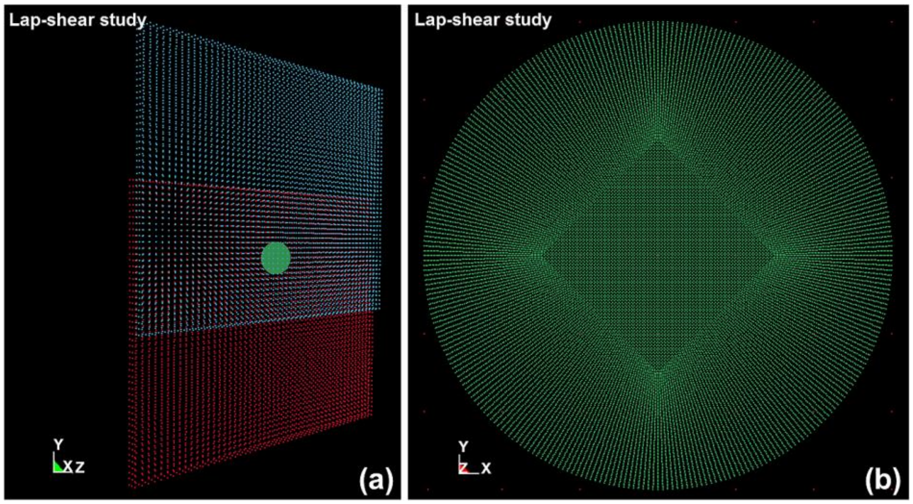

Figure 5.4 – Lap-shear model setup in grid mode showing a) the whole model and b) the center epoxy disk detail.

In Figure 5.4, grid mode, where a point is placed in the geometric center of each element, is used to show the placement and density of all the elements. The two glass plates do not require fine detail as they are linear elastic solids without any failure allowed. The epoxy disk, however, requires small elements such that there are enough nodes attached to the glass surface to model the proper interfacial condition. The nodes on the bottom of the lower glass plate are fixed in position to initially restrain the overall geometry. The nodes on the top of the upper glass plate are given a vertical prescribed displacement to simulate the lap-shear loading. No other boundary conditions are imposed. Similar to the fragmentation test, reduced time scale loading is conducted to simplify the computation.

5.2.2 Simplified Geometry Studies

The first test was again to ensure the simulation converged and to ensure the model is properly set up. Initially, the epoxy disk was set with a thickness of 0.05 mm, with the result shown in Figure 5.5.

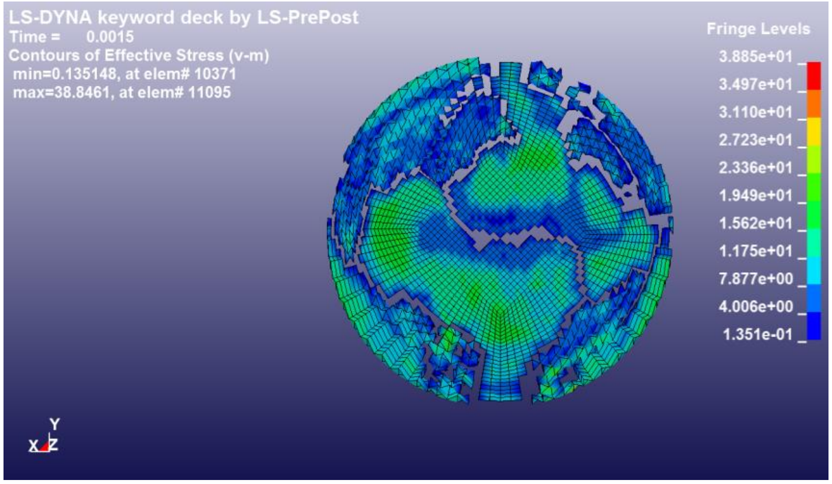

Figure 5.5 – Lap-shear simulated fracture pattern of epoxy disk

This first model did not employ elements with the proper aspect ratios as evidenced by the presence of hour-glassing on the outer elements. However, this type of fracture pattern, where a crack moves back and forth between both sides of the debonding epoxy disk was observed experimentally in all the thin lap-shear samples. One such sample is presented in Figure 5.6 where the epoxy disk was fractured into multiple segments and both glass slides retained a portion of the epoxy fragments.

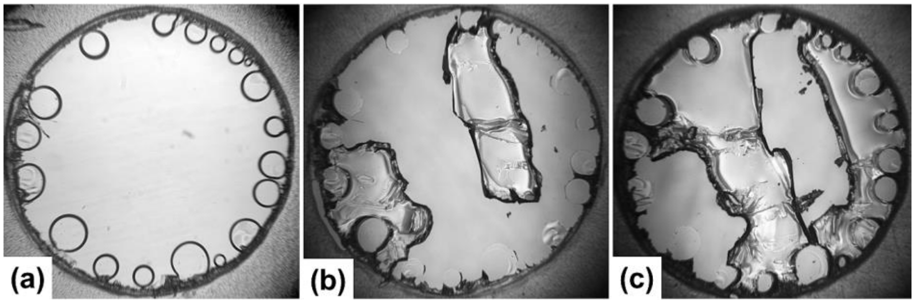

Figure 5.6 – Glass / epoxy lap shear sample with 0.05 mm thick epoxy disk showing a) as fabricated b) fractured top surface and c) fractured bottom surface. For reference, the loading direction was left-right and the disk is 3 mm in diameter.

With a finer mesh, comprising nearly 30,000 solid elements, the next simulation is to investigate the debond fracture process. The simulated epoxy disk is increased to a thickness of 0.18 mm and the number of simulation steps is also increased. Figure 5.7 presents the six consecutive frames at the point of interface failure and epoxy fracture. Since the glass is hidden in the images, the stress distribution in the image is an indication of the state of the interface. As the debond proceeds from Figure 5.7a to Figure 5.7d, the same double crest yield pattern is seen in a sample of the same thickness in Figure 5.8 which was tested very slowly to capture this debond event. Also, the final frames in Figure 5.7 indicates that the lap-shear failure is beginning to change failure modes as only one crack is formed, rather than multiple segments seen previously in Figure 5.5.

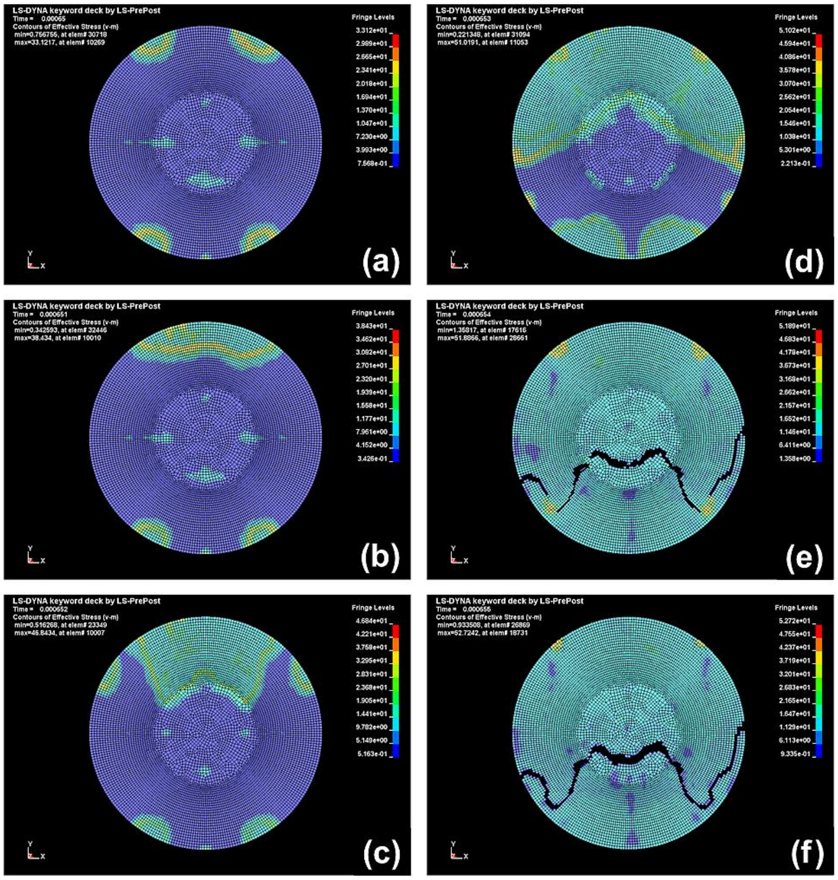

Figure 5.7 – Glass / epoxy lap-shear simulation of 0.18 mm thick epoxy showing six consecutive time steps at the point of failure.

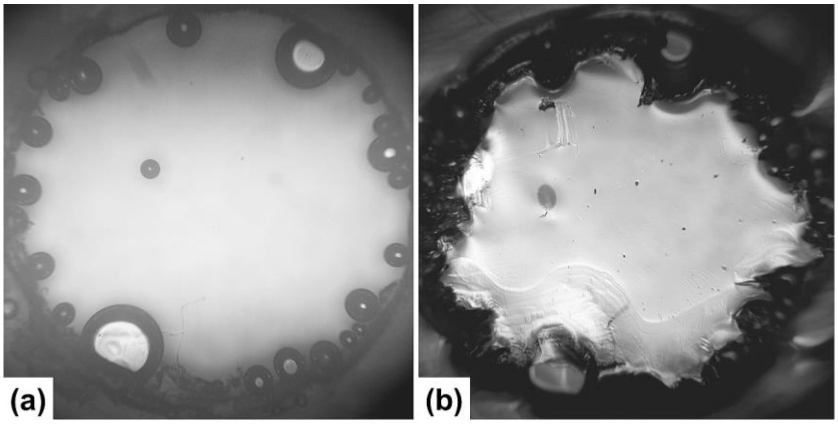

Figure 5.8 – Reference glass / epoxy lap-shear sample with 0.18mm thick epoxy disk a) before testing b) post-fracture

When the simulation was repeated with thicker epoxy disks, no matrix cracking was observed. This is consistent with the increase in mode I crack opening causing the epoxy to peel from one of the surfaces rather than to predominately shear.

5.2.3 Discussion

By recording the stress within the lower glass plate at one of the cross-sections, it is possible to compare the shear stress-strain behaviour between the experimental work and the simulated work. Figure 5.9 presents one such comparison between an epoxy / glass lap shear sample with a disk thickness of 0.20 mm and the associated simulated stress-strain behaviour.

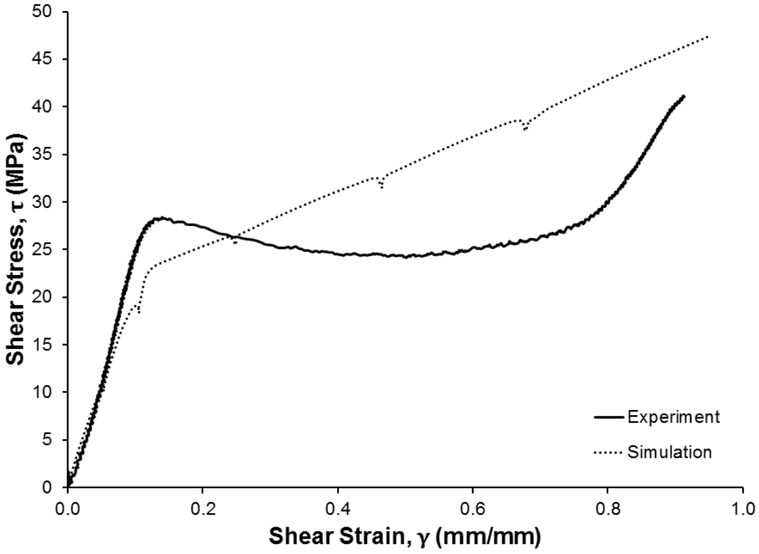

Figure 5.9 – Comparison between experimental and simulated results for a lap-shear test with an epoxy disk thickness of 0.20 mm

Since the simulation is the epitome of a perfect sample, it should come as no surprise that the simulated curve represents an idealized epoxy response according to the selected material model. The undulations in the simulated response are due to stress waves from the reduced time scale simulation, and could be reduced by extending the time scale (slowing down the displacement rate) or adding a damping term to one or both the materials. The sample selected for the comparison in Figure 5.9 was one which contained a minimum amount of porosity to allow a better comparison of a good experimental sample. From Figure 5.9, it the use of the elastic kinematic plastic material for the epoxy is immediately evident. Though this model could be refined to better match the true material, the important comparison is the peak load representing the strength of the interface. Here the simulation predicts a slightly higher shear stress and strain before the interface gives way, which is again to be expected considering the defect-free model. Since the simulation captured the same features as the experiments, this suggests that the interpretation of the experimental data in Chapter 4 correctly identifies the interfacial properties.

From the same simulation as was used to generate Figure 5.9, the normal strain distribution within the epoxy disk is shown in Figure 5.10. This provides a pre-failure glimpse at the epoxy response. The top glass plate is displaced to the right resulting in the shearing of the epoxy disk as seen.

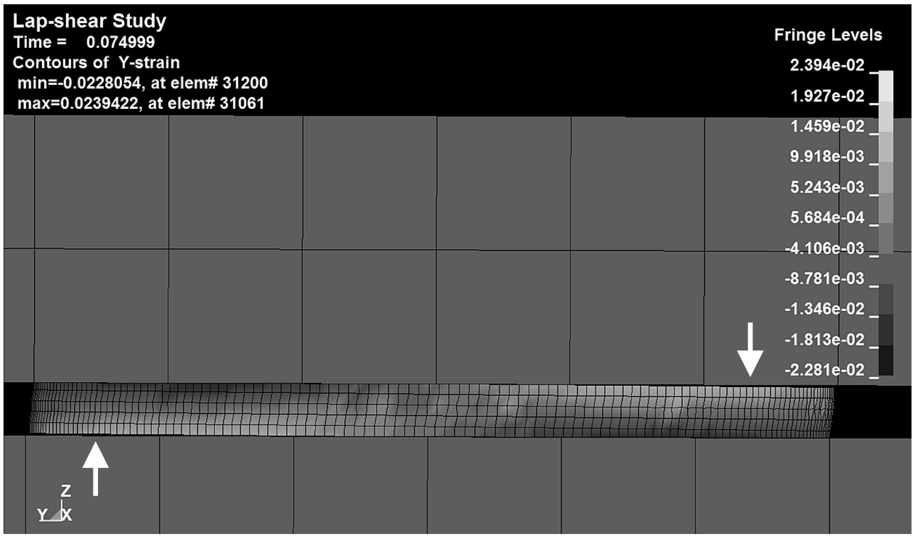

Figure 5.10 – Side view of y-strain distribution in epoxy disk between glass plates.

Note that the epoxy strains are not perfectly symmetric as the simplified analytical solution suggested in Figure 4.52. It is evident, however, that the interface debond is being initiated due to the normal interfacial strength, seen as the slight separations indicated by the arrows. The complete stress and strain profiles in all three orthogonal axis just prior to interfacial failure are presented in Figure 5.11.

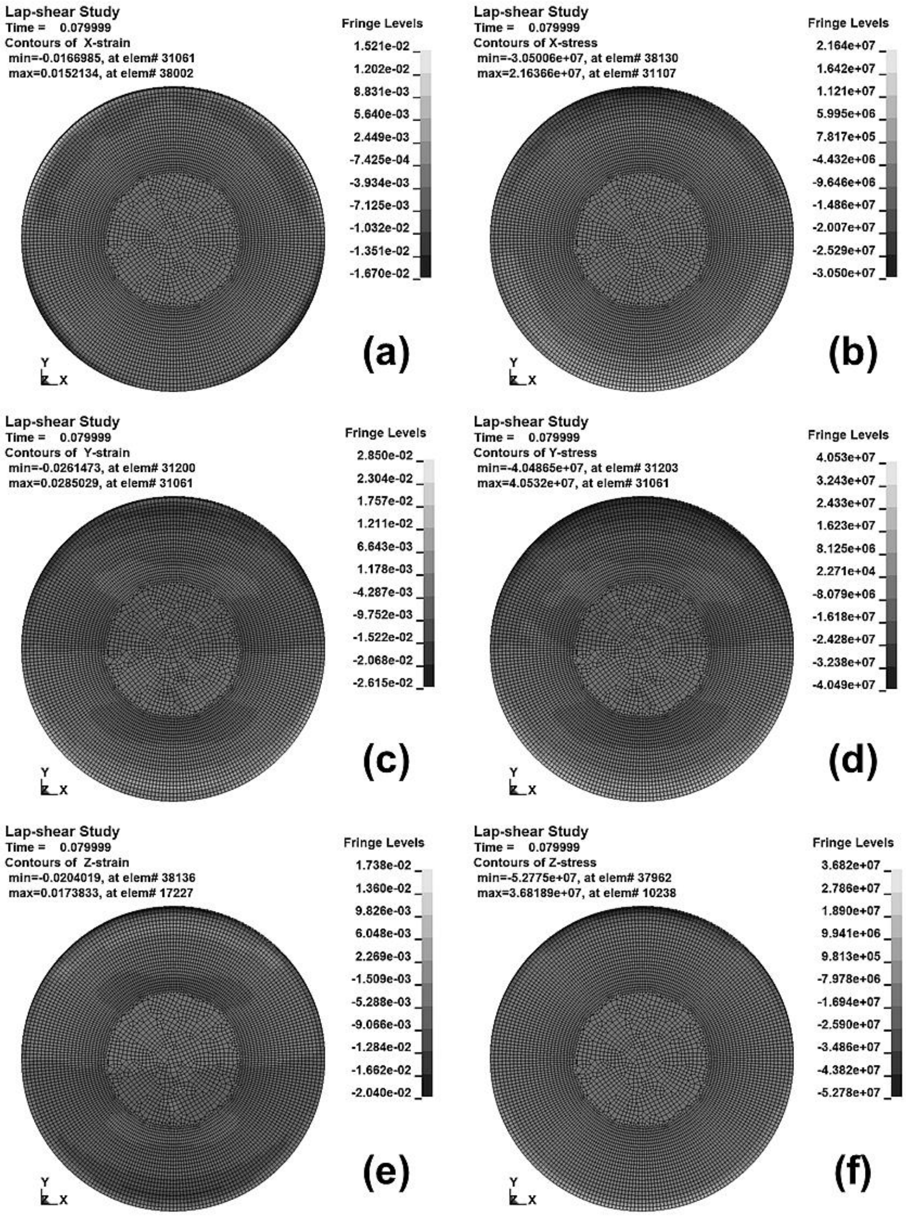

Figure 5.11 – Stress and strain distributions in xyz directions of simulated 0.20mm thick epoxy disk prior to interfacial failure.

The debond event is also correctly simulated from the standpoint of the fractography where the change in loading mode changes the matrix fracture behaviour. Further, the Hashin criteria of the simulated interface generates the same trends as compared to the experimental studies. This last point may seem to suggest that the computer was programmed to give the same answer as the experiments, which is true, but it serves to confirm that the computer was properly programmed to give the same answer, giving credence to the other observations.

To extend this work, future simulations accounting for the size and location of porosity would be really interesting in terms of the fracture initiation and growth behaviour. Further, reusing this simulation to predict the strain energy release rate of the interface would be another method to validate the experimental work.

5.3 Multi-physics Simulations

Simulating the cure behaviour to determine residual stresses has been attempted multiple times [24-28], though none of these authors have considered elevated temperature yield behaviour of the polymer during cure. Integrating multiple physical systems to account for the different processing has only recently been attempted as the computational ability to do so has been realized [25, 118]. To perform the cure simulations, a commercial software COMSOL v4.2 was selected along with the associated user manual [119]. COMSOL, at least at the time, did not yet support a viscoelastic material with plasticity, thus three separate solutions are compared: linear elastic, linear elastic with plasticity, and viscoelastic. Inherent to any simulation are the software-specific implementation choices that impact the trade-off between efficiency and accuracy of the generated solutions. Two items are noted as important to achieve such a balance within COMSOL: when to calculate the Jacobian and the error tolerance to achieve solution convergence. In the presented simulations, the Jacobian is calculated at every time step, while the error tolerance is set higher than the default. The effect of which results in a smooth integration between time steps, but at the expense of greater overall calculation error.

5.3.1 Modeling Viscoelastic Response

Using the methods presented in Chapter 2, the viscoelastic model in COMSOL is populated with the experimental work for the epoxy from Chapter 3. A first simulation is to test the implementation of the epoxy model to ensure it accurately models the same physically real system as observed. A simple rectangular slab was modeled to examine the cure properties over a variety of thicknesses between 0.2 – 2.6 mm in 0.2 mm increments. The simulation was conducted using the viscoelastic material model for a 2 hour isothermal cure at 60°C. Figure 5.12 illustrates the basic model, and the von Mises stresses at the top center location of the plate. Two planes of symmetry are used to simplify the problem such that point A in Figure 5.12 is the center of the epoxy slab.

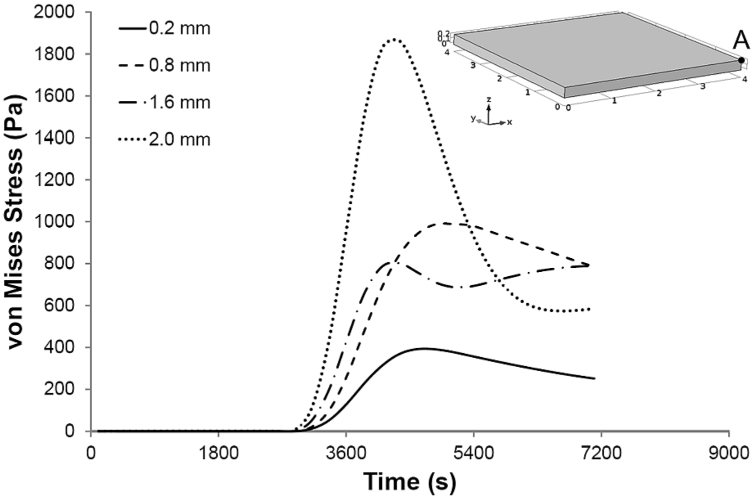

Figure 5.12 – Cure induced stresses in neat epoxy simulated at several sheet thicknesses. The inset model indicates the basic geometry and location of the depicted stresses.

The data indicates exactly what is observed in the lab: as the thickness of the plate is increased (the surface area to volume ratio decreases), heat generated by the cure process cannot rapidly dissipate and causes a spike in the cure residual stresses. The solution failed to converge at the 2.6 mm thick interval, which aligns to the experimental observation that sheets of neat epoxy over 2.5 mm thick exhibit entrapped air from boiling and significant stress fractures. Though not the epoxy that was used for the simulations, this same phenomena is presented in Figure 5.13 during some cure trials of polyester. In an effort to determine the best cure parameters, several plates of different thickness were cured at 90°C. Initially, the left-hand plate shows out-of-plane warping and significant distortion due to the rapid cure behaviour from thermal instability. As the plate thickness was reduced, the ability to produce a uniform and defect-free plate was increased.

Figure 5.13 – Cured polyester slabs with decreasing thickness from left to right.

To compare the three solid mechanics implementations (linear elastic, linear elastic with plasticity, and viscoelastic), a 2D plane stress model was created with a single fibre surrounded by epoxy. The stresses were determined at the fibre-matrix interface for each of the models during a simulated 2 hour isothermal cure at 60C, as seen in Figure 5.14. As expected, in all three cases, there is a residual compressive stress around the fibre due to the cure shrinkage.

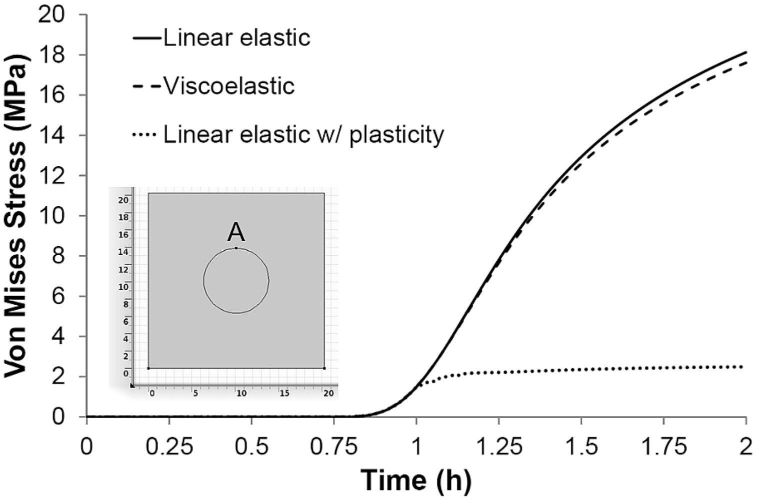

Figure 5.14 – Residual stress at the fibre matrix interface around a single fibre; the inset plane strain model indicates the location of the calculated stresses.

The linear elastic solution indicates the highest residual stress, with the viscoelastic model relaxing some of that stress with comparable magnitudes to those in the literature [28]. The plasticity model prevents the stress from climbing, as the epoxy is yielding during the elevated temperature cure. If the epoxy were cooled to room temperature, the stress would increase approximately 4.4 MPa for all the three cases to account for the additional thermal shrinkage. These residual stresses are of similar magnitude to those that have been previously calculated [120, 121].

5.3.2 Simulating Residual Stress

One practical use of this type of simulation is the prediction of residual stress in a highly-filled composite, where fibre proximity drives additional modes of stress build-up due to the high compliance provided by the stiff fibres. In a linear elastic implementation, two fibres are initially separated by 0.5 μm in a 2D plane stress parametric simulation; the setup is shown in Figure 5.15. At each parametric step, the fibres separation is changed, and the model is re-meshed using an automatic curvature-based scheme to capture the stresses between the fibres.

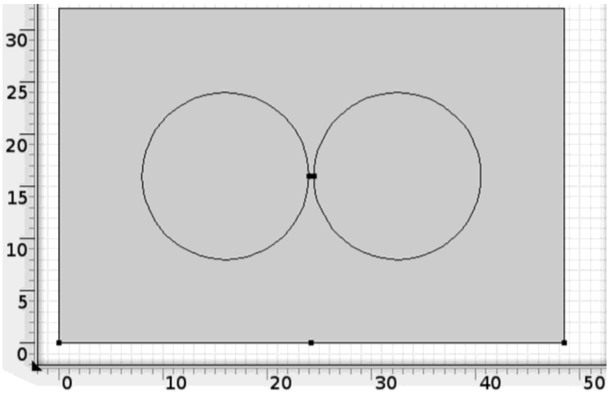

Figure 5.15 – Fibre separation study initial plane stress model setup.

Using one of the points which resides on the interface of the fibre and matrix between the two fibres, the principal stresses are presented for 5 fibre separation distances in Figure 5.16. When the fibres are close together, there is a strong tensile stress in each of the principle directions, which correspond to the radial and tangential directions at the fibre surface. The Tresca criterion is used as it better illustrates the in-plane shear stresses present as the fibre separation increases. The results indicate that highly filled thermoset polymers experience high residual cure stresses. This can lead to partial debonding either during cure or post cure since the portion of the composite under a high constraint stress requires the least additional stress to induce failure, as has been previously observed in dental composites which are rapidly cured, causing a high stress build-up [116, 122].

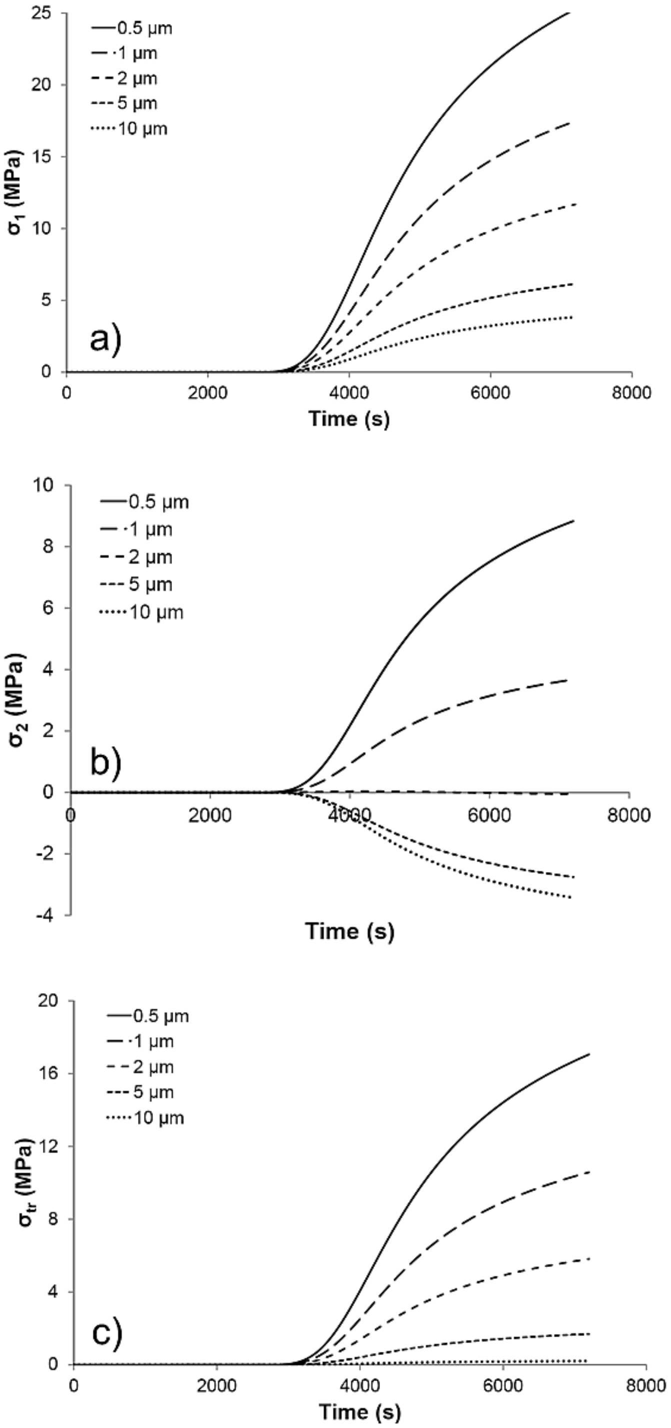

Figure 5.16 – Linear elastic cure stresses between two fibres at several separation distances of a) x-direction b) y-direction c) Tresca

Noticeable in Figure 5.16 is the onset of the gel point around the one hour point where the polymer can support a stress. This point is identical to that as observed experimentally in the rheometry experiments. The biggest result from this simulation is the measure of the residual stress acting on a fibre in a composite of a given volume fraction and processing method.

For reference, in a square or hexagonal array, a fibre separation of 0.5μm corresponds with a fibre volume fraction of 73.9% and 85.3% respectively; 10μm spacing corresponds with volume fractions of 29.7% and 34.3% respectively. Again, if the system were cooled to room temperature, there would be additional thermal stresses.

Philosophically, these sorts of simulations are vital to the future of materials selection for composite design, but require better up-front materials characterization to enable the use of such models. For example, this simulation could be used to determine the processing characteristics which would result in zero residual stresses at room temperature after cure. Also, Patham showed how a similar simulation could capture the effects of springback due to relaxing stresses over time and temperature to result in a better initial mould geometry to suppress this effect [25]. In terms of improving this present model, adding mass and energy loss terms will expand the temperature range at which the model is valid. Combining the viscoelastic and plasticity effects into one material model would allow the most accurate representation of residual stress during cure.

5.3.3 Application to Composite Materials

Using the model from Section 5.3.2, one promising application of such a cure simulation is in regard to the prediction of composite surface finish. Surface finish is a very challenging topic in the composites world. Thermoplastics, which exhibit a large thermal dependence, commonly show waviness on a moulded part due to the uneven contraction of the polymer around the embedded fibres. Thermosets are usually easier to work with to produce a smooth, class-A surface, though the cure shrinkage and thermal shrinkage need to be managed – typically with polymer fillers. The goal during production is to produce a composite part that has a near-mirror finish which can either be painted or coated to achieve an aesthetically pleasing final surface. Though one challenge is to manage the composite part during an automotive paint-bake cycle where the aforementioned springback is a concern, predicting the surface quality of a composite part is an initial need.

To demonstrate this simulation ability, an exploratory simulation was created to investigate two impacts on surface finish: fibre separation and the thickness of the polymer layer above the fibres nearest the free surface. The model setup and deformation pattern is shown in Figure 5.17, below. It is anticipated that the surface curvature will be reduced as fibre separation is reduced or the polymer layer above the outer fibres is increased.

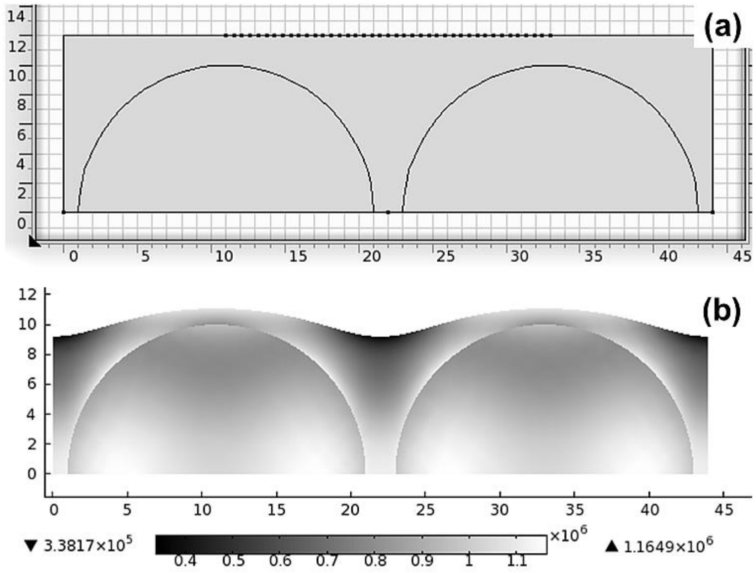

Figure 5.17 – Fibre surface finish model showing a) model setup with surface points for determining curvature and b) the post-simulation deformation behaviour and residual stresses.

To determine the predicted curvature, points are placed on the free surface between the upper midpoints of each fibre as in Figure 5.17a). The displacement of each point will be recorded at the end of each simulation to determine the predicted surface curvature. The two important values that are calculated are the surface roughness and the radius of curvature. Though there are many values which can be used to characterize the roughness of a surface, the arithmetic average is the most common, and is thus currently employed. The arithmetic average of surface roughness, denoted R_a, is calculated as defined: as the average of all the points on the surface, taking the lowest point as the reference point. The surface curvature is calculated from:

$$\kappa_r = \left| \frac{\left(1 + y'^2\right)^{3/2}}{y''} \right| \tag{5.1}$$

where y' and y'' are the first and second derivatives of the Cartesian function defining the curve [123]. Here it is assumed that points on the surface of the simulated composite form a continuous curve which is at least twice differentiable.

While the data produced from the simulation is useful, it is not immediately apparent if the simulations are providing a realistic measure of the surface of a fibrous composite. To coincide with the predictions, several test composites were specifically fabricated to generate some experimental data. The first such sample was composed of unidirectional glass fibres in an epoxy matrix such that there would be fibres near to the upper free surface. This was mounted in a differently coloured epoxy so that polishing would not impose damage to this surface which could now be viewed end-on using a transmitted light setup to see this composite surface as in Figure 5.18a).

At the maximum optical magnification the samples were imaged such that the interface between the composite epoxy and the mounting epoxy was readily apparent. The surface curvature is quite visible and was manually extracted from the image using constructed curves as in Figure 5.18b) for several locations. Both the simulation data and the experimental data are collected in Figure 5.19.

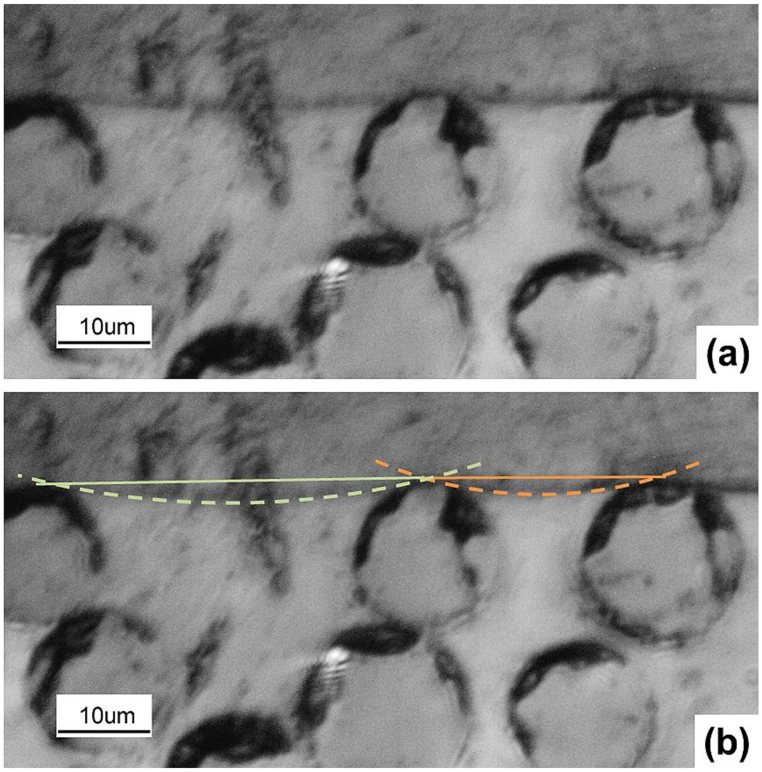

Figure 5.18 – High optical magnification of glass / epoxy fibre surface viewed perpendicular to the fibre direction: a) native b) with lines of curvature.

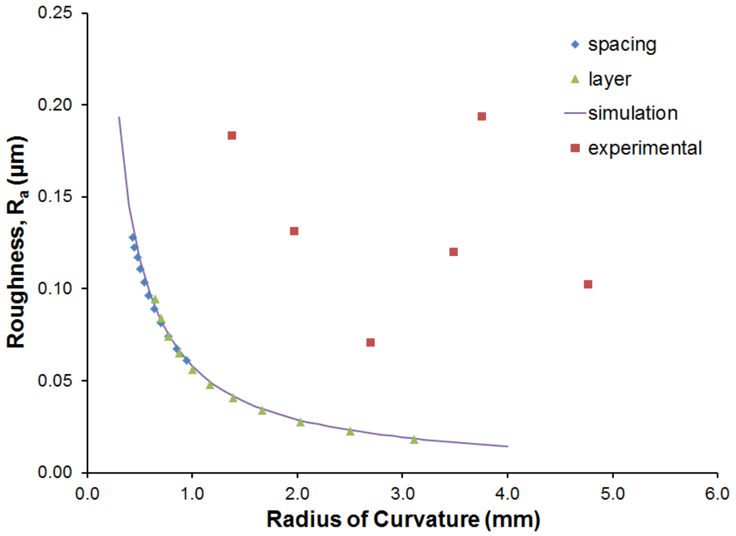

Figure 5.19 – Comparison of predicted and measured surface roughness as related to the surface curvature

The two simulation studies resulted in overlapping trends between the fibre spacing and the polymer layer above the surface fibres. As was predicted, a greater fibre spacing or a decreasing polymer layer tend to sharply increase the roughness and decrease the surface curvature. A fine curvature is undesirable as it implies that light hitting the surface will scatter and the fine features around surface fibres in a composite will be visible. This, for instance, causes the appearance of grooves in the surface after the paint application, and is not attractive to consumers.

The experimental data presented in Figure 5.19 is quite scattered. While the correct magnitude of roughness is attained from the optical measurements, the image resolution prevented the curvature from being accurately assessed. Therefore, two alternate methods were explored to determine their feasibility to generating accurate surface profiles of composite materials. A snapshot of each test method is presented; for the 3D laser scanning in Figure 5.20 and for the high resolution 3D optical scanning in Figure 5.21.

Laser scanning a surface requires that the surface reflect enough of the light for the detector to measure the time-of-flight accurately, and hence map the surface by rastoring the laser. The neat polymer caused too much light scatter to be measured without first gold-coating to increase the reflectivity. Figure 5.20a shows the result for a section of composite with three glass fibres embedded just below the surface. While the roughness can again be determined from this method accurately, the curvature measurement is very sensitive to a clean surface, which was impeded by the gold-coating operation.

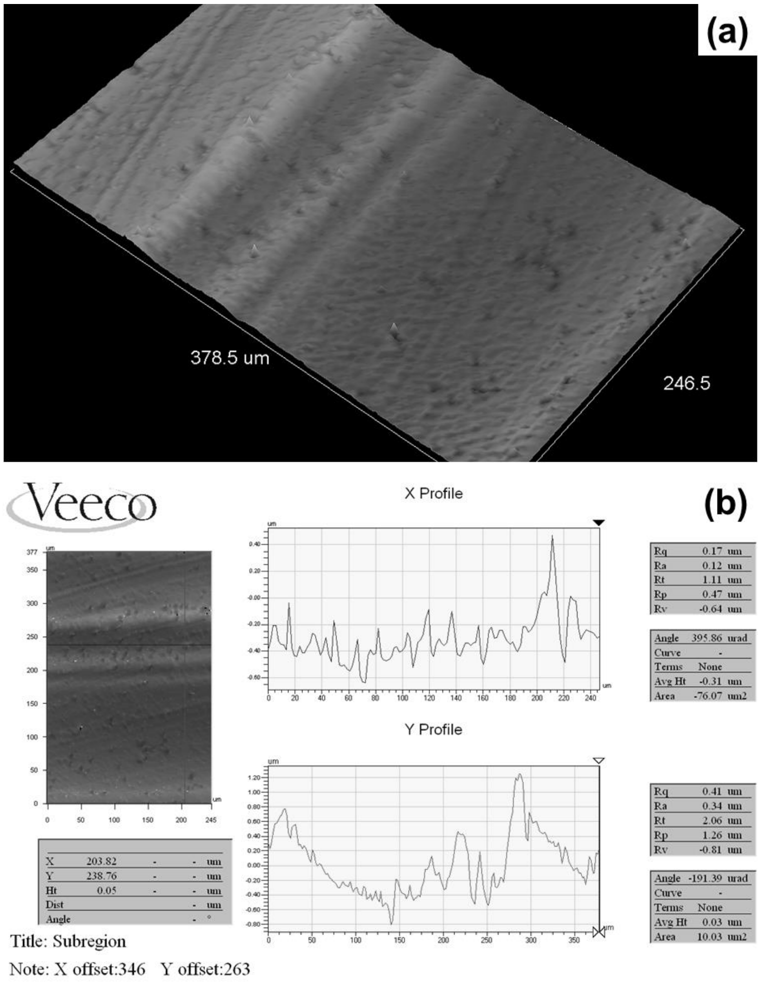

X	203.82	-	-	um
Y	238.76	-	-	um
Ht	0.05	-	-	um
Dist			-	um
Angle			-	°

Title: Subregion
Note: X offset:346   Y offset:263

Rq	0.17	um
Ra	0.12	um
Rt	1.11	um
Rp	0.47	um
Rv	-0.64	um

Angle	395.86	urad
Curve	-	
Terms	None	
Avg Ht	-0.31	um
Area	-76.07	um2

Rq	0.41	um
Ra	0.34	um
Rt	2.06	um
Rp	1.26	um
Rv	-0.81	um

Angle	-191.39	urad
Curve	-	
Terms	None	
Avg Ht	0.03	um
Area	10.03	um2

Figure 5.20 – 3D laser scanned profile map of glass / epoxy fibre surface

The optical scanning did not require gold-coating to be effective, but is here sensitive to proper surface calibration. Since the optical scanning requires a flat reference area to perform the lens distortion correction algorithms, and no flat surface was available on the tested sample, the result is a wavy image as in Figure 5.21a). From this present data, it was not possible to generate accurate roughness or curvature measurements to check against the simulated values.

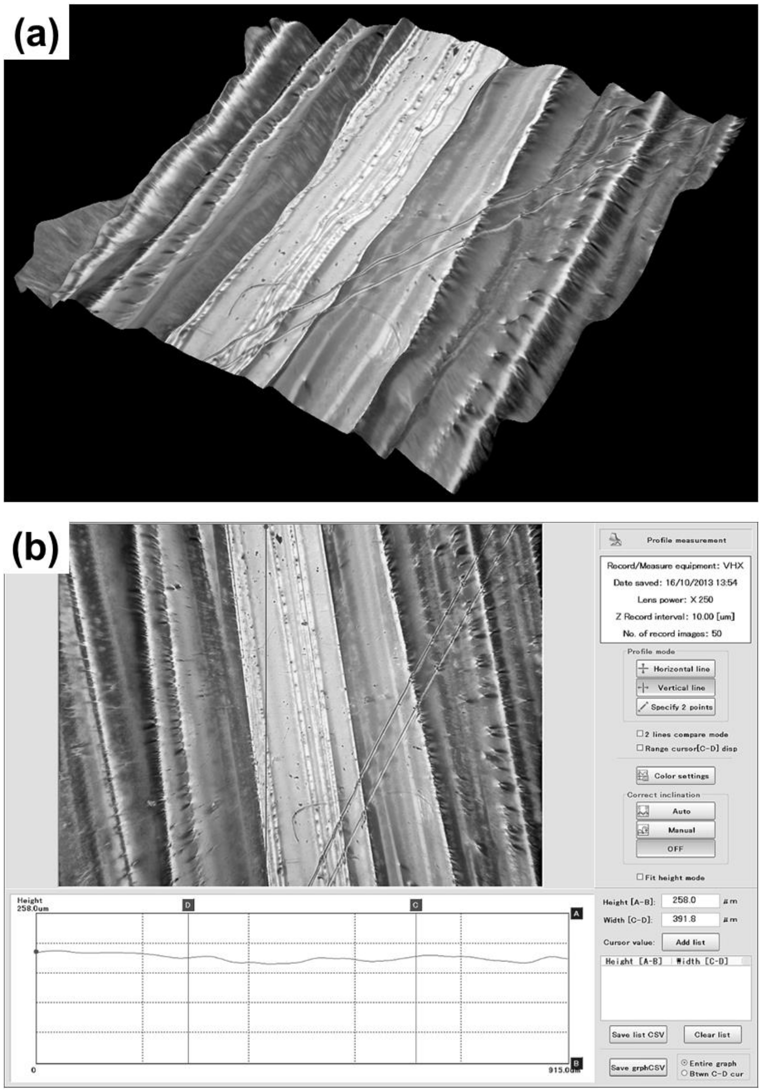

Record/Measure equipment: VHX
Date saved: 16/10/2013 13:54
Lens power: X 250
Z Record interval: 10.00 [um]
No. of record images: 50

Height [A-B]: 258.0 µm
Width [C-D]: 391.8 µm

Height [A-B]	Width [C-D]

Figure 5.21 – 3D optical profile map of glass / epoxy fibre surface

These techniques show much promise as experimental methods to vet the cure simulation, but require a dedicated study through which careful and systematic analysis can be conducted. It is concluded that it is possible with the present technology to measure the surface characteristics of a polymer composite if given enough time to determine the proper measurement setup parameters. It is also concluded that the composite model as presented is capable of predicting such phenomena as the surface roughness of a composite part. Future work could examine how a mould-wall might impact the surface quality and what steps are needed to produce a consistent class-A surface given the polymer and composite properties.

6 Applying Interfacial Failure

The crux of the research is hereby reached: adding interfacial strength into a composite material model to facilitate an accurate failure prediction. Two supporting experimental studies are used to demonstrate the application of the failure criterion on different material systems and to provide a measure of the accuracy of the criterion. The criterion is discussed in detail with comments toward its application, strengths, and outstanding areas for further research.

6.1 Interface-Modified Failure Criteria

There is always a challenge when beginning the discussion on material failure regarding where to start. While there is some utility in the historical perspective beginning with the pioneers in fracture, Griffith, Irwin, and Orowan, whole texts have already been devoted to the subject of fracture mechanics [124-126]. The equations of Westergaard describing the stress state around a crack, the process of determining a J-integral to determine the energetic favourability for a crack to advance, or analyzing stress magnification factors given notch geometries are considered mature fields. However, these fields have been advanced primarily for the common engineering materials, and there is a wide gap in understanding when it comes to composite materials which are microscopically heterogeneous. As was presented in the literature review, Chapter 2, there are multiple approaches possible to determining how a composite will fail, what constitutes failure, and predicting the failure of certain composite geometries.

By selecting the energy approach to failure, a composite can be described as a whole or as a sum of parts. If a top-down approach is taken, whereby a composite is thought of as a macroscopically homogenous material with a given unit cell, then bulk testing of the composite will yield failure data related to the specific formulation properties which were used to create that material. This approach is useful for characterizing an individual material where fracture needs to be measured, but not understood. No consideration is needed toward the different fracture mechanisms, but neither does the result allow for predictive capability. At most, testing multiple composite formulations will only ever yield an empirical relation or rules-of-thumb between the type and magnitude of failure.

Conversely, a bottom-up approach examines the associated energy with each mode of failure. This approach requires substantially more up front effort to isolate and measure individual failure modes, but allows modes to be combined in such a way as to predict failure given a loaded geometry. Here failure modes can be effectively ignored if their magnitude is small or combined to build the overall observed failure in a composite. Consider first the standard fracture toughness relation which says that the critical fracture toughness of a material is directly related to the Young's modulus and the critical strain energy release rate (CSERR) under a plane stress condition:

$$K_c = \sqrt{EG_c} \tag{6.1}$$

The plane stress formulation is considered as most composites are thin-walled in nature, resulting in negligible through-thickness stress during the propagation of a crack. For mixed-mode loading, this typically gets subdivided into the different fracture components for each mode and requires some assumption regarding the type of failure to combine the failure modes. For an arbitrary composite, the modulus is dependent on the homogenization scheme used to combine the elastic properties of the fibre and matrix. Here, the fibre geometry and spatial arrangement within the matrix are required. The strain energy release rate, which is based on the energy required for a crack to move, requires the same fibre knowledge but also knowledge about any and all mechanisms which consume this energy, such that:

$$G_c = G_{matrix} + G_{fibre} + G_{interface} + \ \dots \tag{6.2}$$

From Equation 6.2 it is evident that combining two materials is not a simple combination of deformation mechanisms. Other mechanisms not listed include fibre kinking or buckling, fibre twist and pullout, and delamination. With the exception of the fibre strain energy release rate, all are (at least) partially (or fully) based on the matrix material which has already been shown to be non-linear in nature. Additional consideration must be made for the effects of hydrostatic pressure (which can suppress certain failure modes), residual cure and thermal stress, edge effects (geometric starting points for failure), manufacturing method (fibre stacking and/or matrix distribution), and statistical effects, among others. Further, what constitutes failure, or when these predictions become important to composite modeling is crucial. Some possible descriptions of failure in a composite include:

- The stress at which the first fibre break occurs
- The stress at which a loss of load carrying capacity occurs
- The onset of micro-cracking in the matrix
- The point at which micro-cracks coalesce
- A given departure from linear behaviour

A recent trend in composite failure modeling is to give bounds to failure by predicting a damage initiation point and an ultimate failure point [8], though there is still no agreement on how these points should be defined. Given the discussion thus far, it is an understatement to say that composite failure is a complicated phenomenon.

To best contribute to the understanding and prediction of failure several assumptions will be made to bound the analysis and give shape to the developed theory. First, only positive, biaxial loading will be considered. While this immediately discards compressive failure modes and certain rare loading cases, this does account for the majority of composite design scenarios. Next, as the focus is on random fibre composites, fibres will not be assumed continuous throughout the structure and fibres will be assumed to have a uniform spatial and angular distribution. Further, these composites will be assumed as planar such that fibres will be considered to reside in a plane parallel to that of the composite so that the composite could be decomposed into individual lamina of randomly oriented fibres with identical volume fractions. Also, this model will assume room temperature and quasi-static behaviour, as no effort is made to incorporate strain-rate phenomena.

Before discussing all the effects of these assumptions, the model will be built up considering several initial composite geometries and presenting the relevant failure. Afterward, it will be possible to revisit these assumptions and examine if they were necessary or what steps would be needed to use the model without making these assumptions in the first place.

6.1.1 Case I: The Neat Polymer

The first geometry is a neat, isotropic polymer. In this ‘composite’, there is no reinforcing phase thus the composite failure is simply the polymer failure:

$$G_c = G_{matrix} \tag{6.3}$$

where the matrix is proportional to some function of the global loading mode. Depending on the matrix behaviour, there are many schemes to combine the mode I and mode II critical strain energy release rates in mixed mode loading, as shown in Figure 6.1.

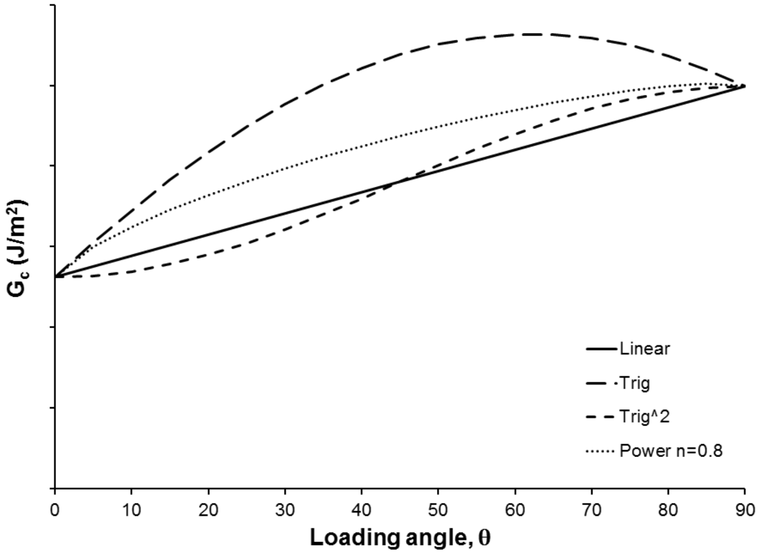

Figure 6.1 – Total strain energy release rate for neat epoxy as a function of loading angle which describes the ratio of normal to shear loading.

The four mixed mode schemes presented in Figure 6.1 correspond to the following relations for the Linear, Trig, Trig^2, and power laws respectively in Equations 6.4-6.7:

$$G_{matrix} = G_{Ic,m}\left(1 - \frac{\theta}{90°}\right) + G_{IIc,m}\left(\frac{\theta}{90°}\right) \tag{6.4}$$

$$G_{matrix} = G_{Ic,m} \cos\theta + G_{IIc,m} \sin\theta \tag{6.5}$$

$$G_{matrix} = G_{Ic,m} \cos^2\theta + G_{IIc,m} \sin^2\theta \tag{6.6}$$

$$G_{matrix} = G_{Ic,m}\left(1 - \frac{\theta}{90°}\right)^n + G_{IIc,m}\left(\frac{\theta}{90°}\right)^n \tag{6.7}$$

where $G_{Ic,m}$ and $G_{IIc,m}$ are the CSERR for mode I and mode II loading of the matrix. This assumes that a given load can be decomposed into the normal and shear components of loading and separately applied to their individual contributions to failure. Jamali [127], found that Equation 6.6 provided the best fit to the experimental data for the previously selected epoxy matrix. This does not suggest that all polymers will follow this relation, but rather that the versatility of the failure model can accept different types of polymer failure criteria. It is expected, however, that the mode II CSERR will generally be larger in magnitude than the mode I CSERR for most polymer systems. Bruce [96] demonstrated a mechanistic model to explain an observed connection between the mode I and mode II CSERRs as:

$$G_{IIc,m} = \left(1 + \sqrt{2}\right) G_{Ic,m} \tag{6.8}$$

which arises due to the fact that cracks formed during shear loading propagate under a mode I load. Thus the mode II critical strain energy release rate need only account for this increased crack length. Combining Equation 6.6 and Equation 6.8 yields the matrix CSERR as a function of the mode I critical strain energy and the global loading mode:

$$G_{matrix} = G_{Ic,m}\left(\cos^2\theta + \left(1 + \sqrt{2}\right)\sin^2\theta\right) \tag{6.9}$$

This means that the failure of a neat polymer can be predicted given only knowledge of the mode I strain energy release rate. Though initially considered as a neat polymer, one modification is made to Equation 6.3 to account for any fillers:

$$G_c = G_{matrix}\eta_\phi \tag{6.10}$$

where

$$\eta_\phi = 1 - v_{fillers} \tag{6.11}$$

and $v_{fillers}$ is the volume fraction of fillers. This assumes that the addition of fillers to a polymer is homogeneous, does not change the primary fracture mode of the polymer, that the fillers only act to decrease the polymer strength (non-bonding), and that no change to the plastic radius of the matrix occurs.

6.1.2 Case II: Simple Reinforced Polymer

Now that the matrix has been described void of fibres, a small amount of reinforcement is added to the matrix to consider how this would affect failure. In this case, “fibres” with an aspect ratio of unity are added to the matrix. The aspect ratio, s, is defined as the length of a fibre divided by its diameter. With an aspect ratio of one, this reinforcement could also be viewed as a spherical reinforcement. To account for the addition, the composite failure criteria, Equation 6.10, is extended as:

$$G_c = G_{matrix}\eta_\phi\eta_p\eta_m + G_{interface}\eta_\phi\eta_i \tag{6.12}$$

where the added correction factors η_m and η_i are the ratio of matrix area to fracture area and interface area to fracture area respectively. Equation 6.12 also includes a factor η_p to describe the reduced plastic zone size of the matrix ahead of a crack. The same filler correction is applied to the interface and the same non-bonding assumption is made that the filler does not contribute to strength at the interface. Since there is not any shear stress transfer to the reinforcement, no term is added for the failure of the reinforcement. This assumes that the matrix is weaker than the reinforcement, which it is for most polymer composites. Consider then a crack approaching a spherical reinforcement surrounded by matrix as in Figure 6.2.

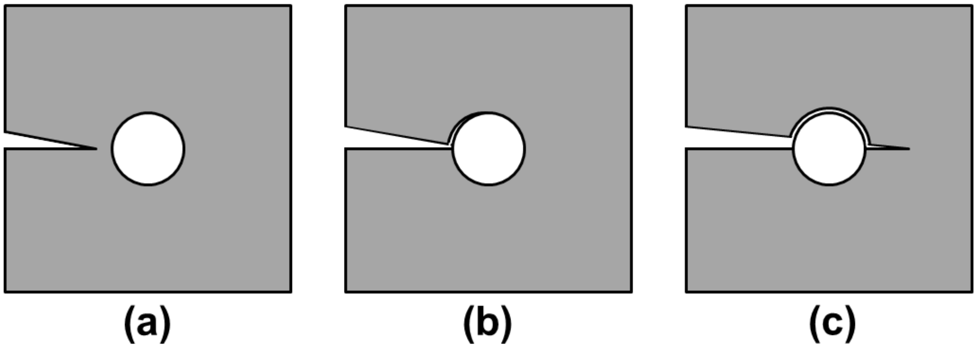

Figure 6.2 – Side view of a crack approaching a spherical particle showing a) before the crack reaches the particle b) the partial debonding of the particle and c) the crack moving past the debonded particle.

As has already been discussed, cracks in a polymer open under a mode I loading. Thus if a spherical particle were to be in the path of such a crack, it too would experience a normal load. The only location for shear to build up on such a particle is at the equator of the embedded particle, which is small considering the surface area of the sphere. Had the crack been slightly below the equator, the debond would have progressed along the shorter path, below the particle, in a horizontal mirror image of Figure 6.2c). In this case, the interfacial strain energy release rate needs only to consider the normal component of the interface CSERR and the areal correction is only related to the normal interfacial area ratio:

$$G_{interface} = G_{Ic,i} \tag{6.13}$$

$$\eta_i = \eta_{i,n} \tag{6.14}$$

With these reinforcements added, some method is needed to describe their dispersion within the matrix. The volume fraction is an obvious choice, but does not directly relate to an areal dispersion. Therefore, two planar packing geometries are considered, as shown in Figure 6.3, to relate the volume fraction to the area ratios.

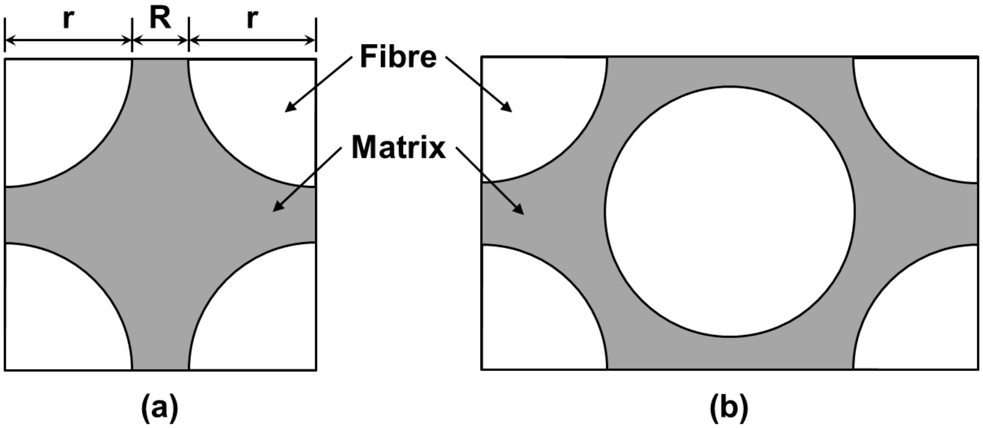

Figure 6.3 – Planar packing unit cells of both the a) square and b) hexagon.

From Figure 6.3a), ‘r’ is the radius of the reinforcement and ‘R’ is the separation distance. The values of R for square and hexagonal arrays have long been known since the first proof by Axel Thue in 1890 [128]:

$$R_{sq} = 2r\left(\sqrt{\frac{\pi}{4v_f}} - 1\right) \tag{6.15}$$

$$R_{hx} = 2r\left(\sqrt{\frac{\pi}{2\sqrt{3}v_f}} - 1\right) \tag{6.16}$$

where v_f is the volume fraction of fibres and r is the fibre radius. The previous assumption of randomly distributed fibres is at odds with the use of a unit cell to describe the spatial orientation. These geometries are, however, useful to relate the volume fraction to an areal distribution in the ideal sense to provide a mechanistic upper bound to failure. In a real composite, the areal distribution could be obtained via metallographic techniques and these relations would not be needed, but that would eliminate the predictive ability of this method. These ideal cases will provide the theoretical trends needed to form the model, while allowing for future modification if better unit cell representations are devised.

Now that the volume fraction can be related to an areal distance, it is possible to calculate the corrections for the relative areas of matrix and interface present during fracture. The additional factors η_m and $\eta_{i,n}$ from Equation 6.12 and Equation 6.14 respectively are the corrections to relate the area of fracture due to the given phenomena to the total area of fracture. This is easily simplified with relation to a unit cell area and is presented for hexagonal packing as:

$$\eta_m = \frac{A_{matrix}}{A_{unit\ cell}} \tag{6.17}$$

$$\eta_{i,n} = \frac{A_{normal\ to\ reinforcement}}{A_{unit\ cell}} \tag{6.18}$$

Analytical relations for these and all the correction factors are fully described in Appendix C for both the hexagonal and square unit cells. The other factor not yet described, η_p, is the ratio of the reduced plastic zone size due to the stiff embedded reinforcement, and is calculated as the ratio of the plastic zone in the constrained composite to that of the neat matrix:

$$\eta_p = \frac{r_{p,constrained}}{r_{p,neat}} \tag{6.19}$$

where the neat plastic radius is calculated as:

$$r_{p,neat} = \frac{E_m G_{Ic,m}}{2\pi\sigma_{y,m}^2} \tag{6.20}$$

The neat plastic radius is calculated from a plane stress condition using the matrix modulus, yield strength and mode I CSERR.

6.1.3 Case III: Random, Short-fibre Reinforced Polymer

The next step up from a spherical-reinforced polymer system is a short fibre system where the length of the fibre is less than the critical length required for complete stress transfer from the matrix to the fibre. The implication being that no matter the fibre orientation, the fibres will never fracture. The updated composite failure criterion is presented in Equation 6.21:

$$G_c = G_{matrix}\eta_\phi\eta_p\eta_m + G_{interface}\eta_i\eta_\phi + G_{pullout}\eta_o f(\varphi) \tag{6.21}$$

For reference, the fibre critical length, calculated using the shear lag model [46, 129], is given by:

$$l_c = \frac{3}{16}\frac{r\sigma_f^*}{\tau_i} \tag{6.22}$$

From Equation 6.21, the interface will now utilize both the normal and shear components, another term is added for the extra energy associated with pullout, and a function is implemented to describe the fibre orientations with respect to the applied load. With fibre aspect ratios greater than unity, additional assumptions are required for this analysis. Initially with spherical reinforcements a uniform spatial distribution was assumed, whereas an additional uniform angular distribution is now also assumed with the fibres. The short fibre requirement assumes that the initial crack path remains matrix-dominated. This means that if a crack were to approach an angled fibre, the crack would not change direction to follow the fibre, similar to the crack progression in Figure 6.2. However, what is important is recognizing that fibres at different angles to a crack (and hence the applied load) will have different impacts to the interface debond mode and subsequent pullout, as depicted in Figure 6.4.

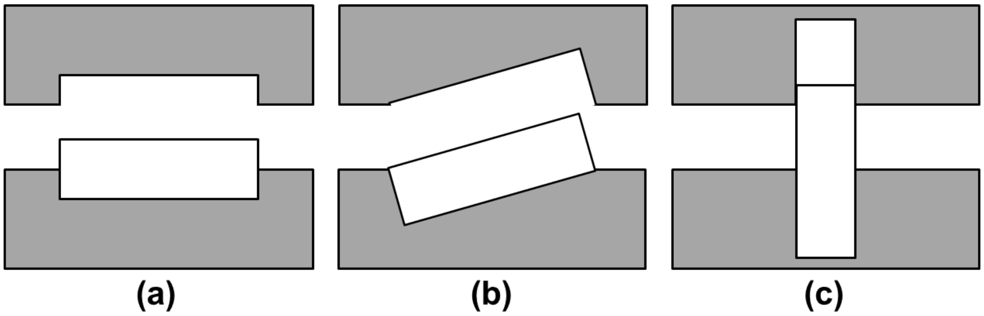

Figure 6.4 – Three crack scenarios when a fibre is a) aligned to the crack plane b) low-angled to the crack plane c) high-angled to the crack plane.

In Figure 6.4a), if a crack is running through the matrix and encounters a fibre aligned to the crack plane, then similar to the spherical case, only a normal debond is considered. A low angled fibre, as in Figure 6.4b) now requires that both the shear and normal components of interfacial debond be considered, but no pullout. If a crack encounters a fibre at a high angle (shown perpendicular in Figure 6.4c) then in addition to the interfacial considerations, the pullout work of friction must be considered. Similar to the critical fibre length issue for load transfer, there now exists a critical fibre angle above which fibre pullout is present. To further complicate the issue, an approaching crack will not always meet an embedded fibre at its midpoint, so there will be a distribution of lengths which must also be considered. It is assumed, however, that this problem can be treated as symmetric in the sense that a fibre with a positive angle has the same effect as a fibre with a negative angle of the same magnitude with respect to the crack plane.

Similar to how the toughness of the matrix could be described by a mixed-mode relationship based on loading angle, the interface can also be decomposed into its loading components based on fibre angle. From the work in Chapter 4, a linear relationship between the mode I and mode II interfacial CSERR is used. Further, a similar simplification that applied to the matrix is possible by assuming a link between the mode I and mode II interfacial CSERR values as:

$$G_{IIc,m} = 2G_{Ic,m} \tag{6.23}$$

This simplification is done primarily as a means of expressing the interfacial failure entirely in terms of the shear interfacial debond, as this is the most often reported value for fibre composites and the easiest to determine. Thus, the interfacial term from Equation 6.21 becomes:

$$G_{interface} = G_{IIc,i}\eta_i\eta_\phi \tag{6.24}$$

where

$$\eta_i = \frac{\eta_{i,n}}{2} + \eta_{i,s} \tag{6.25}$$

The subscripts in Equation 6.25 indicate the areal correction due to the normal and shear components of interfacial debond. In the area ratios, no fibre angle is specified as the uniformity assumption allows a straight average between their minimum and maximum values. If the distribution of fibres was known (and not uniform), then an integration would be necessary to sum the contributions of all fibres at each angle to the unit area.

The pullout CSERR is calculated from the origin of G = dU/da, where dU is the change in energy and da is the change in area. The energy, U, is the work due to friction over a given distance, U=μFl_p, where μ is the dynamic coefficient of friction, l_p is the length of pullout, and the normal force F is the pressure acting on the pullout area. If the assumption is made that any fibre being pulled-out is completely pulled-out, then the pullout area is the same as the change in area. Thus the pullout CSERR is:

$$G_{pullout} = \mu P l_p \tag{6.26}$$

The coefficient of friction between many polymers and different fibre surfaces has received some attention so there is already data available for different composite systems [94, 130]. The residual stress follows directly from the polymer simulations of Chapter 5. The ratio of pullout area to unit cell area currently takes on an identical form to that of the interfacial shear area, though this will change during the next case when the fibre length is increased. Since the length of fibres in this case is limited to less than the critical length, the pullout length will always be limited to half the critical length.

The last new addition to the model, $f(\varphi)$, is a function describing the effect of fibres at each angle φ to the loading angle on the pullout energy. Even if a fibre is exactly perpendicular to the crack path, as in Figure 6.4c), there will still be a statistical distribution of pullout lengths ranging from half the fibre pullout length to zero. The current function presented as Equation 6.27 has the desired boundary conditions, but is purely empirical:

$$f(\varphi) = \sum_{\varphi=0}^{\pi/2} \frac{\cos^2\varphi\,(1-\sin^2\varphi)}{4} \tag{6.27}$$

With a better knowledge of the actual fibre distribution, this function is expected to be improved. Other models have been proposed to account for the fibre distribution, but are also empirical and considerably more complicated [131, 132]. Further, if the actual distribution of fibre angles is known to be non-uniform, then this function should include the pullout CSERR such that the sum of the contributions at each angle is computed rather than just the contribution fraction.

6.1.4 Case IV: Random, Long-fibre Reinforced Polymer

At last is reached the long, random fibre-reinforced polymer failure criterion:

$$\begin{aligned} G_c = {} & G_{matrix}\eta_\phi \eta_p \eta_m \left[1 + f(\varphi)v_f\right] + G_{interface}\eta_i \eta_\phi \\ & + G_{pullout}\eta_o f(\varphi) + G_{fibre}\eta_f f(\varphi) \end{aligned} \tag{6.28}$$

Since the fibre length is greater than the critical stress transfer length, fibre breakage is included as well as a crack-path extension. Fibres are still assumed to break perpendicular to their longitudinal axis so the area fraction calculation is straightforward, though only a fraction of fibres are expected to break – the same fraction as is also pulled out. The crack path extension suggests that the same fraction of fibres that affect the fibre and pullout modes incur a penalty to the total length of the matrix crack dependent on the volume fraction of fibres. So, a highly fibrous composite will see a jagged crack as compared to a lower volume fraction composite of the same materials.

Though not yet stated, it is assumed that fibre debonding and pullout are separate phenomena. Though there might be some link between the interfacial debond length and the pullout length, this model treats these as separate. The reasoning is best illustrated in Figure 6.5 depicting three scenarios for a crack approaching a fibre.

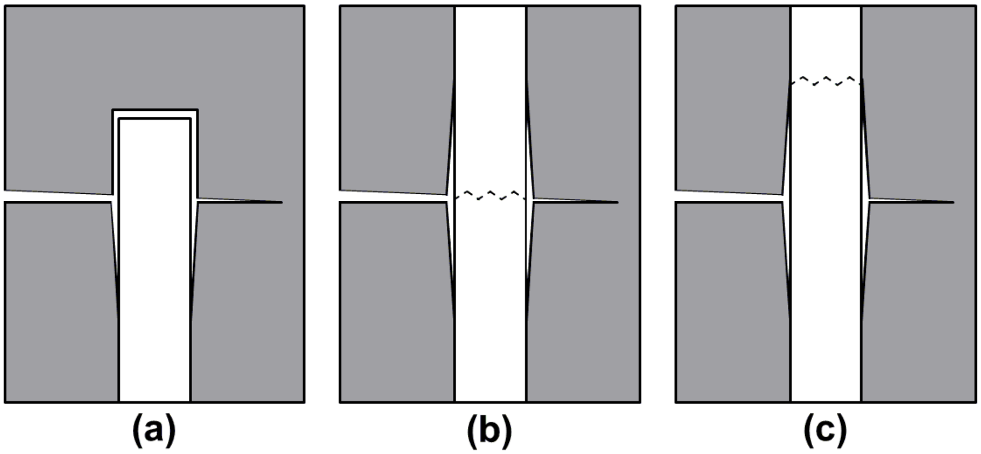

Figure 6.5 – Crack approaching a perpendicular fibre which experiences a) debond and pullout b) debond and fracture c) debond, fracture and pullout

In Figure 6.5a), a crack approaches a prostrate fibre causing shear debonding along the fibre until one of the fibre ends is reached. Here, the fibre does not fracture, and the debond length is longer than the pullout length as the debond partially extends below the crack plane similar to [74, 131]. From Figure 6.5b), the same crack approaches a fibre that extends above and below the crack plane a length greater than the critical stress transfer length suggesting the fibre is likely to fracture rather than pull-out. If the fracture location occurs near the crack plane, then there will be no pullout length despite the debond and fibre breakage. The final frame in Figure 6.5c) depicts a scenario where all three mechanisms are present; note that the fibre pullout length is still less than the fibre debond length. Extending this logic to all effective fibre angles for fracture and debond suggests that the debond length will always be equal to or greater than the pullout length.

Up to this point, a strong, but not perfect interface has been assumed. In reality, there will be three possible interfacial strength scenarios which will change how a failure model like Equation 6.28 will behave. In the first instance where the interfacial shear strength is between the yield and tensile strength of the matrix, $\tau_{y,m} < \tau_i < \tau_{ts,m}$, everything will be as presented. If the interfacial shear strength is less than the yield strength of the matrix, $\tau_i < \tau_{y,m}$, then the interface will debond around fibres long before substantial matrix plasticity can take place. This would require a degradation of the matrix critical strain energy release rates depending on magnitude of the difference and an increase to the debond length around fibres. If, however, the interfacial shear strength were greater than the matrix tensile strength, $\tau_{ts,m} < \tau_i$, then debonding would be suppressed. Not only would the interface CSERR tend to zero and would be replaced by a longer matrix crack length, but the pullout frictional coefficient would need to change to reflect a roughened matrix-on-matrix value rather than matrix-on-fibre.

6.1.5 Case V: Delamination

So far, the types of failure have all suggested that a crack will move transverse to the material plane. However, this same criterion is capable of predicting an in-plane failure such as delamination. Delamination is essentially matrix and interfacial failure with neither fibre failure nor pullout, shown in Figure 6.6.

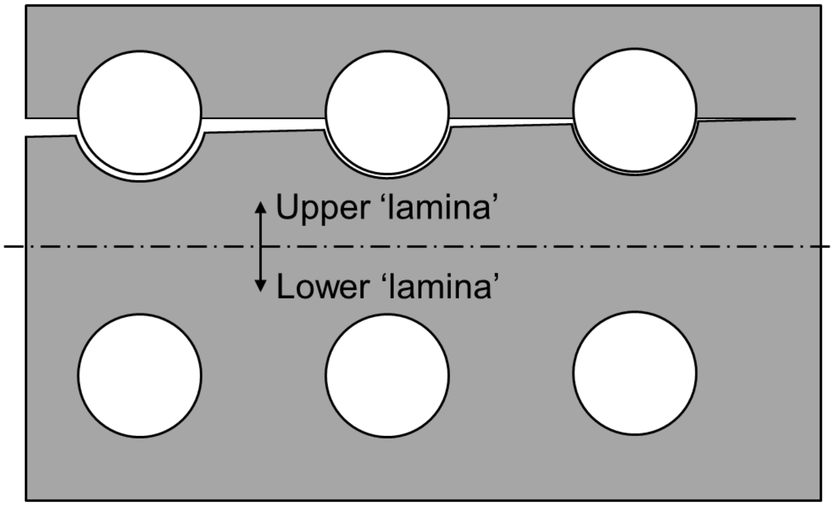

Figure 6.6 – Idealized delamination in a long-fibre composite.

The picture of delamination shows the idealized case where fibres, viewed end-on, are parallel to each other, but perpendicular to an advancing crack. The critical assumption being that the composite is indeed planar so that the composite could be decomposed into individual lamina of randomly oriented fibres with identical volume fractions, as previously stated. From Figure 6.6, the fibres do not need to actually align parallel to each other for this criterion to apply, and was only drawn this way to demonstrate the average, ideal case. Here, the composite failure reduces to terms similar to the simple reinforced composite case:

$$G_c = G_{matrix}\eta_\phi \eta'_p \eta'_m + G_{interface}\eta_\phi \eta'_i \qquad (6.29)$$

where the factors with the prime, $'$, symbol indicate a modification. The volume fraction gives rise to the average fibre separation, which in turn gives rise to the values for η'_m and η'_i for this planar case, and are also elucidated in Appendix C.

The plastic radius ratio also needs to be changed to account for the difference in crack propagation geometry. In the resin-rich layer between the idealized lamina, the plastic radius is larger than in the fibre / resin side of failure, though both are still smaller than would be expected from the neat polymer. To account for this increased radius, an average is taken such that the resin rich side is allowed to have double the plastic radius of the constrained fibre side:

$$\eta_p' = \frac{3\eta_p}{2} \tag{6.30}$$

If this model were to be applied to the delamination of a fabric laminate composite then the plastic radius would need to change to account for the fabrication pressure. To more rigorously predict the plastic radius reduction, the individual lamina thickness and weight without resin would be required to determine the expected resin-rich layer thickness.

6.1.6 Case VI: Non-uniform or Aligned Long-fibre Composite

The model presented in Section 6.1.4 made the assumption that fibre angles were uniformly distributed. However, in a practical industrial composite, there is always expected to be some preferential fibre alignment. In some injected-moulded composites, there might even be complete alignment in sections of a composite part where fibres were able to align to the mould-filling direction. Further, if given the functions for the volume fraction distribution and fibre angle distribution it would be highly advantageous to predict the corresponding distribution of composite strength and toughness. To do so, the composite model will not be permitted to take advantage of the uniform angular distribution assumption and must provide complete terms for all the energy mechanisms. To illustrate the extreme cases, Figure 6.7 shows the four cases of either normal or shear loading for either vertically or horizontally aligned long fibres.

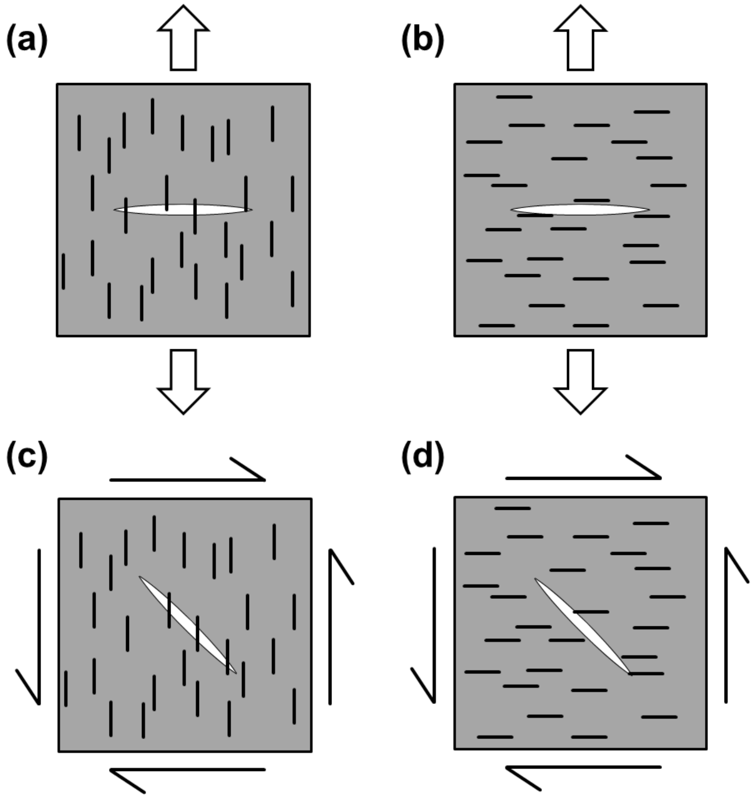

Figure 6.7 – Extreme fibre alignment cases under (a-b) normal loading and (c-d) shear loading.

Where a normal load is present, the failure has already been captured with ratios of fibre and interfacial debonding. The challenging case to predict, Figure 6.7 (c-d), is when the composite experiences a shear load and the fibres bridging the matrix crack plane experience a combined normal and shear load. With a uniform fibre spatial distribution both Figure 6.7c and Figure 6.7d result in identical loading on the fibres, matrix, and interface. To account for this shear loading case, the interface, pullout, and fibre failure are all reconsidered with respect to the principle stress direction using the well-known Mohr's circle approach:

$$\begin{aligned} G_c &= G_{Ic,m}\left(\cos\theta + \left(1+\sqrt{2}\right)\sin\theta\right)\eta_\phi\eta_p\eta_m\left[1+f(\varphi)v_f\right] \\ &\quad + G_{IIc,i}\eta_\phi\left(\frac{\eta_{i,n}}{2}\tan\left(\frac{\pi/2-\varphi}{2}\right)+\eta_{i,s}\tan\frac{\varphi}{2}\right) \\ &\quad + G_{Ic,f}\eta_o f(\varphi)\tan\frac{\varphi}{2} + G_{Ic,f}\eta_f f(\varphi)\tan\frac{\varphi}{2} \end{aligned} \tag{6.31}$$

where again, φ is the angle between the loading direction and the fibre alignment. This represents the ultimate version of the composite failure model, capable of describing the many failure modes and composite types as presented. Even though the composite is still functioning as a long-fibre composite, by now it should be evident that this model can be extended to continuous-fibre composite as the only outstanding phenomena to predict are fibre fracture length and change to the crack path due to fibre alignment. The reduced form of all the correction factors is presented in Table 6.1 for both the hexagonal and square packing assumptions from Appendix C.

Table 6.1 – Area correction factors for both square and hexagonal fibre packing.

Area ratio	Sym.	Square packing	Hexagonal packing
Matrix	η_m	$1-\frac{\pi r(3r+R)}{(2r+R)^2}$	$\frac{\left(12-\sqrt{3}\pi-2\pi\right)r^2-(\pi-12)rR+3R^2}{3(2r+R)^2}$
Matrix radius	η_p	$\frac{3(2r+R)}{2r_p}$	$\frac{\sqrt{3}(2r+R)+R}{2r_p}$
Normal interface	$\eta_{i,n}$	$\frac{\pi r(3r+R)}{2(2r+R)^2}$	$\frac{\pi r\left(\sqrt{3}r+2r+R\right)}{3(2r+R)^2}$
Shear interface	$\eta_{i,s}$	$\frac{\pi r l_d}{4(2r+R)^2}$	$\frac{2\sqrt{3}\pi r l_d}{9(2r+R)^2}$
Pullout	η_o	$\frac{\pi r l_p}{2(2r+R)^2}$	$\frac{4\sqrt{3}\pi r l_p}{9(2r+R)^2}$
Fibre	η_f	$\frac{\pi r^2}{2(2r+R)^2}$	$\frac{\pi r^2}{\sqrt{3}(2r+R)^2}$
Filler	η_ϕ	$1-v_{fillers}$	

This model consists of fifteen independent mechanical properties, fewer if property models are adopted, to mechanistically predict the composite strain energy release rate for a long-fibre composite subjected to positive loading. Processing effects are captured by way of fibre orientation, volume fractions and residual stress. The bonding characteristics using the interfacial strength and strain energy release rate are incorporated into this model. The CSERR values represent real mechanical properties, and all the corrections are based on physical and geometric phenomena. Though some simplifications to the matrix and interface fracture were expressed, they are not required, and hence this model is fully predictive without empirical variables or constants.

6.2 Discussion and Application of Failure Criterion

To better understand how this failure criterion operates, a sensitivity analysis and comparative studies were undertaken. All the presented curves represent a random fibre distribution for a glass / epoxy composite, whose values can be found in Table 6.2.

Long fibre composite fracture was assumed to be matrix controlled. This does not mean that the matrix contributes the most to the fracture toughness, but rather that the crack path will follow from the fracture of the matrix. The reason the matrix does not contribute much to fracture is highlighted in Figure 6.8 indicating the area fraction corrections for the matrix.

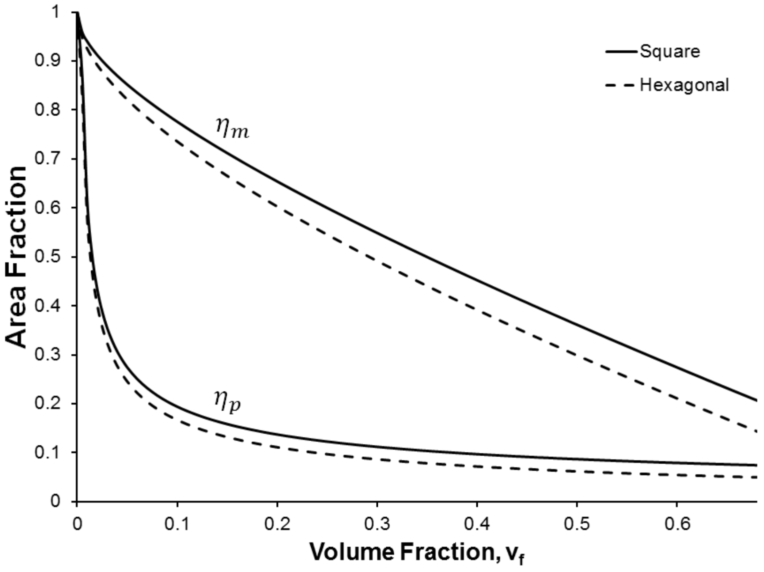

Figure 6.8 – Matrix correction factors as a function of volume fraction for both square and hexagonal unit cell formulations.

As the volume fraction increases, the area fraction of the matrix is steadily decreasing. More importantly, though, is the reduction in plastic radius which dramatically reduces the amount of plastic deformation of the matrix. Together, these reductions act to completely inhibit the composite toughness stemming from the matrix deformation. This effect is better presented in Figure 6.9 showing the contributions to toughness from the different mechanisms.

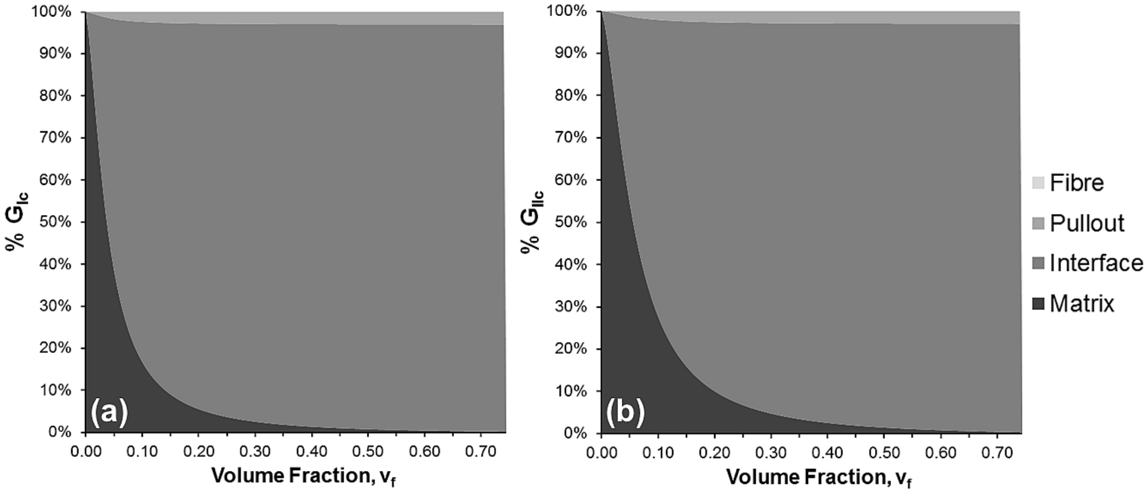

Figure 6.9 – Matrix CSERR component breakdown for a) pure mode I and b) pure mode II loading using the hexagonal unit cell.

Figure 6.9a) presents the pure mode I toughness as a function of volume fraction, while Figure 6.9b) presents the same breakdown for mode II. In both cases, as the volume fraction increases, the matrix contribution rapidly decreases. Using the brittle glass fibre results in a near-zero contribution to toughness by way of the fibre fracture. What the fibre does contribute is an interface which can be debonded and pulled out of the matrix. This interface is seen to contribute to the majority of the composite toughness at volume fractions above 10%. Interestingly, in the present model, the pullout does not substantially contribute to the overall composite toughness. This suggests that if the matrix and fibre are both brittle, then the composite toughness could be approximated using only knowledge of the interface and fibre length and distribution. Another observation is that by using a brittle fibre, such as carbon or glass, the fibre toughness can be ignored; this would not be the case with a ductile fibre, such as an aramid, where the fibre toughness may contribute a greater amount to the composite toughness.

Another way to examine the model is to plot the total composite toughness as a function of the loading mode, as in Figure 6.10. Here, as the volume fraction increases, the matrix deformation is suppressed, and the overall toughness reduces to a near constant. This makes sense as the various toughening mechanisms are more related to the distribution of fibres than the matrix plasticity. If the distribution is truly random, then the toughness in mode I and mode II loading should approach equality.

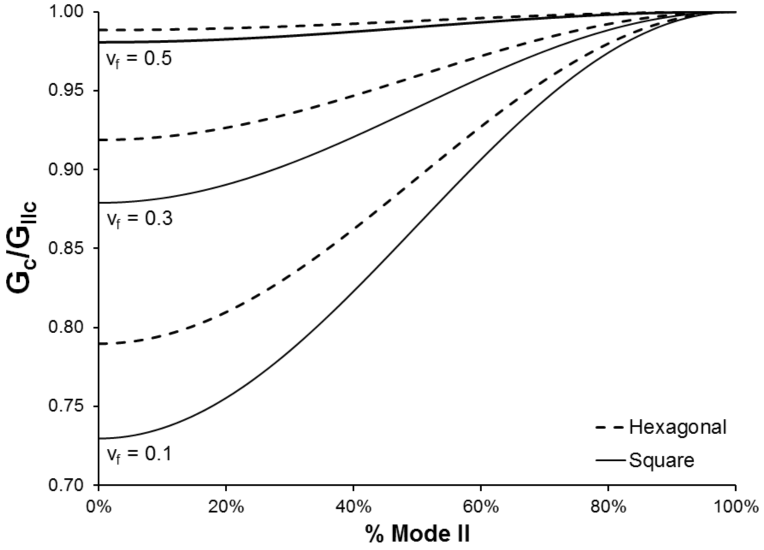

Figure 6.10 – Normalized random-fibre composite CSERR as a function of loading mode for several volume fractions using both the square and hexagonal unit cells.

The biggest single factor in the whole model is the calculation of the critical fibre length. This value, as calculated from Equation 6.22, is a constant related to the ideal stress transfer from the matrix onto a single fibre and drives the calculation for both the debond length and pullout length. However, in a composite where the fibre separation is less than the distance required for single-fibre stress transfer to occur, R < 10r, then the fibre interaction can cause multiple small diameter fibres to behave like one larger diameter fibre. Bruce [96] recognized this by relating this behaviour to the number of embedded fibres for a fragmentation test. In the present model, this relation will not work, as fibres can be disperse and not all nearest fibres will cause this shielding action. Currently, no correction is made to increase the critical fibre length to account for this interacting fibre behaviour. The result of such a correction would be to increase the energy due the work of pullout and consequently would also increase the interfacial debond length. Moreover, many industrial fibres are twisted together during their manufacture. If this twist is applied to the fibre early in production such that it retains this geometry then fibres can have additional mechanical linking between fibres; notably the carbon fibre as presented in Chapter 4. This mechanical increase to the pullout energy is also not accounted for in the current model, as there was no basis to form an estimate of this mechanical strengthening. Together, these issues describe the true critical fibre length and warrant further study to refine the prediction of long fibre composites toughness.

One further prediction regarding these random long fibre composites is the prediction of the composite Young's modulus. This was accomplished using the work of Hashin-Shtrikman and averaging the upper and lower bounds their theory describes [56] as per Equation 2.25 through Equation 2.27.

Together, the predicted composite toughness and composite modulus are plotted in Figure 6.11, where the toughness is shown for pure mode I and pure mode II loading separately. This graph essentially predicts the composite critical stress intensity factors for both modes of loading with Equation 6.1. Interestingly, the composite modulus initially drops with small volume fractions of fibres as there is not enough interface to balance the loss of matrix toughness. This supports the notion that a minimum volume fraction is required to realize toughness gains from a random-fibre composite over the neat polymer. Further, as the volume fraction increases, the CSERR for mode I and mode II converge to a common value which is also supported by the prior random fibre assumption.

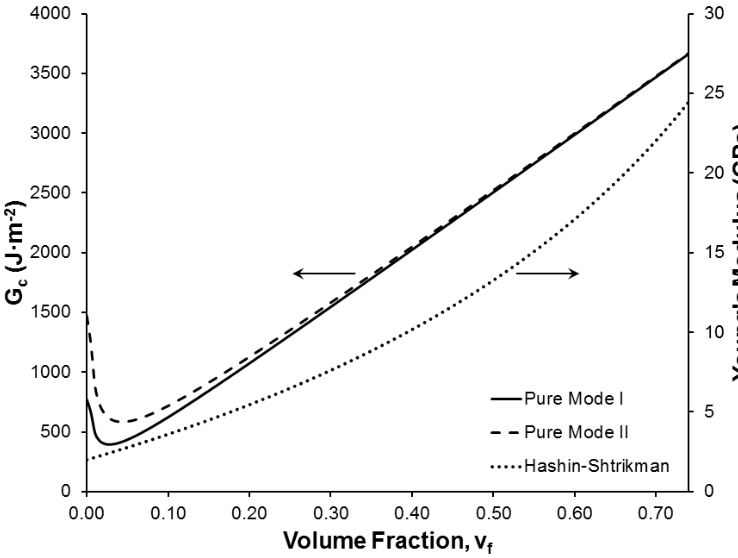

Figure 6.11 – Predicted composite toughness and modulus vs. volume fraction.

6.3 Composite Failure Studies

To test the above theoretical failure predictions, two experimental studies were conducted in addition to comparing to similar studies from the literature. A carbon / epoxy (C-E) system represents a simplified laboratory processed sample, while the glass / polyester (G-P) system is an industrially fabricated sample. While the individual experiments will be presented in further detail, the values used for the predictive modeling are here presented in Table 6.2 with their data source. While every effort was made to experimentally determine all the needed parameters, some of the experiments were outside the scope of the research. Notably, the value for the CSERR of the polyester was estimated from the polyester mechanical behaviour. This is deemed acceptable as the value doesn’t actually change the prediction. Since the matrix CSERR also appears in the calculation of the reduced plastic radius, the value cancels from the calculation, resulting in no net change. The analytical model retains the value in the event that an improved plastic radius correction is developed independent of the matrix CSERR.

Table 6.2 – Random fibre composite properties used for predicting failure.

Variable	C-E Value	G-P Value	Data source
Coefficient of friction, μ	0.25	0.35	[94],[130]
Residual stress, P (MPa)	4.5	3.7	Section 5.3.4
Matrix modulus, E_m (MPa)	2000	1600	Section 3.3.1
Matrix yield, $\sigma_{y,m}$ (MPa)	27.7	19.0	Section 3.3.1
Fibre strength, $\sigma_{ts,f}$ (MPa)	4900	2600	Appendix A
Fibre radius, r (μm)	3.5	9	Appendix A
Volume fraction fibres, v_f	0.50	0.15	Section 6.3
Volume fraction fillers, v_ϕ	0.05	0.37	Section 6.3
IFSS, τ_i (MPa)	52.0	39.7	Section 4.1
Interface CSERR, $G_{IIc,i}$ ($J\cdot m^{-2}$)	477.5	401.6	Section 4.3
Matrix CSERR, $G_{Ic,m}$ ($J\cdot m^{-2}$)	780	600	Section 3.3.5
Fibre CSERR, $G_{Ic,f}$ ($J\cdot m^{-2}$)	1	10	[133], [96]

6.3.1 Pseudo-Random-Tow Carbon Reinforced Epoxy

A pseudo-random tow carbon reinforced epoxy panel was made in a modified hand lay-up method, as seen in Figure 6.12. The same T700 carbon from the previous interfacial studies was used to make the panel by cutting the 12k roving into 25mm segments. Here the fibres do not separate in a random fashion, but retain their tow geometry as produced. To attempt at least a random distribution of the tow segments, a bag of cut tows was violently shaken to mix the fibres. This was layered in a soft mould by alternating some of the cut tows with some mixed epoxy, as seen in Figure 6.12a). The resulting panel

(Figure 6.12b) was cut into multiple test specimens (Figure 6.12c) for mechanical and fracture testing. The epoxy was the same as previously characterized in Chapter 3.

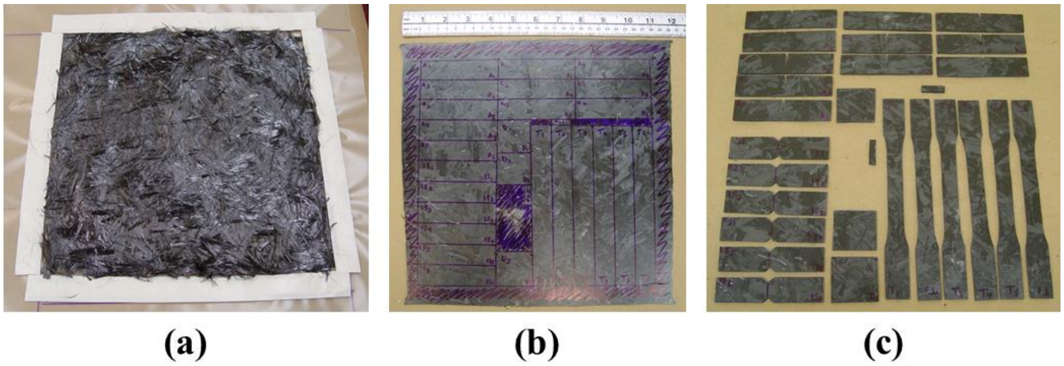

Figure 6.12 – Fabrication steps of the carbon/epoxy samples with a) constrained, multi-layer impregnation b) cured panel c) machined test specimens.

Despite the best efforts, both the tow geometry and the hand layup process are expected to impart some overall orientation to the fibres. However, the limited panel size meant that multiple orientations of samples were not possible and that sample sets were limited to six samples rather than the typical eight. A whole suite of tests was conducted to characterize the mechanical performance of this material with the results summarized in Table 6.3. Each value is listed with its standard deviation and units, as well as the governing standard by which the value was determined. The modified ASTM 5045 test is the same asymmetric four-point shear test as previously used to characterize the mode II fracture properties of the neat epoxy.

Table 6.3 – Random carbon/epoxy composite mechanical properties.

Parameter	Value	Std. Dev.	Units	Test Method
Density, ρ	1.484	0.007	$g \cdot cm^{-3}$	ASTM 792
Volume fraction fibres, v_f	49.9	1.3	%	ASTM 2584
Composite porosity, v_ϕ	5.0	0.8	%	
Young's modulus, E_c	33.90	3.34	GPa	ASTM 638 Type II
Tensile strength, σ_{ts}	185.2	28.2	MPa	
Shear modulus, G_c	3.27	0.20	GPa	ASTM 5379
Shear strength, τ_{ts}	118.6	7.2	MPa	
K_{Ic}	5.59	0.26	$MPa \cdot m^{½}$	ASTM 5045
G_{Ic}	897	100	$J \cdot m^{-2}$	
K_{IIc}	5.81	0.28	$MPa \cdot m^{½}$	Modified ASTM 5045
G_{IIc}	925	36	$J \cdot m^{-2}$	

To give some connection to the experimental data, the stress-strain curves for the tensile testing are provided in Figure 6.13 together with the two failure theories of Tsai-Wu and Bogetti from Chapter 2. In this sense, the statistical nature of the random tow composite is seen clearly with a wide spread in observed response. Both theories over predict the failure stresses by a wide margin, despite predicting the modulus within 5%. It was thought that the reason for such a prediction was based on the difference between a random fibre and a random tow composite. In a random tow composite, the cut tows exhibit a small aspect ratio in plane of the tow, acting more like a small, oriented lamina. This has the effect of allowing local delamination which weakens the composites ability to resist a propagating crack.

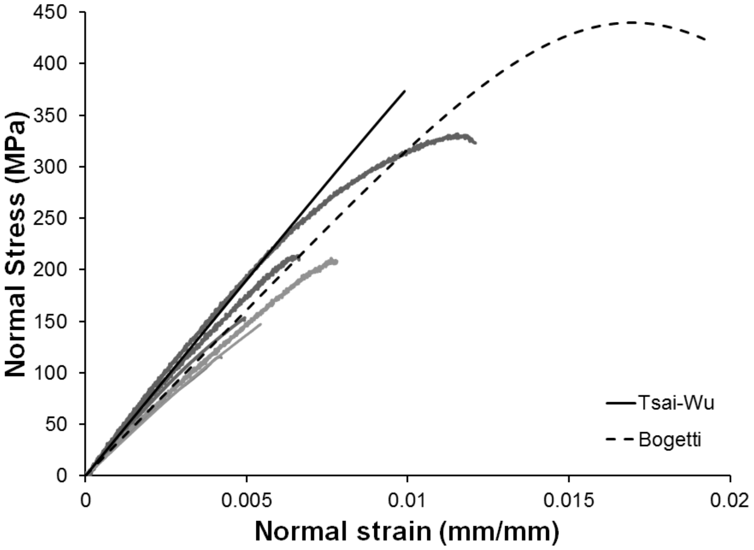

Figure 6.13 – Carbon / epoxy random tow stress strain curves plotted against the Tsai-Wu and Bogetti failure theories.

Both models use the Hashin-Shtrikman modulus prediction and the Ramberg-Osgood model for the matrix plasticity and reduced modulus. The Tsai-Wu criterion is an interactive quadratic failure criterion, in this case terminating when the induced shear stress in the matrix reaches a critical value. The Bogetti model only terminates when the matrix reaches the failure strain of the fibres. While this allows for some predicted composite plasticity, it comes at the expense of grossly over predicting the failure strain and composite toughness. It should be stated that the reason for the difference in the model elastic moduli is due to a reduction in the fibre aspect ratio to account for the tow geometry aspect ratio; this correction was only applied to the Bogetti theory as shown.

Using the newly developed model, Equation 6.28, the experimental and predicted properties for this composite are presented in Table 6.4 along the percent difference. The critical stress intensity factor for each mode was calculated from Equation 6.1 using the predicted modulus and predicted composite CSERR values.

Table 6.4 – Experimental and predicted values for carbon / epoxy composite.

Property	Experimental	Predicted	% Difference
Young's modulus (GPa)	33.90 ±3.34	37.08	8.6
K_{Ic} (MPa·m^{½})	5.59 ±0.26	6.23	10.3
G_{Ic} (J·m^{-2})	897 ±100	1047	14.3
K_{IIc} (MPa·m^{½})	5.81±0.28	6.28	7.4
G_{IIc} (J·m^{-2})	925 ±36	1062	12.9

Though all the predicted values for the carbon / epoxy composite are above the experimental values, there exists a simple explanation: the tow geometry. Because this composite was not composed of random fibres, but rather random tows, the tows prevent both a uniform fibre orientation and a uniform fibre angle. Assuming that the overall tow alignment was not parallel to the tensile axis, which was unlikely, the experimental modulus is expected to be lower than the predicted value. Because the tow fibres are also partially mechanically twisted together, a crack is likely not to shear through a tow. Instead, since the tows represent a locally uniform fibre geometry, they behave more like a single flat ellipsoidal fibre. This platelet type of behaviour presents a much reduced aspect ratio, with a large flat swath of interface along which a crack can run. Together, this explains the lower observed experimental values.

6.3.2 Random Glass Reinforced Polyester

A second experimental suite of tests was performed on an industrial-made composite. Using the SMC process, the Fraunhofer Project Center in London, Ontario kindly fabricated several random glass-polyester plates. The SMC process produces a near true random distribution of individual fibres (rather than tows) within a compounded polyester matrix. This process does mean that the polyester is no longer in its neat formulation as measured in the lab. The same tests as conducted on the carbon / epoxy composite were performed on the glass / polyester version with the results compiled into

Table 6.5. In the data below, there is volume fraction reported for the fillers. This parameter was determined by analyzing just the paste produced from the SMC process without any glass fibre. Using the ratio of polyester to solid fillers obtained by burn-testing the paste, this was applied to the overall composite to determine the amounts of glass, paste, and polymer present in the SMC panel. The value for the volume fraction of fillers accounts for all the myriad of solid additives into the polyester, but treats them as having approximately the same density as that of the main component, calcium carbonate.

Table 6.5 – SMC glass/polyester composite mechanical properties.

Parameter	Value	Std. Dev.	Units	Test Method
Density, ρ	1.855	0.004	$g\cdot cm^{-3}$	ASTM 792
Volume fraction fibres, v_f	15.0	0.7	%	ASTM 2584
Volume fraction fillers, v_ϕ	37.2	1.7	%	
Young's modulus, E_c	6.79	0.23	GPa	ASTM 638 Type II
Tensile strength, σ_{ts}	85.8	5.5	MPa	
Shear modulus, G_c	2.39	0.13	GPa	ASTM 5379
Shear strength, τ_{ts}	68.1	4.9	MPa	
K_{Ic}	1.50	0.27	$MPa\cdot m^{½}$	ASTM 5045
G_{Ic}	456	45	$J\cdot m^{-2}$	
K_{IIc}	1.74	0.30	$MPa\cdot m^{½}$	Modified ASTM 5045
G_{IIc}	529	64	$J\cdot m^{-2}$	

In addition to the bulk mechanical testing, some of the industrially compounded paste was reserved for lap-shear testing to compare to the neat polyester previously characterized. The samples were fabricated and tested in the same way as described in Chapter 4 for the polyester with both clean and Z6030 coated glass. All the samples with the clean glass failed to be cured properly in what looked to be a result of a poorly bonded interface. The coated lap-shear samples are compared to the previously obtained results in Figure 6.14. Though the filled polyester is slightly stiffer than its neat counterpart, it shows dramatically lower interfacial strength and strain to failure.

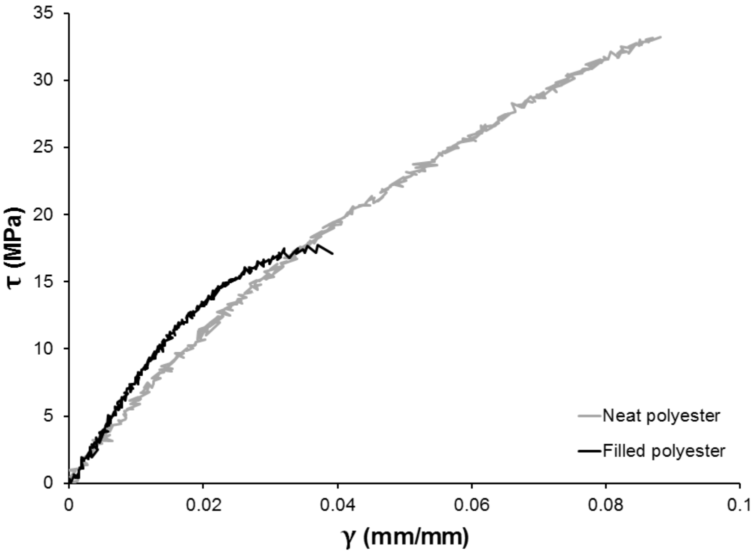

Figure 6.14 – Lap-shear comparison between neat and filled polyester bonded to Z6030 coated glass.

Similar to the carbon / epoxy composite, the glass / polyester composite is compared between the experimental and predicted values in Table 6.6.

Table 6.6 – Experimental and predicted values for glass / polyester composite.

Property	Experimental	Predicted	% Difference
Young's modulus (GPa)	6.79 ±0.22	6.57	3.3
K_{Ic} (MPa·m^{½})	1.50 ±0.27	1.51	0.7
G_{Ic} (J·m^{-2})	456 ±45	343.6	32.7
K_{IIc} (MPa·m^{½})	1.74 ±0.30	1.76	1.1
G_{IIc} (J·m^{-2})	529 ±64	472.0	12.1

Here the Young's modulus is under predicted, but within a standard deviation – enough to be consistent. The majority of the fracture values are almost exactly predicted with a lower predicted toughness, likely due to the polymer additive assumption. Since all the predicted values are taken for the neat polyester with a simple deduction for the filler amount, the effects the additives have on the polymer, interface, and debond are not considered. It is probable that the fillers contribute somewhat to the composite toughness, rather than simply degrading all parameters. Even with the simplified matrix prediction, the fracture values average within 10% of the experimental values generating confidence in the model.

7 Conclusion

To achieve understanding of the interfacial strength of a polymer matrix composite novelty was sought in the form of testing methods, extensive experimental reporting, and a new long fibre composite failure model. This thesis documents the complete process of identifying the current research areas, proposing and conducting tests to pursue tangible answers, and interpreting the data to produce meaningful contributions to the engineering field.

7.1 Summary

This research has investigated one of the fundamental properties of composite materials – the interface between constituent materials. Discussion of this interface bordered its chemical and mechanical nature. The research goals comprised the characterization of two different thermoset polymers, the measurement of interfacial strength under a wide variety of influences, and incorporating interfacial strength into the fracture mechanics of composite materials.

The initial research identified issues with the currently utilized methods to measure interfacial strength. The four main techniques investigated were the pull-out test, the push-out test, the fragmentation test, and the lap-shear test. From this starting point, both the push-out test and lap-shear test were geometrically modified to improve the test sensitivities and generate results for in situ and rapid assessment respectively. A full range of interfacial conditions were assessed to determine trends and inputs which are the most important to the measured strength. The lap-shear test was further used to generate measures for the critical strain energy release rate in both mode I and mode II loading based on the sample geometry. The ability to determine the mode I and mode II interfacial critical strain energy release rates from one test was not previously available from the literature.

Using state-of-the-art simulation software, a new combined physics simulation of a curing thermoset polymer was used to determine the residual stress acting on a fibre after processing. This information can be used to further predict composite surface finish, component springback, and the determination of better processing parameters to tailor final composite part performance. Critically, however, the residual stress values can be used to determine the effect of pullout of a random fibre composite in greater detail.

Further exploration yielded a snapshot of the composite failure landscape. Issues surrounding the definition of failure in composite materials and how to predict the onset of damage remain outstanding challenges. Though this research has added the ability to predict failure with from a phenomenological standpoint, the next step remains to incorporating such a capacity into the commercial software landscape. The proposed model breaks failure down into each of the mechanisms and has been shown to apply to a variety of composite formulations including particulate reinforcements, short and long fibre composites, and even some cases of continuously reinforced composites. The model utilized a combination of material, processing, geometric and interface properties to predict the composite critical strain energy release rate, with no empirical variables. This model was validated on two completely separate material systems demonstrating good agreement between the experimental and predicted values showing the range and versatility of this new, comprehensive model.

7.2 Future Work

Because of the success of this current work, the natural conclusion would be to continue investigating how the interfacial strength can be manipulated and utilized to control both the fracture mechanism and the energy absorbed during fracture. Tailored interfaces with specific bonding and debonding behaviour would enable this type of detail in design. It would also be prudent to continue the base work, examining the factors influencing interfacial strength such as in chemically reactive environments or specific industrial additives. Further distinguishing between impacts which may separately affect the shear or normal interfacial strength would result in a complete understanding of the nature of the interface as it forms and gives strength to the composite. Cataloguing the interfacial strengths based on chemical bonding or even creating a predictive chemical bond simulation tool would further the design optimization goals. Along this line, a future vision might be chemically designing the interfacial bonding mechanisms which can be repaired in the event of damage, selectively broken for component recycling, or modified to bond better with polymer fillers for strengthening. What is greatly needed is a link between the chemistry of the interface and the mechanical strength of the interface, possibly via molecular dynamic simulations [78]. Offshoot areas also needing development include methods to cheaply produce the constituent materials, such as carbon fibre.

Another major area which is ripe with opportunities for a research breakthrough is in regard to damage modeling. As has already been shown, there are multiple current approaches each with their areas of expertise and their drawbacks. A complete model to predict and model the many types of continuous woven fibre reinforced polymer composite materials, free of the many empirical fitting parameters, has yet to be produced. Such a breakthrough would be immensely valuable to the material simulation community, to component designers, and to researchers investigating multi-material systems. These future improvements not only affect the design and use of composite materials, but also the repair and scheduling of preventive maintenance of these components. Long term studies on the use and degradation behaviour of these materials is vital to realizing their implementation in consumer markets.

7.2.1 Proposed Study: Matrix Microcracking

Specifically, consider an advancing crack front as seen in Figure 7.1. Here, a crack is shown to run parallel to long embedded fibres with a reduced plastic deformation zone due to the fibre constraint. Also pictured are numerous micro cracks forming between the differentially loaded fibres. This obviously precludes a strong interface condition, where the interfacial strength is at least greater than the matrix yield strength, and possibly greater than the matrix tensile strength. One observation is that the additional surface area of the matrix cracking is likely to require a large amount of energy. Another important observation is that this picture suggests that the matrix plastic radius extends around fibres, and is not immediately constrained to the small unit cell area as the proposed model would indicate.

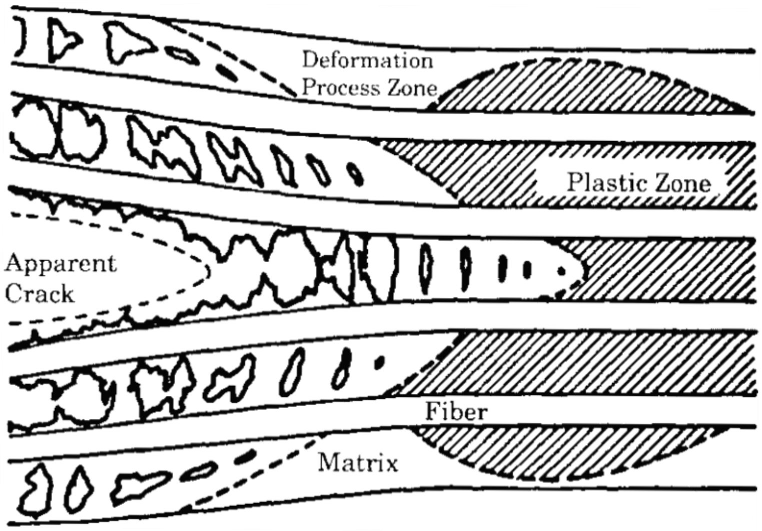

Figure 7.1 – Mode I interlaminar fracture from Su [134].

For any such system, even in a random fibre composite, where the fibre length is greater than the critical length required for stress transfer, it is expected that such microcracks between fibres would consume a great deal of energy in the production of new matrix surfaces. Their roughness would contribute to the work of fibre pull-out, as sliding friction is increased with a rough surface. Thus the work of fracture would be greater than a purely brittle matrix, or even a system in which microcrack did not form but the interface debonded instead. However, to prove the presence of such behaviour would represent a completely new study in itself. A method to image the development of microcracks during a fracture event would be needed, along with a method to determine the strain energy released. This proposed study would greatly advance composite failure theories allowing composite unit cells to be completely modeled and their fracture predicted with sufficient accuracy.

This study would propose to refine the matrix plasticity area fraction prediction, improve the calculation of the matrix deformation itself, and refine the crack path extension prediction. It is likely that in the course of such a study, a model would be needed to better represent the fibre angular distribution, which would eliminate on of the current major assumptions.

7.2.2 Proposed Study: Fibre Length Contribution

Building from the model discussed in Chapter 6, three critical parameters were discussed: the distribution function of fibres which contribute to the interface and pullout energies, the length of the debonded interface, and the length of the fibre pullout. By inspection, these parameters are linked, with the fibre angle giving rise to the fibre debond length, and the debond length being equal to or greater than the pullout length. Further, there is expected to be some connection to the packing of the fibres, as greater packing leads to the suppression of matrix plasticity and subsequent stress transfer to the fibres.

To examine these variables, a project is proposed to examine the fractography of short fibre composites. The study would take fibres of a known diameter and determine their critical stress transfer length independent of orientation or fibre packing. Then using a range of lengths around this critical transfer length, the subsequent debond length and pullout length could be examined in a fragmentation style test but with a notched specimen to ensure the starting location of the crack is controlled based on the location of the embedded fibres. Fibre angle could be controlled using an injection-moulded placard since short fibres tend to align to the flow direction based on shear; samples could then be cut at the appropriate angle.

It is expected that as the volume fraction increases, so too do the interfacial debond length and pullout length increase. This is due to the same fibre shielding effect noted by Bruce [96] in the multi-fibre fragmentation tests. From the proposed testing, this shielding could be combined with the fibre angular distribution to predict the lengths as a function of fibre angle. The result would effectively yield a method to optimize the fibre length in random fibre composites. This study would also examine the long assumed critical transfer length from shear lag theory and extend this notion with multiple interacting filaments. A great benefit would be to conduct this study in conjunction with industrial process simulations such that one refined model can be created to both predict fibre orientation and distribution, and use that information to generate the critical fibre length values needed to predict the composite fracture behaviour.

7.3 A Final Word

The proposed failure model and the new composite simulation and experimental method advance the science toward the goal of complete numerical optimization and design of custom composite materials.

References

1 Schnell HJ. (editor) (2008) Material science and engineering in Germany: recommendations on image building, teaching and research. German National Library, Augustin.

2 Cheah L. and Heywood J. (2010) Meeting U.S. passenger vehicle fuel economy standards in 2016 and beyond. Energy Policy, 39(2): 454-466.

3 Jacob GC et al. (2002) Energy Absorption in Polymer Composites for Automotive Crashworthiness. J Compos Mater, 36:813-850.

4 Henning, F. (2014) Basics of vehicle lightweight design. Institute for vehicle system technology, lecture.

5 Ashby M (2005) Material Selection in Mechanical Design, 3nd ed. Elsevier, Burlington, MA, Chap. 4.

6 Hull D and Clyne TW (1996) An introduction to composite materials, 2nd ed. Cambridge, New York.

7 Zhong Z and Meguid SA (1997) On the elastic field of a spherical inhomogeneity with an imperfectly bonded interface. J Elasticity, 46: 91-113.

8 Hinton MJ, et al (eds) (2004) Failure criteria in fiber reinforced polymer composites: The world-wide failure exercise. Elsevier, San Diego, CA.

9 Tay TE et al (2008) Progressive failure analysis of composites. J Compos Mater, 42(18):1921-1966.

10 Pinho ST et al. (2012) Material and structural response of polymer-matrix fibre-reinforced composites. J Compos Mater, 46(19-20): 2313-2341.

11 Carrere N, Laurin F and Maire J-F (2012) Micromechanical-based hybrid mesoscopic 3D approach for non-linear progressive failure analysis of composite structures. J Compos Mater, 46 (19-20): 2389-2415.

12 Puck A and Schürmann H. (1998). Failure analysis of FRP laminates by means of physically based phenomenological models. Compos Sci Technol, 58, 1045-1067.

13 Deuschle HM and Kroplin B-H (2012) Finite element implementation of Puck's failure theory for fibre-reinforced composites under three-dimensional stress. J Compos Mater, 46(19-20): 2485-2513.

14 Kalpakjian S. and Schmid S.R. (2007) Manufacturing Processes for Engineering Materials, 5th ed., Prentice Hall, New Jersey, Chap. 10.

15 Ozawa T (1970) Kinetic analysis of derivative curves in thermal analysis. J Therm Anal, 2(3): 301-324.

16 Borchardt HJ and Daniels F (1956) The application of differential analysis to the study of reaction kinetics. J Am Chem Soc, 79(1): 41-46.

17 Sourour S and Kamal MR (1976) Differential scanning calorimetry of epoxy cure: isothermal cure kinetics. Thermochim Acta, 14(1-2):41-59.

18 DiBenedetto AT (1987) Prediction of the glass transition temperature of polymers: A model based on the principle of corresponding states. J Polym Sci Part B Polym Phys, 25: 1949-1969.

19 Williams ML et al. (1955) The temperature dependence of relaxation mechanisms in amorphous polymers and other glass-forming liquids. J Ameri Chem Soc, 77(14): 3701-3707.

20 Chern CS and Poehlein GW (1987) A kinetic model for curing reactions of epoxides with amines. Polym Eng Sci, 27(11):788-795.

21 Blest DC et al. (1999) Curing simulation of thermoset composites. Compos Part A-Appl Sci, 30: 1289-1309.

22 Bogetti TA and Gillespie Jr JW (1992) Process-induced stress and deformation in thick-section thermoset composite laminates. J Compos Mater, 26(5):626-660.

23 Eom Y et al. (2000) Time-cure-temperature superposition for the prediction of instantaneous viscoelastic properties during cure. Polym Eng Sci, 40(6):1281-1292.

24 Gigliotti M et al. (2011) Local shrinkage and stress induced by thermo-oxidation in composite materials at high temperatures. J Mech Phys Solids, 59(3):696-712.

25 Patham B. (2009) COMSOL implementation of a viscoelastic model with cure-temperature-time superposition for predicting cure stresses and springback in a thermoset resin. In: Proceedings of COMSOL Conference. Bangalore.

26 White SR and Hahn HT (1992) Process modeling of composite materials: residual stress development during cure. Part I. model formulation. J Compos Mater, 26(16): 2402-2422.

27 Yang DG et al. (2004) Prediction of process-induced warpage of IC packages encapsulated with thermosettng polymers. In: Proceedings of ECTC-54, p. 98-105.

28 Zhao LG et al. (2007) A thermo-viscoelastic analysis of process-induced residual stress in fibre-reinforced polymer-matrix composites. Mat Sci Eng A-Struct, 452-453:483-498.

29 Zoibery N et al. (2010) Computationally efficient pseudo-viscoelastic models for evaluation of residual stresses in thermoset polymer composites during cure. Compos Part A-Appl S, 41(2):247-256.

30 Ruiz E and Trochu F (2005) Thermomechanical properties during cure of glass-polyester RTM composites: elastic and viscoelastic modeling. J Compos Mater, 39(10):881-916.

31 Adolf D and Chambers R (1997) Verification of the capability for quantitative stress prediction during epoxy cure. Polymer, 38(21): 5481-5490.

32 Nawab Y et al. (2013) Characterization of the cure shrinkage, reaction kinetics, bulk modulus and thermal conductivity of thermoset resin from a single experiment. J Mater Sci, 48(6):2394-2403.

33 Rabearison N, Jochum C and Grandidier JC (2009) A FEM coupling model for properties prediction during the curing of an epoxy matrix. Comp Mater Sci, 45: 715-724.

34 Cox HL (1952) The elasticity and strength of paper and other fibrous materials. Brit J Appl Phys, 3:72-79.

35 Lawrence P (1972) Some theoretical considerations of fibre pullout from an elastic matrix. J Mat Sci, 7: 1-6.

36 Chua PS and Piggott MR (1985) The glass fiber-polymer interface: II--work of fracture and shear stresses. Compos Sci Technol, 22:107-119.

37 Hsueh CH (1990) Interfacial debonding and fiber pull-out stresses of fiber-reinforced composites. Mater Sci Engng A, 123:1-11.

38 Zhandarov S and Mäder E (2005) Characterization of fiber/matrix interface strength: applicability of different tests, approaches and parameters. Compos Sci Technol, 65:149-160.

39 Qui Y and Schwartz P (1993) Single fiber pull-out from a microcomposite test. Compos Sci Technol, 48: 5-10.

40 Baillie CA (1991) The effect of an oxidative surface treatment on the adhesion of carbon fibres in and epoxy resin matrix. Ph.D. Thesis. University of Surrey.

41 Kim JK et al. (1992) Interfacial debonding and fiber pull-out stresses: Part I. A critical comparison of existing theories with experiments. J Mater Sci, 27:3143-3154.

42 Zhou L et al (1993) Micromechanical characteristics of fiber/matrix interfaces. Compos Sci Technol, 48:227-236.

43 Kallas MN et al. (1992) Interfacial stress state present in a thin slice fiber push-out test. J Mater Sci, 27:3821-3826.

44 Netravali AN et al. (1989) Continuous micro-indenter push-through technique for measuring interfacial shear strength of fiber composites. Compos Sci Technol, 34:289-303.

45 Kim JK, Mai YW (1998) Engineered interfaces in fiber reinforced composites. Elsevier, New York.

46 Kelly A and Tyson WR (1965) Tensile properties of fiber-reinforced metals: copper/tungsten and copper/molybdenum. J Mech Phys Solids, 13:329-350.

47 Favre JP and Jacques D (1990) Stress transfer by shear in carbon fiber model composites: Part I Results of single fiber fragmentation tests with thermosetting resins. J Mater Sci, 25:1373-1380.

48 Zhou X-F, Nairn JA and Wagner HD (1999) Fiber-matrix adhesion from the single–fiber composite test: nucleation of interfacial debonding, Compos Part A-Appl S, 30: 1387-1400.

49 Detassis M et al. (1996) Interface toughness in fiber composites by the fragmentation test, Compos Part A-Appl Sci, 27A:769-773.

50 Termonia Y (1993) Dependence of fibre critical length on the modulus in single fiber composites. J Mater Sci Let, 12: 732-733.

51 Liu HY et al. (1997) Stress transfer in the fibre fragmentation test. Part 3: effect of matrix cracking and interface debonding. J Mater Sci, 32: 633-641.

52 Mendels DA (2001) Analysis of the single-fibre fragmentation test. NPL Report MATC(A) I 7, Teddington, UK.

53 Ramberg W and Osgood WR (1943) Description of stress-strain curves by three parameters. Technical Note No. 902, National Advisory Committee For Aeronautics, Washington DC.

54 Eshelby JD (1957) The determination of the elastic field of an ellipsoidal inclusion and related problems. Proc Royal Soc, A241: 376-396.

55 Mori T and Tanaka K (1973) Average stress in matrix and average elastic energy of materials with misfitting inclusions. Acta Metall, 21: 571–574.

56 Hashin Z and Shtrikman S (1963) A variational approach to the theory of the elastic behaviour of multiphase materials. J Mech Phys Sol, 11: 127-140.

57 Berryman JG (2005) Bounds and self-consistent estimates for elastic constants of random polycrystals with hexagonal, trigonal, and tetragonal symmetries. J Mech Phys Solids, 53: 2141-2173.

58 Christensen RM (1990) A critical evaluation for a class of micro-mechanics models. J Mech Phys Solids, 38: 379–404.

59 Pan N (1996) The elastic constants of randomly oriented fibre composites: a new approach to prediction. Sci Eng Compos Mater, 5(2): 63-72.

60 Manera M (1977) Elastic properties of randomly oriented short fiber-glass composites. J Compos Mater, 11: 235-247.

61 Halpin JC and Tsai SW (1969) Effects of environmental factors on composite materials. AFML-TR67-423.

62 Christensen RM and Waals FM (1972). Effective stiffness of randomly oriented fibre composites. J Compos Mater, 6: 518-532.

63 Bogetti TA et al. (2012) Predicting the nonlinear response and progressive failure of composite laminates under tri-axial loading. J Compos Mater, 46(19-20): 2443-2459.

64 Chou PC, Carleone J and Hsu CM. (1972) Elastic constants of layered media. J Compos Mater, 6: 80–93.

65 Huang Y, Xu L and Ha K. (2012) Prediction of three-dimensional composite laminate response using micromechanics of failure. J Compos Mater, 46(19-20): 2431-2442.

66 Liu K-S and Tsai SW. (1998) A progressive quadratic failure criterion for a laminate. Compos Sci Technol, 58(7), 1023-1032.

67 Tsai SW and Wu EM (1971) A general theory of strength for anisotropic materials. J Compos Mater, 5, 58-80.

68 Bentur A and Mindess S (1990) Fibre reinforced cementitious composites. Elsevier Science Publishing Co., New York, NY, Chap. 5.

69 Wecharatana M and Shah SP (1983) A model for predicting fracture resistance of fibre reinforced concrete. Cem Concr Res, 13: 819–29.

70 Outwater JO and Murphy MH (1969) On the fracture energy of unidirectional laminates. In Proc. 26th Annual Conf. on Reinforced Plastics, Composites Division of Society of Plastics Industry, 1–8.

71 Hibbert AP and Hannant DJ (1982) Toughness of fibre cement composite, Composites, 13: 105–111.

72 Phillips AJ, Clegg WJ and Clyne TW (1993) Fracture of ceramic laminates in bending. Part II – comparison of model predictions with experimental data. Acta Metall Mater, 41: 819-827.

73 Thomason JL and Yang L (2014) Temperature dependence of the interfacial shear strength in glass–fibre epoxy composites. Compos Sci Technol, 96: 7-12.

74 Cook J and Gordon JE (1964) A mechanism for the control of crack propagation in all-brittle systems. Proc Roy Soc, 282A, 508-520.

75 Yeung P and Broutman LJ (1978). The effect of glass-resin interface strength on the impact strength of fiber reinforced plastics. Polym Eng Sci, 18:62-72.

76 Park S, Jin J and Lee J (2000) Influence of silane coupling agents on the surface energetics of glass fibers and mechanical interfacial properties of glass fiber-reinforced composites. J Adhesion Sci Technol, 14(13): 1677-1689.

77 Ramos JA et al. (2005) Cure kinetics and shrinkage model for epoxy-amine systems. Polymer, 46: 3323-3328.

78 Yarovsky I, Evans E. (2002). Computer simulation of structure and properties of crosslinked polymers: application to epoxy amines. Polymer, 43: 963-969.

79 Sun L (2002) Thermal rheological analysis of cure process of epoxy prepreg. Ph.D. thesis. Louisiana State University.

80 Kissinger HE (1957) Reaction kinetics in differential thermal analysis. Anal Chem, 29(11):1702-1706.

81 Han S et al. (1998) Kinetic study of the effect of catalysts on the curing of biphenyl epoxy resin. J Appl Polym Sci, 68(7):1125-1137.

82 ASTM E1356 (2014) Standard test method for assignment of the glass transition temperatures by differential scanning calorimetry. ASTM International, West Conshohocken, PA.

83 ASTM D4473 (2008) Standard test method for plastics: dynamic mechanical properties: cure behavior. ASTM International, West Conshohocken, PA.

84 ASTM D2566 (1986) Standard test method for linear shrinkage of cured thermosetting casting resins during cure. ASTM International, New York, NY.

85 Shah DU and Schubel PJ (2010) Evaluation of cure shrinkage measurement techniques for thermosetting resins. Polym Test, 29(6):629-639.

86 DasGupta A (2008) Asymptotic theory of statistics and probability. Chapter 18. Springer, New York, NY.

87 ASTM D638 (2010) Standard test method for tensile properties of plastics. ASTM International, West Conshohocken, PA.

88 Sadeghinia M, Jansen KMB and Ernst LJ (2012) Characterization and modeling the thermo-mechanical cure-dependent properties of epoxy molding compound. Int J Adhes Adhes, 32: 82-88.

89 ASTM D5045 (2007) Standard test methods for plane-strain fracture toughness and strain energy release rate of plastic materials. ASTM International, West Conshohocken, PA.

90 Bakker A (1990) Compatibility compliance and stress intensity expressions for the standard three-point bend specimen. Fatigue Fract Eng M, 13(2): 145-154.

91 Slepetz JM, Zegas TF and Prabhakaran P (1978) In-plane shear test for composite materials, Report No. AMMRCTR78-30, Army Materials and Mechanics Research Center, Watertown, MA.

92 ASTM D5379 (2005) Standard test method for shear properties of composite materials by the v-notched beam method. ASTM International, West Conshohocken, PA.

93 Yoshihara H (2013) Mode II critical stress intensity factor of medium-density fiberboard measured by asymmetric four-point bending tests and analysis of kink crack formation. Bioresources 8(2): 1930-2126.

94 Detassis M, Pegoretti A and Migliaresi C. (1995) Effect of temperature and strain rate on interfacial shear stress transmission in carbon/epoxy model composites. Compos Sci Technol, 53:39-46.

95 Feih S et al. (2004) Establishing a testing procedure for the single fibre fragmentation test. Riso National Laboratory. Pitney Bowes, Denmark.

96 Bruce TP (2011) Mechanistic mixed-mode failure criterion for continuous fiber-polymer composites. Ph.D. thesis. University of Western Ontario, London.

97 Gelest (2006) Silane coupling agents: connecting across boundaries. Gesest, Inc., Morrisville, PA.

98 Drzal LT et al. (1980) Interfacial shear strength and failure mechanisms in graphite fiber composites. In 35th Annual Tech Conf, Reinforced Plast Composites Inst, SPI, Paper 20C.

99 Drzal LT and Madhukar M (1993) Fibre-matrix adhesion and its relationship to composite mechanical properties. J Mater Sci, 28: 569-610.

100 Zhou X et al (2001) Interfacial properties of polymer composites measured by push-out and fragmentation tests. Compos A, 32:1543-1551.

101 Liang C and Hutchinson JW. (1993) Mechanics of the fiber pushout test. Mech. Mater. 14:204-221.

102 Zhou LM et al. (1995) Analysis of fiber push-out test based on the fracture mechanics approach. Compos Eng, 5:1199-1219.

103 Kafkaldis MS and Thouless MD (2002) The effects of geometry and material properties on the fracture of single lap-shear joints. Int J Solids Struct, 39:4367-4383.

104 Tsai MY, Morton J (1995) An experimental investigation of non-linear deformations in single-lap joints. Mech Mater, 20:183–194.

105 Ferreira JM et al. (2005) Stress analysis of lap joints involving natural fibre reinforced interface layers. J Compos Part B, 36:1-7.

106 Sitterle VB (2008) A modified lap test to more accurately estimate interfacial shear strength of bonded tissues. J. Biomech., 41: 3260-3264.

107 Chowdhuri MAK and Xia Z (2013) Interface bonding strength measurement of a joint between elastic and viscoelastic materials. J. Compos. Part B, 44:253-259.

108 Koyanagi J and Ogihara S (2011) Temperature dependence of glass fiber/epoxy interface normal strength examined by a cruciform specimen method. J Compos Part B, 42: 1492–1496.

109 Swentek I and Wood JT (2013) Measuring polymer composite interfacial strength. Compos. B, 58:235-241.

110 Swentek I and Wood JT (2013) Using the lap-shear test to measure polymer composite interfacial strength, The 19th International Conference on Composite Materials, proceedings.

111 Hashin Z and Rotem A (1973) A fatigue failure criterion for fiber reinforced materials. J Compos Mater, 7:448-464.

112 Gao X et al. (2008) Effect of fiber surface texture created from silane blends on the strength and energy absorption of the glass fiber/epoxy interphase. J Compos Mater, 42:513-534.

113 Gupta V et al. (1993) Calculation, measurement and control of interface strength in composites. J Am Ceram Soc, 76:305-315.

114 Tanoglu M et al (2001) The effects of glass-fiber sizings on the strength and energy absorption of the fiber/matrix interphase under high loading rates. Compos Sci Technol, 61:205-220.

115 Zhou LM et al (1992) Interfacial debonding and fibre pull-out stresses: part II. a new model based on the fracture mechanics approach. J Mater Sci, 27(12): 3155-3166.

116 Feng L, et al. (2010) Formation of gaps at the filler-resin interface induced by polymerization contraction stress gaps at the interface. Dent Mater, 26(8):719-729.

117 Livermore Software (2010) LS-DYNA Keyword User's Manual. Version 971. Livermore, CA.

118 Behzad T and Sain M (2007) Finite element modeling of polymer curing in natural fiber reinforced composites. Compos Sci Technol, 67(7-8):1666-1673.

119 COMSOL. Structural Mechanics Module Verification Models. Version 4.2 COMSOL, 2012.

120 Rosso P et al. (2006) The influence of residual stresses implicated via cure volume shrinkage on CF/VEUH-composites. J Mater Sci, 41(2):383-388.

121 Ruiz E and Trochu F (2005) Numerical analysis of cure temperature and internal stresses in thin and thick RTM parts. Compos Part A-Appl S, 36(6):806-826.

122 Petrovic LM, Atanackovic TM (2008) A model for shrinkage strain in photo polymerization of dental composites. Dent Mater, 24: 556-560.

123 do Carmo MP. (1976) Differential geometry of curves and surfaces. Prentice Hall: New Jersey.

124 Broek D (1986) Elementary engineering fracture mechanics. Kluwer academic publishers, Hingham, MA.

125 Sanford RJ. (2002) Principles of fracture mechanics. Prentice Hall, Upper Saddle River, NJ.

126 Kanninen MF and Popelar CH (1985) Advanced fracture mechanics. Oxford University Press, New York, NY.

127 Jamali J and Wood JT (2013) Mixed-mode through-thickness fracture of polymer matrix composites. The 19th International Conference on Composite Materials.

128 Williams, R. (1979) Circle packings, plane tessellations, and networks. Dover Publications Inc., New York.

129 Oshawa T et al. (1978) Temperature dependence of critical fibre length for glass fiber-reinforced thermosetting resins. J Appl Polym Sci, 22: 3203-3212.

130 Piggott MR, Chua PS and Andison D (1985) The interface between glass and carbon fibers and thermosetting polymers. Polym Compos, 6(4): 242-248.

131 Zhou R, Li Z and Sun J (2011) Crack deflection and interface debonding in composite materials elucidated by the configuration force theory. Compos Part B Eng, 42: 1999-2003.

132 Chin W-K and Yang S-W (1995) Material properties of short fiber reinforced thermoplastic composites – I. Elastic properties and predictions. J Polym Res, 2(1): 31-37.

133 Ogihara S et al. (2009) Direct evaluation of fracture toughness in a carbon fiber. The 17th International Conference on Composite Materials.

134 Su KB. (1989) Delamination resistance of stitched thermoplastic matrix composites. ASTM STP 1044, Philadelphia.

Appendices

Appendix A – Product Datasheets

In order, the following datasheets were provided by the manufacturers for the tested materials:

1. Resin, CLR 1180, and hardener, CLH 6560 (Crosslink Technologies)
2. Polyester, T320-70 (AOC)
3. Silane, Z6020 (Dow Corning)
4. Silane, Z6030 (Dow Corning)
5. Silane, Z6040 (Dow Corning)
6. Glass Fibre, TG-18-u (JB Martin)
7. Carbon Fibre, T700s (Toray)

CROSSLINK TECHNOLOGY INC.

FORMULATED EPOXIES, URETHANES - CUSTOM CAST PARTS

ISO
9001
REGISTERED
QUALITY SYSTEM

SINCE 1981

Our strength is in our formulations

TECHNICAL BULLETIN: **CLR 1180 / CLH 6560**

PRODUCT DESCRIPTION:

AN EXCEPTIONAL EPOXY CASTING SYSTEM WITH EXCELLENT THERMAL AND MECHANICAL SHOCK RESISTANCE.

SALES SPECIFICATIONS:	**CLR 1180**	**CLH 6560**
COLOR	AMBER	AMBER
VISCOSITY (NOTE 1, NOTE 4)	500 - 1,000 cps	10 - 25 cps
SPECIFIC GRAVITY	1.12 ± 0.02 gm/cm³	0.98 - 1.02 gm/cm³
SHELF LIFE	12 MONTHS	12 MONTHS

HANDLING:

MIX RATIO BY WEIGHT (A:B) (NOTE 2)	100:30.0
MIXED VISCOSITY (NOTE 4)	150 cps @ 22 ºC
POT LIFE OF 200 gm. mass (NOTE 4)	30 Min. @ 22 ºC
GEL TIME OF 200 gm. mass (NOTE 4)	40.0 Min. @ 22 ºC

CURE SCHEDULE (NOTE 3):

RECOMMENDED CURE SCHEDULE:	48 Hrs. @ 22 °C
ALTERNATE CURE SCHEDULE:	4 Hrs. @ 60 °C

CURED PROPERTIES: (NOT INTENDED FOR PREPARATION OF SPECIFICATIONS)

COLOUR	AMBER
DENSITY (gm/cm³)	1.08
SHORE HARDNESS	83D
GUIDE TO OPERATING TEMPERATURE (°C) (Note 6)	125
LINEAR SHRINKAGE (in/in) (ASTM D 2566)	0.0060
TENSILE STRENGTH (psi) (ASTM D 638)	8,500
TENSILE ELONGATION (%) (ASTM D 638)	10.0
HDT (°C) (ASTM D 648)	42
COEFFICIENT OF THERMAL EXPANSION (in/in/°C)	55X10^-6
MOISTURE ABSORPTION (%)	0.400

World Leader in Resin Technology

T320-70
Polyester Resin

Product Information

Pultrusion Polyester Resin

TYPICAL CAST MECHANICAL PROPERTIES * see back page (1)

Test	Units of Measure	Nominal	Test Method
Tensile Strength	psi/MPa	9,100/62.8	ASTM D 638
Tensile Modulus	psi/GPa	538,000/3.7	ASTM D 638
Tensile Elongation	%	2.1	ASTM D 638
Flexural Strength	psi/MPa	13,800/95.2	ASTM D 790
Flexural Modulus	psi/GPa	593,000/4.1	ASTM D 790
Heat Distortion Temperature	°F/°C @264 psi	260/127	ASTM D 648

TYPICAL LIQUID PROPERTIES @ 25°C * see back page (2)

Test	Units of Measure	Nominal Value
Viscosity, Brookfield RV #3 @ 20 rpm	cps	2350
Non-Volatiles	%	70
Specific Gravity		1.06
180°F/82°C SPI Gel Exotherm Test 1.0% Luperox 98 BPO		
150°F/66°C - 190°F/88°C	minutes	3.0
190°F/88°C - Peak	minutes	1.3
Peak Temperature	°F/°C	280/138

*Typical properties are not to be construed as specifications.

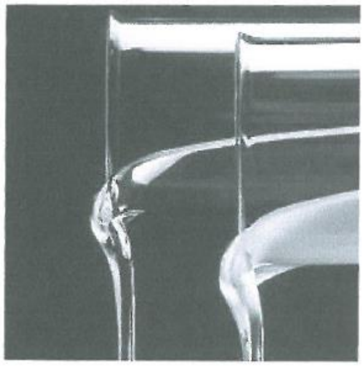

DESCRIPTION

AOC's T320-70 is an unpromoted, non-thixotropic base resin formulation.

FEATURES

- Ingredients comply with Title 21 CFR, parts 170 to 199 relative to FDA criteria
- High reactivity
- Excellent compatibility with polyvinyl acetate shrink control additives

APPLICATION

AOC's T320-70 is designed specifically for use in pultrusion. T320-70 is particularly suited for thin profiles because of the high reactivity. It can also be used in SMC/BMC applications.

DOW CORNING

Product Information
Organofunctional Silanes

Dow Corning® Z-6020 Silane

FEATURES

- Coupling agent
- Improved adhesion
- Increased wet and dry tensile strength and modulus to the composite
- Increased wet and dry flexural strength and modulus to the composite
- Increased wet and dry compressive strength
- Improved compatibility between inorganic filler and organic polymer

Diaminofunctional silane

APPLICATIONS

- *Dow Corning*® Z-6020 Silane has been found to be an effective coupling agent for clay reinforced elastomers such as natural and nitrile rubber. The silane-treated clay provides improvement in both physical and dynamic properties compared to similar cured elastomers containing untreated clay.
- *Dow Corning*® Z-6020 Silane has been reported to be an effective coupling agent for mineral reinforced nylon 6, nylon 6/6 and polybutyleneterephthalate
- Fiberglass reinforced phenolic, melamine and epoxy thermoset composites, either as a fiberglass finish or as a resinous additive.
- As an additive to improve the performance of these types of thermoset resins when they are used as mineral binders in foundry and abrasive composite applications.
- Coupling agent for phenolic, melamine and other organic resins used as binders for glass and mineral wood insulation, abrasives and moulding components.

TYPICAL PROPERTIES

Specification Writers: These values are not intended for use in preparing specifications. Please contact your local Dow Corning sales office or your Global Dow Corning Connection before writing specifications on this product.

CTM*	ASTM*	Property	Unit	Value
0176		Appearance		Clear liquid
0001A		Specific gravity at 25°C (77°F)		1.03
0002		Refractive index		1.445
		Neutral equivalents	g/eq	115
		Color		Light straw to yellow
004		Viscosity	mm2/s	5
0090A		Flash Point - closed cup	°C	85
			°F	185

*CTM: Corporate Test Method, copies of CTM's are available on request.
*ASTM: American Society for Testing and Materials.

DESCRIPTION

Dow Corning® Z-6020 Silane has the chemical formula:

N-(β-aminoethyl)-γ-aminopropyl-trimethoxysilane

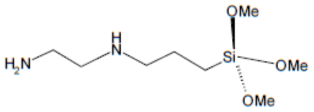

Possessing both organic and inorganic reactivity, *Dow Corning*® Z-6020 Silane can react with organic polymers and glass or other inorganic mineral surfaces.

HOW TO USE

When used as a resin additive, generally the silane is added at a level of less than 1% based on the weight of the resin solids. For each specific application, the optimum level of

Product Information
Organofunctional
Silanes

Dow Corning® Z-6030 Silane

FEATURES

- Methacrylate organoreactive group
- Trimethoxy hydrolyzable groups on silicon
- High purity

BENEFITS

- Coupling agent to improve adhesion of organic resins to inorganic surfaces
- Increased composite tensile and flexural strength—both dry and wet
- Improved chemical bonding
- Increased transparency of polyester fiberglass composites

COMPOSITION

- γ-Methacryloxypropyltrimethoxysilane

Methracrylate functional alkoxysilane

APPLICATIONS

- *Dow Corning*® Z-6030 Silane is used as a coupling agent to improve adhesion of free radical cured resins, such as polyester, to inorganic surfaces, including fiberglass, clay, quartz, and other siliceous materials. The improved adhesion increases dry and wet flexural compressive strength of the composite. Wet strength improvements of approximately 100% are possible.
- *Dow Corning*® Z-6030 Silane can also be used as a resin additive in mineral-reinforced polyester resin. When used as an additive, this silane can provide improvements in composite properties similar to those obtained from a composite fabricated with a silane-treated mineral reinforcement.

TYPICAL PROPERTIES

Specification Writers: These values are not intended for use in preparing specifications. Please contact your local Dow Corning sales office or your Global Dow Corning Connection before writing specifications on this product.

CTM*	Property	Unit	Value
0176	Appearance		Clear, white to light-straw
0001A	Specific gravity at 25˚C (77˚F)		1.04
0002	Refractive index at 25˚C (77˚F)		1.43
0021A	Flash point, closed cup	˚C (˚F)	138 (280)
	Purity	%	98
	Boiling point at 760mm Hg	˚C (˚F)	190 (374)
	Viscosity at 25˚C (77˚F)	cst	2.5
	Molecular Weight	g/mol	248.35
	CAS #		2530-85-0

CTM: Corporate Test Method, copies of CTM's are available on request

DESCRIPTION

Dow Corning® Z-6030 Silane is a bifunctional silane containing a methacrylate reactive organic group and a trimethoxysilyl inorganic group.

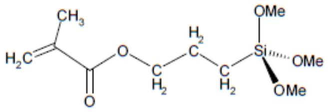

The product is designated γ-methacryloxypropyltrimethoxysilane. *Dow Corning*® Z-6030 Silane possesses both organic and inorganic reactivity, reacting with organic thermoset resins as well as inorganic minerals such as glass and silica. The chemical bonding at the organic/inorganic interface that can occur with organofunctional silanes provides a variety of benefits listed above.

Dow Corning® Z-6030 Silane is one of a series of *Dow Corning* organo functional silane chemicals. Other reactive silanes include the amine (*Dow Corning*® Z-6020 Silane), epoxy (*Dow Corning*® Z-6040 Silane), vinyl *Dow Corning*® Z-6300 Silane) and chloroalkyl (*Dow Corning*® Z-6076 Silane).

DOW CORNING

Product Information
Organofunctional
Silanes

Dow Corning® Z-6040 Silane

FEATURES

- Epoxy reactivity
- Methoxysilyl inorganic reactivity

BENEFITS

- Improves adhesion
- Increases composite strength properties
- Increased composite wet and dry tensile strength and modulus
- Increased composite wet and dry flexural strength and modulus
- Increased wet and dry compressive strength
- Better filler wet-out and dispersion
- Lower viscosity of filled liquid resins
- Improved processability

COMPOSITION

- γ-Glycidoxypropyltrimethoxysilane

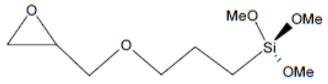

Coupling agent to improve adhesion of organic resins to inorganic surfaces

APPLICATIONS

- Broad range of coupling applications because of the useful epoxy functionality
- Used to treat fiberglass, fillers and other inorganic surfaces
- Can be used with epoxies, urethanes, polyesters, polyamide and other resins, both thermoset and thermoplastic

TYPICAL PROPERTIES

Specification Writers: These values are not intended for use in preparing specifications. Please contact your local Dow Corning sales office or your Global Dow Corning Connection before writing specifications on this product.

CTM*	Property	Unit	Value
0176	Appearance		Clear liquid
0005	Color	APHA	50
0004	Viscosity	cst	3
0001A	Specific gravity at 25˚C (77˚F)		1.07
0002	Refractive index		1.428
0021A	Flash point-closed cup	˚C (˚F)	>101 (>213)
0625B	Purity by GC	%	>98.5
0018	Chloride	ppm	100
	Molecular weight	g/mol	236.34
	CAS #		2530-83-8

* CTM: Corporate Test Method, copies of CTM's are available on request.

DESCRIPTION

Dow Corning® Z-6040 Silane is a bifunctional silane containing a glycidoxy reactive organic group and a trimethoxysilyl inorganic group. It is designated γ-glycidoxypropyltrimethoxysilane. This glycidoxy functional silane is reactive with many different types of organic polymers. It is one of a series of organofunctional silanes from Dow Corning Corporation. Other reactive silanes include amines *Dow Corning*® Z-6020 and *Dow Corning*® Z-6026 Silanes, vinyl-benzylamine *Dow Corning*® Z-6032 Silane and *Dow Corning*® Z-6224 Silane, methacrylate *Dow Corning*® Z-6030 Silane, vinyl *Dow Corning*® Z-6300 Silane, *Dow Corning*® Z-6518 Silane and chloropropyl *Dow Corning*® Z-6076 Silane.

USES

Dow Corning® Z-6040 Silane possesses both organic and inorganic reactivity that allows it to react with or "couple" organic polymers to an inorganic surface. This dual reactivity should be considered when using *Dow Corning*® Z-6040 Silane in specific applications.

Dow Corning® Z-6040 Silane is particularly recommended as:

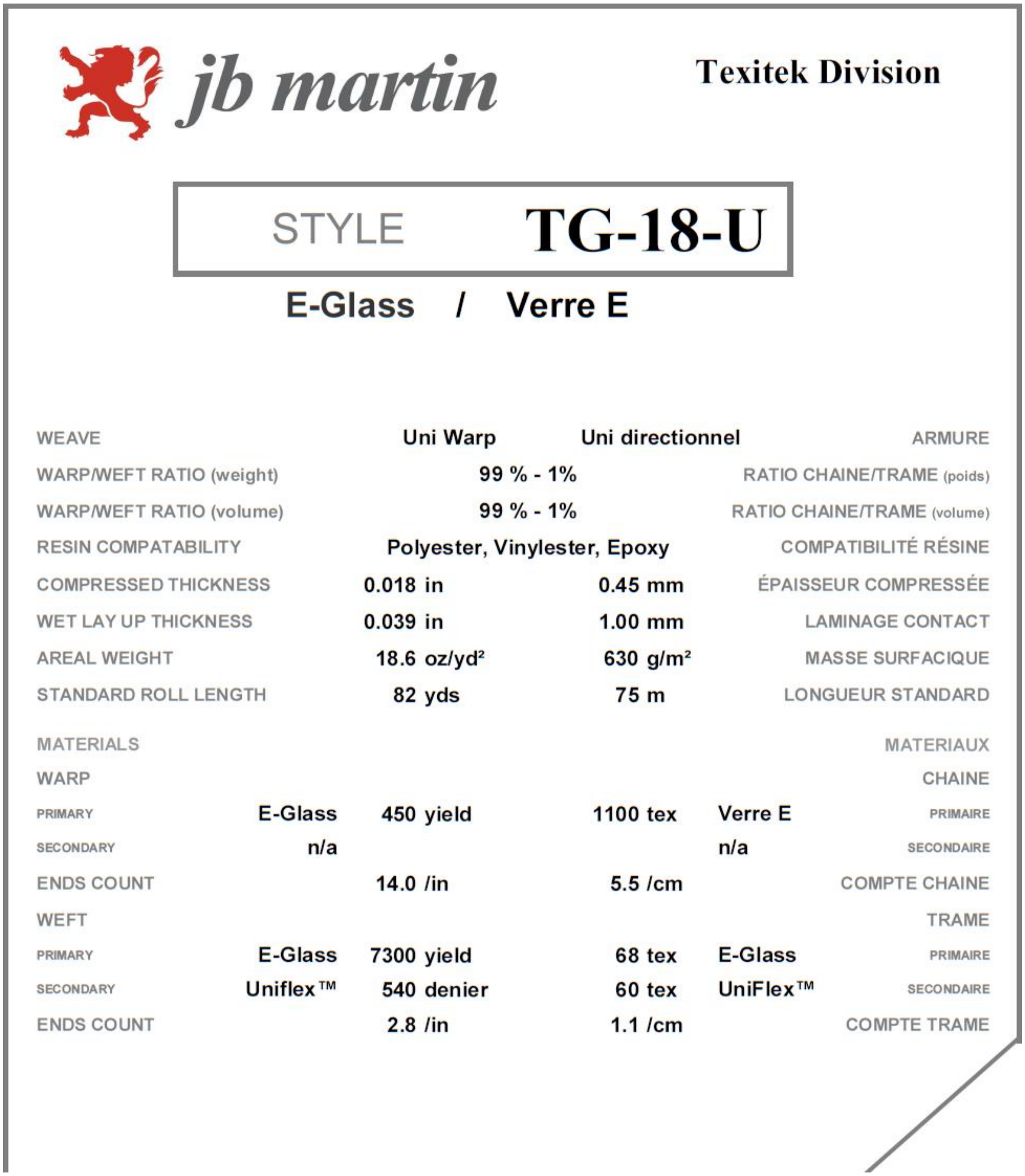

jb martin

Texitek Division

STYLE **TG-18-U**

E-Glass / Verre E

WEAVE		Uni Warp	Uni directionnel		ARMURE
WARP/WEFT RATIO (weight)		99 % - 1%			RATIO CHAINE/TRAME (poids)
WARP/WEFT RATIO (volume)		99 % - 1%			RATIO CHAINE/TRAME (volume)
RESIN COMPATABILITY		Polyester, Vinylester, Epoxy			COMPATIBILITÉ RÉSINE
COMPRESSED THICKNESS		0.018 in	0.45 mm		ÉPAISSEUR COMPRESSÉE
WET LAY UP THICKNESS		0.039 in	1.00 mm		LAMINAGE CONTACT
AREAL WEIGHT		18.6 oz/yd²	630 g/m²		MASSE SURFACIQUE
STANDARD ROLL LENGTH		82 yds	75 m		LONGUEUR STANDARD
MATERIALS					MATERIAUX
WARP					CHAINE
PRIMARY	E-Glass	450 yield	1100 tex	Verre E	PRIMAIRE
SECONDARY	n/a			n/a	SECONDAIRE
ENDS COUNT		14.0 /in	5.5 /cm		COMPTE CHAINE
WEFT					TRAME
PRIMARY	E-Glass	7300 yield	68 tex	E-Glass	PRIMAIRE
SECONDARY	Uniflex™	540 denier	60 tex	UniFlex™	SECONDAIRE
ENDS COUNT		2.8 /in	1.1 /cm		COMPTE TRAME

TORAYCA®

T700S DATA SHEET

Highest strength, standard modulus fiber available with excellent processing characteristics for filament winding and prepreg. This never twisted fiber is used in high tensile applications like pressure vessels, recreational, and industrial.

FIBER PROPERTIES

		English	Metric	Test Method
Tensile Strength		711 ksi	4,900 MPa	TY-030B-01
Tensile Modulus		33.4 Msi	230 GPa	TY-030B-01
Strain		2.1 %	2.1 %	TY-030B-01
Density		0.065 lbs/in^3	1.80 g/cm^3	TY-030B-02
Filament Diameter		2.8E-04 in.	7 µm	
Yield	6K	3,724 ft/lbs	400 g/1000m	TY-030B-03
	12K	1,862 ft/lbs	800 g/1000m	TY-030B-03
	24K	903 ft/lbs	1,650 g/1000m	TY-030B-03
Sizing Type	50C		1.0 %	TY-030B-05
& Amount	60E		0.3 %	TY-030B-05
	FOE		0.7 %	TY-030B-05
	Twist	Never twisted		

FUNCTIONAL PROPERTIES

CTE		-0.38 $\alpha \cdot 10^{-6}/^{\circ}C$
Specific Heat		0.18 Cal/g·°C
Thermal Conductivity		0.0224 Cal/cm·s·°C
Electric Resistivity		1.6 x 10^{-3} Ω·cm
Chemical Composition:	Carbon	93 %
	Na + K	<50 ppm

COMPOSITE PROPERTIES*

Tensile Strength	370 ksi	2,550 MPa	ASTM D-3039
Tensile Modulus	20.0 Msi	135 GPa	ASTM D-3039
Tensile Strain	1.7 %	1.7 %	ASTM D-3039
Compressive Strength	215 ksi	1,470 MPa	ASTM D-695
Flexural Strength	245 ksi	1,670 MPa	ASTM D-790
Flexural Modulus	17.5 Msi	120 GPa	ASTM D-790
ILSS	13 ksi	9 kgf/mm^2	ASTM D-2344
90° Tensile Strength	10.0 ksi	69 MPa	ASTM D-3039

* Toray 250°F Epoxy Resin. Normalized to 60% fiber volume.

Appendix B – Chemical Analysis

Mass Spectroscopy Results

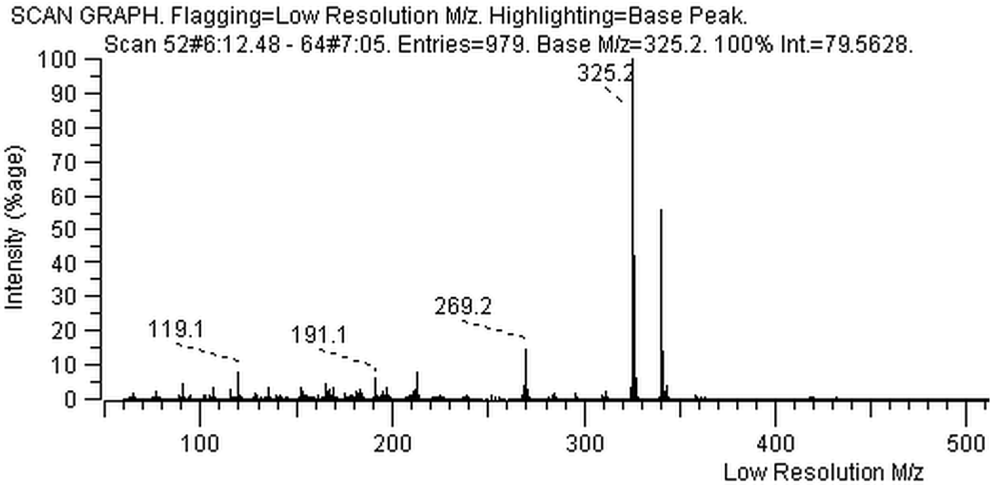

Figure B.1 – Mass spectroscopy of epoxy resin, CLR 1180

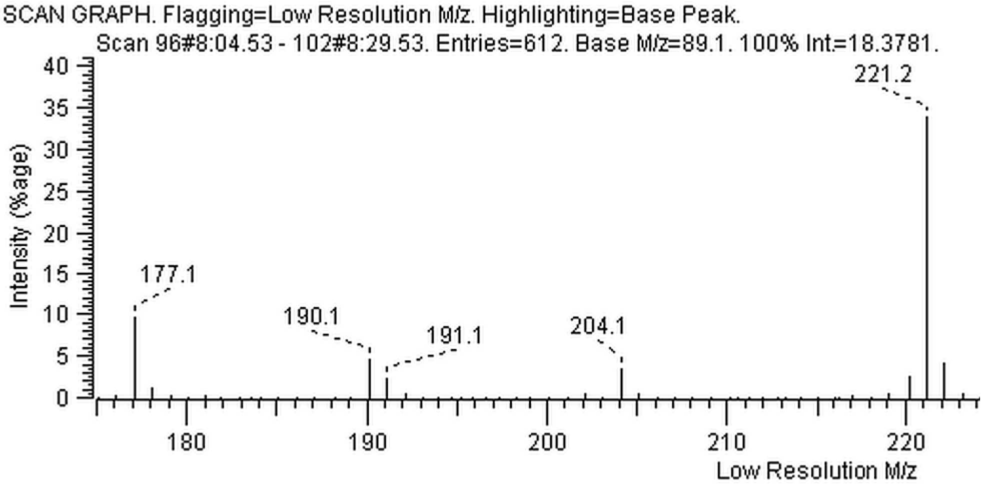

Figure B.2 – Mass spectroscopy of epoxy hardener, CLH 6560

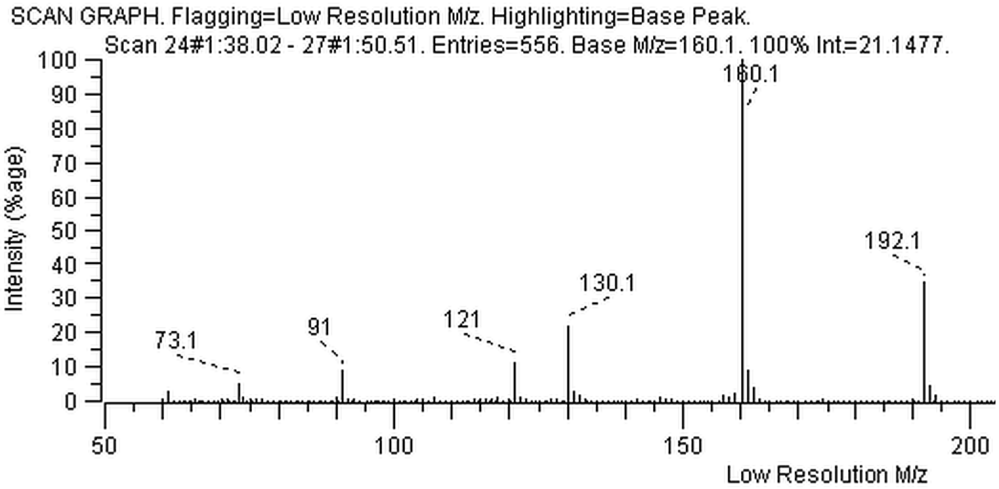

Figure B.3 – Mass spectroscopy of silane Z6020

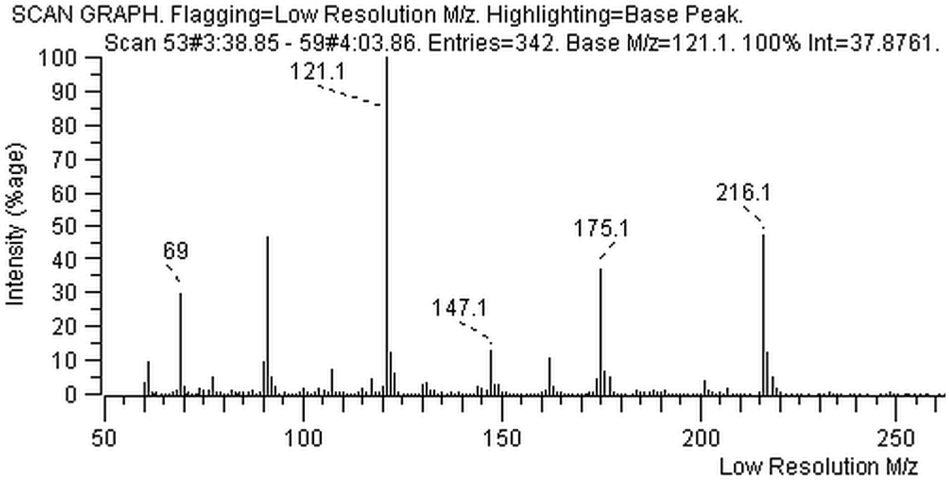

Figure B.4 – Mass spectroscopy of silane Z6030

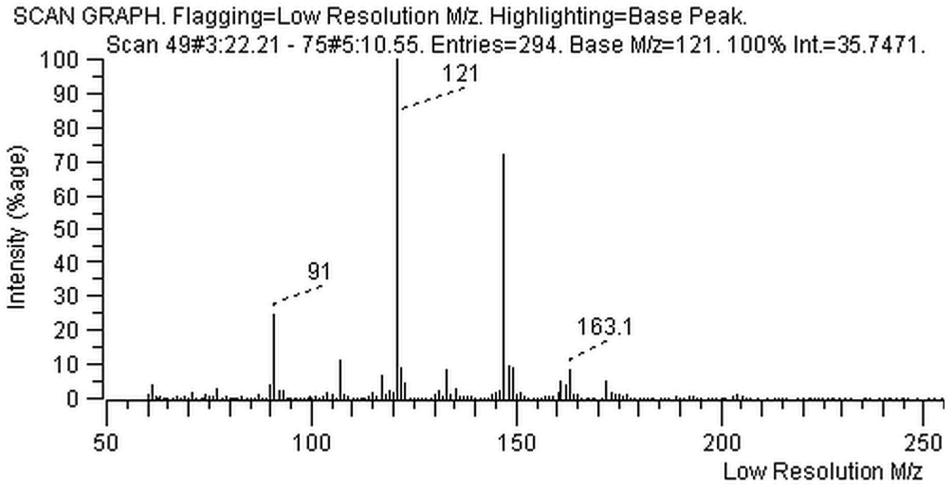

Figure B.5 – Mass spectroscopy of silane Z6040

Nuclear Magnetic Resonance Results

The full nuclear magnetic resonance (NMR) spectra for each of the analyzed compounds are presented below. All the spectra were obtained using proton NMR with deuterated methanol at room temperature. Since all the chemical signatures matched to the expected compounds from the mass spectroscopy, only the aggregate results are show, and no detailed analysis is presented. Noted chemist Dr. Kim Baines who kindly reviewed the spectra is quoted as saying, “At long last I have had a chance to review the spectra. I am happy to say that all looks well.” Expanded sections of each spectrum are available upon request.

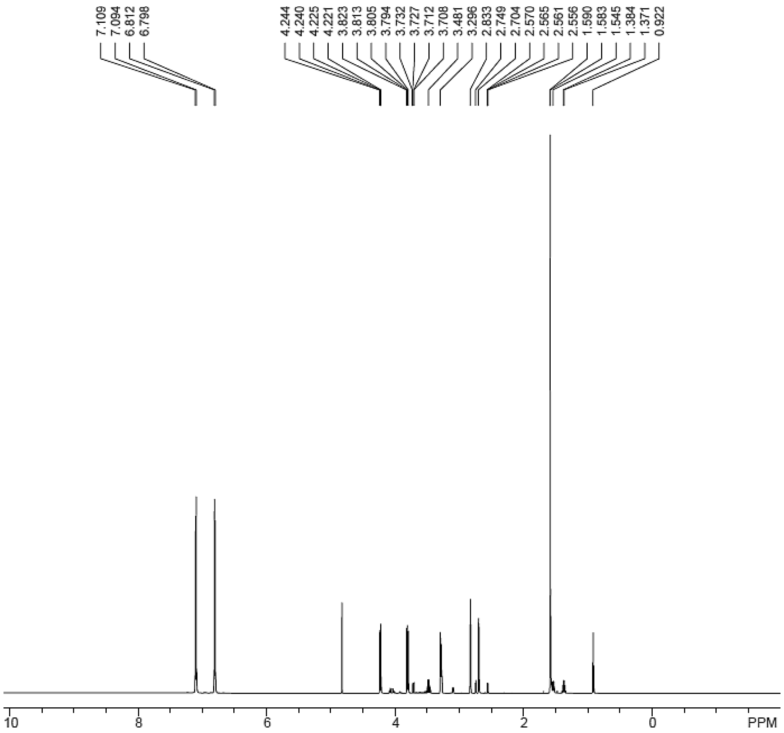

Figure B.6 – NMR spectra for CLR 1180

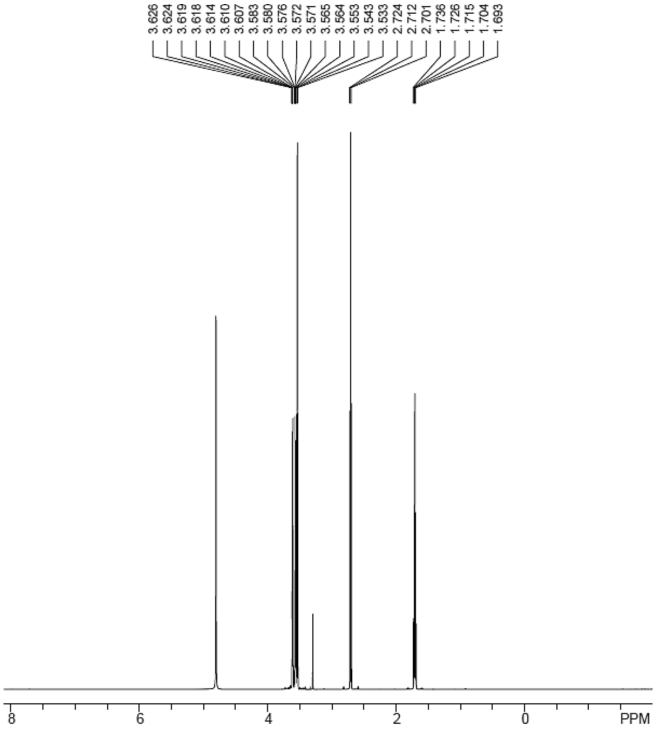

Figure B.7 – NMR spectra for CLH 6560

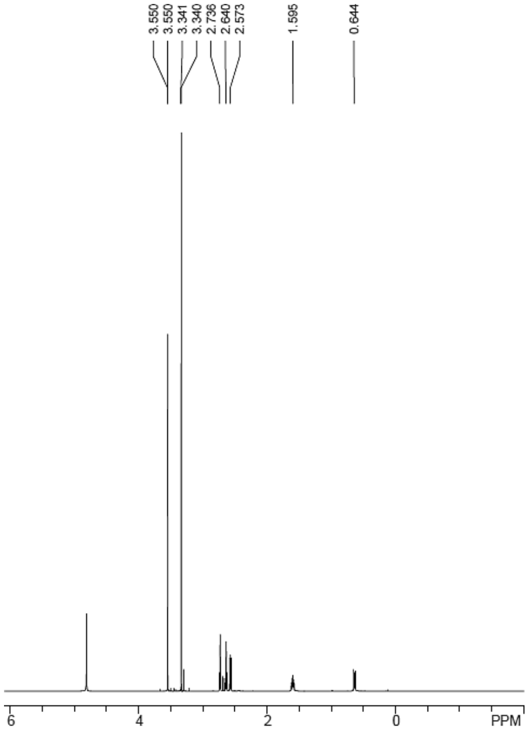

Figure B.8 – NMR spectra for Z6020

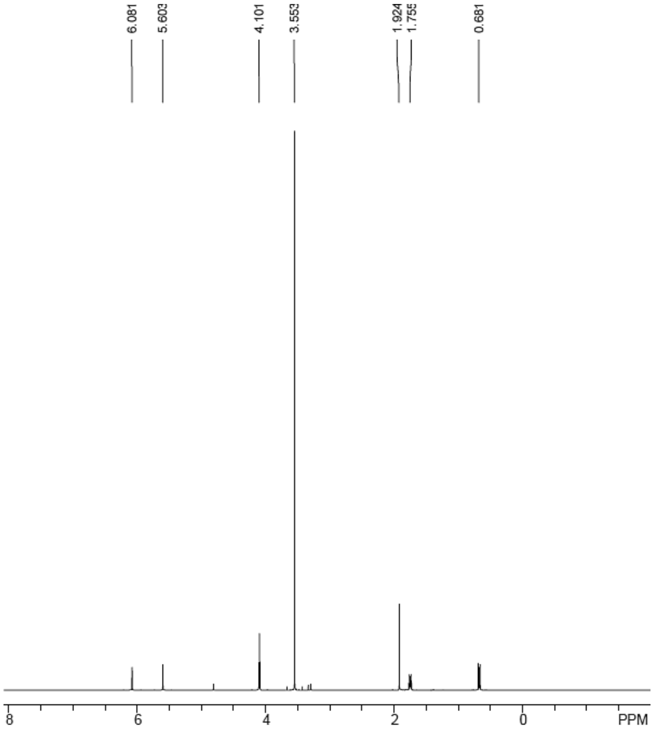

Figure B.9 – NMR spectra for Z6030

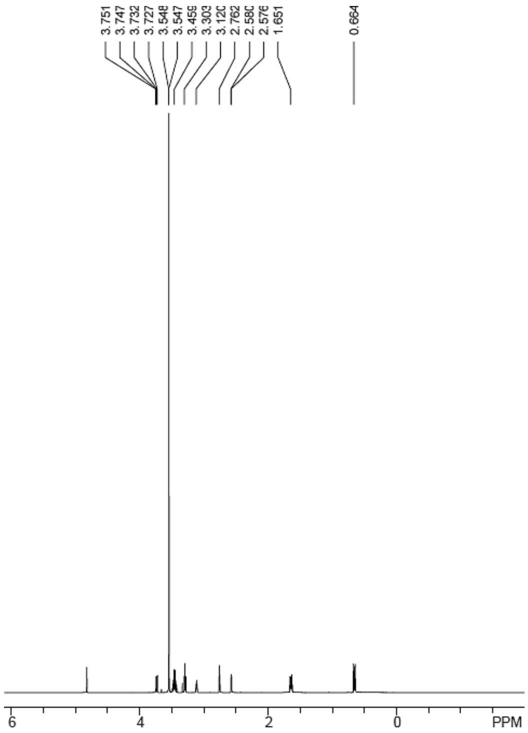

Figure B.10 – NMR spectra for Z6040

Appendix C – Fracture Model Area Derivations

This appendix contains the derivations for the area ratios of fibre, matrix, interface and pullout areas as related to the unit cell areas. This is divided into separate sections detailing the derivations for the square and hexagonal unit cells as presented in Chapter 6, as well as the modified parameters for dealing with delamination.

Square unit cell

Recall the unit cell image:

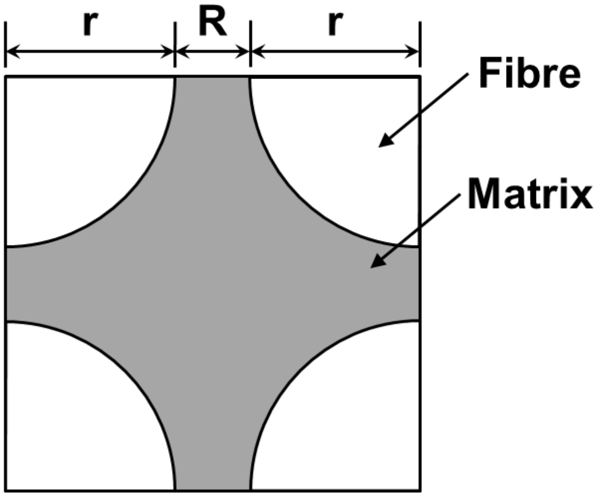

Figure C.1 – Square unit cell indicating fibre, matrix, and dimensions

There are two extremes to consider in order to generate the area fractions: when the fibre axis is parallel to the crack plane and when the fibre axis is perpendicular to the crack plane. In Figure C.1, the fibres are shown perpendicular to the crack plane, while the parallel direction is interpreted as perpendicular one edge of the unit cell into the page. For consistency in identifying the variables, the perpendicular case will be termed normal, and the parallel case termed shear. The average value will also be shown for random fibre cases where there is no need to integrate for each fibre orientation angle.

Normal and shear areas of the unit cell:

$$A_{sq,n} = (2r + R)^2 \tag{C.1}$$

$$A_{sq,s} = (2r + R)l \tag{C.2}$$

where r is the fibre radius, l is the length, and R, the fibre separation distance, is equal to:

$$R_{sq} = 2r\left(\sqrt{\frac{\pi}{4v_f}} - 1\right) \tag{C.3}$$

Normal and shear areas of fibres within the unit cell:

$$A_{f,n} = \pi r^2 \tag{C.4}$$

$$A_{f,s} = \pi r l \tag{C.5}$$

Normal and shear areas of matrix within the unit cell as the difference between Equations C.1 & C.2 and C.4 & C.5:

$$A_{m,n} = (2r + R)^2 - \pi r^2 \tag{C.6}$$

$$A_{m,s} = (2r + R)l - \pi r l \tag{C.7}$$

Normal and shear matrix area fractions from Equations C.1, C.2, C.6, and C.7:

$$\eta_{m,n} = \frac{A_{m,n}}{A_{sq,n}} = \frac{(2r + R)^2 - \pi r^2}{(2r + R)^2} = 1 - \frac{\pi r^2}{(2r + R)^2} \tag{C.8}$$

$$\eta_{m,s} = \frac{A_{m,s}}{A_{sq,s}} = \frac{(2r + R)l - \pi r l}{(2r + R)l} = 1 - \frac{\pi r}{2r + R} \tag{C.9}$$

The average matrix area fraction then becomes:

$$\bar{\eta}_m = \frac{\eta_{m,n} + \eta_{m,s}}{2} = 1 - \frac{\pi r(3r + R)}{2(2r + R)^2} \tag{C.10}$$

Equation C.10 does not need to be combined per the mixed-mode ratio as with the critical strain energy release rates, as this will simply govern the ratio of the debond area encountered ahead of a crack for a random fibre distribution. The mixed-mode condition for the CSERR will take care of the global strain energy value.

Normal and shear matrix plastic radius area fractions; the normal fraction is limited to the size of the unit cell while the shear extends between two unit cells:

$$\eta_{p,n} = \frac{2r + R}{r_p} \tag{C.11}$$

$$\eta_{p,s} = \frac{2(2r + R)}{r_p} = 2\eta_{p,n} \tag{C.12}$$

where the plastic radius is given as:

$$r_p = \frac{E_m G_{Ic,m}}{2\pi\sigma_{y,m}^2} \tag{C.13}$$

Note, for small volume fractions, if the unit cell size is greater than the unconstrained plastic radius, the area fraction is set to unity:

$$\eta_{p,x} = \begin{cases} \eta_{p,x} & \eta_{p,x} < 1 \\ 1 & \eta_{p,x} \geq 1 \end{cases} \tag{C.14}$$

The average plastic radius area fraction then becomes:

$$\bar{\eta}_p = \frac{\eta_{p,n} + \eta_{p,s}}{2} = \frac{3(2r + R)}{2r_p} \tag{C.15}$$

Normal and shear pullout area fractions:

$$\eta_{o,n} = \frac{A_{pullout}}{A_{sq,n}} = \frac{\pi r l_p}{(2r + R)^2} \tag{C.16}$$

$$\eta_{o,s} = 0 \tag{C.17}$$

Where l_p is the pullout length based half on the statistical critical fibre stress transfer length, l_c, from [95] as:

$$l_p = \frac{4}{3}\frac{l_c}{2} = \frac{2l_c}{3} \tag{C.18}$$

where the critical stress transfer length is given by:

$$l_c = \frac{3}{16}\frac{r\sigma_f^*}{\tau_i} \tag{C.19}$$

Substituting Equation C.19 into Equation C.18:

$$l_p = \frac{r\sigma_f^*}{8\tau_i} \tag{C.20}$$

The average pullout area fraction is then given by:

$$\bar{\eta}_o = \frac{\eta_{o,n} + \eta_{o,s}}{2} = \frac{\pi r l_p}{2(2r+R)^2} \tag{C.21}$$

The interfacial normal area fractions in both the fibre extreme orientations are:

$$\eta_{i,n,n} = \frac{A_{f,n}}{A_{sq,n}} = \frac{\pi r^2}{(2r+R)^2} \tag{C.22}$$

$$\eta_{i,n,s} = \frac{A_{f,s}}{A_{sq,s}} = \frac{\pi r}{2r+R} \tag{C.23}$$

Averaging Equations C.16 and C.17 yields the average interfacial normal area fraction:

$$\bar{\eta}_{i,n} = \frac{\eta_{i,n,n} + \eta_{i,n,s}}{2} = \frac{\pi r(3r+R)}{2(2r+R)^2} \tag{C.24}$$

The interfacial shear area fractions in both the fibre extreme orientations are:

$$\eta_{i,s,n} = \frac{A_{f,s}}{A_{sq,n}} = \frac{\pi r l_d}{(2r+R)^2} \tag{C.25}$$

$$\eta_{i,s,s} = 0 \tag{C.26}$$

Averaging Equations C.16 and C.17 yields the average interfacial normal area fraction:

$$\bar{\eta}_{i,s} = \frac{\eta_{i,s,n} + \eta_{i,s,s}}{2} = \frac{\pi r l_d}{2(2r+R)^2} \tag{C.27}$$

Similar to the pullout case, l_d, the debond length, is based on the critical stress transfer length. However, here a fibre can debond above and below the crack plane, utilizing the full critical fibre stress transfer length:

$$l_d = l_c \tag{C.28}$$

In a mixed-mode case when the normal and shear components can be combined, the interfacial area fraction becomes:

$$\bar{\eta}_i = \eta_{i,s} + \frac{\eta_{i,n}}{2} = \frac{\pi r(2l_d + 3r + R)}{4(2r + R)^2} \tag{C.29}$$

For fibre failure, fibres are assumed to only fracture perpendicular to their axis, or in the normal orientation so the average area fraction is:

$$\bar{\eta}_f = \frac{1}{2}\frac{A_{f,n}}{A_{sq,n}} = \frac{\pi r^2}{2(2r + R)^2} \tag{C.30}$$

The only remaining correction is that of the fillers, which is based on the filler volume fraction:

$$\eta_\phi = 1 - v_{fillers} \tag{C.31}$$

Hexagonal unit cell

Recall the hexagonal unit cell as segmented into an equilateral triangle:

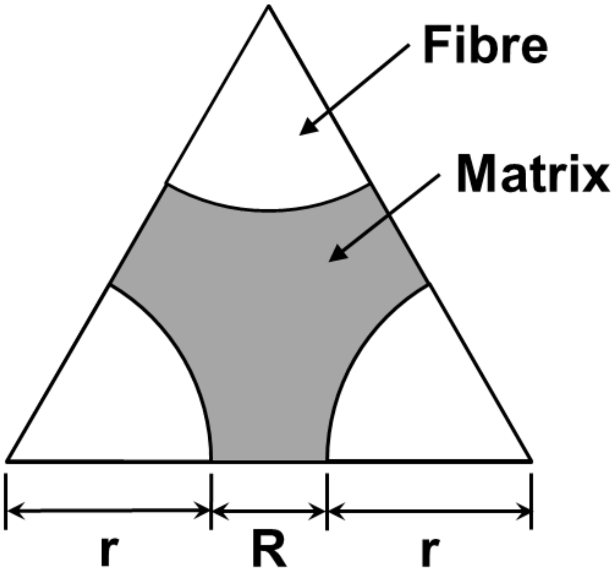

Figure C.2 – Hexagonal unit cell segment with fibre, matrix, and dimensions

The same process is used to generate the area fractions as with the square unit cell, with the same initial assumptions.

Normal and shear areas of the hexagonal unit cell:

$$A_{hx,n} = \frac{\sqrt{3}}{4}(2r + R)^2 \tag{C.32}$$

$$A_{hx,s} = (2r + R)l \tag{C.33}$$

where r is the fibre radius, l is the length, and R, the fibre separation distance, is equal to:

$$R_{hx} = 2r\left(\sqrt{\frac{\pi}{2\sqrt{3}v_f}} - 1\right) \tag{C.34}$$

Normal and shear areas of fibres within the unit cell:

$$A_{f,n} = \frac{\pi r^2}{2} \tag{C.35}$$

$$A_{f,s} = \frac{2\pi r l}{3} \tag{C.36}$$

Normal and shear areas of matrix within the unit cell as the difference between Equations C.32 & C.33 and C.35 & C.36:

$$A_{m,n} = \frac{\sqrt{3}}{4}(2r + R)^2 - \frac{\pi r^2}{2} \tag{C.37}$$

$$A_{m,s} = (2r + R)l - \frac{2\pi r l}{3} \tag{C.38}$$

Normal and shear matrix area fractions from Equations C.1, C.2, C.6, and C.7:

$$\eta_{m,n} = \frac{A_{m,n}}{A_{hx,n}} = \frac{\frac{\sqrt{3}}{4}(2r + R)^2 - \frac{\pi r^2}{2}}{\frac{\sqrt{3}}{4}(2r + R)^2} = 1 - \frac{2\pi r^2}{\sqrt{3}(2r + R)^2} \tag{C.39}$$

$$\eta_{m,s} = \frac{A_{m,s}}{A_{hx,s}} = \frac{(2r + R)l - \frac{2\pi r l}{3}}{(2r + R)l} = 1 - \frac{2\pi r}{3(2r + R)} \tag{C.40}$$

The average matrix area fraction then becomes:

$$\bar{\eta}_m = \frac{\eta_{m,n} + \eta_{m,s}}{2} = \frac{-\sqrt{3}\pi r^2 - 2\pi r^2 + 12r^2 - \pi rR + 12rR + 3R^2}{3(2r + R)^2} \tag{C.41}$$

Normal and shear matrix plastic radius area fractions:

$$\eta_{p,n} = \frac{2r + R}{r_p} \tag{C.42}$$

$$\eta_{p,s} = \frac{2\left(\sqrt{(2r + R) - \left(r + \frac{R}{2}\right)^2} - r\right)}{r_p} = \frac{\sqrt{3}\sqrt{(2r + R)^2} - 2r}{r_p} \tag{C.43}$$

The average plastic radius area fraction then becomes:

$$\bar{\eta}_p = \frac{\eta_{p,n} + \eta_{p,s}}{2} = \frac{\sqrt{3}(2r + R) + R}{2r_p} \tag{C.44}$$

The average pullout area fraction is given by:

$$\bar{\eta}_o = \frac{2\sqrt{3}\pi r l_p}{9(2r + R)^2} \tag{C.45}$$

The interfacial normal area fractions in both the fibre extreme orientations are:

$$\eta_{i,n,n} = \frac{A_{f,n}}{A_{hx,n}} = \frac{\frac{\pi r^2}{2}}{\frac{\sqrt{3}}{4}(2r + R)^2} = \frac{2\pi r^2}{\sqrt{3}(2r + R)^2} \tag{C.46}$$

$$\eta_{i,n,s} = \frac{A_{f,s}}{A_{hx,s}} = \frac{\frac{2\pi r l}{3}}{(2r + R)l} = \frac{2\pi r}{3(2r + R)} \tag{C.47}$$

Averaging Equations C.46 and C.47 yields the average interfacial normal area fraction:

$$\bar{\eta}_{i,n} = \frac{\eta_{i,n,n} + \eta_{i,n,s}}{2} = \frac{\pi r\left(\sqrt{3}r + 2r + R\right)}{3(2r + R)^2} \tag{C.48}$$

The interfacial shear area fractions in both the fibre extreme orientations are:

$$\eta_{i,s,n} = \frac{A_{f,s}}{A_{hx,n}} = \frac{\frac{2\pi r l}{3}}{\frac{\sqrt{3}}{4}(2r + R)^2} = \frac{4\sqrt{3}\pi r l_d}{9(2r + R)^2} \tag{C.49}$$

$$\eta_{i,s,s} = 0 \tag{C.50}$$

Averaging Equations C.49 and C.50 yields the average interfacial normal area fraction:

$$\bar{\eta}_{i,s} = \frac{\eta_{i,s,n} + \eta_{i,s,s}}{2} = \frac{2\sqrt{3}\pi r l_d}{9(2r+R)^2} \tag{C.51}$$

In a mixed-mode case when the normal and shear components can be combined, the interfacial area fraction becomes:

$$\bar{\eta}_i = \eta_{i,s} + \frac{\eta_{i,n}}{2} = \frac{\pi r\left(8\sqrt{3}l_d + 3\sqrt{3}r + 6r + 3R\right)}{18(2r+R)^2} \tag{C.52}$$

For fibre failure, fibres are assumed to only fracture perpendicular to their axis, or in the normal orientation so the average area fraction is:

$$\bar{\eta}_f = \frac{1}{2}\frac{A_{f,n}}{A_{hx,n}} = \frac{\pi r^2}{\sqrt{3}(2r+R)^2} \tag{C.53}$$

The same correction is made to the fillers as with the square unit cell:

$$\eta_{\phi} = 1 - v_{fillers} \tag{C.54}$$

Delamination parameters

Recall the picture of delamination:

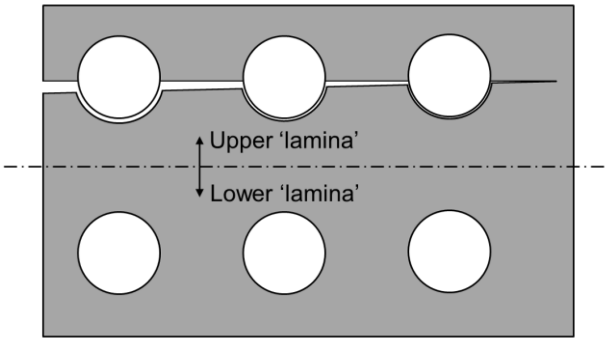

Figure C.3 – Idealized delamination in a long-fibre composite

where the delamination is predominately a matrix and interfacial feature. The three delamination parameters are the area fractions for fibres, matrix, and matrix plastic radius for the in-plane fracture condition. From the previous assumption that the fibres are uniformly distributed, the thickness of the resin-rich layer between the random fibre lamina will be R, the fibre separation distance. For delamination where this is not the case, as with fabric lamina, then this initial assumption will need to change to reflect the proper calculation for the matrix plastic area fraction.

The modified matrix area fraction becomes:

$$\eta_p' = \frac{\eta_p + 2\eta_p}{2} = \frac{3\eta_p}{2} \tag{C.55}$$

which allows for a plastic radius of one unit cell above the crack plane, and two below (or vice versa).

The lower crack plane is expected to be entirely matrix, with the upper plane a combination of matrix and fibres. The unit cell in this case is assumed uniform following the parallel (shear) case from above. The matrix area fraction is thus:

$$\eta_m' = \frac{R}{2r + R} \tag{C.56}$$

The interface is interesting in the delamination case, as there can now be fibres aligned or perpendicular, but always in plane of the crack. Again the assumption of randomly angled fibres drives this calculation, where the interfacial cases are identical, but would change with the use of a fibre angle distribution function. So, the interface becomes the average as:

$$\eta_i' = \frac{\eta_{i,\parallel} + \eta_{i,\perp}}{2} = \frac{\pi r}{2r + R} \tag{C.57}$$

Curriculum Vitae

Ian Swentek

EDUCATION

Doctor of Philosophy 2014

Department of Mechanical and Materials Engineering, Western University
Thesis: Interfacial fracture mechanics of long-fibre polymer composites
Supervisor: Dr. Jeffrey Wood

M.Eng.	Mechanical Enigneering	U. Western Ontario	2010
B.E.Sc.	Mechanical Engineering	U. Western Ontario	2008
B.Sc.	Computer Science	U. Western Ontario	2008

RESEARCH CONTRIBUTIONS

1. **Swentek, I**., Bhakhri V., Wood, J.T., Klassen R. (2014) A new geometry for the fibre push-out test with reinforced polymer composites. Composites Part A: Science. (Submitted).
2. **Swentek, I.**, Wood, J.T, and Charpentier P. (2014) Experimental and simulation studies of a thermoset polymer composite during cure. Composites Science and Technology. (Submitted).
3. **Swentek, I.** and Wood, J.T. (2013) Measuring polymer composite interfacial strength. Composites Part B: Engineering. 58, 235-241.
4. **Swentek, I.** and Wood, J.T. (2013). Using the lap-shear test to measure polymer composite interfacial strength. The 19th International Conference on Composite Materials. International conference, oral presentation of paper.
5. **Swentek, I.** and Wood, J.T. (2013) Development of a multi-physics simulation of a thermoset polymer composite. The 20th Center for Materials and Biomaterials Research Day, oral presentation.
6. **Swentek, I.** and Wood, J.T. (2012) Interfacial strength of an epoxy/glass model system for composite material. The 24th Canadian Materials Science Conference. National conference, oral presentation.

PROFESSIONAL EXPERIENCE

July 2014 - Present

Research Engineer

Fraunhofer Project Center at the University of Western Ontario

- Responsible for fibre simulation and draping study
- Ongoing SMC customer development and project management

Summer 2013, 2014

Limited duties instructor

The University of Western Ontario

- Composed and delivered a first-year engineering course
- Developed in-class demonstration modules to augment the lecture series

January 2011 – April 2014

Teaching Assistant

The University of Western Ontario

- Lead TA for various courses, coordinating other TA activities
- Prepared teaching aids, interactive laboratories, and experiments
- Regularly provided instruction to ~40 students

June 2010 – February 2011

Senior Release Document Analyst

General Dynamics Land Systems Canada

- Provided training and support for afternoon shift team
- Produced company-wide training materials for system roll-out

PROFESSIONAL SKILLS

Project management
Interdepartmental collaboration
Continuous improvement

LEADERSHIP

Graduate representative; MME department council	2012 – 2014
Leadership and mentorship program; mentor	2014
Engineering Decanal Search Committee	2013

VOLUNTEERING

President, Board of Directors, Medway Housing Cooperative	2011 – Present
FSAE Alumni Consultant; energy management	2012 – 2014
CAMBR Research Day; volunteer	2013

AFFILIATIONS

Society of Plastics Engineers (SPE)
Canadian Association for Composite Materials and Structures (CACSMA)
Society for the Advancement of Material and Process Engineering (SAMPE)